Development of New Fluorophore-Tethered ortho-Carborane Systems: An Approach for Unique Photophysics and Applications

Sohini Sinha

Universitat Autònoma de Barcelona

Development of New Fluorophore-Tethered *ortho*-Carborane Systems: An Approach for Unique Photophysics and Applications

Sohini Sinha

DOCTORAL THESIS

Ph. D. in Chemistry

Supervisor

Dr. Rosario Núñez

Institut de Ciència de Materials de Barcelona (ICMAB)-CSIC

Departament de Química - Facultat de Ciències

2022

Presented to aspire to the Doctorate in Chemistry Degree by Sohini Sinha.

Dr. Rosario Núñez
Research Scientist of Consejo Superior de Investigaciones Científicas
INSTITUT DE CIÈNCIA DE MATERIALS DE BARCELONA-CSIC

Bellaterra, 23rd September 2022

La Doctora ROSARIO NÚÑEZ, Investigadora Científica del Consejo Superior de Investigaciones Científicas (CSIC) en el Instituto de Ciencia de Materiales de Barcelona (ICMAB),

CERTIFICA:

Que Sohini Sinha, licenciada en Química, ha realizado bajo su dirección la tesis doctoral titulada "**Development of new fluorophore-tethered *ortho*-carborane systems: An approach for unique photophysics and applications**" y que se recoge en esta memoria para optar al grado de Doctora en Química por la Universitat Autònoma de Barcelona.

Y para que así conste y tenga los efectos oportunos, firmo este certificado en Bellaterra, a 23 de Septiembre de 2022.

Dr. Rosario Núñez
ICMAB-CSIC

This work was financially supported by MINECO (CTQ2016-75150-R), Agencia Estatal de Investigación AEI from MICINN (PID2019-106832RB-100/AEI/10.13039/501100011033, Proof of Concept project PDC2021-121183-I00, and the Severo Ochoa Program for Centers of Excellence through SEV2017-0706 and FUNFUTURE CEX2019-000917-S projects and Generalitat de Catalunya (2017/SGR/1720). S. S. acknowledges financial support from DOC-FAM, the European Union's Horizon 2020 research and innovation programme under the Marie Sklodowska-Curie grant agreement No 754397.

The dissertation defense of the present work is scheduled for 26th October 2022. The thesis Committee consists of the following:

- President: Jordi Poater, Universitat de Barcelona (UB)
- Secretary: Arántzazu González Campo, Institut de Ciència de Materials de Barcelona (ICMAB-CSIC))
- Vocal: Annamaria Deagostino, Università degli Studi di Torino (Italy)

Committee substitutes:

- Substitute 1: Claudio Roscini, ICN2
- Substitute 2: M. Isabel Romero, Universitat de Girona (UdG)

This thesis is dedicated to my parents.

Acknowledgements

Now that I am at the end of this incredible journey as a PhD student of ICMAB-CSIC and at department of chemistry, UAB, I would try to express my gratitude towards many people for their continuous patience, support and knowledge. I am extremely grateful to my supervisor, group members, collaborators, friends and family.

Firstly, I would like to thank my supervisor Dr. Rosario Núñez for giving me this opportunity to become a part of this wonderful research group as a PhD candidate. I am going to carry all the memories of long hour discussions regarding problems and challenges experienced not only in the laboratory but also in personal life. Her immense patience, knowledge and guidance cannot be just described in words, she has always encouraged me and boosted my confidence with her motivating words, kindness, and way of solving problems. Thank you for always guiding me through all the processes during the entire PhD tenure and keep pushing me forward towards the finish line. I have learned a lot, starting from basic concepts to complex molecules, and I shall continue to learn.

I would also like to extend my deepest gratitude towards Prof. Francesc Teixidor, Prof. Clara Viñas and Dr. Jose Giner. Whenever I got an opportunity, I have tried to make a note from their useful feedbacks and comments, which has helped me a lot in my presentations and understanding some fundamental concepts. Their vast knowledge in the field of boron cluster chemistry has always been very helpful and encouraging.

It was a pleasure working closely and briefly with Dr. Marisa Romero and her TFG students, she has been very patient, kind and interested in knowing all the techniques and calculations used and as well as share her own ideas. Jordi

Cortés Donaire has been super helpful in the laboratory with his fast and efficient way of working.

Now I would like to mention some of the most important collaborators and facilities used in the laboratory of Dr. Jordi Hernando from UAB, Dr. Claudio Roscini from ICN2 and Salvador Bartolome from UAB, for their incredible support right from using fluorescence techniques to their knowledge and suggestions at any given point of time throughout the year. Since most of our research line is related to fluorescence, without their support I would not have accomplished my work. Thanks to Dr. Zsolt Keleman and Dr. Pacal Lacroix for sharing their many years of experience in DFT calculations and having the patience to make me understand some of the theoretical concepts. I am also grateful for participating in the interesting projects which involves Prof. Cristina Prandi and Dr. Norberto Farfan. Without all the support from the experts mentioned above, I would not have been able to finish my PhD. So, thanks to my supervisor again, for introducing me to these wonderful scientists that I have got an opportunity to work with and share publications.

It is well known that, sometimes you face challenges in experiments, and it seems impossible to proceed or find an application, and exactly then Dr. Aleksandr Perevendentsev and now Dr. Jose Piers Jurado helped me to find a probable solution to my problem by collaborating and carrying out some interesting thin film experiments. Thanks to Dr. Imma Ratera from, NANOMOL (ICMAB-CSIC) for providing her laboratory services and her expertise on organic nanoparticles. Finally, I would like to thank Dr. Albert Ferrer Ugalde, Dr. Isabel Guerrero and Dr. Maria José Mostazo López for always being super welcoming and helpful me in the laboratory.

What is a good work without a good team? So, I would like to thank the rest of our current and ex-group members, Miquel Nuez, Jewel Anna Maria

Xavier, Zhen Li, Xiaobao Li, Flavia, Lei, Isabel, Arpita and Abhishek. Although many of them are doctors now but I know them first as friends. I would specially like to thank Jewel, Miquel and Zhen for their lots of suggestions, incredible support as a colleague and a friend. I will cherish all the memories of having meet ups and attending seminars in Spanish and Catalan. They have taught me to use some techniques in the lab, shared their knowledge and helped me at work, in personal life and for numerous documents required by the administration. I am grateful for your friendship for all these years, I always say that I have a great team at ICMAB and it is true. Having said that, I have met some people at ICMAB and now they have turned out to be great friends, a special thanks to Dr. Adara Babuji for always being there throughout all these years whether at ICMAB or in my house and now on calls. Her support and words have helped me a lot to overcome some of the difficult situations and I will always cherish all the fond memories. Thanks to my DOC-FAM team members, all of them have supported and showed interest in conducting workshops and conferences together.

Thanks to all my housemates Mani, Marc, Kelly, Alex, Judith and some more friends for making my stay here in Barcelona memorable. Thanks to Umair, for helping me to use ICN2 facilities and for all the fruitful discussions. Special thanks to my family, including my parents, my big brother, sister-in-law and my beloved niece. Thanks for your support and encouragement, especially for what I have chosen throughout my life, I will be forever indebted to you. Finally, I want to express my gratitude to the DOC FAM Marie Sklodowska-Curie grant, Severo Ochoa Program and LMI group, who sponsored for my entire PhD tenure including, some of the lab resources, living cost, research stay and other expenses. I also would like to thank MICINN though Proof of Concept project PDC2021-121183-I00 and all the grants that covered my experimental cost.

The present PhD thesis has been carried out at the Laboratory of Inorganic Materials and Catalysis (LMI) of the Materials Science Institute of Barcelona ICMAB (CSIC) following the Doctoral Programme in Chemistry of the Autonomous University of Barcelona (UAB). According to the decision of the PhD commission, this Thesis is presented as a compendium of publications. Additionally, and with the idea of providing a more complete thesis, some additional results obtained before the deposit of the present work and in process of publication are also included.

The publications accepted in the compendium are listed below in order of their appearance in the Thesis:

1) Red light-emitting Carborane-BODIPY dyes: Synthesis and properties of visible-light tuned fluorophores with enhanced boron content. Chiara Bellomo, Davide Zanetti, Francesca Cardano, Sohini Sinha, Mahdi Chaari, Andrea Fin, Andrea Maranzana, Rosario Núñez, Marco Blangetti and Cristina Prandi, *Dyes & Pigments*, 2021, 194, 109644.

2) *o*-Carborane-based fluorophores as efficient luminescent systems both as solids and as water-dispersible nanoparticles. Sohini Sinha, Zsolt Kelemen, Evelyn Hümpfner, Imma Ratera, Jean-Pierre Malval, José Piers Jurado, Clara Viñas, Francesc Teixidor and Rosario Núñez, *Chem. Commun*. 2022, 58, 4016.

Figures

Structures boranes and carboranes:

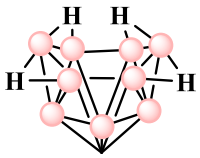

$B_{10}H_{14}$

Decaborane

1

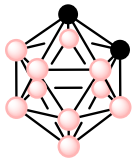

$1,2\text{-}C_2B_{10}H_{12}$

o-carborane

R = H, **2**

R = CH_3, **3**

R = Ph, **4**

R = $C_{10}H_{13}$, **5**

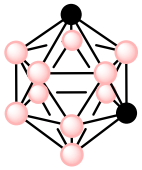

$1,7\text{-}C_2B_{10}H_{12}$

m-carborane

R = CH_3, **6**

R = Ph, **7**

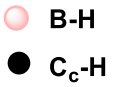

Chapter 3: *o-Carborane based fluorophores: a journey from solution to water dispersible nanoparticles*

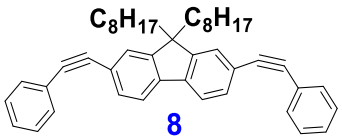

8

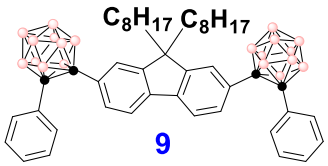

9

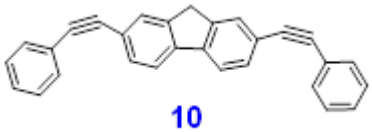

10

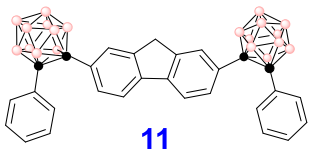

11

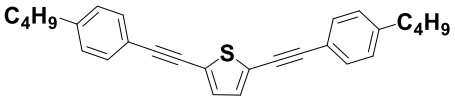

12

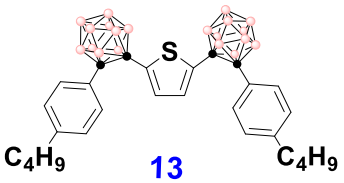

13

Chapter 4: *Synthesis, characterization and properties of red-light emitting carborane-BODIPY dyes*

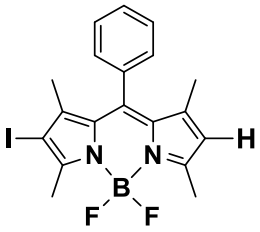

14a-c

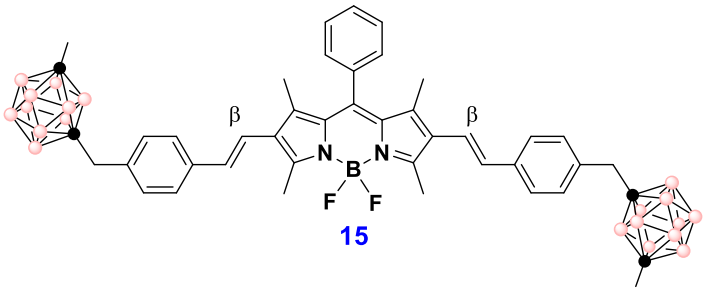

15

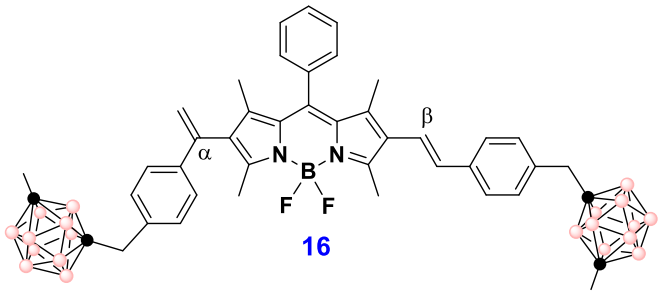

16

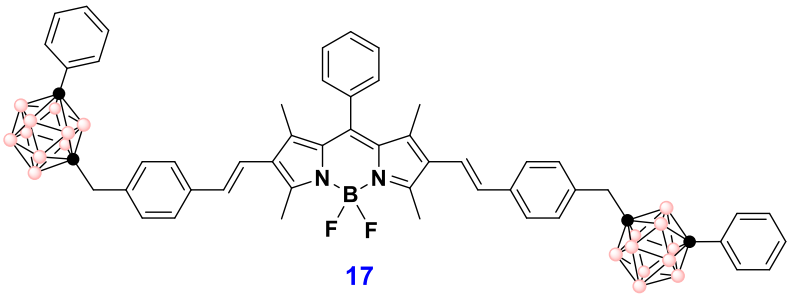

17

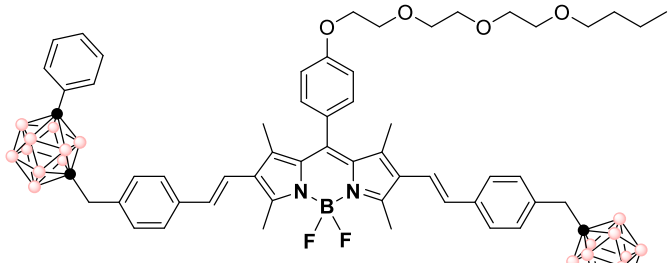

18

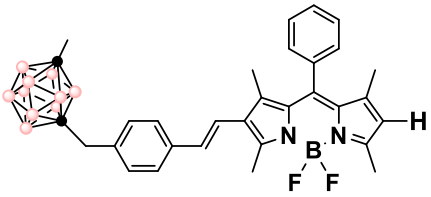

19

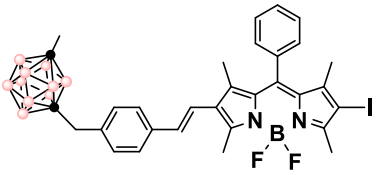

20

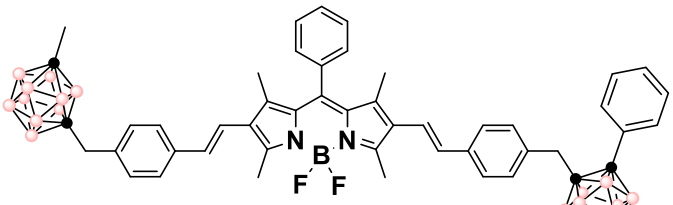

21

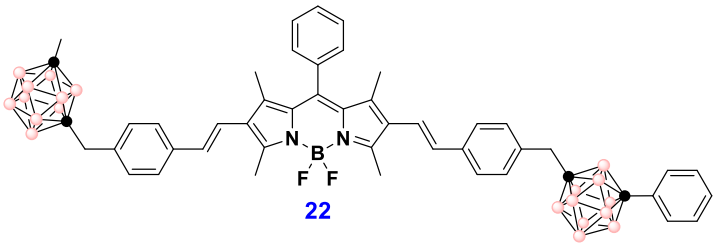

22

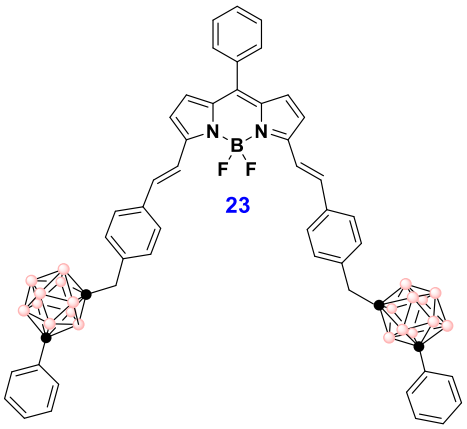

23

Chapter 5: *Luminescent behaviour of systems containing o-carborane linked to perylenediimide (PDI) fluorophores*

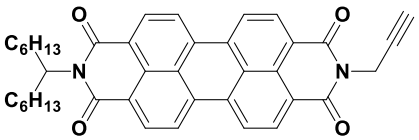

24

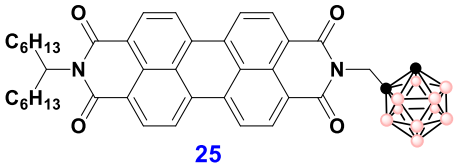

25

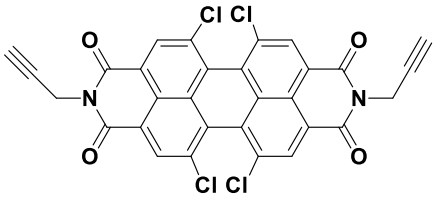

26

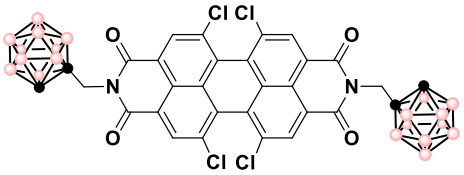

27

Chapter 6: *Synthesis, characterization and photophysical properties of new tri-branched fluorene & truxene systems bearing o-carborane clusters*

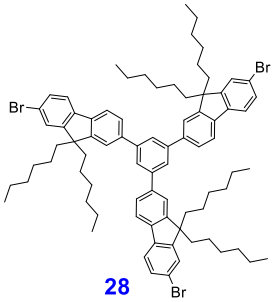

28

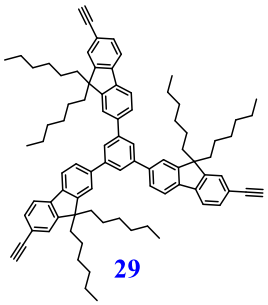

29

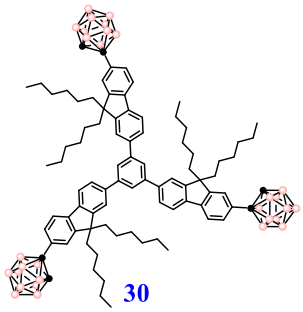

30

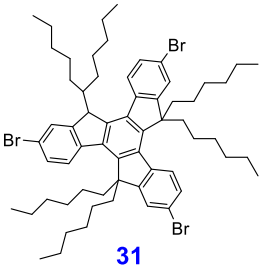

31

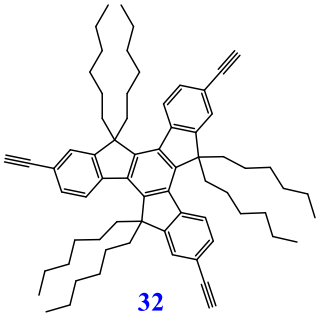

32

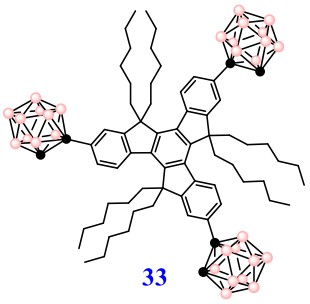

33

Abbreviations

ATR-FTIR	Attenuated total reflectance fourier transform infrared spectroscopy
AIE	Aggregation induced emission
AIEgen	Aggregation induced emission luminogen
ACQ	Aggregation caused quenching
B	Boron
BNCT	Boron neutron capture therapy
CB	Carborane
COSAN	Cobaltabis(dicarbollide)
CV	Cyclic voltammetry
CT	Charge transfer
DMSO	Dimethyl sulfoxide
DLS	Dynamic light scattering
DFT	Density functional theory
EtOH	Ethanol
$\mathbf{E_{onset}}$	Onset oxidation potential
$\mathbf{E_{gap}}$	Optical band gap
FL	Fluorescence
HOMO	Highest occupied molecular orbital
ICT	Intramolecular charge transfer
LUMO	Lowest unoccupied molecular

	orbital
LE	Locally excited
Me	Methyl
MeLi	Methyllithium
MeOH	Methanol
***m*-carborane or *m*CB**	*meta*-carborane
MS	Mass spectroscopy
MO	Molecular orbital
***n*-BuLi**	*n*-butyl lithium
NMR	Nuclear magnetic resonance
NPs	Nanoparticles
***o*-carborane or *o*CB**	*ortho*-carborane
***p*-carborane or *p*CB**	*para*-carborane
PDI	Perylene diimide
PL	Photoluminescence
Q.Y	Quantum yield
SEM	Scanning electron microscopy
TEM	Transmission electron microscopy
THF	Tetrahydrofuran
TLC	Thin layer chromatography
TPA	Two-photon absorption
UV-Vis	ultraviolet-visible
λ_{abs}	Absorption wavelength
λ_{em}	Emission wavelength
ε_m	Molar extinction coefficient

Abstract

The work presented in this manuscript follows with research lines initiated in the Inorganic Materials and Catalysis Laboratory (L M I) at Institute of Material Sciences of Barcelona (ICMAB-CSIC), based on the synthesis, characterization and study of new boron cluster derivatives with photoluminescent properties and their potential applications. Various types of carborane functionalized fluorophores (i.e fluorene, thiophene, BODIPY, perylenediimide, truxene) have been synthesized and characterized. The photoluminescence behavior of all these systems has been studied in details and specially, the influence of the *o*-carborane cluster on these properties. Some potential applications of those systems have been proposed and presented. It is important to note that in the last decade there has been a growing interest in the synthesis of molecular materials based on carborane clusters and especially in the study of their fluorescence properties, both in solution and in the solid state. The first publication related to this topic was from our group, in 2007, and since then we have been working to explore this new field within boron clusters. The contribution and progress that our group has made within this area of research has been very extensive, and in the recent years, more focused research has been carried out on the application of these materials in both optoelectronics and biomedicine.

Herein, the results and discussion chapters have been described briefly, highlighting the novelty in each case.

Chapter 3: *o-Carborane based fluorophores: a journey from solution to water dispersible nanoparticles*. This chapter describes the synthesis of donor-acceptor-donor (D-A-D) systems based on π-conjugated compounds (fluorene and thiophene) bound to *o*-carborane clusters and the study of their photophysical properties in solution, aggregate state, solid and film. It is important to notice that after linking the *o*-carborane cluster to the fluorene, a quenching of the fluorescence in solution was observed. Moreover, computational studied using density functional theory (DFT) were also performed in collaboration with Dr. Zsolt Kelemen from Budapest University of Technology and Economics, to support these experimental results. In contrast, one of the fluorene derivatives, containing alkyl chains, exhibited high fluorescence in the solid state, a phenomenon known as aggregation induced emission (AIE). This inspired us to prepare water-dispersible nanoparticles (NPs), which, to our knowledge, is the first example reported in the literature. These NPs exhibited extraordinary fluorescence, which makes them potential candidates for bioimaging applications in cells. As well as when deposited on thin films, it retained the quantum yield, which allowed us to do some preliminary tests in optoelectronics. This work has recently been published in Chemical Communication,, 2022, 58, 4016.

Chapter 4: *Synthesis, characterization and properties of red-light emitting carborane-BODIPY dyes.* This chapter covers the synthesis of a family of compounds based on BODIPY-carborane derivatives, their characterization and luminescence properties. Different derivatives of

BODIPY have been prepared, where C-substituted *o*- and *m*-carborane clusters where linked at the 3,5 and 2,6 positions. These starting BODIPYs have been prepared in collaboration with Prof. Cristina Prandi from the University of Torino, Italy. In general, it is observed that the introduction of the styrenyl-carborane cluster to the BODIPYs slightly affects the absorption and enhances the emission of the groups BODIPY. In general, the 2,6-disubstituted derivatives with an asymmetric morphology showed a decrease in fluorescence quantum yield when compared to the 3,5-disubstituted homologues. These systems showed high stability in organic solvents. Likewise, the fluorescence of the compounds increased in solutions of THF:H_2O (60:40) indicating an interaction of the compounds with water molecules. The fluorescence properties of the compounds and their high boron content make these compounds perfect candidates for biomedical applications, both for diagnosis (cell marking) and for use in anticancer therapy of BNCT. This work has been published in Dyes & Pigments, 2021, 194, 109644.

Chapter 5: *Luminescent behavior of systems containing o-carborane linked to perylenediimide (PDI) fluorophores.* This work has been carried out in collaboration with Dr. Jordi Hernando from the Autonomous University of Barcelona (UAB). The perylenediimides (PDI) are dyes with very intense fluorescence that has two important drawbacks: low solubility due to strong π-π stacking and loss of their excellent emission properties in the solid state, where the characteristic red shift of the excimer emission is observed with low efficiency. To overcome these limitations, in this work we have prepared various PDI derivatives containing *o*-carborane units, which are bulky boron clusters intended to discourage close molecular packing of these dyes through π interactions.

Photophysical properties were measured in solution, aggregation, nanoparticles and in solid. As a result, the PDI-*o*-carborane conjugates show a significant improvement in solubility in many organic solvents, while showing excellent optical properties in solution, with quantum yield up to 100%. However, no improvement in the emission behavior is observed in nanoparticles nor solid state relative to carborane-free PDI fluorophores. Notably, the introduction of carboranes in some of these dyes does not hinder their organized self-assembly to form defined supramolecular nanostructures.

Chapter 6: *Synthesis, characterization and photophysical properties of new tri-branched fluorene & truxene systems bearing o-carborane clusters.* New fluorophores based on truxene and 9,9´-dioctylfluorene containing *o*-carborane has been prepared and characterized. The new final compounds were obtained by insertion reaction using decaborane ($B_{10}H_{14}$) and a Lewis base. These systems were designed looking for two photon absorption (TPA) properties. The carborane-free precursors were prepared by the group of Dr. Norberto Farfán from the UNAM, Mexico. Finally, the optical properties in solution, aggregate state and thin films were studied. The photophysical results showed a significant quenching of the fluorescence quantum yield in solution due to the direct binding of the *o*-carborane units to the highly luminescent fluorophores, which was later checked theoretically using DFT calculations. These studies have been done in collaboration with Prof. Pascal Lacroix from Université de Toulouse, France. Our approach consisted in considering one arm of these three-branched systems and optimizing as well as calculating their UV spectrum, both in the ground state and in the excited state, using the CAM-B3LYP/6-31G* method and the solvent as THF. Two-

photon absorption (TPA) measurements were done in collaboration with Dr. Jean Pierre Malval from Université de Haute-Alsace, France, which did not give satisfying results, probably due to the low quantum efficiency. Along with DFT calculations, cyclic voltammetry studies showed that the band gap energy values of HOMO and LUMO for all the compounds matched well with TPA band gap values.

Resumen

El treball presentat en aquesta tesi doctoral segueix les línies de recerca iniciades al Grup de Materials Inorgànics i Catàlisi (LMI) de l'Institut de Ciència de Materials de Barcelona (ICMAB-CSIC), basades en la síntesi, caracterització i estudi de nous derivats de clústers de bor amb propietats fotoluminiscents i les seves potencials aplicacions. S'han sintetitzat i caracteritzat diversos tipus de fluoròfors (fluorè, tiofè, BODIPY, perilendiimida, truxè) funcionalitzats amb carborà. S'ha estudiat en detall el comportament de la fotoluminescència de tots aquests sistemes i, especialment, la influència del clúster *o*-carborà en aquestes propietats. És important destacar que en l'última dècada hi ha hagut un interès creixent per la síntesi de materials moleculars basats en clústers de bor i especialment per l'estudi de les seves propietats de fluorescència, tant en solució com en estat sòlid. La primera publicació relacionada amb aquest tema va ser del nostre grup, l'any 2007, i des de llavors estem treballant per explorar aquest nou camp dins dels clústers de bor. L'aportació i el progrés que ha fet el nostre grup dins d'aquesta àrea de recerca ha estat molt àmplia, i en els darrers anys s'ha fet una recerca més centrada en l'aplicació d'aquests materials tant en optoelectrònica com en biomedicina.

A continuació, s'han descrit breument els resultats i els capítols de discussió, destacant la novetat en cada cas.

Capítol 3: Aquest capítol descriu la síntesi de sistemes donador-acceptor-Donador (D-A-D) basats en compostos π-conjugats (fluorè i tiofè) units a *o*-carborà i l'estudi de les seves propietats fotofísiques en solució, estat

agregat, sòlid i pel·lícules primes. És important destacar que després d'enllaçar l'*o*-carborà al fluorè, es va observar un apagament de la fluorescència en solució. Es va estudiar aquest fenomen provocat pel clúster de caborà i, a més, també es van realitzar estudis computacionals mitjançant DFT en col·laboració amb el Dr. Zsolt Keleman de la Budapest University of Technology and Economics, Hongria, per donar suport a aquests resultats experimentals. En canvi, un dels derivats del fluorè, que conté cadenes alquils, presentava una alta fluorescència en estat sòlid, un fenomen conegut com a emissió induïda per agregació (en anglès AIE). Això ens va inspirar a preparar nanopartícules (NPs) que es dispersen en aigua, i que, segons el nostre coneixement, és el primer exemple que hi ha a la literatura d'aquest tipus de NPs amb clústers de bor. Aquestes NPs van mostrar una fluorescència extraordinària, que les converteixen en sistemes interesants per aplicacions en bioimatge de cèl·lules mitjançant microscòpia confocal. Així mateix, quan aquestes NPs es van dipositar sobre pel·lícules primes, van conservar el rendiment quàntic de fluorescència, fet que ens va permetre fer algunes proves preliminars per aplicacions en optoelectrònica. Aquest treball s'ha publicat recentment a Chemical Communications, 2022, 58, 4016.

Capítol 4: En aquest capítol es descriu de la síntesi d'una família de compostos basats en derivats de BODIPY-carborà, la seva caracterització i propietats de luminescència. S'han preparat diferents derivats de BODIPY, on els clústers d'orto i meta-carborà substituïts al carboni del clúster (C_c) es van unir a les posicions 3,5 i 2,6 dels BODIPYs. Aquests BODIPYs inicials s'han preparat en col·laboració amb la Prof. Cristina Prandi de la University of Torino, Itàlia. En general, s'observa que la introducció del clúster estirenil-carborà als fragments de BODIPY afecta

lleugerament l'absorció i millora l'emissió dels grups BODIPY. En general, els derivats 2,6-disubstituïts amb una estructura asimètrica van mostrar una disminució del rendiment quàntic de fluorescència en comparació amb els homòlegs 3,5-disubstituïts. Aquests sistemes van mostrar una alta estabilitat en dissolvents orgànics. Així mateix, la fluorescència dels compostos va augmentar en solucions de THF:H_2O (60:40). Les propietats de fluorescència dels compostos i el seu alt contingut en bor fan que aquests compostos siguin candidats perfectes per a aplicacions biomèdiques, tant per al diagnòstic (marcatge cel·lular) com per al seu ús en la teràpia anticancerígena de BNCT. Aquest treball s'ha publicat a Dyes & Pigments, 2021, 194, 109644.

Capítol 5: Aquest treball s'ha realitzat en col·laboració amb el Dr. Jordi Hernando de la Universitat Autònoma de Barcelona (UAB). Les perilendiimides (PDI) són colorants amb una fluorescència molt intensa que presenten dos inconvenients importants: una baixa solubilitat a causa del fort apilament π-π i la pèrdua de les seves excel·lents propietats d'emissió en estat sòlid, on s'observa el característic desplaçament al vermell de l'emissió d'excimers amb baixa eficiència. Per superar aquestes limitacions, en aquest treball hem preparat diversos derivats de PDI que contenen unitats d'o-carborà, per tal de evitar l'empaquetament molecular d'aquests colorants mitjançant interaccions π. Les propietats fotofísiques es van mesurar en solució, agregació, nanopartícules i en sòlid. Com a resultat, els conjugats PDI-*o*-carborà mostren una millora significativa en la solubilitat en molts dissolvents orgànics, alhora que mostren excel·lents propietats òptiques en solució, amb un rendiment quàntic de fins al 100%. Tanmateix, no s'observa cap millora en el comportament d'emissió en nanopartícules ni en estat sòlid en relació

amb els fluoròfors PDI lliures de carborà. En particular, la introducció de carborans en alguns d'aquests colorants no dificulta el seu autoassemblatge organitzat per formar nanoestructures supramoleculars definides.

Capítol 6: S'han preparat i caracteritzat nous fluoròfors a base de truxè i 9,9´-dioctilfluorè que contenen *o*-carborà. Els nous compostos finals es van obtenir per reacció d'inserció utilitzant decaborà ($B_{10}H_{14}$) i una base de Lewis. Aquests sistemes van ser dissenyats buscant propietats d'absorció de dos fotons (TPA en anglès). Els precursors sense carborà van ser sintetitzats pel grup del Dr. Norberto Farfán de la UNAM, Mèxic. Finalment, es van estudiar les propietats òptiques en solució, estat agregat i pel·lícules primes. Els resultats fotofísics van mostrar una disminució significativa del rendiment quàntic de fluorescència en solució a causa de la unió directa de les unitats d'*o*-carborà als fluoròfors altament luminescents, que es va comprovar posteriorment teòricament mitjançant càlculs DFT. Aquests estudis s'han fet en col·laboració amb el Prof. Pascal Lacroix de la Université de Toulouse, França. El nostre enfocament va consistir a considerar només un braç d'aquests sistemes i optimitzar-ho, així com calcular el seu espectre UV, tant en estat fonamental com en estat excitat, utilitzant el mètode CAM-B3LYP/6-31G* i com dissolvent THF. Les mesures d'absorció de dos fotons (TPA) es van fer en col·laboració amb el Dr. Jean Pierre Malval de la Université de Haute-Alsace, França, però no van donar resultats satisfactoris degut al baix rendiment quàntic de fluorescència. Juntament amb els càlculs de DFT, els estudis de voltametría cíclica mostren que els valors d'energia entre els orbitals HOMO/LUMO de tots els compostos som molts similars als valors obtinguts per TPA.

Resum

El trabajo que se presenta en esta tesis doctoral se enmarcaría dentro de las líneas de investigación iniciadas en el Grupo de Materiales Inorgánicos y Catálisis (LMI) del Instituto de Ciencia de Materiales de Barcelona (ICMAB-CSIC), basadas en la síntesis, caracterización y estudio de nuevos derivados de clústeres de boro con propiedades fotoluminiscentes y sus aplicaciones. Se han sintetizado y caracterizado varios tipos de fluoróforos (fluoreno, tiofeno, BODIPY, perilendiimida, truxeno) funcionalizados con clústeres de carborano. Se ha estudiado a fondo el comportamiento fotoluminiscente de todos estos sistemas y, especialmente, la influencia del clúster de *o*-carborano en estas propiedades. En algunos casos, se presentan y propones algunas aplicaciones potenciales de los mismos. Es importante señalar que en la última década ha habido un creciente interés en la síntesis de materiales moleculares basados en clústeres de carborano y especialmente en el estudio de sus propiedades de fluorescencia, tanto en disolución como en estado sólido. La primera publicación relacionada con este tema fue de nuestro grupo, en 2007, y desde entonces hemos estado trabajando para explorar este nuevo campo dentro de los clústeres de boro. La contribución y el progreso que nuestro grupo ha realizado dentro de esta área de investigación ha sido muy amplia, y en los últimos años se han realizado investigaciones más centradas en la aplicación de estos materiales tanto en el campo de la optoelectrónica como en biomedicina. En este capítulo se han descrito brevemente los resultados y la discusión, destacando la novedad en cada caso.

Capítulo 3: En este capítulo se describe la síntesis de sistemas dador-aceptador-dador (D-A-D) basados en compuestos π-conjugados (fluoreno y tiofeno) unidos a clústeres de *o*-carborano y el estudio de sus propiedades fotofísicas en disolución, estado agregado, sólido y depositados formando películas delgadas. Es importante destacar que tras la unión del clúster de *o*-carborano al fluoreno, se observó un apagado de la fluorescencia en disolución. Hemos estudiado este fenómeno provocado por el clúster de boro y, además, en colaboración con el Dr. Zsolt Keleman, de la Budapest University of Technology and Economics, Hungria, se realizaron estudios computacionales utilizando la teoría funcional de la densidad (DFT) para apoyar estos resultados experimentales. Por el contrario, uno de los derivados del fluoreno, que contenía cadenas alquílicas, presentaba una elevada fluorescencia en estado sólido, un fenómeno conocido como emisión inducida por agregación (AIE). Esto nos inspiró para preparar nanopartículas (NPs) que presentan una alta dispersabilidad en agua, que, hasta donde sabemos, es el primer ejemplo reportado en la literatura de este tipo de NPs con clústeres de boro. Hay que destacar que estas NPs mostraron una extraordinaria fluorescencia, lo que las convierte en sistemas de interés para aplicaciones en bioimagen de células, mediante microscopía confocal. Además, al depositarse sobre películas delgadas, conservaron el rendimiento cuántico, lo que nos permitió hacer algunas pruebas preliminares para su uso en dispositivos optoelectrónicos. Este trabajo se ha publicado recientemente en Chemical Communications, 2022, 58, 4016.

Capítulo 4: Este capítulo recoge la síntesis de una familia de compuestos basados en derivados de BODIPY-carborano, su caracterización y propiedades de luminiscencia. Se han preparado diferentes derivados de BODIPY, en los que los clústeres de *orto*- y *meta*-carborano sustituidos en el átomo de carbono (C_c) se han enlazado a través de las posiciones 3,5 y 2,6 del. Estos BODIPYs de partida se han preparado en colaboración con la Prof. Cristina Prandi de la Universidad de Turín, Italia. En general, se observa que la introducción del clúster de estirenil-carborano en los BODIPYs afecta ligeramente a la absorción y potencia la emisión de los grupos BODIPY. En general, los derivados 2,6-disustituidos con morfología asimétrica mostraron una disminución del rendimiento cuántico de fluorescencia en comparación con los homólogos 3,5-disustituidos. Estos sistemas mostraron una alta estabilidad en disolventes orgánicos. Asimismo, la fluorescencia de los compuestos aumentó en disoluciones de THF:H_2O (60:40). Las propiedades de fluorescencia de los compuestos y su alto contenido en boro hacen que estos compuestos sean candidatos perfectos para aplicaciones biomédicas, tanto para el diagnóstico (marcado de células) como para su uso en la terapia anticancerígena del BNCT. Este trabajo ha sido publicado en Dyes & Pigments, 2021, 194, 109644.

Capítulo 5: Este trabajo se ha realizado en colaboración con el Dr. Jordi Hernando de la Universidad Autónoma de Barcelona (UAB). Las perilendiimidas (PDI) son colorantes con una fluorescencia muy intensa que presentan dos importantes inconvenientes: su baja solubilidad debido al fuerte apilamiento π-π y la pérdida de sus excelentes propiedades de emisión en estado sólido, donde se observa el característico desplazamiento al rojo de la emisión excimero con baja

eficiencia cuántica de fuorescencia. Para superar estas limitaciones, en este trabajo hemos preparado varios derivados de PDI que contienen unidades de *o*-carborano, que son fragmentos relativamente voluminosos destinadas a evitar el empaquetamiento molecular estrecho de estos colorantes a través de las interacciones π. Se midieron las propiedades fotofísicas en disolución, agregación, nanopartículas y en estado sólido. Como resultado, los conjugados PDI-o-carborano muestran una mejora significativa de la solubilidad en muchos disolventes orgánicos, al tiempo que muestran excelentes propiedades ópticas en solución, con un rendimiento cuántico de hasta el 100%. Sin embargo, no se observa ninguna mejora en el comportamiento de emisión de las nanopartículas ni en estado sólido en comparación con los fluoróforos PDI sin carborano. Por tanto, el clúster no mejoró las propiedades de fluorescencia en estado sólido. Cabe destacar que la introducción de carboranos en algunos de estos colorantes no impide su autoensamblaje organizado para formar nanoestructuras supramoleculares definidas.

Capítulo 6: Se han preparado y caracterizado nuevos fluoróforos basados en truxeno y 9,9'-dioctilfluoreno que contienen *o*-carborano. Los nuevos compuestos se obtuvieron por reacción de inserción utilizando decaborano ($B_{10}H_{14}$) y una base de Lewis. Estos nuevos sistemas se diseñaron en busca de propiedades de absorción de dos fotones (TPA en inglés). Los precursores sin carborano fueron preparados por el grupo del Dr. Norberto Farfán de la UNAM, México. Finalmente, se estudiaron las propiedades ópticas en disolución, en estado agregado y en películas delgadas. Los resultados fotofísicos mostraron un apagado significativo del rendimiento cuántico de fluorescencia en disolución debido a la unión directa de las unidades de *o*-carborano a los fluoróforos, lo cual fue

posteriormente comprobado teóricamente mediante cálculos de DFT. Estos estudios se han realizado en colaboración con el Porf. Pascal Lacroix de la Universidad de Toulouse, Francia. Nuestro enfoque consistió en considerar únicamente un brazo de estos sistemas y optimizarlos, así como calcular su espectro UV, tanto en el estado fundamental como en el estado excitado, utilizando el método CAM-B3LYP/6-31G* y como disolvente THF. Se realizaron mediciones de absorción de dos fotones (TPA) en colaboración con el Dr. Jean Pierre Malval de la Universidad de Haute-Alsace, Francia, que no dieron resultados satisfactorios, debido a la baja eficiencia cuántica de fluorescencia de los sistemas. Junto con los cálculos DFT, los estudios de voltamperometría cíclica muestran que los valores de energía entre los orbitales HOMO/LUMO de todos los compuestos son muy similares a los obtenidos mediante TPA.

Table of contents

Chaper 1 **Introduction** 1

1.1 History of boron 5

1.2 Boranes

1.3. Carboranes

1.3.1 Synthesis of *ortho*-carborane 9

1.3.2 Thermal isomerization of *ortho*-carborane 10

1.2.1 Reactivity of carboranes 11

1.4. Formation of metallacarboranes 17

1.5. Photoluminescence

1.5.1 Photoluminescence of polyhedral boron cluster derivatives in solution 21

1.5.2 Photoluminescence of ortho-carborane in solid state and aggregation-induced emission (AIE) 27

1.6. Applications of boron-containing fluorescent systems

1.6.1 Two-photon absorption (TPA) properties 31

1.6.2 Carborane-appended luminescent systems for bioimaging 32

1.6.3 Boron-neutron capture therapy (BNCT) 33

1.7. References

Chapter 2 Objectives 49

Chapter 3 *o*-Carborane based fluorophores : a journey from solution to water dispersible nanoparticles 55

3.1 Introduction 59

3.2 Results and Discussion 61

3.3 Conclusions 84

3.5 References 85

Chapter 4 Synthesis, characterization & properties of red-light emitting carborane-BODIPY dyes 89

4.1 Introduction 93

4.2 Results and Discussion 95

4.3 Conclusion 111

4.5 References 113

Chapter 5 Luminescent behaviour of systems containing *o*-carborane linked to perylenediimide (PDI) fluorophores 119

5.1 Introduction 123

5.2 Results and discussion 125

5.3 Conclusions 154

5.4 References 156

Chapter 6 Synthesis, characterization and photophysical properties of new tri-branched fluorene & truxene systems bearing *o*-carborane clusters 161

6.1 Introduction 165

6.2 Results and discussion 166

6.3 Conclusion 198

6.4 References 199
Chapter 7 General conclusions 201
Annex **205**
Annex for Chapter 3 207
Annex for Chapter 4 243
Annex for Chapter 5 271
Annex for Chapter 6 287
List of publications **321**

Chapter 1

Introduction

CONTENTS

1.1. History of boron

1.2. Boranes

1.3. Carboranes

1.3.1. Synthesis of *ortho*-carborane

1.3.2. Thermal isomerization of *ortho*-carborane

1.3.3. Reactivity of carboranes

1.4. Formation of metallacarboranes

1.5. Photoluminescence

1.5.1. Photoluminescence of polyhedral boron cluster derivatives in solution

1.5.2. Photoluminescence of carborane-containing fluorophores in solid-state and aggregation-induced emission (AIE) phenomenon

1.6. Applications of boron-containing fluorescent systems

1.6.1. Two-photon absorption (TPA) properties

1.6.2. Carborane-appended luminescent systems for bioimaging

1.6.3. Boron neutron capture therapy (BNCT)

1.7 References

Introduction

1.1 History of Boron

The name Boron has been derived from Arabic and Persian burah. Boron represented by the symbol B is the fifth element and first in the group 13 in the periodic table. It is the only element in its group that has no metallic character, but semi-metallic or metalloid character and it is capable of forming covalent bonds such as carbon and silicon. The element has peculiar characteristics as it has a trivalent electronic configuration and vacant p orbital that makes the coordination with other atoms complex and interesting in nature. As boron has 3 valence electrons, it has the property of catenation which makes it capable of forming special type of bonds with itself and other atoms to create polyhedral clusters. The element can be three or four coordinated due to formation of sp^2 and sp^3 hybrid structures because of the promotion of one electron from 2s to 2p orbital to form a $2s^1 2p^2$ electronic configuration. [1]

The boron has two isotopes, ^{11}B (80%) and ^{10}B (20%), and reacts with oxygen to form borates such as borax ($Na_2B_4O_7 \cdot 10H_2O$) and colemanite ($Ca_2B_6O_{11} \cdot 5H_2O$). The use of borax is known for over 4000 years, first by the Babylonians to use in soldering of golds, also in ancient Egyptian culture for the application of medicine, metallurgy, mummifications, and fabrication of glass (borosilicates). In addition to that boron minerals and borax was used in the Romans and Chinese civilizations.[2]

1.2. Boranes

After numerous analysis and experiments, in 1912 the German chemist Alfred Stock reported the first hydrogen and boron based compounds

called Boranes or Boron hydrides. These compounds were of a primary research interest until World War II. In the sixties, carboranes were first time introduced as polyhedral clusters of boron and incorporated carbon atoms in the molecule.[3] Later on, the study of boranes and carboranes became a popular areas of interest in inorganic chemistry and in 1976 William N Lipscomb received Nobel Prize for his discovery on structure of boranes illuminating the problems of chemical bonding.[4] He also explained that the polyhedral boron clusters can be denoted as species with occupied orbitals and multicentric bonds in various resonance forms.[5] In this way, boranes were no longer considered as electron deficient compounds and were called as superatomics.[6] More recently, Teixidor and co-workers have demonstrated that these clusters are aromatic, clearly obeying the Huckel's rule.[7] Herbert Charles Brown received a Nobel Prize in Chemistry for his work on the reducing effect of B-H units over unsaturated organic compounds and thus, there is an impactful research been carried out on boron hydrides that has a high role to play in organic synthesis.[8]

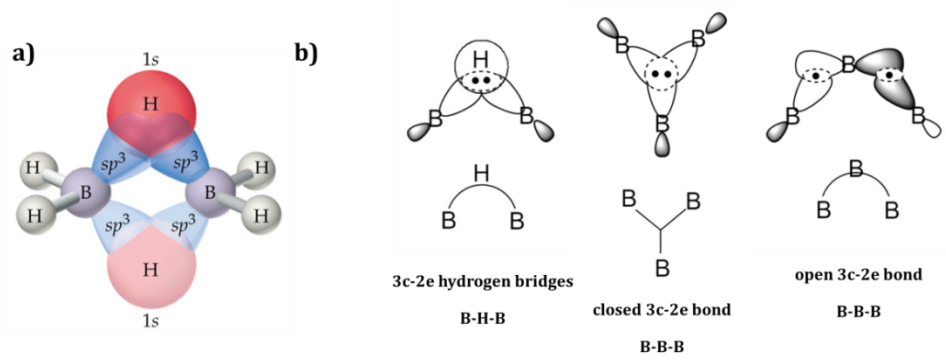

Figure 1.1. a) Structure of B_2H_6, b) 3c-2e links proposed by Lipscomb for boranes

Borane compounds, which do not exist in nature, have the empirical formula [B_nH_m]. They can be prepared from minerals such as borax using different reaction pathways.[9] In this case, atoms in the cluster have access to an octet of electrons but some bonding electron pairs are shared between three atoms in three center two electron (3c-2e) bonds to understand the connectivity between atoms in the structure. In Figure 1.1a it can be observed the formation of these unusual 3c-2e bonds in the diborane (B_2H_6). In larger boranes, different types of bonds are involved: 3c-2e B-H-B hydrogen bridges, as well as closed and open 3c-2e B-B-B bonds apart from 2c-2e (B-B, B-H and BH_2, Figure 1.1b).[5]

Polyhedral boranes are boron clusters that are anionic or neutral in nature and they are formed by triangular face shaped containing a B-H unit at each vertex. Heteroatoms substituting one or more of these vertices, leads to the family of heteroboranes. Among the heteroboranes, the most studied ones are carboranes or carbaboranes. This class of heteroboranes has at least one carbon atom that has replaced an atom of boron in the cluster.

The electronic requirements of boranes and heteroboranes were explored extensively by Wade, Rudolph, Mingo and Williams.[10] If the number of polyhedral vertices is considered as n and the number of electron pairs maintaining the cluster together is n+1, then the cluster has a *closo* structure. In case of n+2, the compound is *nido,* whereas for n+3 is *arachno* and finally n+4 is a *hypo* structure. Boranes with *closo* structure need 2n+2 electrons to maintain the cohesion of cluster, considering n as number of polyhedral vertices (Figure 1.2). Boranes *with nido* structure

do not have a closed structure due to the loss of one B-H vertex from the corresponding *closo* cluster and they require 2n+4 electrons. Boranes with *arachno* and h*ypo structures* are generated from the loss of two vertices and three vertices respectively; *arachno* boranes need 2n+6 electrons, whereas *hypo* boranes need 2n+8 electrons to maintain the cohesion of the cluster.

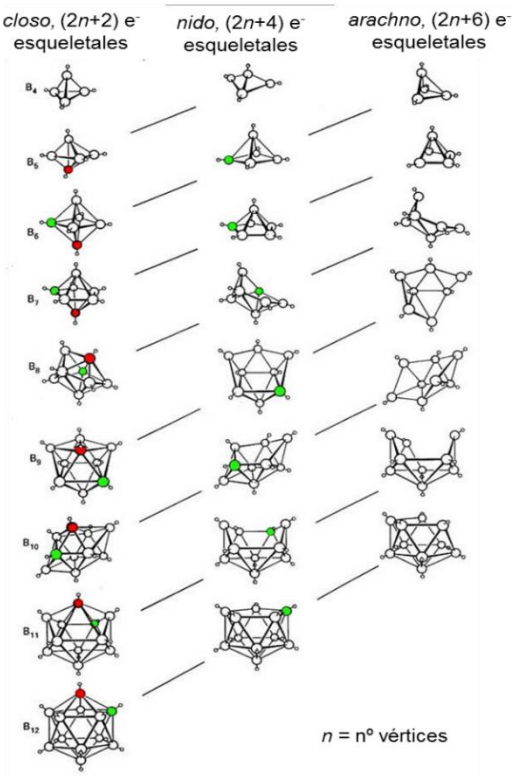

Figure 1.2. Structural relationship between closo, nido, and arachno boranes and hetero-substituted boranes

1.3. Carboranes

Carboranes are those heteroboranes in which one or more vertices of the cluster has carbon atoms ($C_{cluster}$ or C_c) and molecular formula $[C_nB_mH_{n+m+p}]^{-x}$, where n is the number of carbon atoms, m is the number of boron atoms, p is the number of bridging hydrogen atoms and x is the charge of the molecule. One vertex consisting of B-H unit gives two electrons to the skeletal cluster and one carbon vertex made by a C-H unit gives three electrons. In a *nido*-carborane cluster the bridge hydrogen gives only one electron. Among all the possible clusters, we will mainly

focus on icosahedral clusters containing 12 vertices, originally named dicarba-*closo*-dodecaboranes or simply carboranes, in the next part of introduction.

Dicarba-*closo*-dodecaboranes is a group of icosahedral clusters consisting of two C-H vertices and ten B-H vertices, with an empirical formula $C_2B_{10}H_{12}$. In this geometry, the C and B atoms adopts an environment with total six bonds out of which five are bonded to the cluster atoms and one to the exohedral bond to a H atom.[11] The C-H and B-H vertices are arranged in such a way that it gives rise to three different isomers: *ortho*-carborane (1,2-$C_2B_{10}H_{12}$) where the two carbon atoms are adjacent, *meta*-carborane (1,7-$C_2B_{10}H_{12}$) in which a boron atoms is placed between two carbon atoms (C atoms are in meta position to each other) and *para*-carborane (1,12-$C_2B_{10}H_{12}$), in which the two carbon atoms are in antipodes (see isomerization in section 1.3.2, Figure 1.4). .[12] More than half a century ago, the first carborane discovered and characterized was the *ortho*-carborane (Figure 1.3).

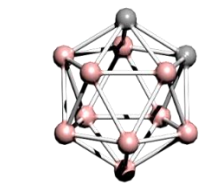

Figure 1.3. Structure of the *ortho*-carborane (1,2-$C_2B_{10}H_{12}$)

1.3.1. Synthesis of *ortho*-carborane

The preparation of *ortho*-carborane was first reported in 1963.[13] The *nido*-decaborane ($B_{10}H_{14}$) first reacts with a Lewis base, such as CH_3CN, Et_2S, Et_3N, to obtain a Lewis base adduct, which further reacts with

alkynes.[13,14] In the scheme below (Scheme 1.1), when $B_{10}H_{14}$ reacts with acetylene derivatives in presence of a Lewis base (L), through the formation of an adduct (6,9-$L_2B_{10}H_{12}$), gives rise to the corresponding *ortho*-carborane (1,2-RR'$C_2B_{10}H_{12}$).[15] However, in the last decade the use of ionic liquids exhibited the presence of Lewis base dispensable and was reported to accelerate the reaction enormously and provided increase in yields.[16] Other methodologies, as the use of $AgNO_3$ in catalytic amounts in toluene have been also used in the reactions between alkynes and $B_{10}H_{14}$ to increase the yields.[17]

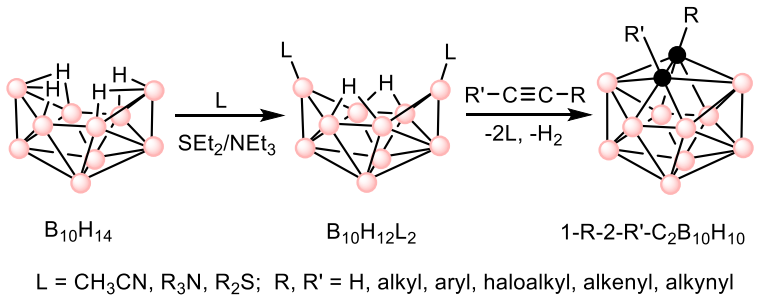

Scheme 1.1 Insertion reaction of alkyne into *nido*-decaborane cluster to form carborane icosahedron 1,2-RR'-$C_2B_{10}H_{10}$

1.3.2. Thermal isomerization of *ortho*-carborane.

As the distance between the two C-H vertices of carborane increases, dipole moment decreases, and the thermodynamic stability increases which leads to thermal isomerization. Thus, *ortho*-carborane under inert atmosphere at 500 °C can be thermally converted to *meta* isomer and finally over 600 °C to *para* isomer (Figure 1.4).[12, 18] From the earlier investigations, it has been confirmed that the stability of isomers increases with a greater separation between the two carbon atoms of the

cluster. Hence, order of stability follows as: *para*-isomer>*meta*-isomer>*ortho*-isomer.

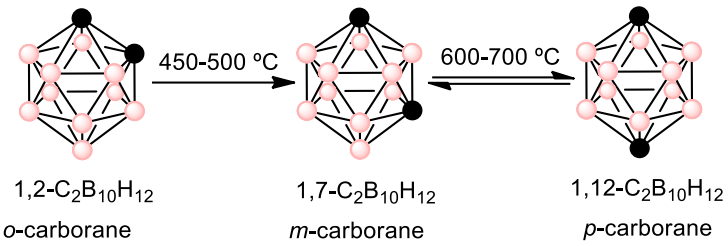

Figure 1.4: Thermal isomerization of dicarba-*closo*-dodecaboranes

The uniquely delocalized 3-center-2-electron bonds make these icosahedron boron clusters chemically and thermally stable throughout the skeletal framework. Both Mulliken and natural population analysis (NPA) have described a complex electronic structure by determining the electric charges.[19] NPA additionally shows that the hydrogen atoms bonded to carbon atoms are more acidic than at the boron vertices. The three isomers have a HOMO-LUMO gap of 8 eV.[19] Due to the presence of two different atoms with different electronegativity in the cage and the icosahedral geometry of the cluster, there is a large dipole moment of *o*-carborane (4.5 D) and a dipole moment of *m*-carborane (2.9 D).

1.3.3. Reactivity of carboranes:

The highest electronegativity of the carbon atoms of the cluster usually makes the carbon atoms of carboranes electron-withdrawing in nature with respect to their substituents.[20] Therefore, due to the specific

electronic structure, it has been demonstrated their three dimensional aromaticity as mentioned before.[7c]

It is of great importance to understand the type of functionalization that can be performed on each position of a cluster. For example, C_c in all isomers have an "electron-withdrawing" effect on the substituents they contain and its effect will be transmitted to neighboring atoms, while the behavior of B atoms will depend on its position in the cluster and also on the isomer type; thus, if the B atom is bound to 2 C_c (eg - B (3,6) in *o*-carborane) they will be slightly "electron-attracting" (due to their low electron density), the B that are bound to 1 C_c they practically do not present this effect and, in the case of B atoms at the antipodal of the C_c (eg- B(9,10) in *m*-carborane or B(9,12) in *o*-carborane) they may have an effect of "electro-donation".[21,22] As a consequence, each region of the cluster will be susceptible to different types of reactions, especially in the *o*- and *m*-carborane because they are asymmetric (Figure 1.5).

Compared to other isomers, *o*-carborane is the most reactive one, because of its higher inductive electron attraction effect.[23] Studies have shown that it has the largest range of inductive constant (σ_I) from -0.23 to +0.38, whereas in *m*-carborane ranged from -0.12 to +0.21 and *p*-carborane from -0.04 to +0.14.[24] Hence, this is another form of representation to say that electron withdrawing effect of cluster carbon atoms on attaching substituents depends upon the isomers and positions of the atoms.

Of the three isomers, *o*-carborane, has attained a particular attention. [23,25] Also, it is usually easier to functionalie with different organic systems than the others, which requires harsh reaction conditions. The *ortho* isomer possesses three-dimensional structure, electron withdrawing

property and highly polarized σ-aromatic character, these various features allow *o*-carborane cage to act as an acceptor group when is attached to a *π*-conjugated system, which can provide interesting electronic and photoelectronic properties to their derivatives.[26]

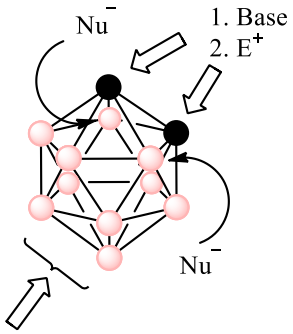

Figure 1.5. Reactivity of *ortho*-carborane

Due to the significant acidic character of the protons bonded to the carbon atoms of the carborane, the more facile functionalization at C_c-H unit is via nucleophilic substitution using alkaline and alkaline earth metals (Figure 1.5).[22,27,28] Presence of strong bases such as *n*-butyllithium (*n*-BuLi), Grignard reagents or sodium hydride (NaH) is required and the reaction is carried out using organic solvent like n-pentane, n-hexane, THF, toluene and ethers. The acidic C-H protons can be removed with a base forming carboranyl nucleophile that finally reacts with an electrophile to give substituted clusters. As the lithium bases emerge as standard base for the reaction with *ortho*-carborane,[29] first lithiated carborane precipitates in the solution depending upon solvent used. Later, as most of the electrophiles used are halides, this results in formation of corresponding lithium salt. The process of lithiation is very important and it indicates the yield of the reaction essentially depends

upon electrophile used. Other factors contributing to the course of reaction are solvent, temperature, and reaction time.

The scheme 1.2 exhibits substitutions at one or both C_c atoms of carborane that can be disubstituted both symmetrically and asymmetrically. Monosubstitution of carborane carbon atoms (or C_c) can lead to a mixture of the disubstituted species, because of conversion of monolithiated to dilithiated carborane, and neutral cluster.[30,31,32]

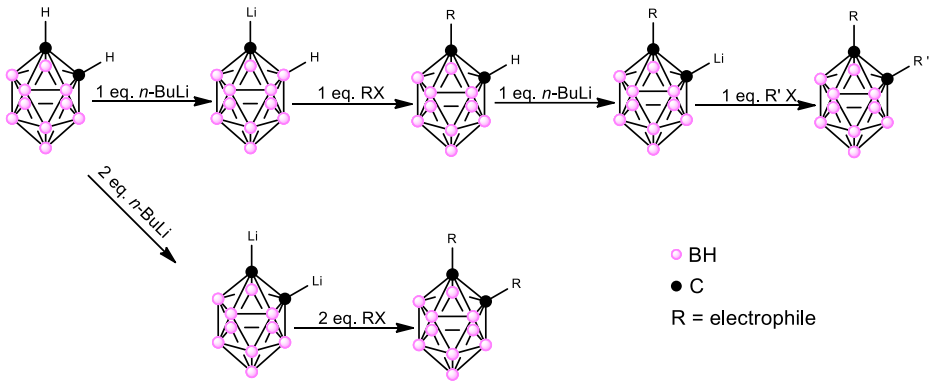

Scheme 1.2. Substitution reaction of C_c-H vertices with electrophilic agents.

It is possible to introduce the same substituent at both C_c after dilithiation, which leads to symmetrically substituted carborane, whereas asymmetrical disubstituted carborane cluster can be obtained by a first monosubstitution followed by lithiation and substitution at the second C_c atom. Steric hindrance of electrophilic substituent can however obstruct one-pot disubstitution in case of *o*-carborane.[12]

Synthesis of monosubstituted carborane derivatives compared to disubstituted products is much more complex in nature due to the disproportionation of $Li[1,2\text{-}C_2B_{10}H_{11}]$ into $Li_2[1,2\text{-}C_2B_{10}H_{11}]$ and $1,2\text{-}C_2B_{10}H_{12}$.[23] To overcome this problem, several reaction conditions have

been developed, such as mono-substitution reaction in ethereal solvents at low temperature and particular carborane concentration. Thus, to facilitate the largest degree of mono-substitution, it has been suggested to focus on type of electrophile and to find various combinations of reaction conditions (temperature, carborane concentration, ethereal solvent).[32]

The alkynyl substitution at carbon atoms of carborane is a popular example and the preparation requires synthesis of C-vinyl substituted clusters via copper (I) and a corresponding halide (Scheme 1.3).[33] This ethynyl carbaboranes obtained are much fascinating for applications in nanotechnology than medicinal uses.[34]

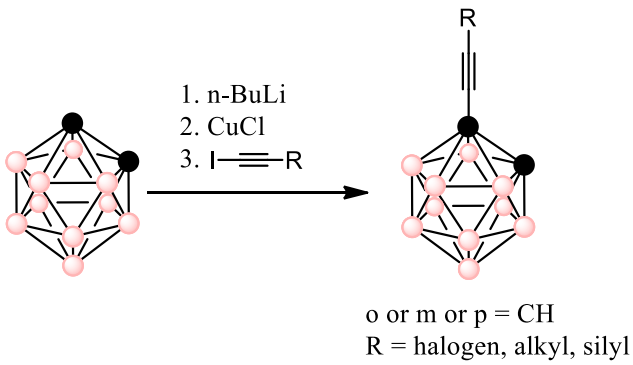

Scheme 1.3. Synthesis of C-Alkynylcarboranes

The substitution of various functional groups at boron atoms of carborane is difficult compared to traditional organic molecules. The reason behind it is the hindered steric environment, variable electronic character and non-hydridic B-H bonds. As the B-H bonds are less polar than C_c-H units and are comparatively less reactive towards nucleophiles, they are inert to nucleophilic attack by Grignards and organolithium reagents (RMgX, R = organic group, X = halide).[35] However, Friedel Craft's

halogenation has been an important reaction pathway to harness the electrophilic reactivity at electron rich boron vertices of carboranes. Therefore, the resulting B-halogenated carborane electrophiles permit access to B-C, B-O or B-N substitution through metal catalyzed cross coupling.[12]

The diversity of carboranes application requires various synthetic methods which can provide vertex selective modifications. From the past literature it has been observed that the synthetic pathways to obtain subsequent selective functionalization with electrophiles at carbon vertices under basic conditions are still limited in order to achieve efficient substitution reaction. Often transition metal reagents are required to carry out this type of reactions or metal catalyzed cross coupling reactions are used to achieve B-vertex functionalization. To improve some of the limitations of this kind of functionalization K.P. Anderson et al. has reported a high yielding B-vertex substitution method for B-substituted carboranes and a transition metal free C-vertex substitution of hetero-aryl substrates.[36]

This particular isomer upon nucleophilic attack easily undergoes deboronation (i.e. loss of a B-H), to give the corresponding 11-vertex *nido*-[7,8-$C_2B_9H_{12}$] species.[12,15c] It is an important reaction of carborane chemistry, where instead of introducing new substituents to the cluster there is a removal of an entire vertex. The elimination of B(3)-H or its equivalent B(6)-H vertex from 1,2-$C_2B_{10}H_{12}$ yields a single optically inactive *nido* [7,8-$C_2B_9H_{12}$]$^-$ anion (Scheme 1.4).[37]

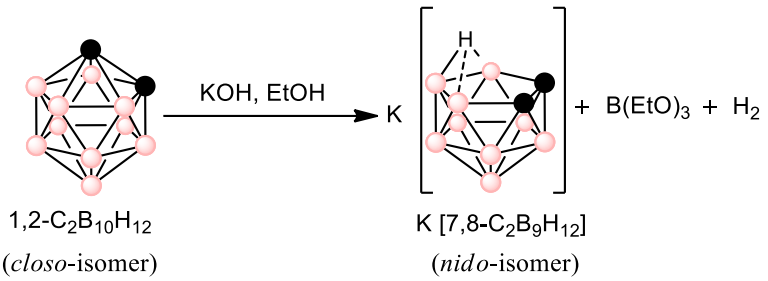

Scheme 1.4: Partial deboronation reaction of *ortho*-carborane

Based on the carborane isomer, different deboronation compounds were obtained, for example 1,2-$C_2B_{10}H_{12}$ gives *nido*-[7,8-$C_2B_9H_{11}$]$^-$, 1,7-$C_2B_{10}H_{12}$ gives *nido*-[7,9-$C_2B_9H_{11}$]$^-$ and 1,12-$C_2B_{10}H_{12}$ gives *nido*-[2,9-$C_2B_9H_{11}$]$^-$.[38]

For years, carborane has been an intriguing topic for research in fact a substantial amount of work has shown that some of the carborane based compounds have better prospect than many organic counterparts. The unique and tunable steric bulk, stability, rigidity and fascinating electronic properties of these compounds provides a highly attractive organomimetic inorganic substituent platform.[39] It has wide range of applications from supramolecular chemistry to catalysis, molecular imaging and radiotherapy, medicine, ionic liquids, OLEDs in the form of film and others.

1.4. Formation of metallacarboranes

Metallacarboranes are generally a class of inorganic polyhedral clusters consisting of carbon, boron, hydrogen and metal atoms in various combinations. Typically, it is a sandwiched complexes formed between

two dicarbollide clusters $[C_2B_9H_{11}]^{2-}$ with a metal atom in the center. The metal atom in this cluster fills the vacancy and completes a 12 vertex closo-MC_2B_9 icosahedral cage and in this way closo anionic icosahedral metallacarboranes with formulae, $[3,3\text{-}M(1,2C_2B_9H_{11})_2]^{n-}$ wereare generated, where M = Co(III), Co(II), Fe(III), Fe(II), Ni(III), Cu(III), Au(III) and n = 1 or 2.[40] The first metallacarborane reported in 1965 was FESAN $[3,3\text{-}Fe(1,2C_2B_9H_{11})_2]^{n-}$ (n = 1, 2).[41] It was obtained by Hawthorne and his scientific research group. Soon after this, an analogous sandwich type coordinated by cobalt, COSAN $[3,3\text{-}Co(1,2C_2B_9H_{11})_2]^{n-}$ was reported (Scheme 5).[42] This anion has shown good chemical stability, low nucleophilic character, high molecular volume and low charge density. $[C_2B_9H_{11}]^{2-}$ behaves as η^5 ligand and is isolobal to the cyclopentadienyl ligand for example in ferrocene. Each of the dicarbollide ligand contributes two negative charges and is coordinated to the metal, resulting negative charge is delocalized all over the complex and thus, the molecule has low charge density.[43]

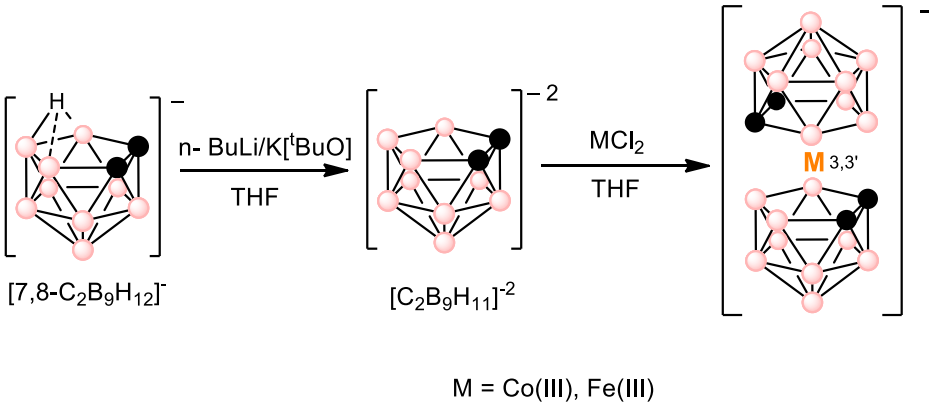

Scheme 1.5. Synthesis of COSAN [M = Co(III)] and FESAN [M = Fe(III)]

Metallacarboranes have become a subject of interest owing to their unique features including rigidity of the cages, relative rotary motion, hydrophobicity etc. The carbon atoms in the framework causes various reactivity, either acidic (carbon bound) or hydridic (boron bound) hydrogen atoms. With the change in metals there is a further increase in variability, influencing redox properties of the entire complex structure.[44]

1.5. Photoluminescence

One of the main research lines in the last decade has been the study and influence of boron clusters in luminescence processes. The luminescence can be defined as the process of ultraviolet, visible or infrared emission by a material as a consequence of a relaxation process from an excited state.[45] If the source that produces the excitation of the material is photons that come from light, then it is a case of photoluminescence. Within the photoluminescence can be identified two phenomena, fluorescence and phosphorescence (Figure 1.6). The fluorescence results from the electronic relaxation from a singlet excited state (S_1) to the fundamental state of the molecule (S_0), with half-life times around nanoseconds ($\tau = 10^{-10} – 10^{-7}$ s). The phosphorescence takes place with electronic relaxation from an excited triplet state (T_1) to the ground state (S_0), with half-life times from microseconds to seconds ($\tau = >10^{-6}$ s).[46]

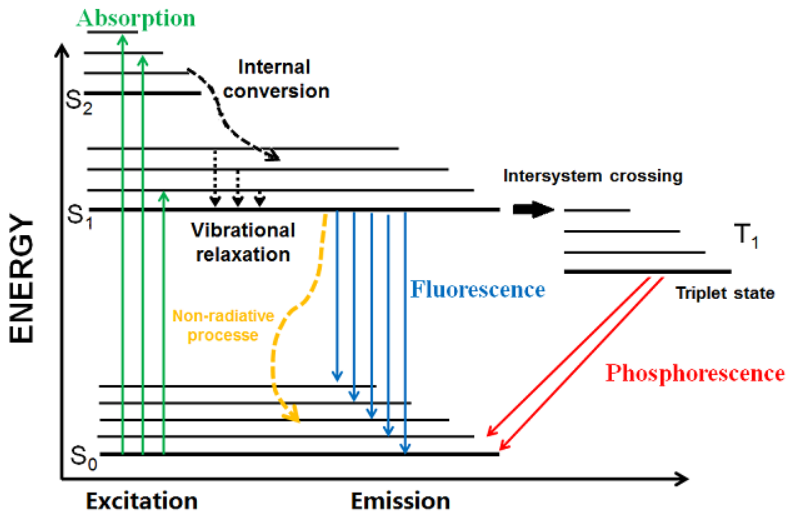

Figure 1.6. Perrin Jablonski diagram

Therefore, fluorescence and phosphorescence are radiative relaxation processes, since the emission of photons is produced. However, in excited species other non-radiative processes may take place such as internal conversion (IC), intersystem crossing (ISC), intramolecular charge transfer (ICT) and conformational changes in the molecule. Besides, non-radiative deactivation processes by interaction with other molecules: electron transfer, proton transfer, energy transfer, or excimer formation can also occurs.[45] All non-radiative deactivation processes compete with the fluorescent emission if they occur on a time scale comparable to the τ of the fluorescence emission process. Thus, the fluorescence quantum yield (ϕ_F) is defined as the fraction of excited molecules that return to the S_0 state with fluorescence photon emission, or also expressed as the ratio of photons emitted by fluorescence with respect to the photons initially absorbed.

Many photoluminescent materials have been developed with broad fields of application, as chemical species sensors, [47, 48, 49] detection of

biomolecules,[50] fluorescence microscopy,[51] quantum dots,[52] organic light-emitting diodes (OLEDs),[53] among others.

1.5.1. Photoluminescence of polyhedral boron cluster derivatives in solution

With the advent of initial use in organometallic chemistry and catalysis, boron clusters have proved it´s immense attention in biological applications (boron-neutron capture therapy or BNCT) and photoluminescence. In recent times, there has been a continuous growth as non-linear optical materials, luminescent materials, liquid crystals, thermally stable polymers and precursors of nanomaterials.[54]

Boron clusters by themselves don't show fluorescence in solution at room temperature. The first time a study was published that linked photoluminescence concepts with boron clusters was relatively recent, when in 2004 A. Volge and H. Kunkely published the work entitled 'Is *o*-carborane photoluminiscent?'.[55] Although the clusters don't show a remarkable emission, their special electronic properties,[56] stability, relative easy functionalization and σ-aromaticity,[55,57] have determined that these clusters are means of great interest in the study of their influence on different fluorophores, this will be highlighted henceforth along with the design of various types of luminescent materials.[58] It is therefore almost a recent area, which in the last decade has generated a multitude of scientific works.[59,60,61,62]

Within the field of carborane, it has been proven through theoretical and experimental studies that the relative position of the C_c in the 3 isomers has an important influence on the properties of the fluorophore to which it is attached, due to the fact that the electron-acceptor capacity decreases

in the order *ortho* >> *meta* >> *para,* basically it is higher for lower symmetry of the cage.[63,64]This has been attributed to a greater asymmetry in the distribution of electronic density that follows the same order.[65]

In our research group, it was established for the first time that the neutral *closo* or anionic *nido* nature of the *o*-carborane clusters well as the substituents linked to the C_c atoms have a direct effect on the emission properties of the final molecules.[66] We studied the emission of aryl-ether cores functionalized with 4 clusters of *o*-carborane (Figure 1.7). Surprisingly, although the starting compounds were not fluorescent, after functionalization of the aryl ether nucleus with different carborane derivatives, the final compounds exhibit fluorescence, and it was a first indication of the important role that boron clusters could play in the photophysics of fluorophores.[66]

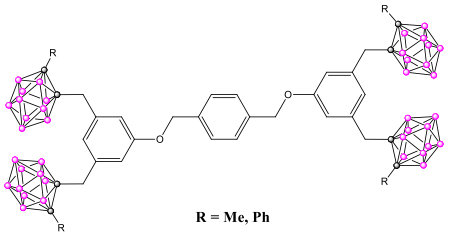

Figure 1.7. Aryl-ether derivatives decorated with 4 clusters of *o*-carborane.

Later on, we prepared different types of fluorophores (anthracene, styrene, stilbene) linked to the C_c atom through a $-CH_2-$ spacer (Figure 1.8). The influence of different substituents (R groups in Figure 1.8) attached to the adjacent C_c of the *o*-carborane was studied, to conclude that the presence of aromatic substituents produces a quenching of the fluorescence due to an intramolecular charge transfer process (ICT) from the donor unit (the fluorophore) to the electron-acceptor unit (the *o*-carborane).[67, 68, 69] The explanation for this kind of behavior was sought in the influence of the substituents on the C_c-C_c bond distance in the *o*-carborane, as this distance plays a fundamental role in the ICT process from the fluorophore to the cluster.[68]

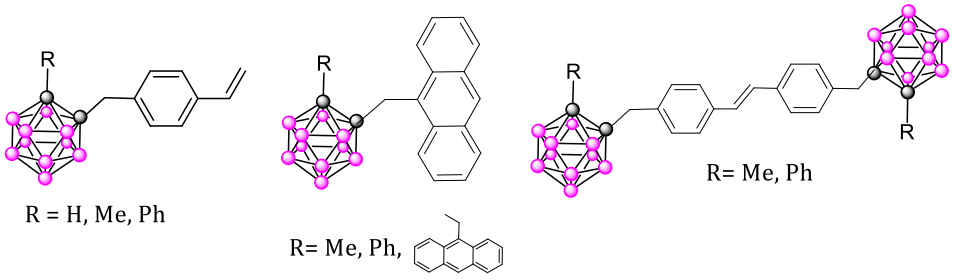

Figure 1.8. C-substituted *o*-carborane derivatives bonded to different fluorophores (styrene, anthracene, stilbene).

A similar influence of the substituent attached to the C_c atom on the photoluminescent properties of dendrimeric systems has also been observed.[70,71,72] Likewise, in 2017, our group has reported the synthesis of fluorescent hybrid materials based on tetrakis(*p*-bromophenyl)ethylene (TPE) functionalized with 4 clusters of *o*-carborane (Figure 1.9). It has been demonstrated that these hybrids exhibit higher fluorescence efficiency (ϕ_F = 12–15 %) than their parent TPE (ϕ_F < 1 %). This phenomenon was ascribed to an effective reduction of the internal conversion (IC), which is due to a considerable extent of conjugation, as well as a significant twist of the stilbene units at the TPE cores.[73]

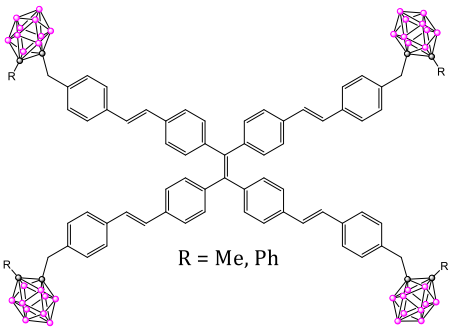

Figure 1.9. TPE functionalized with 4 clusters of *o*-carborane

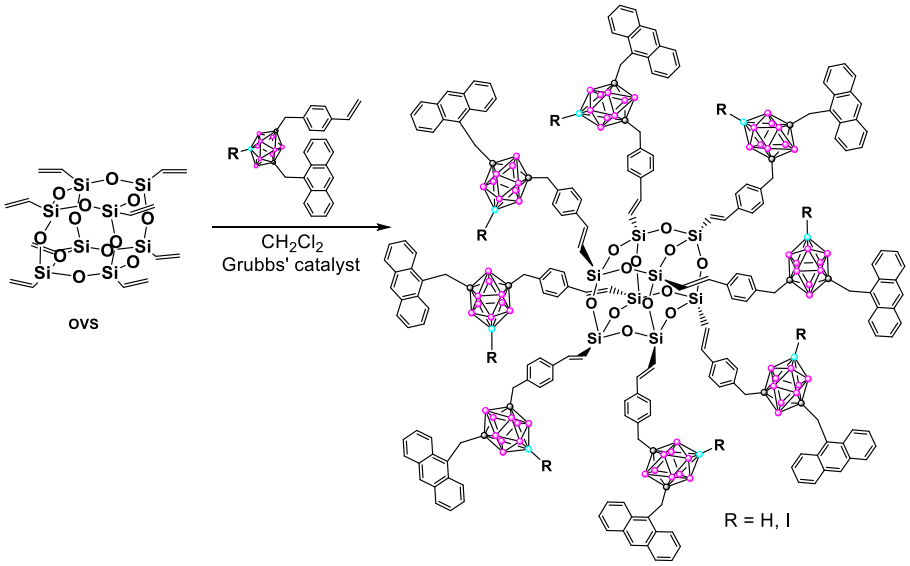

Figure 1.10. Anthracenyl–styrenyl-*m*-carborane triads were synthesized and further attached to octavinylsilsesquioxane (OVS) via cross-metathesis, giving corresponding hybrid materials.

More recently, fluorescent octasilsesquioxanes were prepared by tethering *m*-carborane triads bearing anthracene and styrene groups to octavinylsilsesquioxane (OVS) (Figure 1.10) It is important to notice that the fluorescence quantum yield efficiency of the anthracene increased to almost 100% on incorporating *m*-carborane in the triad. The DFT and experimental studies referred that *m*-carborane does not alter energy levels in fluorescence emission in solution, this is due to anthracene, however it prevents possible alternative non-radiative transitions. Later on, when the triads are linked to the OVS, a significant decrease of quantum yields occurred to 34–45% in solution. Remarkably, the quantum yield values were still maintained in aggregation state (THF:H_2O).[74]

Our group, in collaboration with Prof. C. Prandi's, group have synthesized carborane-BODIPY/aza-BODIPY dyads through Heck coupling reaction.[75]

Remarkably, some of these extremely luminescent dyads were successfully internalized into cells, confirming cytoplasmic localization. Similarly, another set of carborane-BODIPY dyads were prepared in collaboration with Dr. N. Farfan, where *m*-carborane containing BODIPY dyads exhibit better internalization in HeLa cell lines than *ortho* analogue, having said that it could be potentially used as a fluorescence imaging agent in Boron Neutron Capture therapy (BNCT) (see section 1.5.3).[76] New amphiphilic and water soluble carborane based BODIPY derivatives were synthesized which showed high fluorescence in solution and generated singlet oxygen suggesting photodynamic properties.[77]

Another type of fluorophore with bright fluorescence and n-type semiconductor character is the perylenediimides (PDI) and derivatives,[78] although they present an important drawback as problems of solubility in organic solvents.[79] These are promising candidates to obtain highly emissive derivatives as the bulkiness of the carborane unit enables increase in solubility of the PDI linker attached. In a recent work from our group, conjugates consisting of PDI appended cobaltabisdicarbollide ([3,3'-Co($C_2B_9H_{11}$)$_2$]$^-$, or COSAN) through a short oligooxyethylene spacer fluorophore have been prepared (Figure 1.11).[80] These systems showed electrochemically controlled reversible fluorescence in solution, representing the first example of PDI-COSAN-based redox tunable and controllable fluorescent switches.

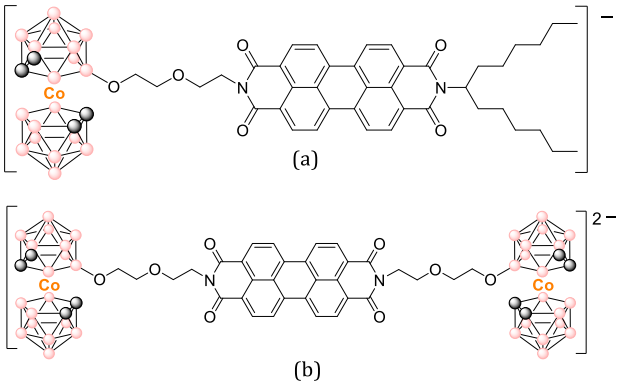

Figure 1.11. Redox-controlled tunable fluorescent molecular switches in solution, consisting of COSAN-PDI conjugates

Apart from our group, others research groups have also worked on carborane-based luminescent systems during the last decade.[62] In 2011, Hosmane et al. prepared a family of star-shaped aromatic fluorophores functionalized with *o*-, *m*- and *p*-carborane directly bonded to aromatic core, concluding that the fluorescence was pronounced in the *m*- and *p*-carborane isomers, but decreases drastically when the fluorophores are directly attached to the *o*-carborane though the C_c atoms (Figure 1.12).[81] Similar conclusions were obtained by Kang et al. in derivatives where *o*-carborane is directly linked to aryl-carbazoles through C_c,[82] and by Fox and Weber in *o*-carborane substituted with diazaborolil.[83] Herein, these studies have revealed that when *o*-carborane is directly bound to the fluorophore it induces a quenching of the fluorescence, attributed to a non-radiative deactivation by an ICT process, from the fluorophore to the cluster. This phenomenon is due to the low energy of the LUMO orbitals located in the Cc-Cc bond of o-carborane. However, it is not the case when a spacer is involved between the fluorophore fragment and cluster cage. Following the publication of these papers, there has been a surge of

interest in the study of luminescent systems based on boron clusters, resulting in a large number of papers.[62]

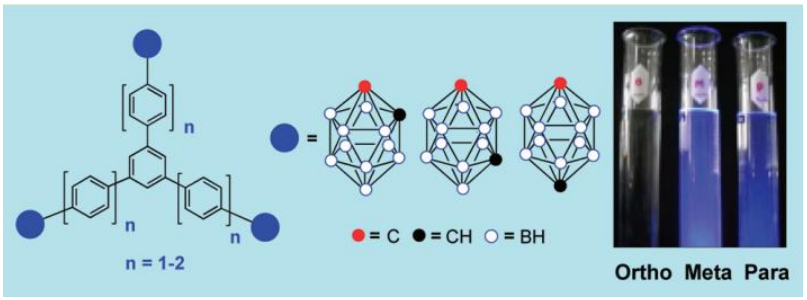

Figure 1.12. Comparison of *o*-, *m*- and *p*- carboranes to enhance fluorescence emission.

1.5.2. Photoluminescence of carborane-containing fluorophores in solid-state and aggregation-induced emission (AIE) phenomenon

Due to the unique properties of *o*-carboranes, it has received a special attention in functional solid-state luminescent materials, as well as in the aggregation-induced emission (AIE) phenomenon.[25] This phenomenon occurs when certain organic fluorophores show enhanced photoemission in aggregation or solid state than in solution, preventing the phenomenon of aggregation caused quenching (ACQ) of the luminescence. In case of *o*-carborane directly attached to a fluorophore, it has been stablished that when the C_c-C_c bond of the cluster is perpendicular to the π-conjugated fluorophore, an intramolecular charge transfer (ICT) takes place. This ICT is usually observed in case of aggregation or solid state, thus exhibiting solid state emission (i.e., an enhancement in emission) leading to AIE.[84,85]

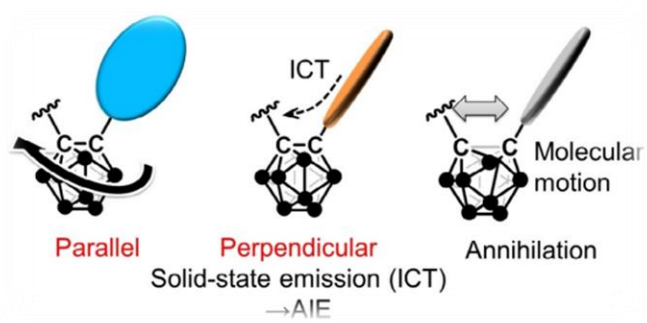

Figure 1.13. Electronic interaction between aryl substituent and *o*-carboranyl unit in aryl-*o*-carborane systems

Chujo and co-workers have a very important contribution towards AIE effect of *o*-carborane based luminescent compounds directly linked to variety of fluorophores. In Figure 1.13 it can be observed that depending on the electronic interaction between the C_c-C_c bond of *o*-carboranyl cluster and the aryl substituent, the emission behavior of the system is classified in locally excited (LE) or intramolecular charge transfer (ICT).[84] One of the first examples of AIE was observed when phenyl *o*-carborane was directly attached to triphenyl amine to produce highly functional systems containing both donor and acceptor units.[86] Weak fluorescence emission was found in solution (Φ_F = 0.007), whereas enhanced emission with maximum at 570nm (Φ_F = 0.05) due to AIE behavior was observed in case of THF/H_2O aggregates. Other triaryl amine carborane systems were also reported by Kang et al. showing similar AIE properties in aggregate state.[87]

Although quantitative analyses between structural geometry and photophysics of fluorescent *o*-carborane containing directly linked aromatic substituents in solid are scarce, Lee and co-workers have focused many of their investigation dedicated to this topic.[88,89]One of such

examples is fluorene and biphenyl-based derivatives directly linked to *o*-carborane units, which has been investigated due to alteration of their photophysical properties. It has been observed that due to flat structural geometry of central biphenyl rings of fluorene-based *o*-carborane derivatives, emissive ICT characteristic was more prevalent (Figure 1.14) however it was almost negligible in biphenyl-based *o*-carborane derivatives due to distorted structure in solid state.[90] Also, the quantum yield efficiency and radiative process was enhanced in case of fluorene-based *o*-carborane compounds in solid, supporting the relationship between structural geometry and enhanced fluorescence intensity of the systems.

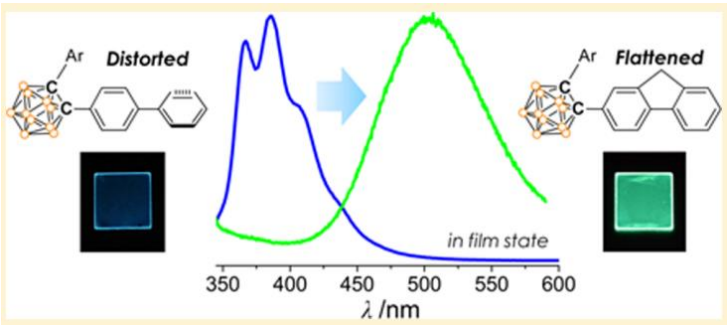

Figure 1.14. Enhanced ICT emissive behavior of flattened fluorene-based *o*-carboranyl compared to distorted biphenyl-based *o*-carboranyl compound

As the fluorescence emission is measured from solution to aggregation and gradually to solid, the presence of bulky *o*-carborane cluster cage has proved to suppress aggregation caused quenching (ACQ) due to steric hindrance. In one of the very recent works, it was established for the first time a direct co-relation between structural geometry and the ICT behavior of the *o*-carborane cluster i.e., with increase in dihedral angle between biphenyl rings (directly attached to cluster) there was a linear decrease in ICT based-radiative decay in crystalline state of a set of

biphenyl-based *o*-carborane compounds.[89] We also tried to recognize this interesting behavior in our set of *o*-carborane based fluorophores (namely fluorene and truxene derivatives) and tried to explain the experimental results that resembles with theoretical studies in the following Chapter 6.

Lee and co-workers[91] further continued to focus on the previous works of Fox et al.,[83] Hosmane et al.[92] and Chujo et al. regarding the emission color tuning behavior of *o*-carborane-containing luminescent dyes.[84.]Different electron-donor and electron-acceptor substituents added at the C_c of *o*-carborane cage showed color-tuning of AIE, the experimental and theoretical studies depicted that depending on the electron-withdrawing or electron-donating ability of substituents appended on aryl group at the Cc, the color tuning of AIE in the system can be achieved (Figure 1.15).[91]

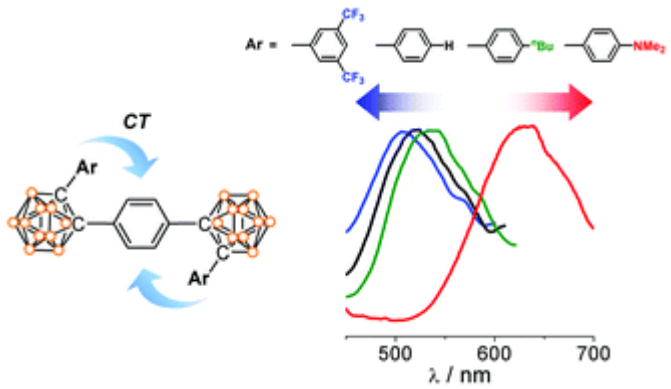

Figure 1.15. A set of 1,4-di-(1-Ar-o-carboran-2-yl) benzene fluorophores exhibiting charge transfer process through a spacer.[91]

Finally, we can say that modulation of the luminescence from the attached fluorophore emitters can be accomplished both in solution and in the solid state thanks to the electronic properties of carboranes.[93,94]

1.6. Applications of boron-containing fluorescent systems

In recent years, non-linear optical materials containing boron clusters has enabled application oriented future prospects in the field of biological imaging, sensors, smart-molecular switches, optical devices such as solar cells, optical fibres and data storage.[95]

In the field of optoelectronics, one important example is the work of Carter and co-workers where they prepared *o*-carborane based polyfluorene derivatives that act as an active and good candidate for polymer-light emitting diodes and transistors. These results gave a new opportunity for the carborane based π-conjugated compounds to play a role in optoelectronic devices.[96] Having said that, there are less studies on monomeric *o*-carborane based fluorene derivatives and its application in the field of optoelectronics, we have tried to investigate in one of our chapters (Chapter 3) and this could be an interesting application for these type of systems.[93]

Some applications that can be related to some of the systems prepared in this work are collected in the following sections.

1.6.1. Two-photon absorption (TPA) properties

One of the crucial applications of non-linear optical (NLO) property is by implementing multiple photon absorption process, such as two-photon absorption (TPA). This phenomenon takes place when a molecule

simultaneously absorbs two photon, then it reaches an excited state via a virtual state of a very short lifetime. This occurs in the presence of a very intense laser pulse using Z-scan technique.[97] The above-mentioned unique characteristics of carborane cluster, inspired H. Yan et al. to explored *o*- and *m*- appended carboranes into star-shaped organic fluorophore namely tris(4-stilbene) amine to study their TPA properties (Figure 1.16).[98] It was concluded that depending on the type of cluster and position of the substitution on it, these systems presented TPA properties. In that case, the star-shaped system containing *m*-carborane was the one exhibiting the largest two-photon absorption and was subsequently applied in two-photon fluorescence 2D and 3D bioimaging. To our knowledge this is the only work on carboranyl-containing systems for TPA.

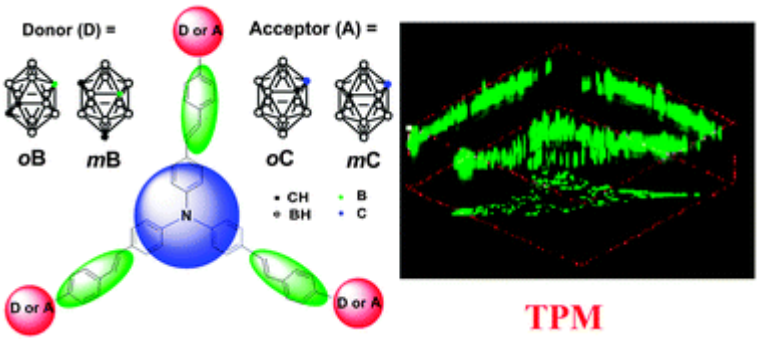

Figure 1.16. Carborane containing star-shaped fluorophores for two-photon absorption imaging

1.6.2. Carborane-appended luminescent systems for bioimaging

Owing to the excellent luminescent properties and good cellular uptake in HeLa cells, some carborane-BODIPY/aza-BODIPY conjugates have demonstrated to be good fluorescence dyes for *in vitro* cell tracking.[75,76]

Moreover, di-iodinated *m*-carborane based anthracene derivatives which exhibited excellent fluorescence quantum yield of almost 100% in solution, were also successfully internalized by HeLa cells through endocytic process, demonstrating to be good fluorescence probes for fixed cells (Figure 1.17).[99]

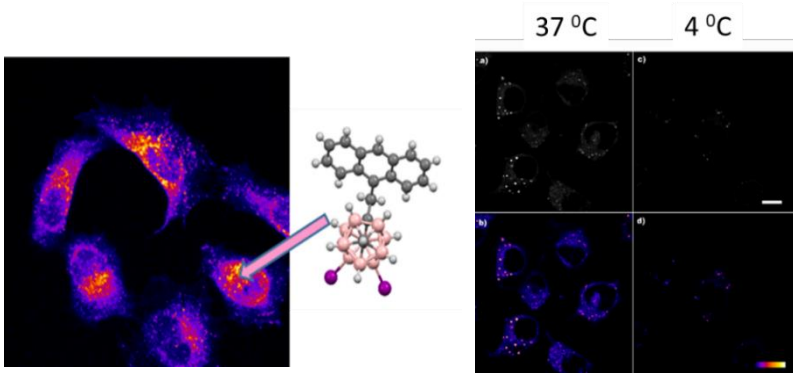

Figure 1.17. Fuorescence intensity emitted by HeLa cells incubated 4 h with 10 μM of diiodinated antracene-*m*-carborane. Image obtained with confocal microscopy (left). Internalization via endocytosis (right).

1.6.3. Boron neutron capture therapy (BNCT)

Previous boron cluster-based fluorophores that show low toxicity and high cellular uptake could be considered as potential theranostic agents that combine of using one fluorescence unit to identify (diagnose) and a boron content fragment to treat tumors by BNCT.

BNCT[100] is a treatment based on nuclear capture and fission involving the irradiation of ^{10}B with low energy neutrons leading to production of alpha particles and recoiling Li

$$^{10}B_5 + {}^{1}n_{0(th)} \rightarrow [^{11}B_5]^* \rightarrow {}^{4}He_2\ (\alpha) + {}^{7}Li_3 + 2.38\ MeV)$$

Over 900 patients have already undergone BNCT worldwide and effects of BNCT on malignant tumors and healthy surrounding tissue seemed to be established (Figure 1.18).

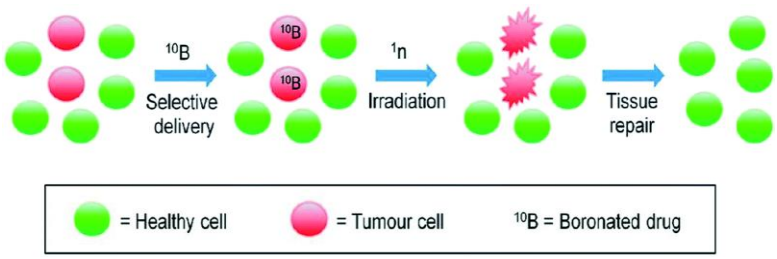

Figure 1.18. BNCT steps: the selective delivery of ^{10}B-containing drugs to tumor cells is followed by irradiation with thermal neutrons (^{1}n) to initiate the destruction of cancer cells and to allow tissue repair

A Deagostino and her group have reported dual therapeutic agents for imaging and treatment i.e., MRI/BNCT agents, that improve the efficacy of BNCT in cancer treatment. This agent consisted of *o*-carborane cluster containing cholesterol unit and a Gd(III)/1,4,7,10-tetraazacyclododecane monoamide complex naming, Gd-B-AC01.[101] Later, the same research group prepared biotin based theranostic (Gd-AL01) agent, which consisted of *o*-carborane clusters and two amino groups, therefore, the high specificity of biotin and selectivity of BNCT was then investigated.[102] The results from biological studies revealed that Gd-AL01 could be used as a theranostic probe for BNCT studies.

Also, our group have developed a carbon-based hybrid material consisting of radioiodinated COSAN covalently attached to graphene oxide (GO). This material is non-cytotoxic neither in vitro for HeLa cells nor in vivo for *C. elegan* worms, resulting almost 100% survival rate. Position emission tomography (PET) images of mice revealed

accumulation of the hybrid material in different organs of the body such as liver, lungs, and kidneys (Figure 1.19). This nanocomposite was retained in the body and eliminated through the gastrointestinal tract after 48 h, what assured that this could be used as a potential boron carrier for BNCT.[103]

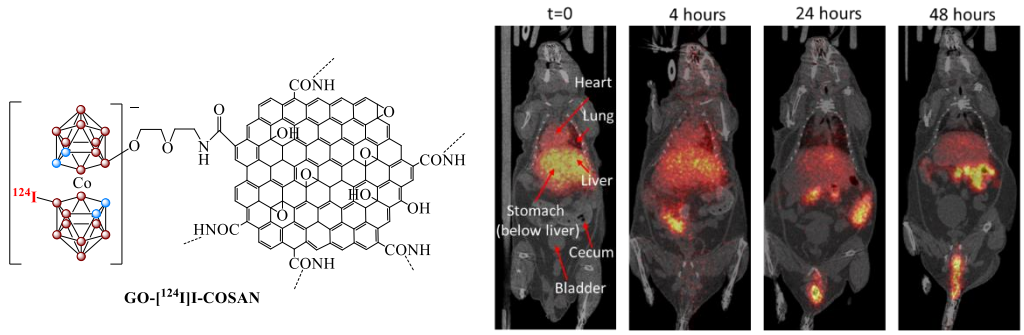

Figure 1.19. Radiolabeled Cobaltabis(dicarbollide) Anion–Graphene Oxide (GO-[124I]I-COSAN) and PET images in the mice at different times.

Furthermore, due to an advancement in boron containing drugs and a more accessible accelerator-based neutron facility, there has been an increase in usage of boron-based compounds for molecular medical diagnostics.[104] In recent works from Viñas *et al*, it was established that Na salt of *o*-COSAN and its di-iodinated derivative could be potential boron carriers for BNCT or promising chemotherapeutic agent for glioblastoma multiforme or GBM (brain tumour). Not only the biological studies were conducted *in vitro* but also *in vivo* with Caenorhabditis elegans (C. elegans), this concluded that the amount of ^{10}B inside cancer cells were sufficient for BNCT irradiation.[105,106]

These interesting results have motivated us to continue working in this line of research, and that is why an important part of this thesis is focused on understanding the role of the carborane cluster in the phenomenon of

photoluminescence and finding its applications in biomedicine and optoelectronics.

1.7. References

[1] https://www.britannica.com/science/boron-chemical-element

[2] W. G. Woods, *Environ. Health Perspect.* 1994, *102*, 5.

[3] (a) I. Shapiro, C. D. Good, R. E. Williams*, J. Am. Chem. Soc*., 1962, 84, 3837; (b) R. N. Grimes, Carboranes, *Academic Press New York*, 1974; (c) T. Onak, E. L Muetterties, Ed., *Academic Press New York*, 1973, 349

[4] http://www.nobelprize.org/nobel_prizes/chemistry/laureates/1976 /

[5] N. W. Lipscomb, Boron Hydrides, Benjamin, New York, 1963 https://www.britannica.com/EBchecked/topic/74358/boron-B/8339/Compounds

[6] (a) R. Hoffmann, W. N. Lipscomb, *J. Chem. Phys*., 1962, 36, 3489; (b) Z. F. Chen, R. B. King, *Chem. Rev*.,2005, 105, 3613.

[7] (a) J. Poater, M. Solà, C. Viñas and F. Teixidor, *Angew. Chemie Int. Ed*., 2014, 53, 12191; (b) J. Poater, M. Solà, C. Viñas and F. Teixidor*, Chem. A Eur. J*., 2016, 22, 7437; (c) J. Poater, C. Viñas, I. Bennour, S. Escayola, M. Solà, F. Teixidor. *J. Am. Chem. Soc*. 2020, 142, 9396.

[8] (a) H. C. Brown, H. I. Schlesinger, A. B. J. Burg*, J. Am. Chem. Soc*., 1939, 61, 673; (b) H. I. Schlesinger, H. C. Brown, H. R. Hoekstra, L. R. Rapp, *J. Am. Chem. Soc*., 1953, 75, 199; (c) K. P. C. Vollhardt, Organic Chemistry, W. H. Freeman and Co., New York, 1987.

[9] (a) W. N.Lipscomb; *Dover Publications*, 2013; (b) A. Earnshaw, *Chemistry of the Elements (Second Edition)*; Butterworth-Heinemann: Oxford, 1997, p 139.

[10] (a) R. W. Rudolph, Acc. Chem. Res., 1976, 9, 446; (b) R. E. Williams, *Inorg. Chem*., 1971, 10, 210; (c) K. Wade, *Adv. Inorg. Radiochem*., 1976, 18, 1; (d) D. M. P. Mingos, *Nature Phy. Science,*1972, 236, 99; (e) R. W. Rudolph, W. R. Pretzer, Inorg. Chem.,1972, 11, 1974; (f) K. Wade, *Chem. Commun*., 1971, 792.

[11] B. J. Eleazer and D. V. Peryshkov Coordination Chemistry of Carborane Clusters Metal-Boron bonds in Carborane, Carboranyl and Carboryne Complexes, Comments on Inorganic Chemistry; *Comments on Inorganic Chemistry*, 2018, 38: 79–109, Ed. Taylor & Francis.

[12] M. Scholz and E. Hey-Hawkins, *Chem. Rev*., 2011, 111, 7035–7062.

[13] (a) M. M. Fein, J. Bobinski, N. Mayes, N. Schwartz, Cohen, M. S. *Inorg. Chem.* 1963, 2, 1111; (b) T. L. Heying, J. W. Ager, S. L. Clark, D. J. Mangold, H. L. Goldstein, M. Hillman, et al. *Inorg. Chem*. 1963, 2, 1089; (c) S. Papetti, T. L. Heying, *Inorg. Chem*. 1963, 2, 1105.

[14] M. F. Hawthorne, T. D. Andrews, P. M. Garrett, F. P. Olsen, M. Reintjes, F. N. Tebbe, L. F. Warren, P. A. Wegner, D. C. Young, *Inorg Synth*. 1967, 10, 91.

[15] M. M.Fein, J. Bobinski, N. Mayes, N. Schwartz, M. S.Cohen, *Inorg. Chem.* 1963, 2, 1111 b) M. Frederick. Hawthorne, Richard L. Pilling, Russell N. Grimes *J. Am. Chem. Soc*, 1967, 89, 1067.

[16] (a) U.; Kusari, Y. Li, M. G. Bradley, L. G. Sneddon, *J. Am. Chem. Soc*. 2004, 126, 8662; (b) Y. Li, P. J. Carroll, L. G. Sneddon, *Inorg. Chem.,* 2008, 47, 9193.

[17] A. Toppino, A. R. Genady, M. E. E. Zaria,J. Reeve, F. Mostofian ,J. Kent, J. F. Valliant* , *Inorg. Chem.* 2013, 52, 15, 8743–8749.

[18] (a) P. M. Garrett, F. N. Tebbe, M. F. Hawthorne, *J. Am. Chem. Soc*. 1964, 86, 5016; (b) M. Hofmann, M. A. Fox, R. Greatrex, P. V. R. Schleyer, R. E. Williams, *Inorg. Chem.* 2001, 40, 1790; (c) Grimes, R. N. Carboranes. *3nd Ed. Academic Press*, Amsterdam, 2016

[19] J. M. Oliva, P. von Rague Schleyer, G. Aullon, J. I. Burgos, A. Fernandez-Barbero, I. Alkorta *Phys. Chem*. *Chem. Phys.* 2010, 12, 5101.

[20] (a) N. Tsuboya, M. Lamrani, R. Hamasaki, M. Ito, M. Mitsuishi, T. Miyashita and Y. Yamamoto, *J. Mater. Chem.,* 2002, 12, 2701–2705; (b) B. Fabre,J. C. Clark,M. Graça H. Vicente *Macromolecules*. 2006, 39, 112–119; (c) M. Karnahl,S. Tschierlei, Ö. F. Erdem,S. Pullen,M.P. Santoni,E. J. Reijerse,W. LubitzS. Ott, *Dalton Trans.* 2012, 41, 12468–12477.

[21] M. Scholz, H. Hawkins, E. *Chem. Rev.* 2011, 111, 7035.

[22] F. Teixidor, G. Barberà, A. Vaca, R. Kivekäs, R. Sillanpää, J. Oliva, C. Viñas, *J. Am. Chem. Soc.* 2005, 127, 10158.

[23] R. N. Grimes, Carboranes, *Academic Press*, Amsterdam, 2016.

[24] V. I. Bregadze, *Chem. Rev*. 1992, 92, 209.

[25] J. Ochi; K. Tanaka; Y. Chujo, *Angew. Chem. Int. Ed*. 2020, 59, 9841-9855.

[26] R. Núñez, M. Tarrés, A. Ferrer-Ugalde, F. Frabrichi de Biani., F. Teixidor, *Chem. Rev.* 2016, 116,14307–78.

[27] A. M. Spokoyny, C. D. Lewis, G. Teverovskiy, S. L. Buchwald, *Organometallics*, 2012, 31, 8478–8481.

[28] K. Hermansson, M. Wójcik, S. Sjöberg, *Inorg. Chem*., 1999, 38, 6039; (b) A. V. Puga, F. Teixidor, R. SillanpäÄ, R. Kivekäs, M. Arca, G. Barberà, C. Viñas, *Chem. Eur. J*., 2009, 15, 9755

[29] W. Clegg, D. A. Brown, S. J. Bryan, K. Wade, *Polyhedron* 1984, 3, 307

[30] L. I. Zakharkin, A. V. Grebennikov, A. V. Kazantsev, I. A Nauk. SSSR. Ser. Khim. 1967, 9, 2077.

[31] (a) F. A. Gómez, M. F. Hawthorne, *J. Org. Chem*., 1992, 57, 1384-1390; (b) C. Viñas, R. Benakki, F Teixidor, J. Cassabó, *Inorg. Chem*., 1995, 34, 3844; (c) J. F. Valliant, K. J. Guenther, A. S. King, P. Morel, P. Schaffer, O. O. Sogbein, K. A. Stephenson, *Coord. Chem. Rev.*, 232, 2002, 173.

[32] A.-R. Popescu, A. D. Musteti, A. Ferrer-Ugalde, C. Viñas, R. Núñez, F. Teixidor, *Chem. A Eur. J*. 2012, 18, 11, 3174–3184.

[33] (a) L. I. Zakharkin, A. I. Kovderov, V. A. Ol'shevskaya, *Russ. Chem. Bull* 1986, 35, 1260; (b) A. S. Batsanov, M. A. Fox, J. A. K. Howard, J. A. H. MacBride, K. Wade, *J. Organomet. Chem.* 2000, 610, 20; (c) M. A. Fox, A. M. Cameron, P. J. Low, M. A. J. Paterson, A. S. Batsanov, A. E. Goeta, D. W. H. Rankin, H. E. Robertson, J. Schirlin, T. *Dalton Trans.* 2006, 3544.

[34] J.-F. Morin, T. Sasaki, Y. Shirai, J. M. Guerrero, J. Tour, M. J. *Org. Chem*. 2007, 72, 9481.

[35] D. Olid, R. Núñez, C. Viñas, F. Teixidor. *Chem Soc. Rev.* 2013, 43, 3318.

[36] K. P. Anderson, *Tetrahedron* 2019, 75, 187-191.

[37] (a) R. A. Wiesboeck, M. F. Hawthorne, J. *Am. Chem. Soc*.,1964, 86, 1642; (b) M. F. Hawthorne, D. C. Young, P. M. Garret, D. A. Owen, S. G. Schwerin, F. N. Tebbe, P. A. Wegner, *J. Am. Chem. Soc*.,1968, 90 (4), 862.

[38] (a) M. A. Fox, A. E. Goeta, A. K. Hughes, A. L. Johnson, *J. Chem. Soc., Dalton Trans*. 2002, 2132; (b) M. A. Fox, K. Wade, *J. Organomet. Chem*. 1999, 573, 279; (c) J. J. Peterson, A. R. Davis, M. Werre, E. B. Coughlin and K. R. Carter, *ACS Appl. Mater. Interfaces*, 2011, 3, 1796–1799; (d) B. P. Dash, R. Satapathy, E. R. Gaillard, J. A. Maguire and N. S. Hosmane, *J. Am. Chem. Soc*., 2010, 132, 6578–6587.

[39] A. M. Spokoyny, *Pure Appl. Chem*. 2013, 85, 903–919

[40] (a) R. Núñez, O. Tutusaus, F. Teixidor, C. Viñas, R. Sillanpää, R. Kivekas, *Chem. Eur. J.,* 2005, 11, 5637; (b) J. G. Planas, C. Viñas, F. Teixidor, M. E. Light, M. B. Hursthouse, H. R. Ogilvie, *Eur. J. Inorg. Chem*., 2005, 4193; (c) O. Tutusaus, R. Núñez, C. Viñas, F. Teixidor, I. Mata, E. Molins, *Inorg. Chem*. , 2004, 43, 6067; (d) I. Rojo, F. Teixidor, C. Viñas, R. Kivekäs, R. Sillanpää, *Chem. Eur. J.,* 2004, 10, 5376; (e) F. Teixidor, J. Pedrajas, I. Rojo, C. Viñas, R. Kivekäs, R. Sillanpää, I. Sivaev, V. Bregadze, S. Sjöberg, *Organometallics,* 2003, 22, 3414.

[41] M. F. Hawthorne, D. C. Young, P. A. Wegner, *J. Am. Chem. Soc*., 1965, 87, 1818.

[42] M. F. Hawthorne, T. D. Andrews, *J. Chem. Soc., Chem. Comm*.,1965, 443

[43] C. Masalles, S. Borrós, C. Viñas, F. Teixidor*, Adv. Mater*., 2000, 16, 1199

[44] P. Farràs, E. J. Juárez-Pérez, M. Lepsik, R. Luque, R. Núñez and F. Teixidor, *Chem. Soc. Rev*., 2012, 41, 3445–3463.

[45] B. Valeur, Wiley-VCH Verlag GmbH, 2001.

[46] J. R. Lakowicz, Springer US, 2007.

[47] L. Basabe-Desmonts, D. N. Reinhoudt, M. Crego-Calama, *Chem. Soc. Rev*. 2007, 36, 993.

[48] D. C. Klonoff, J. *Diabetes Sci. Technol*. 2012, 6, 1242.

[49] J. Qi, D. Liu, X. Liu, S. Guan, F. Shi, H. Chang, H. He, G. Yang, *Anal. Chem.* 2015, 87, 5897.

[50] F. Peccati, J. Hermando, L. Blancafort, X. Solans-Monfort, M. Sodupe, *Phys. Chem. Chem. Phys*. 2015, 17, 19718.

[51] J. W. Lichtam, J. A. Conchello, *Nat. Meth*. 2005, 2, 910.

[52] I. L. Medintz, H. T. Uyeda, E. R. Goldman, H. Mattoussi, *Nat. Mater.* 2005, 4, 435.

[53] C. Qu, G. Xia, Y. Xu, Y. Zhu, J. Liang, J. Wang, Z. Zhang, Y. Wang, *J. Mater. Chem. C*, 2020,**8**, 3846-3854.

[54] B. P. Dash, R. Satapathy, J. A. Maguire and N. S. Hosmane, *New J. Chem*., 2011, 35, 1955–1972

[55] H. Kunkely, A. Volger, Inorg. Chim. Acta, 2004, 357, 4607.

[56] K. Wade, H. J. Emeleus, A. G.Sharpe, Eds., *Academic Press*, 1976, 17, 1.

[57] J. Poater, C. Viñas, M. Sola, F. Teixidor, *Nature Communications*, 2022, 13, 3844, 1-6.

[58] B. P. Dash, R. Satapathy, J. A. Maguire, N. S. Hosmane, *New. J. Chem*., 2011, 35, 1955.

[59] M. Chaari, Z. Keleman, D.C. Lazarte, F. Teixidor, C.Viñas, R. Nuñez, *Inorg. Chem. Front*., 2020, 7, 2370–2380.

[60] A. F. Ugalde, A. G. Campo, J. G. Planas, C. Viñas, F. Teixidor, I. M. Sáez, R. Núñez , *Crystals* 2021, 11, 133, 1-16.

[61] J. C. González, M. Chaari, F. Teixidor, C. Viñas, R. Núñez, *Molecules* 2020, 25, 1210, 1-16.

[62] R. Núñez, M. Tarrés, A. Ferrer-Ugalde, F. F. de Biani, F. Teixidor*, Chem. Rev*., 2016, 116, 23, 14307–14378.

[63] O. Crespo, M. C. Gimeno, A. Laguna, I. Ospino, G. Aullon, J. M. Oliva, *Dalton Trans.,* 2009, 3807.

[64] E. Oleshkevich, F. Teixidor, C. Viñas, *Revista de la Societat Catalana de Química*, 15 ,2016, 49-56.

[65] A.V. Okotrub, L.G. Bulusheva, V.V. Volkov, *J. Mol. Struct*., 520, 2000, 33–38.

[66] F. Lerouge, C. Viñas, F. Teixidor, R. Núñez, A. Abreu, E. Xochitiotzi, R. Santillán, N. Farfán, *Dalton Trans.,* 2007, 1898.

[67] A. Ferrer-Ugalde, E. J. Juárez-Pérez, F. Teixidor, C. Viñas, R. Sillanpää, E. Pérez-Inestrosa, R. Núñez., *Chem. Eur. J.*, 2012, 18, 544.

[68] A. Ferrer-Ugalde, A. González-Campo, C. Viñas, J. Rodriguea-Romero, R. Santilla, N. Farfán, R. Sillanpää, A. Sousa-Pedrares, R. Núñez, F. Teixidor, *Chem. Eur. J*., 2014, 20, 9940-9951.

[69] A. Ferrer-Ugalde, J. Cabrera-González, E. J. Juárez-Pérez, F. Teixidor, E. Pérez-Inestrosa, J. M. Montenegro, R. Sillanpää, M. Haukkad, R. Núñez, *Dalton Trans.,* 2017, 46, 2091.

[70] A. Ferrer-Ugalde, E. J. Juárez-Pérez, F. Teixidor, C. Viñas, R. Núñez, *Chem. Eur. J.,* 2013, 19, 17021.

[71] A. González-Campo, A. Ferrer-Ugalde, C. Viñas, F. Teixidor, R. Sillanpää, J. Rodriguea-Romero, R. Santilla,N. Farfán, R. Núñez, *Chem. Eur. J.*, 2013, 19, 6299.

[72] J. Cabrera-González, E. Xochitiotzi-Flores, C. Viñas, F. Teixidor, H. García-Ortega, N. Farfán, R. Santillan, Teodor Parella, Rosario Núñez, *Inorg. Chem*. 2015, 54, 5021−5031.

[73] J. Cabrera-González, S. Bhattacharyya, B. Milián-Medina, F. Teixidor, N. Farfán, R. Arcos-Ramos, V. Vargas-Reyes, J. Gierschner, R. Núñez, Eur. J. *Inorg. Chem.,* 2017, 38-39, 4575-4580.

[74] M. Chaari, Z. Kelemen, D. C. Lazarte, F. Teixidor, C. Viñas, R. Núñez, *Inorg. Chem. Front.*, 2020, 7, 2370–2380.

[75] C. Bellomo, M. Chaari, J. Cabrera-Gonzµlez, M. Blangetti, C. Lombardi, A. M. Deagostino, C. Viñas, N. Gaztelumendi, C. Nogues, Rosario Nuñez, C. Prandi, *Chem. Eur. J.* 2018, 24, 15622–15630.

[76] P. L. Vazquez, R. F. Cruz, A. G. Hernandez, J. C. Gonzalez, C. G. Cedillo, A. J. Sanchez, P. G. Lacroix, R. Santillan, N. Farfan, R. Nuñez, *Chem. Eur. J.* 2020, 26, 16530 – 16540.

[77] A. V. Zaitsev, E. G. Kononova, A. A. Markova, A. V. Shibaeva, A. A. Kostyukov, A. E. Egorov, V. A. Kuzmin, A. A. Shtil , V. A. Ol'shevskaya, *Dyes and Pigments*, 2022, 207 110711, 1-10.

[78](*a*) F. Würthner, *Chem. Commun.* 2004, 1564-1579; (*b*) A. Nowak-Król and F. Würthner, *Org. Chem. Front.* 2019, 6, 1272—1318.

[79] (a) K. Liu, C. Shang, Z. Wang, Y. Qi, R. Miao, K. Liu, T. Liu and Y. Fang, *Nat. Commun.*, 2018, 9, 1695; (b) K. Liu, Z. Wang, C. Shang, X. Li, H. Peng, R. Miao, L. Ding, J. Liu, T. Liu and Y. Fang, *Adv. Mater. Technol.*, 2019, 4, 1800644; (c) N. Ding, K. Liu, Y. Qi, C. Shang, X. Chang and Y. Fang, *Sens. Actuators B Chem.*, 2021, 340, 129964.

[80] L. Parejo, M. Chaari, S. Santiago, G. Guirado, F. Teixidor, R. Nuñez, J. Hernando, *Chem. Eur. J.* 2021, 27, 270 – 280

[81] B. P. Daash, R. Satapathy, E. R. Gaillard, K. M. Norton, J. A. Maguire, N. Chug, N. S. Hosmane, *Inorg. Chem*., 2011, 50, 5485.

[82] K. R. Wee, W. S. Han, D. W. Cho, S. Know, C. Pac, S. O. Kang, Angew, Chem. Int. Ed. 2012, 51, 2677.

[83] L. Weber, J. Kahlert, R, Brockinke, L. Bohling, A. Brockhkinke, H. G. Stammler, B. Neumann, R. A. Harder, M. A. Fox, Chem. Eur. J., 2012, 18, 8347.

[84] (a) K. Kokado and Y. Chujo, *Macromolecules*, 2009, **42**, 1418−1420; (b) J. Cabrera-González, C. Viñas, M. Haukka, S. Bhattacharyya, J. Gierschner and R. Núñez, *Chem. Eur. J.*, 2016, **22**, 13588−13598; (c) Y. Yin, X. Li, S. Yan, H. Yan and C. Lu, *Chem. Asian J.* 2018, **13**, 3155-3159; (d) X. Wei, M.-J. Zhu, Z. Cheng, M. Lee, H. Yan, C. Lu and J.J. Xu, *Angew. Chem. Int. Ed.*, 2019, **58**, 3162−3166.

[85] (a) R. Furue, T. Nishimoto, I. S. Park, J. Lee, T. Yasuda, *Angew. Chem. Int. Ed.* 2016, 55, 7171 – 7175; *Angew. Chem.* 2016, 128, 7287 – 7291; (b) D. Tu, P. Leong, Z. Li, R. Hu, C. Shi, K. Y. Zhang, H. Yan, Q. A. Zhao, *Chem. Commun.* 2016, 52, 12494 –12497; (c) X. Wu, J. Guo, Y. Quan, W. Jia, D. Jia, Y. Chen, Z. Xie, *J. Mater. Chem. C,* 2018, 6, 4140– 4149; (d) N. V. Nghia, S. Jana, S. Sujith, J. Y. Ryu, J. Lee, S. U. Lee, M. H. Lee, *Angew. Chem. Int. Ed.* 2018, 57, 12483 – 12488; *Angew. Chem.* 2018, 130, 12663 –12668; (e) K. L. Martin, J. N. Smith, E. R. Young, K. R. Carter, *Macromolecules* 2019, 52, 7951 – 7960; (f) Y.-J. Cho, S.- Y. Kim, J.-W. Lee, W.-S. Han, C. H. Kim, H.-J. Son, S. O. Kang, *Chem. Eur. J.* 2019, 25, 8149 – 8156.

[86] S. Inagi, K. Hosoi, T. Kubo, N. Shida, T. Fuchigami, *Electrochemistry* 2013, 81, 368 – 37

[87] (a) S.-Y. Kim, Y.-J. Cho, G. F. Jin, W.-S. Han, H.-J. Son, D. W. Cho, S. O. Kang, *Phys. Chem. Chem. Phys*. 2015, 17, 15679 – 15682; (b) Y. J. Cho, S. Y. Kim, M. Cho, W. S. Han, H. J. Son, D. W. Cho, S. O. Kang, *Phys. Chem. Chem. Phys*. 2016, 18, 9702 – 9708; (c) M. R. Son, Y. J. Cho, S. Y. Kim, H. J. Son, D. W. Cho, S. O. Kang, *Phys. Chem. Chem. Phys*. 2017, 19, 24485 – 24492; (d) S. Y. Kim, J. D. Lee, Y. J. Cho, M. R. Son, H. J. Son, D. W. Cho, S. O. Kang, *Phys. Chem. Chem*. Phys. 2018, 20, 17458 – 17463.

[88] S. H. Lee, M. S. Mun, J. H. Lee, S. Im, W. Lee, H. Hwang, K. M. Lee, *Organometallics* 2021, 40, 959−967

[89] M. Kim, C. H. Ryu, D. K. You, J. H. Hong, K. M. Lee, *ACS Omega* 2022, 7, 24027−24039

[90] N. Shin, S. Yu, J. H. Lee, H. Hwang, K. M. Lee, *Organometallics* 2017, 36, 1522−1529.

[91] H. J. Bae, H. Kim, K. M. Lee, T. Kim, Y. S. Lee, Y. Do, M. H. Lee, *Dalton Trans*., 2014, 43, 4978–4985

[92] B. P. Dash, R. Satapathy, E. R. Gaillard, J. A. Maguire and N. S. Hosmane, *J. Am. Chem. Soc.,* 2010, 132, 6578–6587

[93](*a*) K. Kokado and Y. Chujo, *J. Org. Chem.*, 2011, 76, 316−319; (b) K. Nishino, H. Yamamoto, K. Tanaka and Y. Chujo, *Org. Lett.*, 2016, 18, 4064-4067; (c) R. Furue, T. Nishimoto, I. S. Park, J. Lee and T. Yasuda, *Angew. Chem. Int. Ed.*, 2016, **55**, 7171-7175; (d) D. Tu, P. Leong, Z. Li, R. Hu, C. Shi, K. Y. Zhang, H. Yan and Q. A. Zhao, *Chem. Commun.*, 2016, 52, 12494-12497; (e) H. Naito, K. Nishino, Y. Morisaki, K. Tanaka and Y. Chujo, *J. Mater. Chem. C*, 2017, **5**, 10047-10054; (f) X. Wu, J. Guo, Y. Quan, W. Jia, D. Jia, Y. Chen and Z. Xie, *J. Mater. Chem. C*, 2018, **6**, 4140-4149; (g) N. V. Nghia, S. Jana, S. Sujith, J. Y. Ryu, J. Lee, S. U. Lee and M. H. Lee, *Angew. Chem. Int. Ed.*, 2018, 57, 12483-12488; (h) Y.-J. Cho, S.-Y. Kim, J.-W. Lee, W.-S. Han, C. H. Kim, H.-J. Son and S. O. Kang, *Chem. Eur. J.*, 2019, **25**, 8149-8156; (i) M. S. Mun, C. H. Ryu, H. So, M. Kim, J. H. Lee, H. Hwang and K. M. Lee, *J. Mater. Chem. C*, 2020, 8, 16896-16906.

[94] (a) K. C. Song, H. Kim, K. M. Lee, Y. S. Lee, Y. Do and M. H. Lee, *Dalton Trans.*, 2013, **42**, 2351-2354; (b) N. V. Nghia, J. Oh, S. Sujith, J. Jung and M. H. Lee, *Dalton Trans.*, 2018, **47**, 17441-17449; (c) L. Parejo, M. Chaari, S. Santiago, G. Guirado, F. Teixidor, R. Núñez and J. Hernando, *Chem. Eur. J.*, 2021, **27**, 270-280.

[95] W. Feng, K. Liu, J. Zang, G. Wang, R. Miao, L. Ding, T. Liu, J. Kong, Y Fang, *ACS Appl. Mater. Interfaces* 2021, 13, 28985−28995

[96] A. R. Davis, J. J. Peterson, K. R. Carter, *ACS Macro Lett.* 2012, 1, 469−472.

[97] M. Pawlicki, H. A. Collins, R. G. Denning, H. L. Anderson, *Angew. Chem. Int. Ed.* 2009, 48, 3244 – 3266

[98] L. Zhu, W. Lv, S. Liu, H. Yan, Q. Zhao and W. Huang, *Chem. Commun*., 2013, 49, 10638.

[99] M. Chaari, Z. Kelemen, D. C. Lazarte, N. Gaztelumendi, F. Teixidor, C. Viñas, C. Nogués R. Núñez, *Biomater. Sci*., 2019, 7, 5324–5337.

[100] (a) GL. Locher, *Am J Roentgenol Radium Ther*. 1936, 36, 1–13; (b) K. Nedunchezhian, N. Aswath, M. Thiruppathy, S. Thirugnanamurthy, *Journal of Clinical and Diagnostic Research*, 2016, 10, 1-4; (c) R. F. Barth F., et. al., *Cancer Commun.* 2018, 38:35, https://doi.org/10.1186/s40880-018-0299-7; (d) R. F. Barth et al. *Cancer Commun* 2018, 38:36, https://doi.org/10.1186/s40880-018-0280-5. (e) Zaitsev A. V., et. al., INEOS OPEN, 2020, 3, 188.

[101] D. Alberti, A. Toppino, S. G. Crich, C. Meraldi, C. Prandi, N. Protti, S. Bortolussi, S. Altieri, S. Aime, A. Deagostino *Org. Biomol. Chem.*, 2014,12, 2457-2467.

[102] A. Lanfranco, D. Alberti, S. Parisotto, P. Renzi, V. Lecomte, S. G. Crich, A. Deagostino, *Org. Biomol. Chem*., 2022, 20, 5342–5354.

[103] A. F. Ugalde, S. Sandoval, K. R. Pulagam, A. M. Juan, A. Laromaine, J. Llop, G. Tobias, R. Nuñez, *ACS Appl. Nano Mater.* 2021, 4, 1613−1625.

[104] E. H. Hawkins, C. Viñas, *Pharmaceutical & medicinal chemistry*, 2018, 1-496.

[105] M. N. Martinez, C. I. G. Pinto, J. F. Guerreiro, F. Mendes, F. Marques, A. M. Juan, J. A. M. Xavier, A. Laromaine, V. Bitonto, N. Protti, S. G. Crich, F. Teixidor, C. Viñas, *Cancers*, 2021, 13, 6367.

[106] M. N. Martinez, L. Pedrosa, I. M. Rovira, I. Yousef, D. Diao F. Teixidor, E. Stanzani, F. M. Soler, A. Tortosa, À. Sierra, José Juan Gonzalez C. Viñas *Int. J. Mol. Sci.,* 2021, 22, 9937.

Chapter 2

Objectives

The general objective of this doctoral thesis has been the design, preparation and study of different families of fluorophores that contain carborane clusters, that will be directly linked to the fluorophore at the $C_{cluster}$ atoms or through one spacer. The main aim will be to study how the carborane cluster affects the photophysical properties of the fluorophores and try to stablish a relationship between these properties, the structure of the fluorophores, the role of the cluster, always pursuing potential optical and optoelectronic application. For this purpose, the following specific objectives have been proposed:

1. To synthesize A-D-A systems based on π-conjugated aromatic fluorenes and thiophenes as donor groups, and *o*-carborane as the acceptor group. The main aim is to suppress a dramatic quenching usually observed in most of the fluorophores in solid state. The *o*-carborane units will be introduced directly linked to the aromatic groups without any spacer. We expect that the integration of the *o*-carborane will avoid the aggregation cause quenching (ACQ) phenomenon and facilitate the aggregation induced emission (AIE), producing an increased fluorescence in solid state. Photophysical properties of these systems in solution, aggregation and solid state, nanoparticles, and thin films will be explored looking for optical applications.

2. In this second objective, we will continue with the research work introduced in 2018 by our group in collaboration with Prof. Cristina Prandi´s research group, where for the very first time a small library of carborane-BODIPY/aza-BODIPY systems via Pd catalysed Heck coupling

reaction was reported. Hereafter, we will pursue the synthesis of new red-light emitting carborane-BODIPY dyads. We will follow similar synthetic route to obtain a set of new styrenyl-containing carborane and brominated dipyrromethene fluorophore as starting reagents. The photophysical properties of these fluorophores containing carborane moieties will be studied in detail in different solvents, also to understand the effect of the cluster on their properties. These systems also enable ample opportunities for biomedical applications.

3. To explore the synthetic route and photophysical properties of newly designed perylenediimide (PDI) based *o*-carborane derivatives, where the *o*-carborane clusters, as bulky groups, will be linked to the imide positions of PDIs in order to prevent the π-π interactions and improve the solubility of these systems in organic solvents. The o-carborane will be linked to the PDI through one spacer, to avoid quenching of fluorescence in solution. Besides, we are also interested on the preparation of micro and nanostructures (i.e nanoparticles) from these systems and study the photophysical properties both in solution and solid state, to explore their potential applications.

4. To design, synthesize and characterize *o*-carborane appended systems based on tri-branched π-conjugated fluorene and truxene. The directly attached *o*-carborane clusters to this kind of tri-branched systems has been scarcely explored and thus our objective will be to focus on their photophysical properties and future prospects in the field of opto-electronics and two-photon absorption spectroscopy. The experimental study will be support with theoretical calculations in order to explain the electron-accepting properties of the cluster when directly attached to the

fluorophores and its effect on the luminescent behavior of *o*-carborane appended final systems.

Chapter 3

o-Carborane based fluorophores: a journey from solution to water dispersible nanoparticles

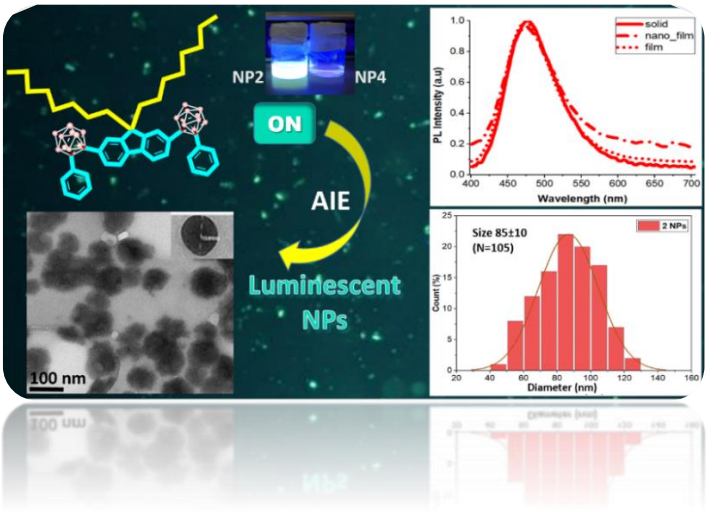

CONTENTS

3.1. Introduction

3.2. Results and discussion

3.2.1. Synthesis of fluorene and thiophene derivatives attached to *o*-carborane units

3.2.2. Characterization of fluorene and thiophene derivatives attached to *o*-carborane units

3.2.3. Photophysical properties in solution and TD-DFT calculations

3.3.4. Photophysical properties in aggregation, solid state and thin films

3.2.5. Preparation and characterization of water-dispersible organic nanoparticles (NPs)

3.2.6. Photophysical properties of NPs

3.3. Conclusions

3.4. References

3.1. Introduction

The solid-state light-emitting organic materials are important for the wide range of applications in the field of optoelectronics i.e., as organic light-emitting diodes, solar cells, semiconductors, or transistors. [1] In general, this type of materials comprises of π-conjugated aromatic structures for example, pyrene, fluorene, thiophene, BODIPY, coumarin and many other derivatives that are been used as fluorescent dyes and markers, owing to their strong fluorescent properties in solution.

Now highlighting the photoluminescent (PL) properties of fluorene and thiophene fluorophores in solution we can say that in the recent decade, fluorene and thiophene based π-conjugated monomer, polymers and oligomers have gained a reasonable spot in various applications, notably in optoelectronic devices such as light-emitting diodes, photovoltaic cells, sensors, lasers, molecular switches etc. Along with the chemical structures, the organization and combination of molecular systems involving π-conjugated fluorene and thiophene derivatives has been one of the important factors for optical and electronic properties. Various research groups have emphasized on the preparation and photophysics of fluorene monomers, oligofluorenes (OFs) and polyfluorenes (PFs) in solution, where the color tuning was easily achieved.[2] With the help of supramolecular order and non-covalent interactions, these systems could be successfully used as active materials for biological sensing and organic electronic devices. [3, 4, 5] Similarly, thiophene based π-conjugated derivatives have been prepared, keeping an eye on the molecular

orientation and structural design by various research groups.[6] This work has given an immense information in terms of synthesis, where Sonogashira cross-coupling reaction was used to achieve D-A or A-D type of systems and further photoluminescence behaviour was studied in solution in order to confirm their role in the fabrication process of organic field-effect transistors. This is a suitable result for organic photodetectors without colour filters in case of imaging applications.[7] One common problem faced by these simple π-conjugated aromatic systems is that the fluorescence is significantly quenched at high concentrations or in solid state due to aggregation caused quenching (ACQ). This reduces the scope for highly emissive solid-state luminogens and these luminogens can be further used as mechanical stimulus-responsive materials and in the biological as solid-state fluorescent dyes.[8]A rapid development has been made since many years to facilitate aggregation induced emission (AIE) by dramatically enhancing emission intensities and decreasing nonradiative decay through restricted intramolecular rotation due to formation of aggregates.[9] It has been observed in previous literature survey[10] that the fluorescence emission of fluorene-based *o*-carborane systems is not suppressed rather enhanced in solid state commencing AIE phenomenon. Thus, in this work we have introduced *o*-carborane units in between π-conjugated aromatic systems of thiophene and fluorene without any spacer, that usually is responsible to avoid ACQ and accelerate aggregation induced emission enhancement (AIEE). We have prepared new luminescent materials based on acceptor-donor type π-conjugated systems containing *o*-carborane clusters that show the property as AIEgen but at the same time gave us opportunity to explore and re-define the luminescent behaviour of these systems in water.

3.2. Results and discussion

3.2.1. Synthesis of fluorene and thiophene derivatives attached to *o*-carborane units

The preparation of fuorene and thiophene-based fluorophores linked to 1,2-dicarba-*closo*-dodecacarborane (or *o*-carborane) can be explained in two parts: a) general synthesis of acetylene precursors and b) a general synthesis of *o*-carborane-functionalized fluorene and thiophene derivatives.

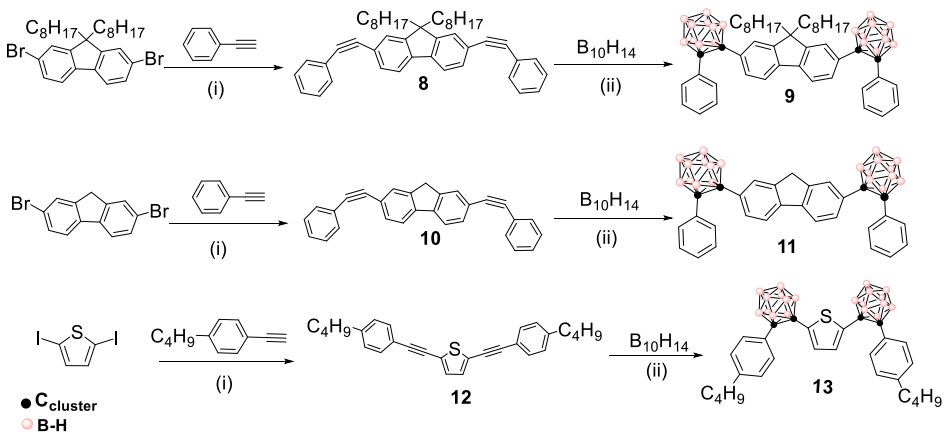

General Scheme. Designing fluorene and thiophene based π-conjugated scaffolds linked to *o*-carborane clusters: (i) Pd $(PPh_3)_2Cl_2$, CuI, TEA and toluene (1:9 v/v); (ii) 5 eq Et_2S, toluene, 72 h, 110 ^oC.

a) In the first part of the synthesis, the acetylene precursors of fluorene and thiophene derivatives were synthesized by Pd-catalyzed Sonogashira cross-coupling reaction (Scheme 3.1).

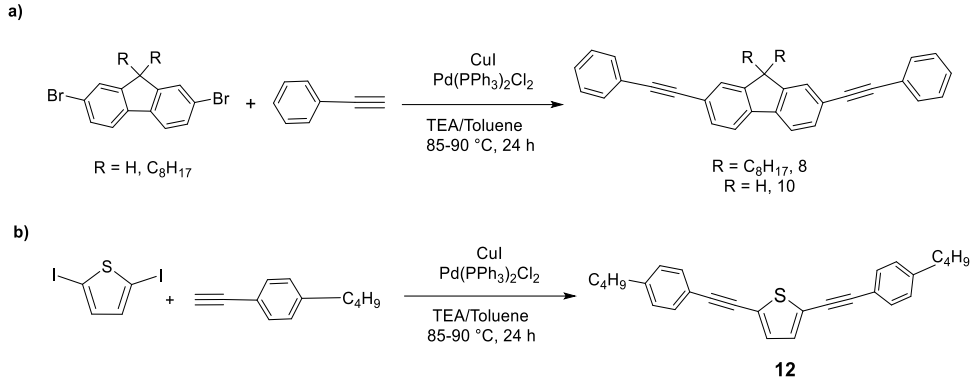

Scheme 3.1. Preparation of fluorene- and thiophene-based acetylene precursors via Sonogashira reactions

In Figure 3.1 we can see the catalytic cycle for the Sonogashira reactions, where the active Pd^0 catalyst converts to Pd^{II} complex through oxidative addition with Ar-X. Then, this complex reacts with copper acetylide yielding palladium acetylide complex and free Cu catalyst followed by reductive elimination to generate the active Pd catalyst again. [11] Therefore, for our reaction, a mixture of the corresponding di-bromo fluorene (Scheme 3.1a) or di-iodo thiophene derivatives (Scheme 3.1b), $Pd(PPh_3)_2Cl_2$ as a catalyst, and CuI as co-catalyst were used. A proportion of 1:9 toluene and TEA were used as solvents. After purification and isolation, compounds **8**, **10** and **12** were obtained in 61%, 64% and 62% yields, respectively.

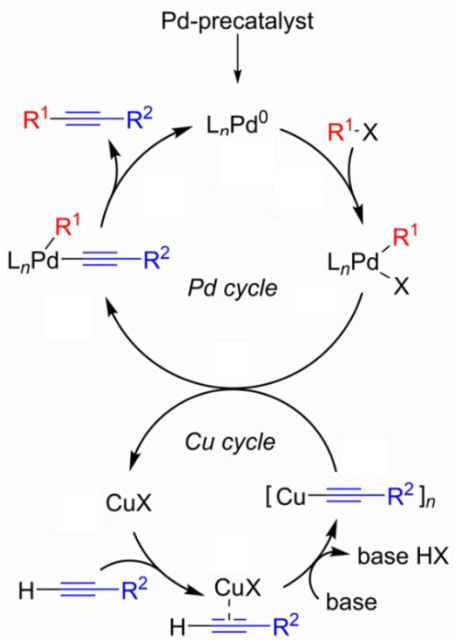

Figure 3.1. A simplified catalytic cycle of the Sonogashira reaction

b) In the second part of the synthesis, insertion reaction has been performed using decaborane, $B_{10}H_{14}$, and corresponding acetylene precursors. This reaction requires a proper selection of Lewis base in order to obtain the best yield. Therefore, several reaction conditions such as solvent, temperature, Lewis base and time were attempted to obtain the optimal conditions with the highest product yield (Table 3.1). In this table we see that ultimately entry 3 gave us 38 %, so these parameters were followed for the preparation of all the *o*-carboranyl compounds containing fluorene and thiophene derivatives.

Table 3.1. Reaction conditions used for insertion reaction of alkyne into decaborane cluster to form carborane icosahedron 1,2-RR'-$C_2B_{10}H_{10}$.

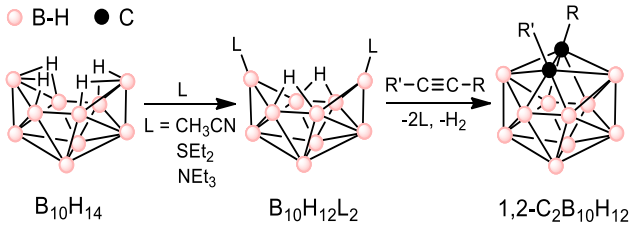

Entry	Lewis base	Solvent	Temperature (^{0}C)	Time (h)	Yield (%)
1	CH_3CN (2.5 equiv)	Toluene	85	52	21
2	CH_3CN (5 equiv)	Toluene	100	60	24
3	Et_2S (5 equiv)	Toluene	110	72	38

The reactions displayed in Scheme 3.2 indicate that fluorene and thiophene derivatives containing two *o*-carborane clusters were afforded following the insertion reaction between decaborane ($B_{10}H_{14}$) and acetylene **8**, **10** and **12** as starting materials, in the presence of an excess of diethyl sulfide (Et_2S, 5 equiv per acetylene precursor) in toluene. The main role of Lewis base is to form an adduct through elimination of two H atoms attached to two boron atoms of the $B_{10}H_{14}$ cluster that leads to formation of $B_{10}H_{12}L_2$, as shown on top of Table 3.1. Then, the adduct reacts with the corresponding acetylene precursor via ring closure step to obtain the target *ortho*-carborane derivative. The insertion reaction is a one-pot reaction, where the formation of adduct is an intermediate step. Finally the reaction stirred at reflux for 72 hours[12] and after purification and isolation final carboranyl-based compounds **9, 11** and **13** with moderate yields of 34%, 38%, and 46 % respectively (Scheme 3.2) were obtained.

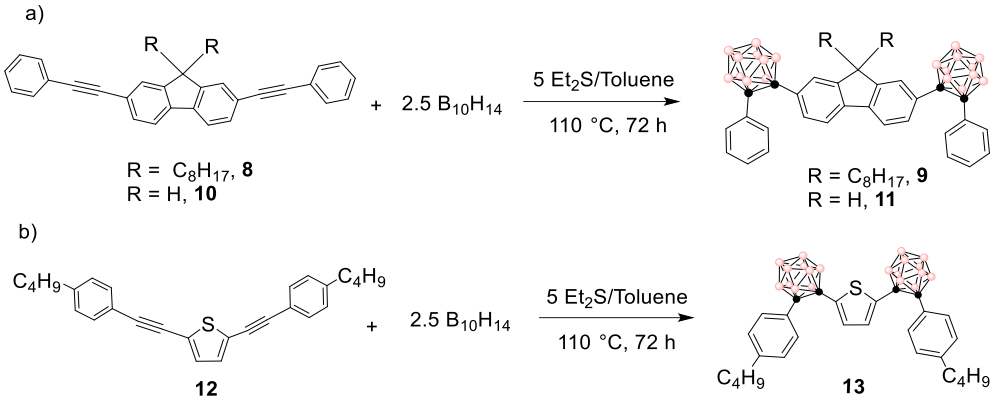

Scheme 3.2. Preparation of *o*-carborane based fluorene and thiophene derivatives

3.2.2. Characterization of fluorene and thiophene derivatives attached to *o*-carborane units

The structures of **8** to **13** were established and easily monitored by FT-IR, ^{1}H, $^{13}C\{^{1}H\}$ and $^{11}B\{^{1}H\}$ spectroscopy techniques, and elemental analyses.

The FT-IR spectra of compounds **9**, **11** and **13** show typical υ(B-H) strong bands for *closo* clusters between 2565 and 2578 cm^{-1} (Figure 3.2). The presence of this band in the spectre is a key indication of the formation of the expected *o*-carborane cluster in the final compounds.

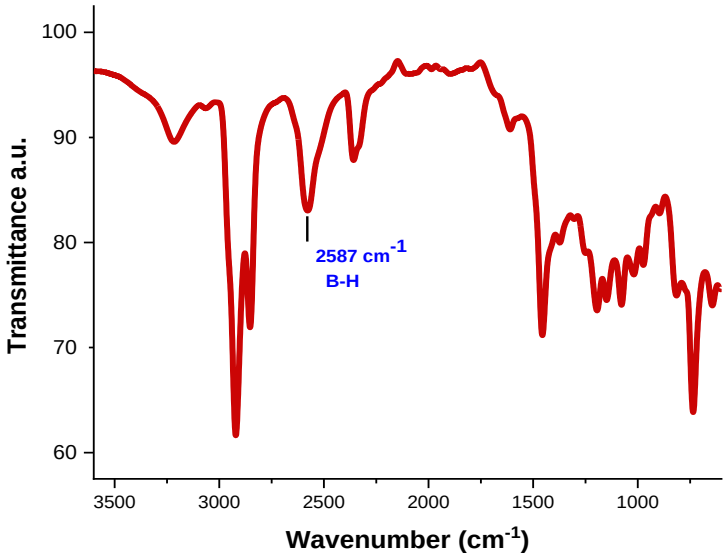

Figure 3.2. FT-IR spectrum of **9** showing typical υ(B-H) band for *o*-carboranyl derivatives

On the other hand, ^{1}H NMR spectra of **9** and **11** display the proton resonances in the aromatic region δ 7.60-7.07 ppm, which was shifted upfield (0.3 ppm) with regards to **8** and **10**; but in the case of **13**, the upfield shift was up to 0.18 ppm from its acetylene precursor, **12**. Also, in the ^{1}H NMR of **8** and **9** the presence of dioctyl chains was confirmed by protons that appeared in the region of δ 1.00 to 1.40 ppm (Figure 3.3). An emphasis on the improved solubility and photophysics of the structure in presence of dioctyl chains (compound **9**) has been discussed later in the chapter. In fact, we observe a very less intense but broad signal for proton attached to boron atoms of the 1,2-$C_2B_{10}H_{10}$ cluster from δ 1.75 to 3.00 ppm, this is a distinct property of *o*-carborane containing compounds, which is absent in case of their corresponding acetylene precursors.

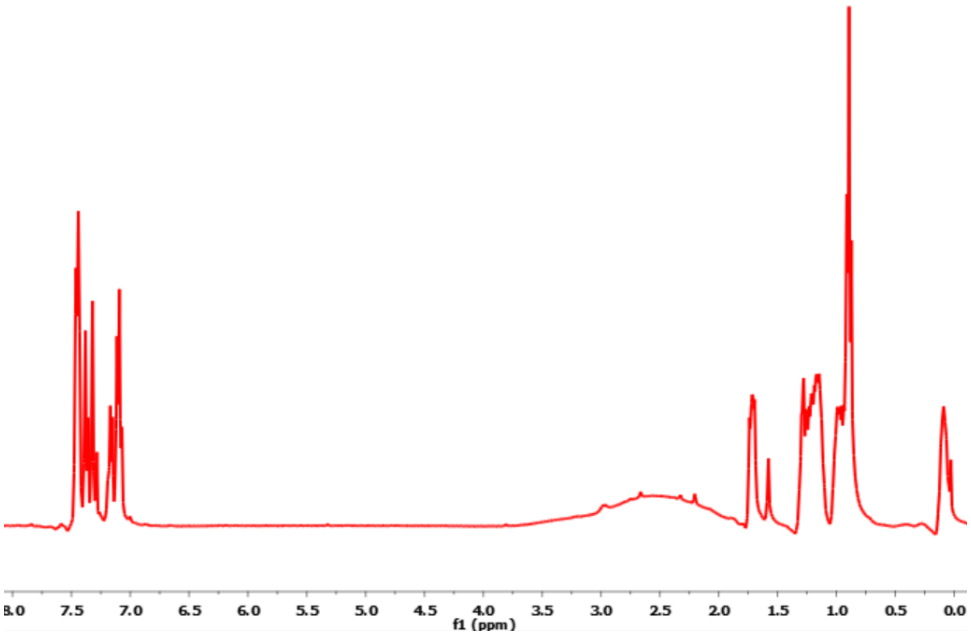

Figure 3.3. ^{1}H NMR spectrum of **9** containing dioctyl chains and *o*-carborane clusters.

The $^{11}B\{^{1}H\}$ NMR spectra for compounds **9**, **11** and **13** show resonances in the characteristic *closo* region, from δ -2.29 to -10.30 ppm, with the general pattern of 2:8, which is the usual pattern for symmetrical and di-substituted *o*-carboranyl derivatives (Figure 3.4). For this kind of reactions, it is important to notice that the ^{11}B NMR spectrum is key to confirm the formation of the expected *o*-carborane derivative. The observation of this usual patterns clearly indicates the presence of the clusters in the molecule.

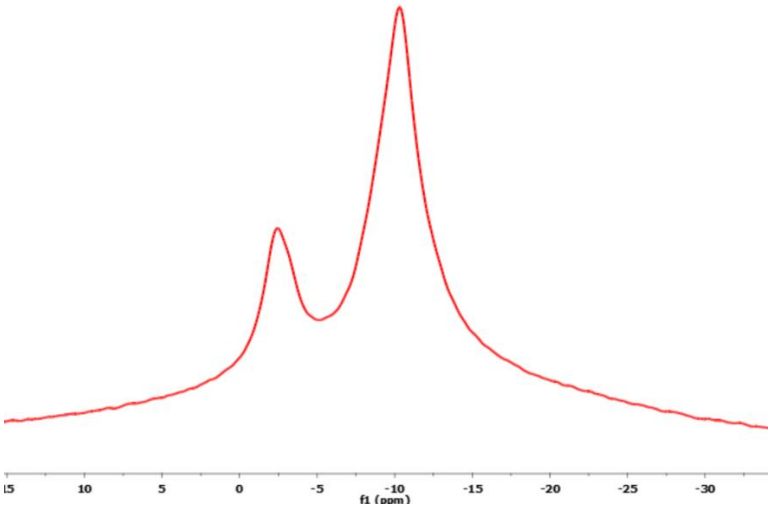

Figure 3.4. $^{11}B\{^1H\}$ NMR highlights the *closo* region of the *o*-carborane unit of **9**

The $^{13}C\{^1H\}$ NMR spectra showed resonances at around δ 85.84 and 85.49 ppm for **9** and **11**, respectively, whereas resonances at around δ 85.95 ppm for **13** are assigned to the C_c carbons of the *o*-carborane fragments. All these final compounds show aromatic resonances in the range of δ 119.91 to 151.14 ppm. The $^{13}C\{^1H\}$ NMR spectrum of compound **9** is displayed in Figure 3.5 as an example. Finally, the elemental analyses also confirmed their stoichiometries.

3.2.3. Photophysical properties in solution and TD-DFT calculations.

Fluorene acetylene precursors **8** and **10** exhibit intense absorption bands with maxima at 349 nm and 346 nm respectively, which mainly comprise of a $\pi-\pi^*$ transition of the aromatic fluorene fragment. These absorption bands undergo a prominent hypsochromic shift (around 31-35 nm) for the respective carboranyl derivatives, **9** and **11,** that absorb at high-energy bands

(314 and 308 nm, respectively) and tails off around 350 nm (Table 3.2 and Figure 3.6). In the case of thiophene derivative, we observe a blue shift from **12** to **13** with a difference of 86 nm between the two compounds, which is much larger in comparison to the fluorene derivatives.

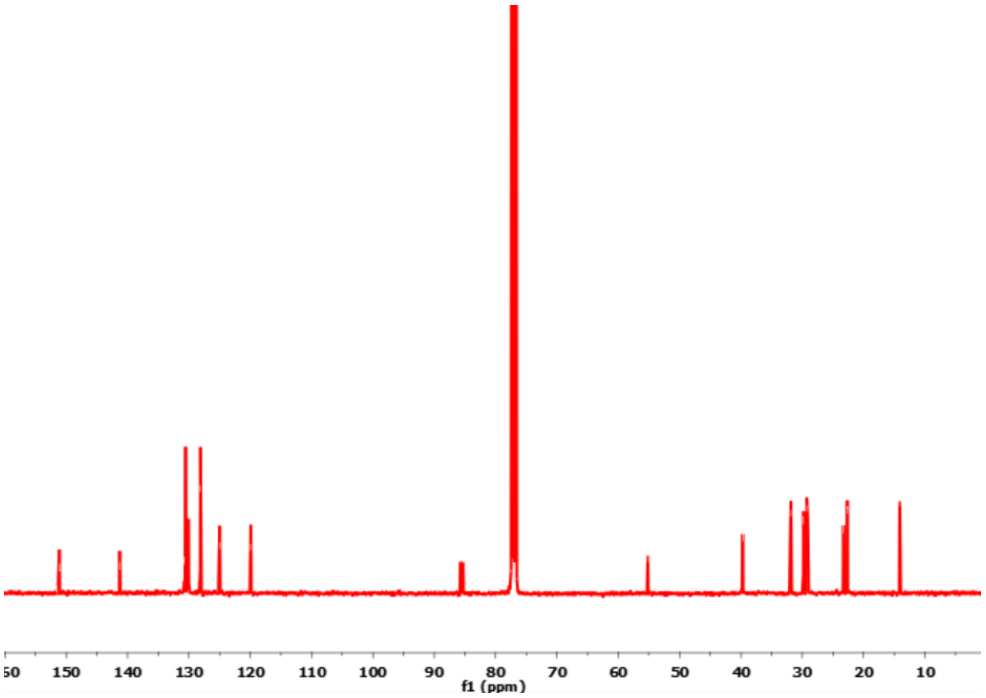

Figure 3.5. $^{13}C\{^{1}H\}$ NMR spectrum of **9**

This blue-shift along with a lower molar extinction coefficient (Ɛ) values indicate a decrease in the conjugation for the fluorene based carboranyl systems and poorer conjugation in case of thiophene based carboranyl system.[13] Also, for **9** and **11** these types of bands are responsible for the transitions originating from ICT between fluorene fragments and *o*-carborane moieties. In case of **13**, local excitation character is more pronounced in *o*-carborane moiety implying shorter absorption wavelength (Figure 3.6).

Table 3.2. Phophysical data of compounds **8-13**

No.	Abs λ_{abs}[a] (nm)	$\varepsilon/10^5$*	λ_{em}[a] (nm)	Φ_F[a]	λ_{em}[b] (nm)	Φ_F[b]	λ_{em}[c] (nm)	Φ_F[c,d]	λ_{em}[e] (nm)	Φ_F[e]	λ_{em}[f] (nm)	Φ_F[f,d]
8	349	2.690	372, 393	0.89	380	< 0.01	435	0.08	-	-		
9	286, 314	0.542, 0.611	404	0.01	483	0.06	477	0.71	478	0.39	473	0.74
10	346	2.322	367, 389	0.64	465	0.04	511	0.18	-	-		
11	293, 308	0.522, 0.572	372	<0.01	536	0.01	500	0.04	528	0.01	546	0.03
12	348	0.2614	389, 407	0.25	452	0.03	_	_	-	-		
13	274	0.3211	390	0.19	_	_	591	0.10	-	-		

[a]THF solutions (3.0×10^{-5} M for **9**, **11-13** and 1×10^{-6} M for **8** and **10**), [b]in aggregate state (THF/H_2O = 1/99 (v/v)), [c]in solid state, [d]absolute Φ_{PL} from the integrating sphere, [e]NPs of **9** and **11** in water suspension, [f]thin films prepared by spin-coating of THF solutions on Spectrosil B quartz substrates. *($M^{-1}cm^{-1}$)

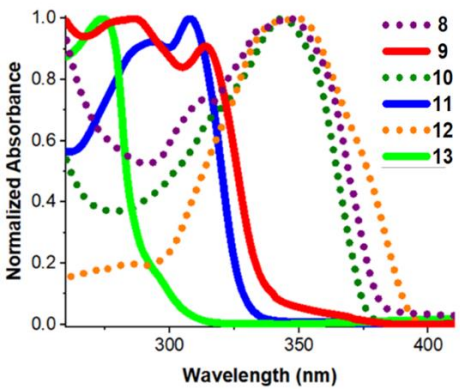

Figure 3.6. Absorption spectra of **8-13** in THF ($3 \cdot 10^{-5}$ M to $1 \cdot 10^{-6}$ M)

To verify these hypotheses a computational study using different DFT functions with B3LYP/6-31G* level of theory for **9**, **11** and **13** (Figure 3.7) was carried out. The DFT calculations were done in collaboration with Dr. Zsolt keleman from Budapest University of Technology and Economics.

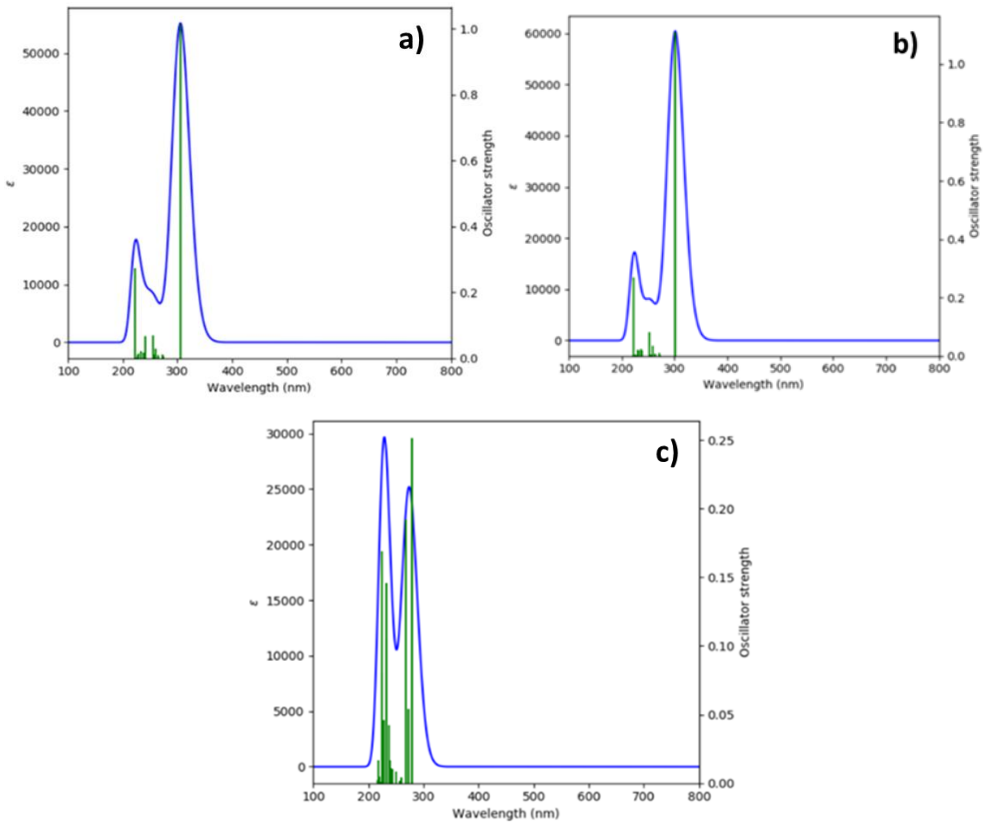

Figure 3.7. Simulated absorption spectra for a) **9**, b) **11** and c) **13** by B3LYP/6-31g*

The results of these calculations were compared with the calculations at ω-B97XD/6-311+G**; nevertheless, the application of the higher level resulted in only marginal structural changes. However, for the purely organic systems **8**, **10** and **12,** CAM-B3LYP functional was used (Figure 3.8), as the hybrid, long-range corrected CAM-B3LYP functional provided better results for extended conjugate organic systems, which was verified by test calculations as well. It could be explained that investigating the calculations using the canonical Kohn-Sham molecular orbitals, the

o-carborane clusters noticeably breaks the conjugation between the π-conjugated linkers.

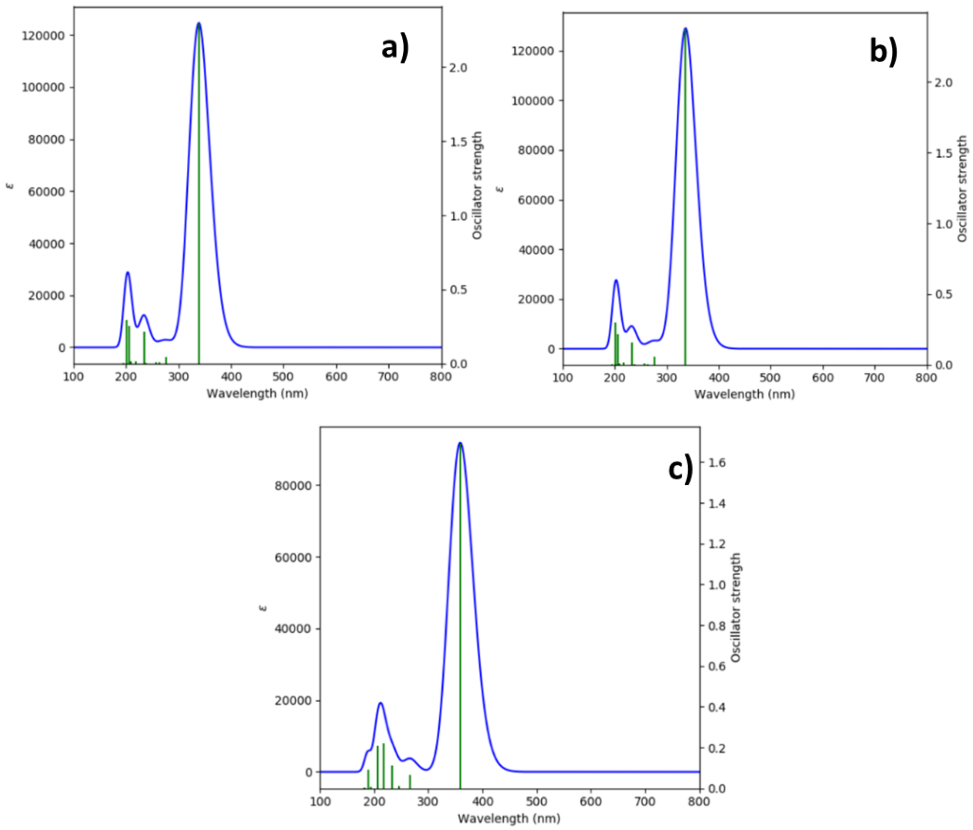

Figure 3.8. Simulated absorption spectra for, a) **8** b) **10** and c) **12** by CAM-B3LYP/6-31g*

In fact, TD-DFT calculations have supported the experimental absorption wavelength by elucidating the observed absorption maxima (Figure 3.6), which is mainly due to HOMO-LUMO orbital transitions. The two types of transitions are more relevant, one of which is the transition originating from a pure organic aromatic system implying a long range π-π^* type electronic delocalisation. In

Figure 3.9, we see that according to Kohn-Sham orbitals, the most stable rotamer of **9** has a decreased electron density at the fluorene ring (HOMO) and an increased electron density at the *o*-carborane clusters (LUMO) after electron excitation, suggesting charge transfer process towards the two carborane units. This result is in accordance with the bond elongation reported recently for $C_{cluster}$-$C_{cluster}$ (C_c-C_c) distance which proceeds when **9** and **11** are shown as single molecules and a weak fluorescence can be expected in organic solvents.[14]

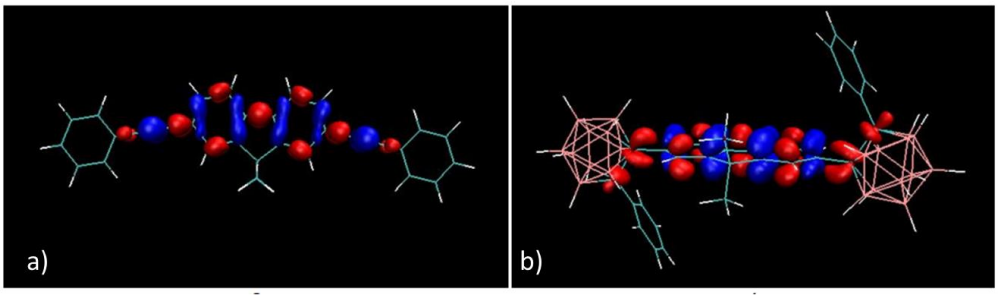

Figure 3.9. Charge density difference map (blue: low electron density and red: high electron density after excitation) of a) **8** and b) **9**

The second type of transition is the *o*-carborane based compounds exhibiting different ICT characteristic features. The experimental UV-Vis measurements as well as TD-DFT calculations were relatable as for compound **12,** it absorbed at a maximum of 348 nm, experiencing a significant blue-shift after the incorporation of *o*-carborane moieties in **13** (274 nm). And these results were in agreement with the theoretical values such that the origin of this shift was attributed to the more significant ICT character of the equivalent transition. The excitation wavelength of **9** and **11**, has moderate ICT characteristic, prevailing from fluorene fragment to the carboranyl moiety. However, the transition type in **13** has an

intense ICT property existing in between the two aromatic rings and the scaffolds of thiophene.

In solution, remarkable fluorescence quantum yield was observed for **8** (Φ_F =0.89) and **10** (Φ_F=0.64) with emission maxima at 372 nm and 367 nm, respectively (Figure 3.10). For the emission spectra, λ_{max} of **9**, **11** and **13** are red shifted from their corresponding acetylene precursors **8**, **10** and **12** by around 17 to 32 nm. However, in case of **9** and **11** where the two *o*-carborane clusters have been incorporated, a severe quenching of the fluorescence emission was produced in solution, where Φ_F values were lower than 0.01 (Table 3.2).

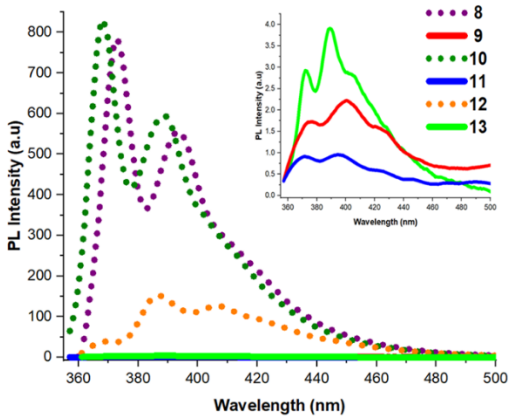

Figure 3.10. Fluorescence emission spectra of **8-13** in THF ($3 \cdot 10^{-5}$ M to $1 \cdot 10^{-6}$ M)

The DFT calculations were in line with the fact that the occurrence of ICT transitions due to the presence of carboranyl clusters confirms the fluorescence emission quenching. Regarding the thiophene precursor **12** and its carboranyl compound **13**, no significant changes in terms of emission patterns were observed

(Table 3.2), which could be explained by the unique nature of excitation bands.[15] Thus, we didn´t observe quenching in solution nor AIE in aggregate state (*vide infra*). Furthermore, the quadrupole nature of the structural morphology of donor-acceptor type systems triggered the idea to study two-photon absorption (TPA) properties. However, we observed very low values for TPA cross section area (δ_{MAX}) in the range 10^{-50} GM. This is due to TPA forbidden character of S_0-S_1 transition with the previously mentioned quadrupole nature of electronic symmetry. Although, the precursors could be potentially activated (two-photon) in the NIR range but the presence of *o*-carborane units reduces the π-conjugation significantly. This is responsible for a blue -shift in the absorption measurements for the *o*-carborane series leading to poor or negligible TPA properties.

It has been observed from the theoretical calculations that the ICT transitions have been much more prevalent among the two terminal phenyl rings and the thiophene units, minimising the participation of *o*-carborane units in the radiative transition.

3.2.4. Photophysical properties in aggregation, solid state and thin films.

Now after determining the PL behaviour of compounds **8** to **13** in solution, we next performed the solid state, aggregation, and thin films photothysical properties of these systems minutely. For aggregates of compounds **9** and **11** obtained in a mixture of THF/H_2O (1:99, v/v), we first noticed a slightly higher ϕ_F value

compared to the solution for **9**, whereas no differences in the ϕ_F value for **11** was observed. Moreover, for compound **13** due to aggregation caused quenching (ACQ) effect, we did not detect fluorescence emission at all in the aggregate state but a quenching of the fluorescence with regards to the solution occurred.

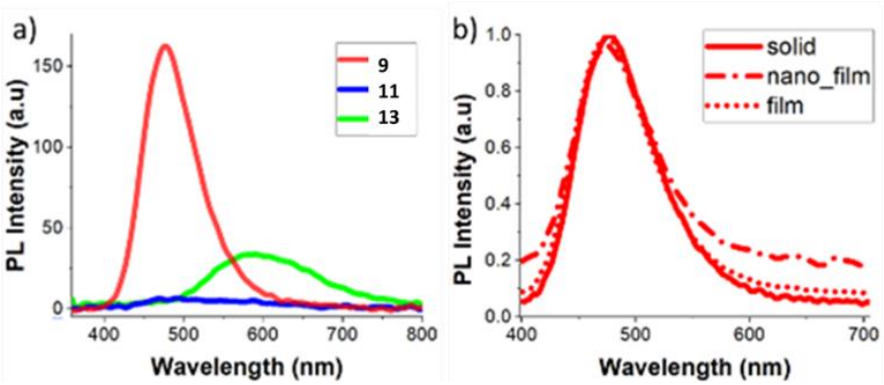

Figure 3.11 (a) PL spectra for **9**, **11** and **13** in solid state. (b) Normalised PL spectra of **9** in solid, film and NPs in film

Remarkably, a significant red shift of the λ_{em} maximum in the solid state (around 70 nm) for compound **9** with regards to the solution was appreciated. In addition, large differences on the solid-state emission efficiency for compounds **9**, **11** and **13** might be observed (Figure 3.11); whereas compound **9** exhibits a high fluorescence quantum yield (Φ_F) of 0.71, very low emissions are given by **11** and **13** (Table 3.2). Even though, **9** and **11** have similar electronic properties, due to the presence of the octyl chains in **9,** the intermolecular organization of the structural morphology clearly plays a crucial role, and this has an impact on PL properties in solid. However, compound **11** showed weak emission in solid state with

Φ_F value = 0.04. On the other hand, solid state fluorescence in case of **12** was completely quenched, where we obtain Φ_{PL} = 0.10 for **13.** Inspired by extremely enhanced solid-state fluorescence emission of **9**, thin films were prepared by spin-coating THF solutions on Spectrosil B quartz substrates. As expected, the λ_{max} values of the fluorescence emission of solid state and thin films for compound **9** matched well (Figure 3.11b) with even higher quantum yield values as shown in Table 3.2.

Fig. 3.12. Preliminary studies using thin films of **9** using DMP-2850 inkjet printer (Fujifilm) and the Molecular Gate S.L. technology, developed by Mariano Campoy-Quiles and Aleksandr Perevedentsev.[16]

Due to the tuning properties and fluorescence quantum yield (ϕ_F) values of compound **9** in solid and thin films, we have carried out a preliminary study where we used **9** in thin films for inkjet printing techniques as it is shown in Figure 3.12.[16,17] We can conclude that among the three final compounds, **9** exhibited enhanced aggregation induced emission (AIE) properties in which the *o*-carborane fragment plays a major role. All these results indicated that compound **9** is a potential AIEgen for optoelectronic devices.[18,19]

To summarize the PL behaviour of the prepared compounds, for the starting materials, **8**, **10** and **12**, a continuous decrease in ϕ_F values were observed in aggregation, solid state and thin films, this is again due to ACQ effect in solid state. For compounds **9**, **11** and **13** in aggregation, solid state and thin film (Figure 3.11), significant differences were found among these three compounds. Notably, compound **9** showed a non-vibronic red shifted emission from THF solution along with an exceptional enhancement in fluorescence emission efficiency due to the AIE phenomenon in solid, that has been attributed to the presence of dioctyl chains.

3.2.5. Preparation and characterization of water-dispersible organic nanoparticles (NPs)

The main purpose behind developing nanoparticles (NPs) in water is to combat the disadvantage that generally fluorophores directly linked to *o*-carborane units face in solution state (using organic solvents) i.e. a significant quenching in fluorescence quantum yield that hinders these systems to be used in biological applications. Due to the challenges faced to develop boron-based luminescent materials for biomedicine or bio(nano)medicine, we tried to attain water-stable, highly soluble and bright fluorescent carborane-cluster based nanoparticles. For this purpose, we considered using the re-precipitation method with a mixture of THF/H_2O (1:99, v/v) and optimal conditions.

The re-precipitation method is a single-step self-assembly method for obtaining organic nanoparticles. It is the most popularly used solvent-exchange process that has been developed over a decade by several research groups such as Nakanishi´s, Majima´s, Yao´s, Park´s, Barbara´s, Horn and co-workers. These various groups have successfully investigated the preparation, size distribution and dependency of the luminescence and emission enhancement of numerous organic nanoparticles.[20,21] Some of the crystalline nanoparticles obtained by these groups have confirmed the formation of J-aggregates which results in enhanced radiative decay rate.[22] The re-precipitation method generally consists of adding a 1 ml of concentrated solution (10^{-3} M in this case) of a water miscible organic solvent solution (THF) of a hydrophobic compound (compound **9**)in 9 ml of milliQ water at the rate of 1ml/hour, and stirred vigorously at 400 rpm. The fast mixing of the two solvents induces the precipitation of the organic compound in micro to nano sized aggregates since the organic molecules get saturated in the new solvent mixture (Figure 3.13). After an hour of continuous stirring, the mixture was kept stirring for another hour, even after the completion of the addition of THF. Gradually, precipitation in the solution mixture appeared and the solubility of the organic material decreased thus these molecules aggregated homogeneously and formed nanoparticles.[23] The final concentration prepared was 10^{-4} M.

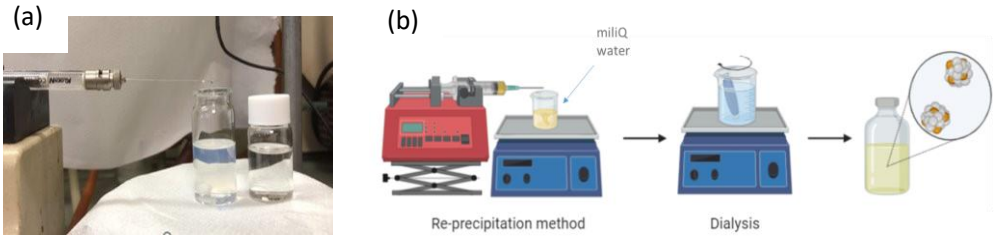

Figure 3.13. (a) Preparation of NPs and aqueous solution turns turbid as **9** dissolved in THF is added dropwise. (b) Schematic representation of reprecipitation method followed by dialysis.

The experimental parameters involved in the preparation technique to control the particle size are temperature, concentrations, volume and velocity of the syringe, nature, and volume of the miscible solvent. As well as the composition, time, and agitation speed (rpm) of the non-solvent. Hence, for the growth of organic nanoparticles both kinetics and thermodynamics processes are being considered.[24] To obtain a NP suspension only in water, the THF was removed with a dialysis procedure using a D9652-100FT dialysis tubing cellulose membrane. Dialysis was done using a 500 mL beaker containing milliQ water, and water was changed every 6 hours during the entire duration of 72 hours. To our knowledge, this is the first example of carborane-based homogeneous nanoparticles in water which shows strong fluorescent emission following this methodology.

The formation of nanoparticles was confirmed by DLS, TEM, Z-potential, UV-Vis and fluorescence spectroscopy (FL) techniques.

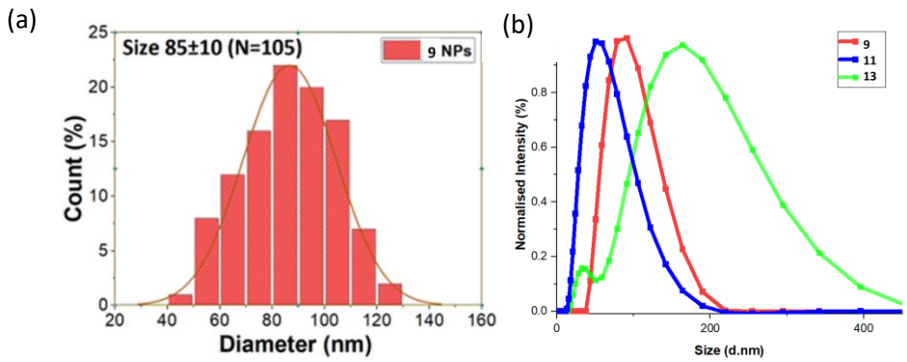

Figure 3.14. (a) Size distribution histogram for NPs of **9** (size 85 ± 10; N = 105) (b) Size distribution by intensity plot of NPs of **9**, **11** and **13.**

The results obtained from TEM and DLS techniques were comparable. From TEM images the average size ranged from 70 to 100 nm. The Table 3.3 shows the DLS average size of **9**, **11** and **13** NPs in the range of 72 to 122 nm with almost 0.1 polydispersity index (PdI), that is a measure of the broadness of the size distribution and should ideally be between 0 to 1. Figure 3.14 shows the size distribution histogram for NPs of **9** and size distribution for NPs of **9**, **11**, and **13.** The DLS results align well with TEM images as shown in Figure 3.15, where the average size of **9** NPs is 73.61 nm. To check the stability of NPs prepared from **9**, they were stored at 4 ºC for two weeks, Z potential was around -43.6, and TEM and DLS measurements confirmed the stability of **9** NPs.

Table 3.3 Size and PDI data of NPs of **9**, **11** and **13**

Compound	Concentration	Average Size (nm)	PdI
9	1.0×10^{-5}	84.30 ± 10	0.09
11	1.0×10^{-5}	72.37 ± 10	0.10
13	1.0×10^{-5}	122.10 ± 10	0.12

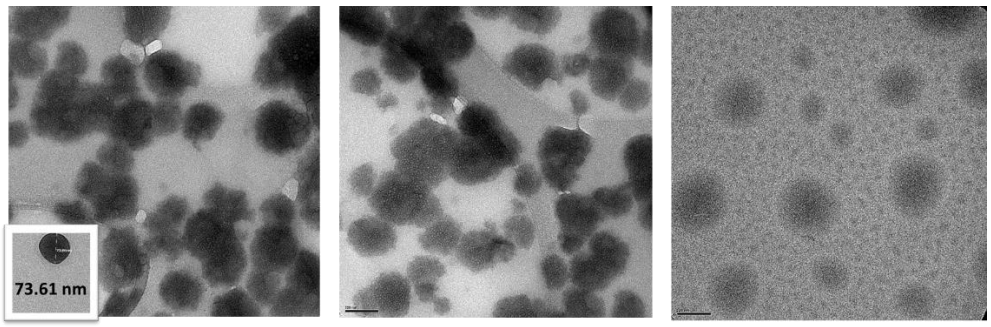

Figure 3.15 TEM image of NPs of **9**.

3.2.6 Photophysical properties of NPs

The UV-Vis absorption spectra indicate that the λ_{max} values for NPs of **9** and **11** match exactly with their corresponding aggregation state (Figure 3.16a). The PL emission spectra for NPs of **9** and **11** and their aggregation states (Figure 3.16b) clearly suggest that we have obtained a much higher fluorescence for **9** in both states but most importantly for NPs of **9** with a 39% quantum yield (Table 3.2).

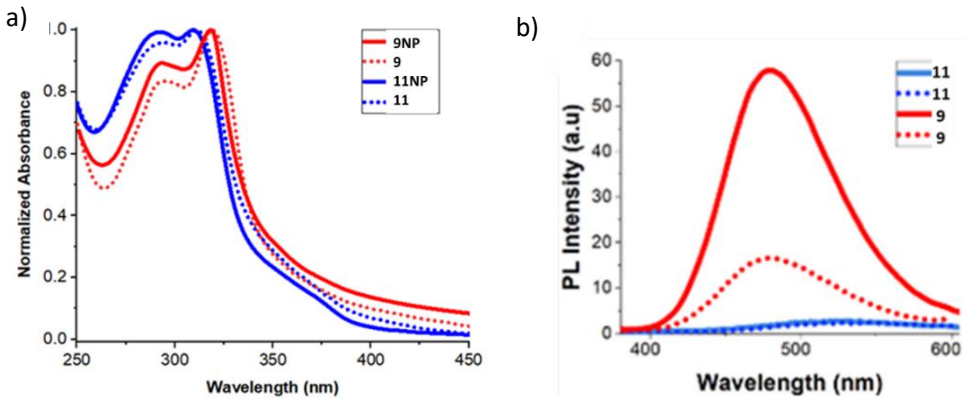

Figure 3.16. (a) Normalised absorption of **9** and **11** in aggregated state (dotted line) and as NPs in water (solid line). (b) Fluorescence emission spectra of aggregates in THF/H_2O (1:99, v/v) (dotted line) and NPs in water (solid line) at $1 \cdot 10^{-5}$ M of **9** and **11** (λ_{exc} = 314 nm).

The fluorescence emission spectra of dispersions of NPs of **9** in water showed a similar pattern to the solid state and thin films with a maximum at 478 nm (Figures 3.11b and 3.16b) along with a high Φ_{PL} value of 0.39, which is much higher than in solution (~0.1). This results confirmed that **9** is a good AIEgen maintaining the excellent fluorescent properties after the formation of NPs (Table 3.2).

Observing the fluorescence enhancement of **9** NPs in water suspension (Figure 3.16), and as they can exhibit intense absorption and downshifted PL, we tried to obtain films doped with NPs (Figure 3.17) for the application of solar cells incorporating luminescent solar concentrators (LSCs). The UV absorption of **9** NPs could be a better match to the absorption spectrum of the photovoltaic cell.[25] Therefore, for the preparation of these film doped NPs we considered this compound, due to its exceptional photophysical properties. The preparation of films was done by drop-casting method where, an aqueous dispersion of NPs of **9** (10^{-3} M) was drop-casted on Spectrosil B quartz substrates. We allowed them to dry in ambient conditions and obtained an outstanding Φ_F of 0.54 from films of NPs (Table 3.2), that´s comparable or higher to quantum yields of previously reported LSC dyes.[26] Due to its high stability as well as tunability of formulation, it could also be used for printing applications. Further studies in this direction will be carried out.

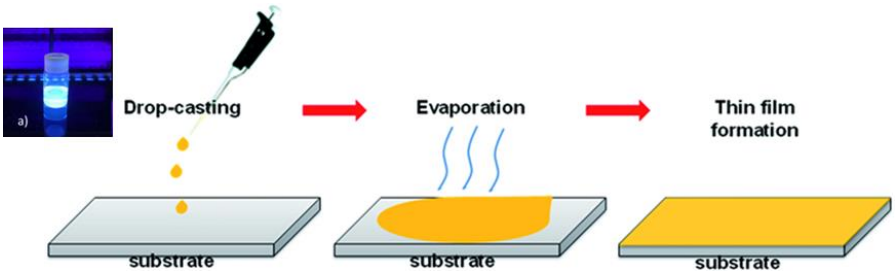

Figure 3.17. Drop casting method used to prepare thin films doped **9**NPs

Apart from its application in electronic devices such as sensors, solar cells and ink for inkjet printing, it can also be used in biomedicine. Some preliminary studies have been done, where these NPs of **9** were

centrifuged in 10% fetal bovine serum (FBS) and 1% DMSO buffer solution and irradiated in the range λ_{exc} = 330-385 nm to observe their strong fluorescent properties under fluorescence microscope (Figure 3.18). Further studies to incubate cancer cells with these NPs to study their cellular uptake and cytotoxicity will be carried out.

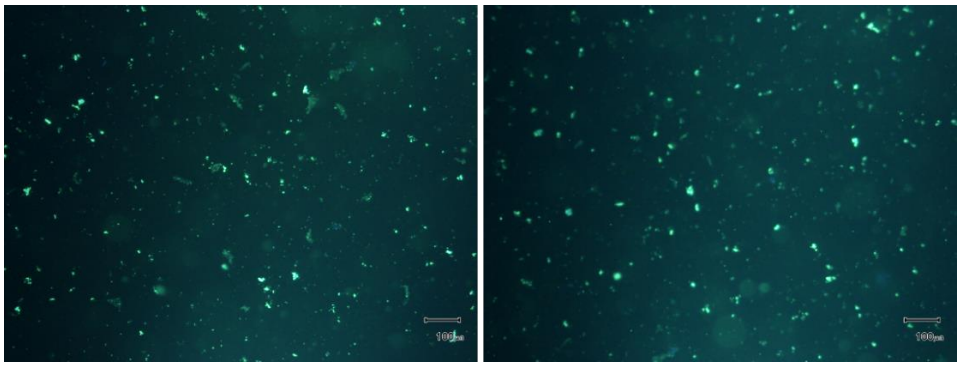

Figure 3.18 Fluorescence microscopy image of **9** NPs in 10% fetal bovine serum (FBS) and 1% DMSO

3.3. Conclusions

In conclusion, we developed A-D-A systems based π-conjugated *o*-carborane moieties and investigated the entire photophysics in solution, aggregation, solid state and films. The extraordinary fluorescence behaviour of the *o*-carborane based octyl-substituted fluorene **9** in solid state encouraged us to prepare water dispersible nanoparticles and this is the first report as per our knowledge. This NPs in water exhibited remarkable fluorescence emission properties (Φ_F = 0.39), leading us for some promising results towards biological applications. Additionally, we doped **9** NPs in films, which showed an excellent PL efficiency (Φ_F = 0.54). NPs doped in thin films

could be effectively used in electronic devices such as sensors and solar cells. A brief study of device/level charge carrier behaviour will be studied thoroughly to understand its role as film transistors. We have demonstrated that well-engineered architectures based on *o*-carborane-containing fluorophores are good light emitters both in solid state and in aqueous medium as nanoparticles. Combining all these results, we can conclude that these type of *o*-carborane based materials have opened up new opportunities in the field of biomedicine and optoelectronic. Research work is currently underway in this direction.

3.4. References

[1](a) Organic Light-Emitting Diodes (OLEDs) in Electronic and Optical Materials in Devices and Applications, Ed. A. Buckley, Woodhead Publishing, 2013; (b) M. Koden in OLED Displays and Lighting, John Wiley & Sons, *Ltd*. 2017, 232; (c) Y. Jiang, Y.-Y. Liu, X. Liu, H. Lin, K. Gao, W.-Y. Lai, W. Huang, *Chem. Soc. Rev*. 2020, 49, 5885-5944; (d) C. Adachi, R. Hattori and H. Kaji, in *Handbook of Organic Light Emitting Diodes*, ed. T. Tsujimura, Springer, Tokyo, Japan, 2020.

[2](a) R. Anéniam, J.-C Mulatier, C. Andraud, O. Stephan, J.-C. Vial, *Chem. Commun.* 2002, 1608–1609; (b) J. Jo, C. Chi, S. Höger, G. Wegner, D. Y. Yoon, *Chem. Eur. J*. 2004, 10, 2681–2688; (c) S. P. Dudek, M. Pouderoijen, R. Abbel, A. P. H. J. Schenning, E. W. Meijer, *J. Am. Chem. Soc.* 2005, 127, 11763–11768; (d) Y. Geng, A. Trajkovska, D. Katsis, J. J. Ou, S. W. Culligan, S. H. Chen, *J. Am. Chem. Soc*. 2002, 124, 8337–8347; (e) D. Katsis, Y. H. Geng, J. J. Ou, S. W. Culligan, A. Trajkovska, S. H. Chen, L. Rothberg, *J. Chem. Mater.* 2002, 14, 1332–1339; (f) Y. Geng, A. Trajkovska, S. W. Culligan, J. J.

Ou, H. M. P. Chen, D. Katsis, S. H. Chen, *J Am. Chem. Soc.* 2003, 125, 14032–14038; (g) Y. Geng, S. W. Culligan, A. Trajkovska, J. U. Wallace, S. H. Chen, *Chem Mater.* 2003, 15, 542–549.

[3] R. Abbel, A. P. H. J. Schenning, E. W. Meijer, *J. Polym. Sci.*: *Part A: Polym. Chem.*, 2009, 47, 4215–4233.

[4] S.-A Chen, H.-H. Lu, C.-W. Huang, *Adv. Polym. Sci.* 2008, 212, 49–84.

[5] D. Neher, *Macromol. Rapid. Commun.,* 2001, 22,1365–1385.

[6](a) M. Iyoda, *J. Synth. Org. Chem*. 2012, 70, 1157–1163; (b) M. Iyoda, J. Yamakawa M. J. Rahman, *Angew. Chem*. *Int. Ed.* 2011, 50, 10522–10553; (c) M. N. Nakao, T. Tamachi, Y. Kuwatani, H. Miyasaka, T. Nishinaga, M. Iyoda, *J. Am. Chem. Soc*., 2006, 128, 16740–16747.

[7] J. M. Santos, L. K. Jagadamma, J. Cameron, A. A. Wiles, C. Wilson, P. J. Skabara, D. W. Samuel, G. Cooke, *J. Mater. Chem*. C, 2021, 9, 16257–16271

[8] (a) Z. Xiang, ZY. Wang, T.B. Ren, W. Xu, Y.P. Liu, X.X. Zhang, *Chem. Commun.* 2019, 55, 11462–5; (b) L. Wang, T. Yu, Z. Xie, E. Ubba, T. Zhan, Z. Yang, *RSC Adv.* 2018, 8, 18613–8; (c) Z. Chen, J. Liang, X. Han, J. Yin, G.A. Yu, S.H. Liu, *Dyes Pigm*. 2015, 112, 59–66; (d) G. Liu, D. Chen, L. Kong, J. Shi, B. Tong, J. Zhi, *Chem. Commun.* 2015, 51, 8555–8; (e) Y. Liu, M. Nishiura, Y. Wang, Z. Hou, *J. Am. Chem. Soc.* 2006, 128, 5592–3; (f) Z. Chen, D. Wu, X. Han, J. Liang, J. Yin, G.A. Yu, *Chem. Commun.* 2014, 50, 11033–5; (g) S. Y, F. Ding, Z. Zhou, C. Li, M. Pu, Yu. Xu, *Proc. Natl. Acad. Sci. USA.* 2019, 116, 1968–73; (h) P. Chopade, S. R. Dugasani, S. Jeon, J.-H. Jeong, S. H. Park, *RSC Adv.* 2019, 9, 31628–35.

[9] S. Yamada, A. Mitsuda, K. Miyano, T. Tanaka, M. Morita, T. Agou, T. Kubota, T. Konno, *ACS Omega* 2018, 3, 9105–9113.

[10] (a) N. Shin, S. Yu, J. H. Lee, H. Hwang, K. M. Lee, *Organometallics* 2017, 36, 8, 1522–1529; (b) X. Wu, J. Guo, Y. Lv, D. Jia, J. Zhao, H. Shan, X. Jina and Y. Ma, *Mater. Chem. Front*., 2020, 4, 257.

[11] S. Fortun, P. Beauclair, A. R. Schmitzer, *RSC Adv.*, 2017, **7**, 21036–21044

[12] N. Shin, S. Yu, J. Hye Lee, H. Hwang, K. Mun Lee, *Organometallics* 2017, 36, 1522–1529

[13] (a) S.-Y. Kim, A.-R. Lee, G. F. Jin, Y.-J. Cho, H.-J. Son, W.-S. Han, S. O. Kang, *J. Org. Chem.*, 2015, 80, 4573–4580; (b)Z. Wang, T. Wang, C. Zhang, M. G. Humphrey, *Phys. Chem. Chem. Phys.*, 2017,19, 12928–12935; (c)N. Shin, S. Yu, J. H. Lee, H. Hwang and K. M. Lee, *Organometallics*, 2017, 36 (8), 1522–1529; (d) Z. Wang, T. Wang, C. Zhang, M. G. Humphrey, *ChemPhotoChem*, 2018,2, 369–379; (e) X. Wu, J. Guo, Y. Lv, D. Jia, J. Zhao, H. Shan, X. Jin, Y. Ma, *Mater. Chem. Front.*, 2020,4, 257–267; (f) D. K. You, H. So, C. H. Ryu, M. Kim, K. M. Lee, *Chem. Sci.*, 2021,12, 8411–8423

[14] J. Ochi, K. Tanaka, Y. Chujo, *Dalton Trans.*, 2021, 50, 1025-1033.

[15] S. Sinha, Z. Kelemen, E. Hümpfner, I. Ratera, J. P. Marval, J. P. Jurado, C. Viñas, F. Teixidor, R. Núñez, *Chem. Commun.*, 2022, 58, 4016–4019.

[16] A. Perevedentsev, M. C. Quiles, *Nat. Commun.*, 2020, 11, 3610

[17] Z. Zhan, J. An., Y. Wei, V. T. Tran, H. Du, *Nanoscale*, 2017, 9, 965–993.

[18] Y. Hong, J.W.Y. Lam, B.Z. Tang, *Chem. Soc. Rev.*, 2011, 40, 5361-5388.

[19] S.W. Thomas III, G.D. Joly, T.M. Swager, *Chem. Rev.,* 2007, 107, 1339-1386.

[20] D. Xiao, L. Xi, W. Yang, H. Fu, Z. Shuai, Y. Fang, J. Yao *J. Am. Chem. Soc.* 2003, 125, 22, 6740–6745.

[21] S. J. Lim, B. K. An, S. D. Jung, M. A. Chung, S. Y. Park, *Angew. Chem. Int. Ed.* 2004, 43, 6346–6350

[22] T. Kim, K. Lee, M. Gong, S-W. Joo, *Langmuir*, 2005, 21, 9524-9528.

[23] D. Blasi, D. M. Nikolaidou, F. Terenziani, I. Ratera, J. Veciana, *Phys. Chem. Chem. Phys*., 2017, 19, 9313.

[24] S. F. Forgues, *Nanoscale,* 2013, **5**, 8428

[25] M. G. Debije, P. P. C. Verbunt, *Adv. Energy Mater*., 2012, 2, 12–35.

[26] H.-Y. Huang, K.-B. Cai, Y.-R. Sie, Kai Li, J.-M. Yeh, C.-T. Yuan, *Sol. RRL* 2019, 3, 1800347.

Chapter 4

Synthesis, characterization and properties of red-light emitting carborane-BODIPY dyes

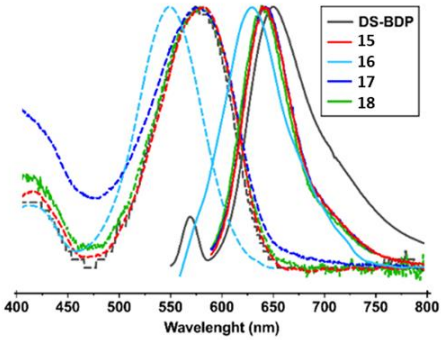

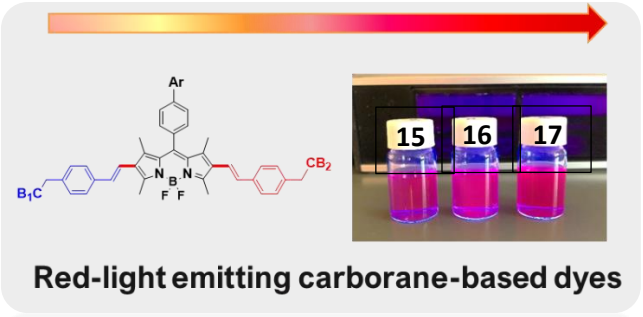

CONTENTS

4.1. Introduction

4.2. Results and discussion

4.2.1. Synthesis of 2,6- and 3,5-distyrenyl substituted carboranyl-BODIPY dyes

4.2.2. Characterization of 2,6- and 3,5-distyrenyl substituted carboranyl-BODIPY dyes

4.2.3. Photophysical studies

4.2.4. Solvatochromic effects

4.2.5. Theoretical calculations

4.3. Conclusions

4.4. References

4.1. Introduction

Since the discovery of boron-carbon clusters in the 1960s, there has been ongoing research owing to the subject of icosahedral carborane derivatives and their unique properties such as delocalised 3D aromaticity,[1] chemical and thermal stability,[2] boron carriers[3] and biocompatibility[4] leads to fascinating and remarkable applications. The physico-chemical features and versatile functionalization of carboranes has given opportunities for applications in several areas such as medicine, optoelectronics, catalysis, and nanomaterials.[5] In the last decade, the development of fluorescent materials based carboranes and their photoluminescence behaviour has significantly increased.[2,6]

Since the pivotal work in 2007 by our group, where carboranyl based fluorophores were first reported,[7] there has been an advancement in research of such kind of systems leading to a crucial investigation of their PL properties having beneficial applications in the field of biomedicine, organic field-effect transistors (OFETs) and organic light emitting diodes (OLEDs).[8] In fact, several research works in the past few years have highlighted the influence of carboranyl cage directly on the photoluminescent (PL) characteristics of the final systems.[9,6,10]

Due to the remarkable spectroscopic properties and ease of functionalization, BODIPY dyes have come into notice as a new class of fluorophores for wide range of applications starting from solid-state luminescent materials for devices to anticancer therapy.[11] Outstanding research has been carried out in designing these types of fluorophores in the field of optical imaging via efficient *in vitro* imaging probes.[12] Additionally, the easy linkage of highly fluorescent fragment such as

BODIPY to carborane derivatives makes the molecular systems very interesting in terms of their chemical morphology and PL properties for optoelectronic devices and anticancer therapy i.e., BNCT.[13] Thus, in the last few years these systems have been developed through Pd-catalyzed Sonogashira and Suzuki cross-coupling reactions or alkyne insertion reactions into decaborane.[14] In a previous work, a set of BODIPY-carboranyl dyads, bearing substituted *m*-carborane and *o*-carborane clusters, were developed using Sonogashira cross-coupling reaction and we observed that the *meta* derivatives exhibited better cell internalization than their *ortho*-analogues due to high lipophilicity of *m*-isomers.[15] In 2018, our group in collaboration with Cristina Prandi´s research group for the very first time reported a small library of carborane-BODIPY/aza-BODIPY systems via Pd catalysed Heck coupling reaction.[16] The compounds showed appreciable fluorescence and therefore almost all of them were internalized by HeLa cells. Hereafter, we continued with this line of research work following the same synthetic route and thus this chapter focusses on synthesis of a set of red-light emitting carborane-(aza) BODIPY dyads, via Heck coupling reaction with styrenyl-containing carborane and brominated (aza) dipyrromethene fluorophore as starting reagents (Figure 4.1).[17] Therefore, we have highlighted the photophysical properties of the fluorophore attached to carborane moieties and these new dyes make their optical properties shift towards near-infrared region, opening opportunities to explore in biomedical applications.[18]

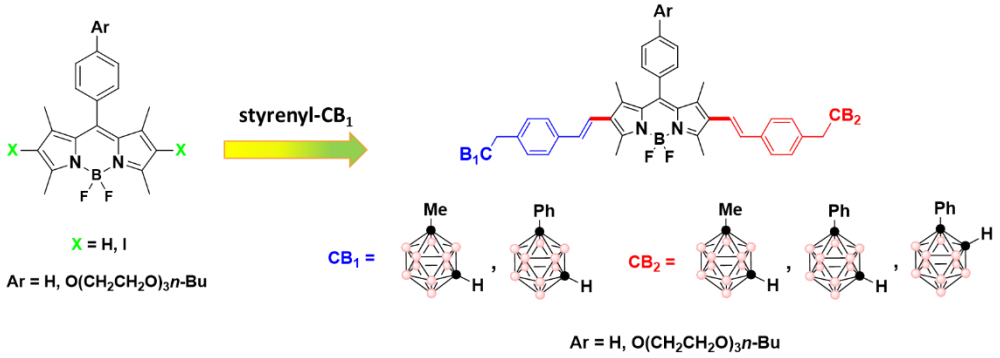

Figure 4.1. The aim of the work

4.2. Results & Discussion

4.2.1. Synthesis of 2,6- and 3,5-distyrenyl substituted carboranyl-BODIPY dyes

Specific iodinated BODIPY dyes, 2,6-diiodo-1,3,5,7-tetramethylBODIPY dyes **14a-c** (**14a**,[19] **14b** and **14c**), were linked to a set of *o*- and *m*-substituted styrenyl-carboranes maned as ***m*-Me-CB**, ***m*-Ph-CB, *o*-Ph-CB,**[6l,i] by Heck coupling reaction (Figures 4.1 and 4.2). The conditions required for this type of coupling reaction has been previously used in our group to prepare carborane-BODIPY dyes.[16] We generally use [$Pd_2(dba)_3$] (3 mol%) as a pre-catalyst and [$Pd(t\text{-}Bu_3P)_2$] (6 mol%) as a source of phosphorous ligand which allows the Pd^0 catalyst to be obtained in situ with great efficiency.[17,20,21] The catalytic cycle for the Mizoroki-Heck coupling reaction is shown in Figure 4.2.

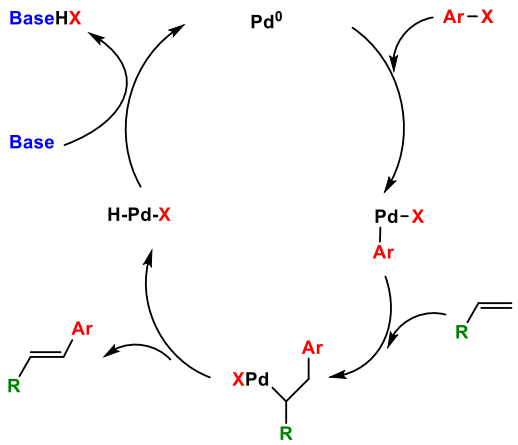

Fig. 4.2. A simplified catalytic cycle of the Mizoroki-Heck reaction

In Figure 4.2 we appreciate that the oxidative addition of Pd(0) into Ar-X bond affords an alkyl-Pd intermediate that undergoes a structural rearrangement to give thermodynamically preferred trans-olefin.[22] We have used Cy_2NMe as a base and 1,4-dioxane as solvent, then we refluxed overnight to obtain compounds **15-19** in yields ranging from 43% to 84%. The starting materials such as Me-*m*-carborane and Ph-*m*-carborane were prepared by thermal isomerization of Me-*o*-carborane and Ph-*o*-carborane at 500 °C and 410 °C respectively.

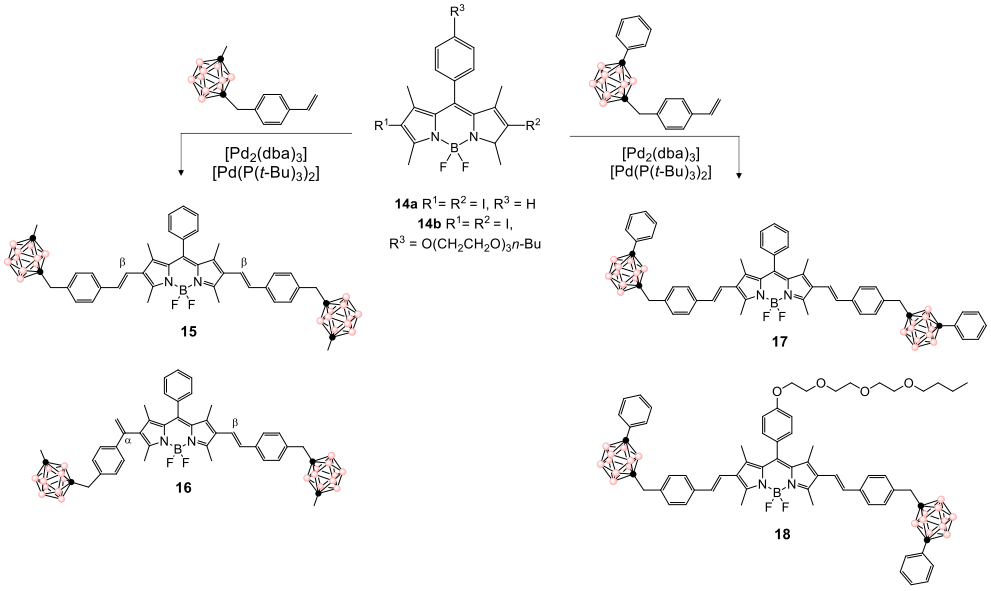

Scheme 4.1. Pd-catalysed Heck coupling reaction for the synthesis of symmetric carborane-BODIPY dyes **15-18**

Compounds **15** to **18** are symmetric carborane based BODIPY derivatives with similar substituents on both the C_c atoms at carborane clusters and were obtained from **14a** and **14b**. The main difference between compounds **17** and **18** is the presence of a ethyleneglycol linked to the BODIPY unit. Besides, we also tried to investigate asymmetric compounds having different substituents at each C_c in carborane units. Therefore, we prepared asymmetric compounds **21** and **22** from **20** and the corresponding styrenyl-carboranes (***o*-Ph-CB** and ***m*-Ph-CB**) as starting materials (Scheme 4.2). We used a higher amount of Pd catalyst for the final step due to increased steric hindrance and asymmetric carborane substituents. For this purpose, precursor **20** was first synthesized by selective iodination reaction at 6-position using **19** that was in turn obtained by using mono-iodinated 1,3,5,7-tetramethyl BODIPY dye, **14c**, as starting material (Scheme 4.2a).

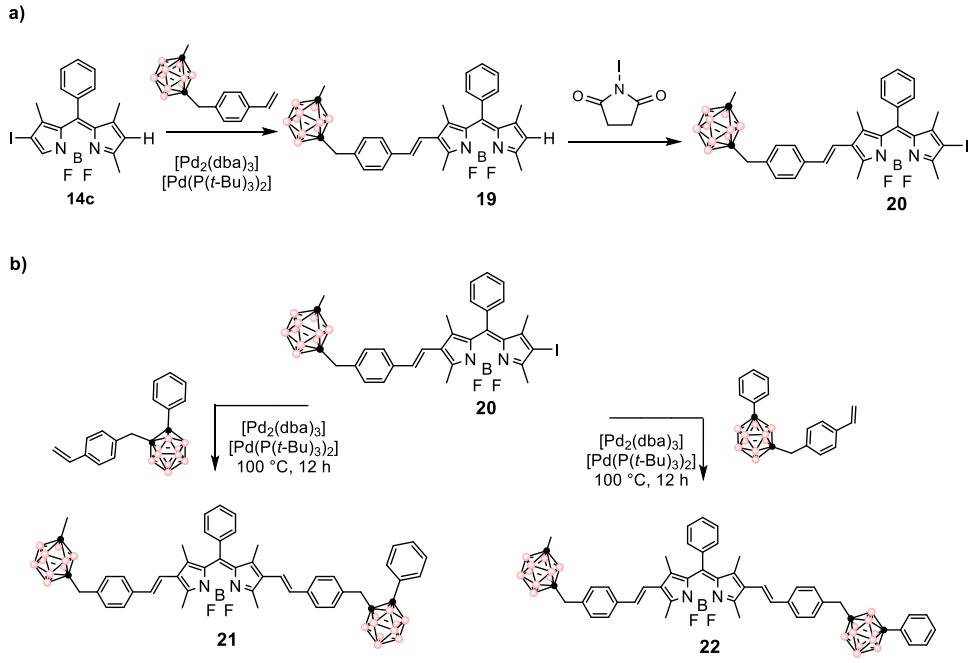

Scheme 4.2. (a) Heck coupling reaction of BODIPY **14c** and **m-Me-CB** followed by iodination reaction to obtain **20**. (b) Synthesis of asymmetric carborane-BODIPY dyes **21** and **22** from **20**

After the successful preparation of 2,6-disubstituted carboranyl BODIPY derivatives, we went one step ahead and prepared 3,5-disubstituted carboranyl BODIPY derivatives. Thus, we developed a small one-step reaction of symmetric derivative **23** of low yield 30%, containing ***m*-Ph-CB** clusters from corresponding BODPIY dye i.e., **14d** (Scheme 4.3).

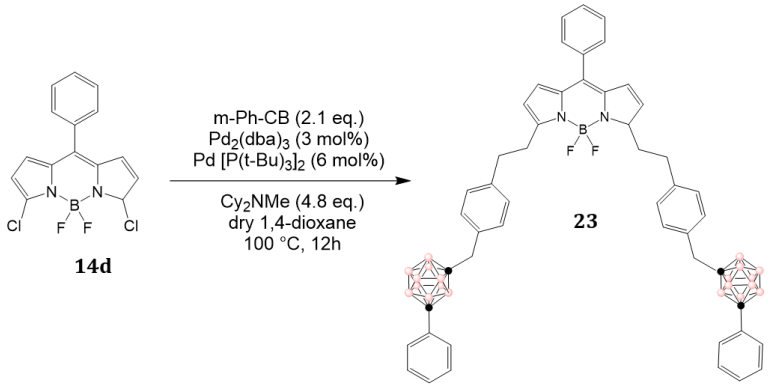

Scheme 4.3. Synthesis of symmetric 3,5-disubstituted BODIPY dye **23**

4.2.2. Characterization of 2,6- and 3,5-distyrenyl substituted carboranyl-BODIPY dyes

After obtaining the purified compounds by flash chromatography on silica gel, compounds **15-23** were characterized by ^{1}H NMR, ^{11}B{^{1}H} NMR, ^{13}C{^{1}H} NMR spectroscopies and elemental analysis.

To confirm the presence of carborane moieties in the case of compounds **15**, we observed a resonance at 1.65 ppm in the ^{1}H NMR, attributed to the protons from C_c-C*H*$_3$. The symmetric structure of **15** showed resonances at 3.18 ppm from the benzylic protons. In the due course of cationic Heck reaction along with **15**, there was a formation of small amount of α,β-isomer **16** (6%). Hence the formation of geminal substituted olefins was unavoidable despite of the influence of strong electron-withdrawing carboranyl clusters. Therefore, compound **15** has two methyl proton signals of BODIPY core at 2.74 ppm and 1.47 ppm, whereas compound **16** has different splitting for each proton signals of the four methyl groups attached, such as 2.74, 2.48, 1.47 and 1.24 ppm. The coupling constants ($^{3}J_{HH}$ = 16.5 Hz) for doublet olefinic protons at 6.87 and 6.63 ppm respectively, suggested *trans*-selectivity of cross coupling reaction for **15**.

As for **16**, terminal olefinic protons show resonances at 5.84 ppm and 5.10 ppm respectively, with $^{3}J_{HH}$ = 1.3 Hz and the deshielded *trans*-olefinic protons appear in the same region as **15** (Figure 4.3). Likewise, the ^{1}H NMR spectra of **17** and **18** also showed benzylic proton signals at 3.18 and 3.26 ppm, respectively, and along with that **18** showed characteristic oligoethylene glycol alkyl chain between 4.25-3.25 ppm. The ^{1}H NMR spectra of **21** and **22** confirmed two different benzylic protons of both spacers adjoining carborane clusters, due to asymmetric CB derivatives and reassured the stereoselectivity of the reaction sequence. Whereas in compound **23** the olefinic proton doublets were slightly shifted to upfield region of the aromatic region due to 3,5-distyrenyl substitution.

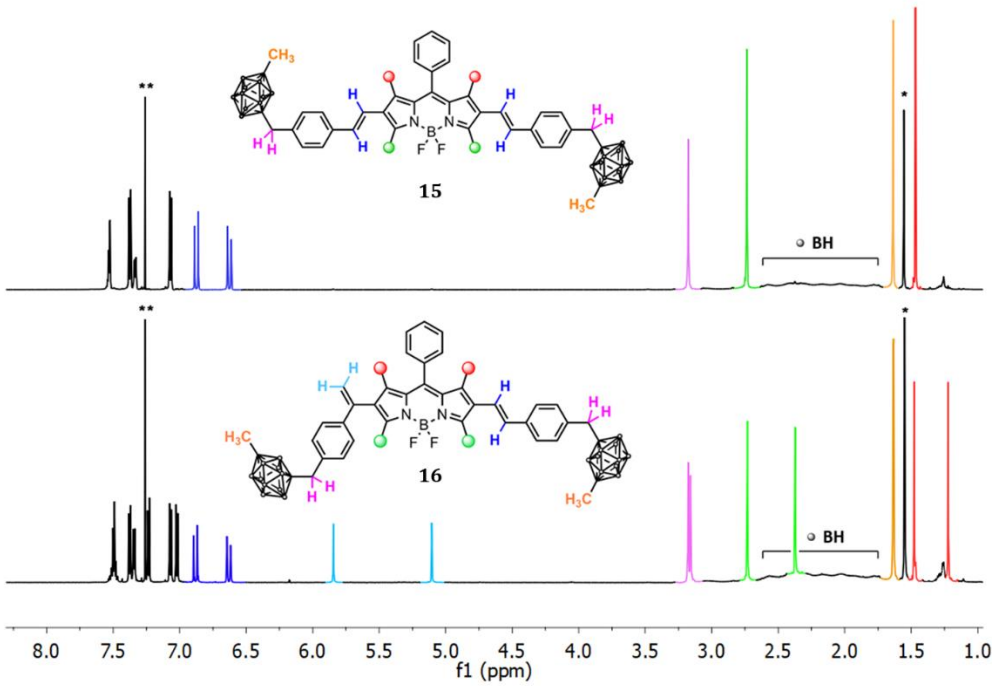

Figure 4.3. Comparison of ^{1}H NMR spectra of bis-β,β-styrenyl carborane BODIPY derivative **15** (top) and its α,β-isomer **16** (bottom) in $CDCl_3$. *H_2O signal; **residual $CDCl_3$ peak.

$^{11}B\{^1H\}$ NMR spectra for β,β-isomer **15** showed a resonance centred at 0.99 ppm assigned to -BF_2 unit, whereas for the α,β-isomer **16** these resonance was slightly shifted at higher frequency (1.01 ppm). Additionally, broad signals were observed in the region from -6.17 ppm to -13.04 ppm, which is the typical 1:1:6:2 pattern characteristic of *m*-carborane clusters. Similarly, $^{11}B\{^1H\}$ NMR peaks in the range of -5.90 to -13.51 ppm with a pattern of 2:6:2 (Figure 4.4) attributed to *m*-carborane moieties were observed for symmetric compounds **17** and **18.** The broad resonances at 0.93 and 0.95 ppm were assigned to -BF_2 units of BODIPY core. Resonances of $^{11}B\{^1H\}$ NMR in case of **21** were shifted upfield in comparison to **17** and **18** and appeared in the range of -3.17 to -12.93 ppm with a 2:1:1:14:2 pattern, due to the asymmetric structure. This unique nature of pattern has been observed because of *m*- and *o*- isomers of *closo*-carborane, which has a combined distribution of 1:1:6:2 and 2:8 respectively. However, **22** had peaks in a region much similar to the previous symmetric compounds and showed 1:1:6:2 distributions, owing to the substitution of Me- and Ph- groups at *m*-carborane moieties. The symmetric disubstituted carborane-BODIPY system **23** shows similar $^{11}B\{^1H\}$ NMR pattern as **17**, due to symmetrically aligned Ph-*m*-carborane fragments.

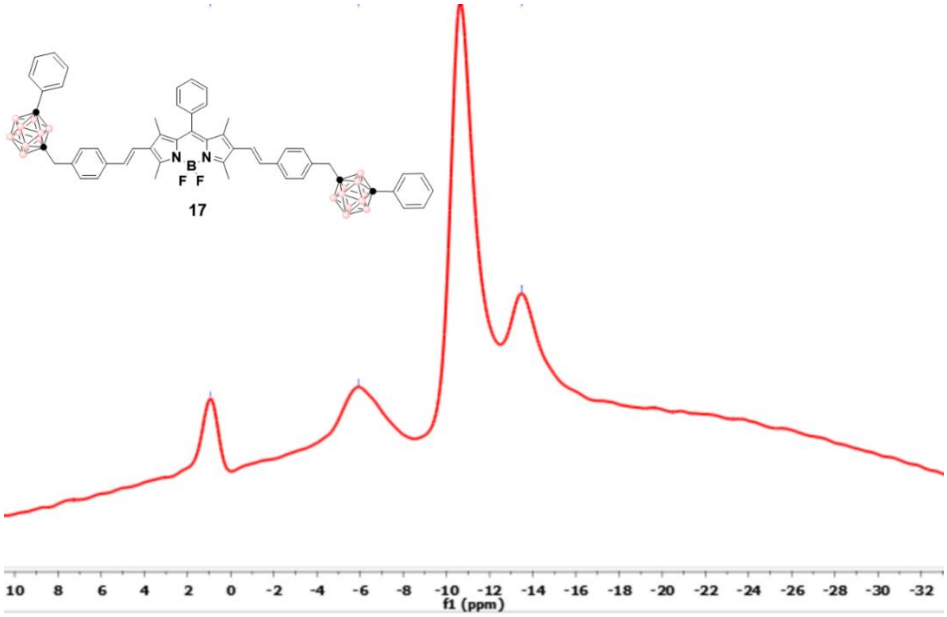

Figure 4.4. $^{11}B\{^{1}H\}$ NMR for symmetric compound **17**

For the symmetric compound **15**, the $^{13}C\{^{1}H\}$ NMR spectrum showed a resonance at 42.8 ppm, which denotes the two identical benzylic C atoms. Similarly, for **17** and **18** we observed single resonances at 42.9 and 43 ppm respectively. Whereas for **16**, **19** and **20** we observed different resonances that split into two different signals in the region between 42.6 to 43.0 ppm, suggesting asymmetric behaviour of the derivatives. Again, for **23** we saw a similar behaviour as for the rest of the symmetric compounds with one resonance signal at 43.1ppm. In **15**, **16**, **19** and **20** $C_{cluster}$-CH_3 could be identified as resonance in the range 24-25 ppm.

4.2.3. Photophysical Studies

A comparison of the photophysical behaviour between the final carboranyl-based BODIPY compounds and parent BODIPY analogues without carborane clusters was performed in THF with concentrations between $2.87*10^{-4}$ M to $3.73*10^{-4}$ M (Figure 4.5).

The UV absorption spectra of both symmetric and asymmetric substituted compounds i.e., **15, 17, 18** and **21-22** have displayed a noteworthy red-shift (2-9 nm) from their parent BODIPY dye **DS-BDP** (table 4.1), suggesting an influence of C_c substituted (Me or Ph) carboranyl units attached to BODIPY core. On the other hand, **16** shows a significant blue-shift when compared with the starting fluorophore and the rest of carboranyl-BODIPY dyes, this could be attributed to the presence of α-styrenyl substituted group. Interestingly, **23** has **Ph-*m*-CB** fragments at 3,5-positions of the core BODIPY showing narrow and intense $S_0 \rightarrow S_1$transition with a λ_{abs} = 641 nm i.e., red shifted (8 nm) with regards to the reference **3,5-BDP** (λ_{abs} maxima =633 nm) and this could be due to a significant planar conformation**.**

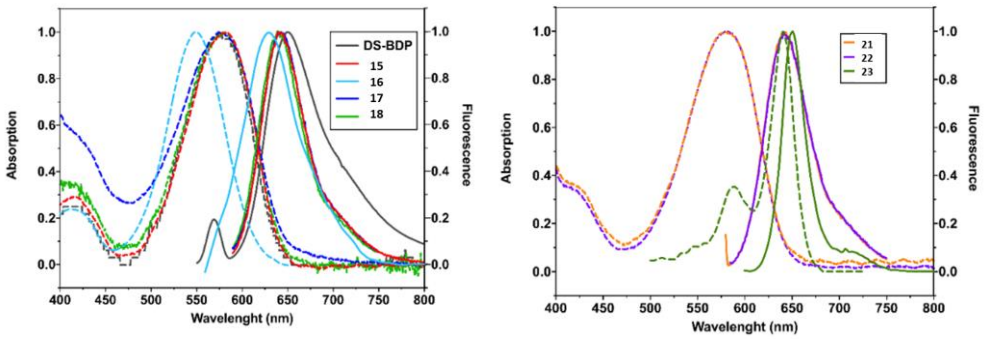

Figure 4.5. Normalized absorption (dashed) and emission (solid) spectra of symmetric (**DS-BDP** and **15**-**18**, left), asymmetric (**21-23**, right) carboranyl-BODIPY derivatives in THF.

We thoroughly studied the fluorescence emission properties of all the compounds and calculated the fluorescence quantum yield (Φ_F) in THF. To evaluate Φ_F values we used Rhodamine 101 in MeOH as standard with Φ_F = 1 and followed the equation:

$$\varphi = \varphi_{STD} \frac{I}{I_{STD}} \frac{Abs_{STD}}{Abs} \frac{n^2}{n_{STD}^2}$$

Φ_{STD} refers to the quantum yield of the standard used, I denote integrated area of emission of the sample and I_{STD} refers to the integrated area of emission of standard. The absorbance of the sample and standard has been denoted by Abs and Abs_{STD} respectively, with n and n_{STD} being the solvent refractive index of sample and standard respectively.

We observed a similar trend in fluorescence emission bands as compared to the absorption bands of **15**-**18** and **21**-**22** with a bathochromic shift from reference compound **DS-BDP** with large Stoke shift values of 56 to 65 nm (Table 4.1), in comparison with other BODIPY dyes.[23] The overall Φ_F values of these compounds displayed an enhanced fluorescence efficiency with respect to **DS-BDP** (Table 4.1). In the 2,6-disubstituted series, **15** showed a moderate fluorescence quantum yield, with a value of 0.14, whereas **16** has the lowest Φ_F value of all the compounds with a hypsochromic shift in UV absorption and FL emission bands. Due to the presence of α-styrenyl unit in α, β-isomer, **16** and the poor conjugation with BODIPY core, there was an increased HOMO-LUMO gap as reported by Shen et. al.,[24] this triggered lowered fluorescence emission, larger Stoke shift and a quenching in Φ_F value. The photophysical properties of **17** and **18** with the introduction of phenyl rings at *m*-carborane clusters did not show a major difference from the, β,β-isomer i.e., **15** and **17**; in fact, the Φ_F value of **15** and **18** are the same although structurally there has been an incorporation of oligoethylene glycol alkyl chain at *meso*-phenyl group on the BODIPY scaffold in **18**. For the record, it was good to know that despite of the functionalization on the fluorophore with an amphiphilic substitution, there was no significant affect in the

photophysics. Moreover, compounds **21** and **22** showed similar PL properties with slight lower Φ_F values than **15-18.** The 3,5-disubstituted compound**23** showed much smaller Stoke shift compared to the rest of the dyes and has the higher Φ_F value compared to all the synthesized compounds and **DS-BDP**, but significantly lower than the reference compound **3,5-BDP**. The reason for higher Φ_F values of 3,5-disubstituted BODIPY dyes than corresponding 2,6-disubstituted ones could be a lower rate of non-radiative decay.

We then investigated the brightness of the dyes that is the product of the molar extinction coefficient (ε) at the excitation wavelength and the fluorescence quantum yield [ε(λ)·ΦF], and we found that **23** displayed maximum brightness of 31320 $M^{-1}cm^{-1}$ among the 3,5-disubstituted stirenyl-carboranyl BODIPY series, whereas in case of 2,6-disubstituted set of compounds, **15** showed the highest brightness (7840 $M^{-1}cm^{-1}$) followed by **22** and **21** with values of 6960 $M^{-1}cm^{-1}$ and 5880 $M^{-1}cm^{-1}$, respectively (Table 4.1).

Table 4.1. Selected photophysical data for the reported compounds **15-18** and **21–23,**[a] and BODIPY dyes **DS-BDP** (entry 1)[b] and **3,5-BDP** (entry 9)[c]

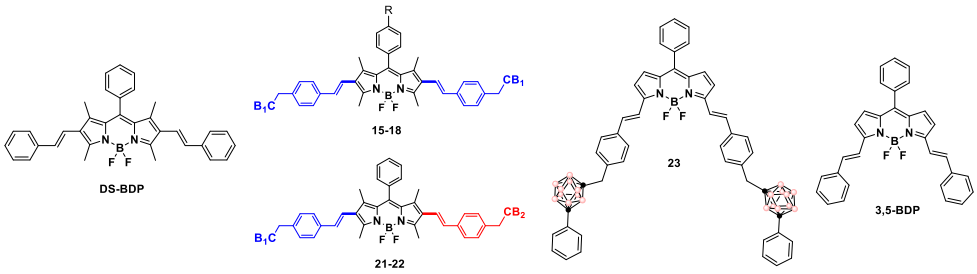

S. No.	Compound	λ_{abs} (nm)	λ_{em}(nm)	$\varepsilon/10^6$ (M^{-1} cm^{-1})	Φ_F[d]	Stokes shift/ 10^3 (cm^{-1})	$\varepsilon\,\Phi_F$ (M^{-1} cm^{-1})
1	**DS-BDP**	575	633	0.031	0.01	1.59	310
2	**15**	584	640	0.056	0.14	1.50	7840
3	**16**	548	627	0.030	0.05	2.30	1500
4	**17**	578	643	0.035	0.11	1.75	3850
5	**18**	580	640	0.029	0.14	1.62	4060
6	**21**	578	643	0.049	0.12	1.75	5880
7	**22**	582	641	0.058	0.12	1.58	6960
8	**23**	641	651	0.087	0.36	0.24	31320
9	**3,5-BDP**	633	646	0.104	0.83	0.32	86320

[a] Measured in THF at room temperature. [b] Data for **DS-BDP** are reported in the literature in CH_2Cl_2[24] [c] Data for **3,5-BDP** are reported in the literature in THF[25] [d] Fluorescence quantum yields were determined using solutions of Rhodamine 101 in methanol (Φ_F=1) as standard[26]

4.2.4. Solvatochromic effects

The phenomenon where the fluorescence peak shifts along with the change in solvent polarity is known as fluorescence solvatochromism. Therefore, solvatochromic effect is a process in which a spectrum of solute appears when dissolved in various polarity-based solvents. So, we recorded the UV-Vis and FL spectra of compounds **15**, **17**, **21** and **23** in different solvents (toluene, THF, MeOH, CH_3CN, DMSO, dioxane and CH_2Cl_2) with dielectric constants ranging from 2.25 to 46.7 at 298 K to evaluate the optical properties. This study has been very important to investigate the solvent effect on our new compounds and to identify polarity-based molecular orientations. Compounds **15** and **17** showed similar absorption and emission behaviour with respect to environmental polarity i.e., the solvatochromic effect was little and as expected it was certainly due to the symmetrical morphology with minimum intrinsic molecular dipole moment (Figure 4.6 a,b). In fact, in

case of the asymmetric compound **21** with the incorporation of *o*- and *m*-carborane clusters, it still showed a similar i.e., very little solvent polarity effect with λ_{abs} = 572 to 584 nm and λ_{em} = 640 to 650 nm (Figure 4.6c). A quite similar behaviour was noticed for the 3,5-disubstituted compound **23.**

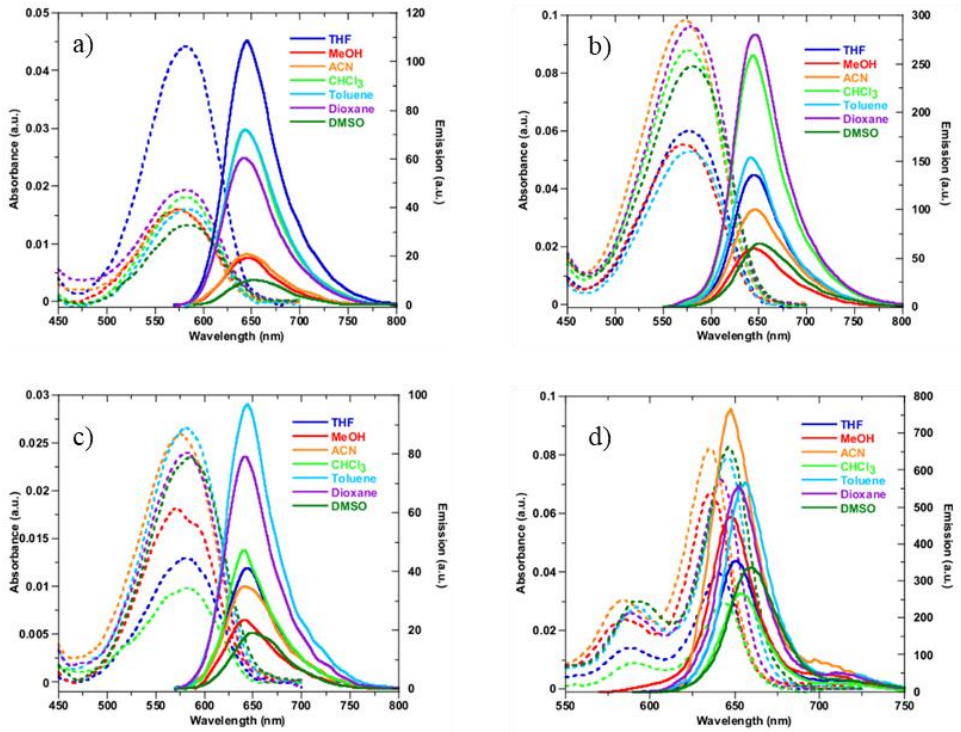

Figure 4.6. Normalized absorption (dashed) and emission (solid) spectra of a) **15**, b) **17**, c) **21** and d) **22** in different solvents.

Finally, we also measured the photophysical behaviour of **17** and **18** in a binary mixture of THF:H_2O (Figure 4.7), to see the formation of aggregates and to track their fluorescence emission intensity at different ratios. With 60% to 80% of water in the mixture, we observed a red-shift predominantly in the absorption spectra, suggesting the presence of aggregates, however the intensity of emission spectra appeared to be

weaker. This result resembled very well with the dyes observed in polar solvents such as MeOH and DMSO (Figure 4.7). Also, we observed a hypochromic effect in the absorption region for a ratio of 60:40 (THF:H_2O, v/v) mixture. However, we obtained a normalized and clear emission profile compared to those observed in THF and looking at the stability of the soluble-aggregates of these dyes in pure water, we can say that it can behave as fluorogenic probes. Experiments are being carried out at present evaluating the internalization of these dyes in cell lines and as well as developing liposomal formulations, the results are currently awaited. Hence, these newly carborane based BODIPY dyes could act as potential candidates for further research in bio-supramolecular assays.

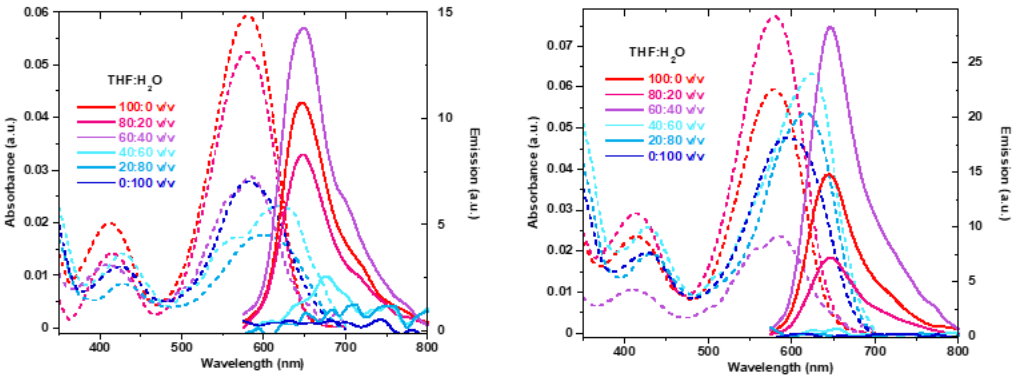

Figure 4.7. UV-Vis absorption (dashed) and fluorescence (solid) spectra of BODIPY dyes **17** (left) and **18** (right) recorded in pure water and THF/water mixtures (60:40, v/v).

4.2.5. Theoretical calculations

Computational studies were done using B3LYP functional (CAM-B3LYP) with 6-31G(d) basis set. The solvent used for the calculations was THF, which was then simulated in SMD and IEF-PCM schemes and all the

theoretical studies were done using Gaussian 16 programs as well as graphical program GaussView.

We considered symmetric *m*-Ph disubstituted styrenyl carborane compounds **17** and **23**, along with reference compounds **DS-BDP** and **3,5-BDP** to perform DFT calculations. From the Table 4.2, we can see that the calculated λ_{abs} values were in accordance with the experimental λ_{abs} values, suggesting major transitions from $\pi \rightarrow \pi^*$ type corresponding to HOMO to LUMO transition. In fact, we observed that this result was also comparable in case of reference compounds. We studied the molecular orbitals of **17** and **18** as well as compared the quantum yield values, there was a significant participation of styrenyl functional group in HOMO and in case of LUMO this contribution was absent, revealing a major contribution of the core fluorophore (Figure 4.8). This resulted in particularly the charge transfer process, suggesting $S_0 \rightarrow S_1$ type transitions leading to lower FL efficiency. However, in case of **23**, the styrenyl fragments were present in both HOMO and LUMO, hence restraining the opportunity for charge transfer FL quenching with a higher Φ_F value of 0.36.

Here we would like to highlight one interesting fact about carboranyl moieties, usually when they are attached to the fluorophore through a spacer (in this case, styrenyl groups) the contribution of *o*-carborane units is almost negligible. Nevertheless, when they are directly attached to fluorophores then there is a contribution of these units in case of LUMO, playing the role of electron acceptors.

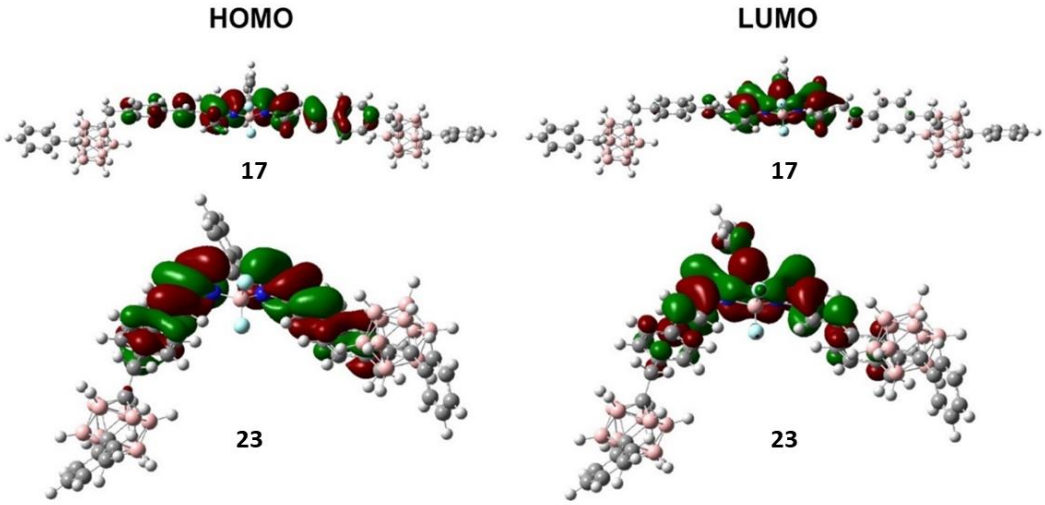

Figure 4.8. CAM-B3LYP/6-31G(d) molecular orbitals HOMO (left) and LUMO (right) of carborane-BODIPY dyes **17** (top) and **23** (bottom).

Table 4.2. Calculated electronic excitation energies, oscillator strengths and the related wave functions for $S_0 \rightarrow S_1$ transitions. Electronic transition data obtained by O3LYP/6-31G(d)//CAM-B3LYP/6-31G(d) for compounds **17**, **23** and references compounds **DS-BDP**[a] and **3,5-BDP**.

	E (eV)	**λ (nm)**	***f***	**Wave function**	**Exp. λ (nm)**
17	2.13	582	0.83	H→L (93%), H-2 →L (7%)	578
23	2.02	613	1.06	H→L (100%)	641
DS-BDP	2.22	559	0.68	H→L (92%), H-2 →L (8%)	575
3,5-BDP	2.06	603	0.99	H→L (100%)	633

[a] Experimental data for DS-BDP in CH_2Cl_2 reported in literature[24]

Considering the mean dihedral angles (Θ) between styrenyl groups and the fluorophore (Table 4.3), it has been evident that dihedral angles for **23** is much lower compared to **3**, **DS-BDP** and **3,5-BDP,** this gave a clarity in coplanarity in 3,5-disubstituted compound. In terms of coplanarity, we

could say that a slightly higher degree was achieved by 2,6-disubstituted compound **17** in comparison to reference compounds, giving rise to an explanation for higher Φ_F value than **DS-BDP**. However, unfortunately we could not establish a possible explanation from theoretical studies regarding the quenching of Φ_F value for **23** than **3,5-BDP**. On the other hand, dihedral angle values depicted larger Stoke shifts in case of **17** than **23** rationalizing the steric hindrance factor leading to loss of coplanarity. Now, these aspects along with formation of conical interactions between S_1 and ground state have made 2,6-distyrenyl BODIPY derivatives less fluorescent efficient than those of 3,5-distyrenyl BODIPY analogues.

Table 4.3. Mean dihedral angles (θ) for compounds **17**, **23**, **DS-BDP** and **3,5-BDP** in the ground state (S_0) and excited state (S_1).

	Compounds			
	17	**23**	**DS-BDP**	**3,5-BDP**
θ (S_0)	28.8°	9.9°	31.6°	10.4°
θ (S_1)	23.1°	3.9°	22.6°	5.4°

4.3. Conclusions

In summary, we would like to emphasize that one of the most researched fields of work in biomedicine and nanoscience is the development of efficient fluorophores that can act as imaging probes for anticancer therapy. A combination of imaging agent and target drug in a one-pot system gives the opportunity to the formation of theranostic agent that allows both diagnosis and therapy of cancer-related diseases. Therefore, keeping in mind this line of work, our group has made several contributions and designed various types of structural architectures of carboranyl-BODIPY dyes. Some of them have shown remarkable

luminescent properties, electronic properties, structural diversity, chemical and thermal stability and a higher degree of functionalization.

This chapter highlights the significance of styrene-containing carboranyl-BODIPY systems synthesized by Pd-catalyzed Heck coupling reaction. All the final compounds were fully characterized, further we did a detailed photophysical study where the absorption and emission patterns were contemplated with the help of DFT studies. In particular, the theoretical calculations were in accordance with experimental values with regards to energy transitions (S_0 and S_1 states) from HOMO to LUMO and coplanarity. Thus, explaining the reason for highest fluorescence quantum yield value of **23** amongst all other compounds except **3,5-BDP**. In fact, in case of 2,6-disubstituted carborane-BODIPY systems, **21** and **22** due to asymmetric morphology, there was a loss in coplanarity which led to decrease in Φ_F value. Overall, 2,6-disubstituted derivatives **15-18** and **21-22** have lower fluorescence efficiency compared to 3,5-disubstituted analogue **23**, due to a loss of coplanarity and steric hindrance, as well as the molecular orbitals involved in ground and excited states. Also, we can say that the solvent polarity did not have a significant effect on new compounds suggesting the stability of these compounds in organic solvents. In a binary mixture of 60:40 (THF:H_2O), the compounds **17** and **18** exhibited high fluorescence emission, suggesting a trace amount of water environment could potentially suggest a binding behavior with the biological molecules. Therefore, these series of 2,6-distyrene-containing carborane-BODIPY dyes and 3,5-distyrene-containing carborane-BODIPY dyes have the ability to highlight their fluorescence properties as well as their high boron content, which might lead to boron carrier drugs for diagnosis (bioimaging) and therapy (BNCT) applications.

4.4. References

[1] (a) J. Poater, C. Viñas, I. Bennour, S. Escayola, M. Solà, F. Teixidor, *J. Am. Chem. Soc.* 2020, *142*, 9396-9407; (b) J. Poater, M. Solà, C. Viñas, F. Teixidor, *Angew. Chem. Int. Ed.* 2014, *53*, 12191-12195.

[2] (a) J. Cabrera-Gonzalez, A. Ferrer-Ugalde, S. Bhattacharyya, M. Chaari, F. Teixidor, J. Gierschner, R. Núñez, *J. Mater. Chem. C* 2017, *5*, 10211-10219; (b) R. Núñez, I. Romero, F. Teixidor, C. Viñas, *Chem. Soc. Rev.* 2016, *45*, 5147-5173.

[3] M. Scholz, E. Hey-Hawkins, *Chem. Rev.* 2011, *111*, 7035-7062.

[4] (a) Z. J. Leśnikowski, *J. Med. Chem.* 2016, *59*, 7738-7758; (b) F. Issa, M. Kassiou, L. M. Rendina, *Chem. Rev.* 2011, *111*, 5701-5722; (c) J. F. Valliant, K. J. Guenther, A. S. King, P. Morel, P. Schaffer, O. O. Sogbein, K. A. Stephenson, *Coord. Chem. Rev.* 2002, *232*, 173-230.

[5] (a) X. Zhang, H. Yan, *Coord. Chem. Rev.* 2019, *378*, 466-482; (b) E. Hey-Hawkins, C. Viñas, *Boron-Based Compounds*, John Wiley & Sons Ltd, Chichester, UK, 2018, p. 496; (c) S. Duttwyler, *Pure Appl. Chem.* 2018, *90*, 733-744; d) D. Olid, R. Núñez, C. Viñas, F. Teixidor, *Chem. Soc. Rev.* 2013, *42*, 3318-3336; e) V. I. Bregadze, *Chem. Rev.* 1992, *92*, 209-223.

[6] (a) J. Cabrera-González, M. Chaari, F. Teixidor, C. Viñas, R. Núñez, *Molecules* 2020, *25*, 1210; (b) M. Chaari, Z. Kelemen, D. Choquesillo-Lazarte, F. Teixidor, C. Viñas, R. Núñez, *Inorg. Chem. Front.* 2020, *7*, 2370-2380; (c) G. Tao, Z. Duan, F. Mathey, *Org. Lett.* 2019, *21*, 2273-2276; (d) M. Chaari, J. Cabrera-González, Z. Kelemen, C. Viñas, A. Ferrer-Ugalde, D. Choquesillo-Lazarte, A. Ben Salah, F. Teixidor, R. Núñez, *J. Organomet. Chem.* 2018, *865*, 206-213; (e) M. Chaari, Z. Kelemen, J. G. Planas, F.

Teixidor, D. Choquesillo-Lazarte, A. Ben Salah, C. Viñas, R. Núñez, *J. Mater. Chem. C* 2018, *6*, 11336-11347; (f) A. Ferrer-Ugalde, J. Cabrera-Gonzalez, E. J. Juarez-Perez, F. Teixidor, E. Perez-Inestrosa, J. M. Montenegro, R. Sillanpaa, M. Haukka, R. Núñez, *Dalton Trans.* 2017, *46*, 2091-2104; (g) J. Cabrera-González, S. Bhattacharyya, B. Milián-Medina, F. Teixidor, N. Farfán, R. Arcos-Ramos, V. Vargas-Reyes, J. Gierschner, R. Núñez, *Eur. J. Inorg. Chem.* 2017, *2017*, 4575-4580; (h) H. Naito, K. Nishino, Y. Morisaki, K. Tanaka, Y. Chujo, *Angew. Chem. Int. Ed.* 2017, *56*, 254-259; (i) J. Cabrera-González, C. Viñas, M. Haukka, S. Bhattacharyya, J. Gierschner, R. Núñez, *Chem. Eur. J.* 2016, *22*, 13588-13598; (j) L. Böhling, A. Brockhinke, J. Kahlert, L. Weber, R. A. Harder, D. S. Yufit, J. A. K. Howard, J. A. H. MacBride, M. A. Fox, *Eur. J. Inorg. Chem.* 2016, *2016*, 403-412; (k) J. Guo, D. Liu, J. Zhang, J. Zhang, Q. Miao, Z. Xie, *Chem. Commun.* 2015, *51*, 12004-12007; (l) A. Ferrer-Ugalde, E. J. Juarez-Perez, F. Teixidor, C. Viñas, R. Sillanpää, E. Perez-Inestrosa, R. Núñez, *Chem. Eur. J.* 2012, *18*, 544-553.

[7] F. Lerouge, C. Viñas, F. Teixidor, R. Nuñez, A. Abreu, E. Xochitiotzi, R. Santillan, N. Farfan, *Dalton Trans*. 2007,1898– 1903.

[8] (a) J. Li, C. Yang, X. Peng, Y. Chen, Q. Qi, X. Luo, W.-Y. Lai, W. Huang, *J. Mater. Chem. C* 2018, 6, 19 – 28; (b) I. Nar, A. Atsay, A. Altındal, E. Hamuryudan, *Inorg. Chem*. 2018, 57, 2199 – 2208; (c) H. Naito, K. Nishino, Y. Morisaki, K. Tanaka, Y. Chujo, *J. Mater. Chem. C* 2017, 5, 10047 – 10054; (d) J. Wang, L. Chen, J. Ye, Z. Li, H. Jiang, H. Yan, M. Y. Stogniy, I. B. Sivaev, V. I. Bregadze, X. Wang, *Biomacromolecules* 2017, 18, 1466 – 1472; (e) A. Wu, J. L. Kolanowski, B. B. Boumelhem, K. Yang, R. Lee, A. Kaur, S. T. Fraser, E. J. New, L. M. Rendina*, Chem. Asian J*. 2017, 12, 1704 – 1708; (f) K. Tanaka, Y. Chujo, *ACS Symp. Ser*. 2016, 1226, 157 – 174; (g) X. Li, H. Yan, Q. Zhao, *Chem. Eur. J*. 2016, 22, 1888 – 1898; (h) Z. Ruan, P. Yuan, L. Liu, T.

Xing, L. Yan, Int. *J. Polym. Mater. Polym. Biomater*. 2018, 67, 720 – 726; (i) K. O. Kirlikovali, J. C. Axtell, A. Gonzalez, A. C. Phung, S. I. Khan, A. M. Spokoyny, *Chem. Sci*. 2016, 7, 5132 – 5138; (j) X. Li, X. Tong, Y. Yin, H. Yan, C. Lu, W. Huang, Q. Zhao*, Chem. Sci*. 2017, 8, 5930– 5940.

[9] R. Núñez, M. Tarrés, A. Ferrer-Ugalde, F. Frabrichi de Biani., F. Teixidor, Chem. Rev. 2016, 116,14307–78.

[10] (a) F. Lerouge, A. Ferrer-Ugalde, C. Viñas, F. Teixidor, R. Sillanpaa, A. Abreu, E. Xochitiotzi, N. Farfan, R. Santillan, R. Nuñez, *Dalton Trans*. 2011, 40, 7541 – 7550; (b) A. Ferrer-Ugalde, A. González-Campo, C. Viñas, J. Rodríguez-Romero, R. Santillan, N. Farfan, R. Sillanpaa, A. Sousa-Pedrares, R. Nuñez, F. Teixidor, *Chem. Eur. J.* 2014, 20, 9940 – 9951; (c) J. Cabrera-Gonzalez, E. Xochitiotzi-Flores, C. Viñas, F. Teixidor, H. Garcia-Ortega, N. Farfan, R. Santillan, T. Parella, R. Nuñez, *Inorg. Chem.* 2015, 54, 5021 – 5031.

[11] (a) S. Xuan, N. Zhao, Z. Zhou, F. R. Fronczek, M. G. H. Vicente, *J. Med. Chem*. 2016, 59, 2109 – 2117; (b) J. H. Gibbs, H. Wang, N. V. S. D. K. Bhupathiraju, F. R. Fronczek, K. M. Smith, M. G. H. Vicente, *J. Organomet. Chem.* 2015, 798, 209 – 213 Part 1; (c) M. Chaari, N. Gaztelumendi, J. Cabrera-Gonzalez, P. Peixoto-Moledo, C. Viñas, E. Xochitiotzi-Flores, N. Farfan, A. Ben Salah, C. Nogues, R. Nuñez, *Bioconjugate Chem.* 2018, 29, 1763 – 1773.

[12]S. Xuan, N. Zhao, Z. Zhou, F. R. Fronczek, M. Graça, H. Vicente, *J. Med. Chem.*, 2016, 59, 5, 2109–2117.

[13] (a) M. Couto, C. Alamón, S. Nievas, M. Perona, M. A. Dagrosa, F. Teixidor, P. Cabral, C. Viñas, H. Cerecetto, *Chem. Eur. J.* 2020, *26*, 14335-14340; (b) C. Alamón, B. Dávila, M. F. García, C. Sánchez, M. Kovacs, E. Trias, L. Barbeito, M. Gabay, N. Zeineh, M. Gavish, F. Teixidor, C. Viñas, M. Couto, H.

Cerecetto, *Cancers* 2020, *12*, 3423; (c) D. J. Worm, P. Hoppenz, S. Els-Heindl, M. Kellert, R. Kuhnert, S. Saretz, J. Köbberling, B. Riedl, E. Hey-Hawkins, A. G. Beck-Sickinger, *J. Med. Chem.* 2020, *63*, 2358-2371; (d) C. Viñas, R. Núñez, I. Bennour, F. Teixidor, *Curr. Med. Chem.* 2019, *26*, 5036-5076; (e) A. Buzharevski, S. Paskas, M.-B. Sárosi, M. Laube, P. Lönnecke, W. Neumann, S. Mijatovic, D. Maksimovic-Ivanic, J. Pietzsch, E. Hey-Hawkins, *ChemMedChem* 2019, *14*, 315-321; (f) G. Calabrese, A. Daou, A. Rova, E. Tseligka, I. S. Vizirianakis, D. G. Fatouros, J. Tsibouklis, *MedChemComm* 2017, *8*, 67-72; (g) H. S. Ban, H. Nakamura, *Chem. Rec.* 2015, *15*, 616-635; (h) M. A. Soriano-Ursúa, B. C. Das , J. G. Trujillo-Ferrara, *Expert Opin. Ther. Pat.* 2014, *24*, 485-500; (i) C. Viñas, *Future Med. Chem.* 2013, *5*, 617-619.

[14] (a) I. Nar, A. Atsay, A. Buyruk, H. Pekbelgin Karaoglu, A. K. Burat, E. Hamuryudan, *New J. Chem.* 2019, *43*, 4471-4476; (b) H.-Q. Wang, J.-T. Ye, Y. Zhang, Y.-Y. Zhao, Y.-Q. Qiu, *J. Mater. Chem. C* 2019, *7*, 7531-7547; (c) S.-Y. Kim, Y.-J. Cho, H.-J. Son, D. W. Cho, S. O. Kang, *J. Phys. Chem. A* 2018, *122*, 3391-3397; (d) E. Berksun, I. Nar, A. Atsay, I. Ozcesmeci, A. Gelir, E. Hamuryudan, *Inorg. Chem. Front.* 2018, *5*, 200-207; (e) S. Xuan, N. Zhao, Z. Zhou, F. R. Fronczek, M. G. H. Vicente, *J. Med. Chem.* 2016, *59*, 2109-2117; (f) J. H. Gibbs, H. Wang, N. V. S. D. K. Bhupathiraju, F. R. Fronczek, K. M. Smith, M. G. H. Vicente, *J. Organomet. Chem.* 2015, *798*, 209-213; (g) G. F. Jin, Y.-J. Cho, K.-R. Wee, S. A. Hong, I.-H. Suh, H.-J. Son, J.-D. Lee, W.-S. Han, D. W. Cho, S. O. Kang, *Dalton Trans.* 2015, *44*, 2780-2787; (h) R. Ziessel, G. Ulrich, J. H. Olivier, T. Bura, A. Sutter, *Chem. Commun.* 2010, *46*, 7978-7980.

[15] P. Labra-Vázquez, R. Flores-Cruz, A. Galindo-Hernández, J. Cabrera-González, C. Guzmán-Cedillo, A. Jiménez-Sánchez, P. G. Lacroix, R. Santillan, N. Farfán, R. Núñez, *Chem. Eur. J.* 2020, *26*, 16530-16540

[16] C. Bellomo, M. Chaari, J. Cabrera-Gonzalez, M. Blangetti, C. Lombardi, A. Deagostino, C. Viñas, N. Gaztelumendi, C. Nogues, R. Nuñez, C. Prandi, *Chem. Eur. J*. 2018, 24, 15622 – 15630.

[17] C. Bellomo, D. Zanetti, M. Chaari, S. Sinha, F. Cardano, E. Priola, A. Fin, R. Nuñez, M. Blangetti, C. Prandi, *Dyes Pigm*. 194, 2021, 109644.

[18] Z. Guo, S. Park, J. Yoon, I. Shin, *Chem. Soc. Rev.* 2014, *43*, 16-29.

[19] Y. Wu, X. Ma, J. Jiao, Y. Cheng, C. Zhu, *Synlett* 2012, *23*, 778-782.

[20] A. F. Littke, G. C. Fu, *J. Am. Chem. Soc.* 2001, *123*, 6989.

[21] S. Sulaiman, J Zhang, I. I. I. T Goodson, R. M. Laine, *J. Mater. Chem.* 2011, *21*, 11177.

[22] M. M. Heravi, V. Zadsirjan**,** Elsevier, 1st Ed., 2021, 107-152.

[23] (a) A. Loudet, K. Burgess, *Chem. Rev.* 2007, 107, 4891–932; (b) G. Ulrich, R. Ziessel, A. Harriman, *Angew. Chem. Int. Ed.,* 2008, 47, 1184–201.

[24] L. Gai, J. Mack, H. Lu, H. Yamada, D. Kuzuhara, G. Lai, Z. Li, Z. Shen, *Chem. Eur. J.* 2014; 20,1091–102.

[25] K. Rurack, M. Kollmannsberger, J. Daub, *New J. Chem.* 2001, *25*, 289-292

[26] AM. Brouwer ,*Pure Appl. Chem.* 2011; 83:2213-2228.

Chapter 5

Luminescent behavior of systems containing o-carborane linked to perylenediimide (PDI) fluorophores

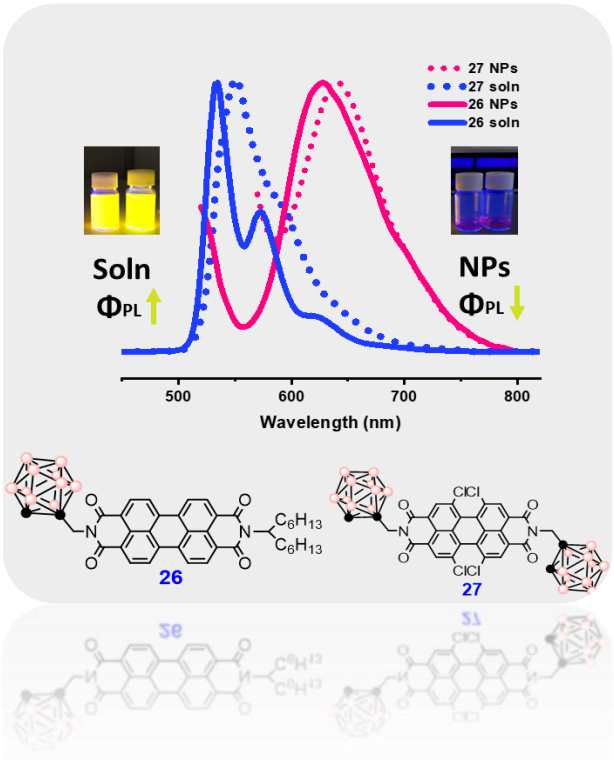

CONTENTS

5.1. Introduction

5.2. Results and discussion

5.2.1. Synthesis and derivatization of perylendiimides

5.2.2. Synthesis and characterization of perylendiimide-carborane conjugates

5.2.3. Photophysical studies of perylendiimide-carborane conjugates in solution

5.2.4. Studies of aggregation of **26** and **27** in different solvents.

5.2.5. Photophysical properties in solid state

5.2.6. Preparation of nanoparticles dispersed in water and photophysical studies

5.2.7. Preparation and characterization of microstructures

5.2.8. Preliminary biological studies

5.3. Conclusions

5.4. References

5.1. Introduction

Perylenes are polycyclic aromatic hydrocarbons; in case they contain tetracarboxylic diimide groups, they are known as perylenediimides (PDIs) and are popularly used as dyes. Henceforth, they will be referred as PDI dyes or PDIs.

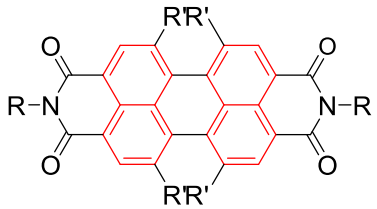

PDI

R = *N*-imide substituent

R´= bay substituents

Fig. 5.1. General structure of perylenediimides (PDIs), where R and R' are the substituents on the imide and bay positions, respectively.

The structural properties of the perylene core have been investigated, which exhibits flat π-systems as observed by X-ray diffraction of single crystals.[1,2] Also, from these studies we can say that the core is composed by the fusion of two naphthalene rings (marked in red, fig 5.1), which combined with the introduction of two imide groups on the *peri* positions 3,4 and 9,10 yield the corresponding PDIs.[2] Based on their unique properties like high structural rigidity, electron delocalization, high thermal and photochemical stability, large molar absorption coefficient (ε) and fluorescence quantum yield and semiconductor character,[3] systems containing PDIs have already been investigated for industrial applications such as dyes and, pigments,[4,5] sensors,[6] photovoltaic cells and organic field effect transistors.[7,8] The electron-deficient character of PDI dyes is a prerequisite for high photochemical stability and thus

behave as strong reductants in photoexcited state. Due to this property, they are being widely used in photoinduced electron transfer systems by various research groups[9,10] finding applications as molecular switches and wires,[11] solar cells,[12] thin films,[13] among others.

On the other hand, one of the main drawbacks of PDIs is the low solubility even in organic solvents, which often makes their synthesis, processing and application as well as leads to poor emissive properties for the resulting solid aggregates. This weakness can be improved by two different ways: (a) the introduction of bulky groups at the bay positions of the PDIs or (b) the introduction of bulky substituents at the imide positions, such as branched alkyl chains, to hamper π-π stacking by steric hindrance.

In this work, we have used the second approach to introduce one and two *o*-carborane clusters to different PDI structures (Figure 5.1) with the aim to obtain soluble PDI derivatives with high luminescence efficiency in a wide range of solvents. We hypothesize that the introduction of this boron clusters as bulky groups in the imide positions of PDIs will prevent π-π interactions to improve the solubility in organic solvents and the photophysical properties both in solution and solid state to be use as fluorescent dyes.[14,15] To this purpose, we have studied the influence of *o*-carborane on the PDI photoluminescence properties. Furthermore, micro and nanostructures of the carboranyl-containing PDIs and their properties have been analysed.

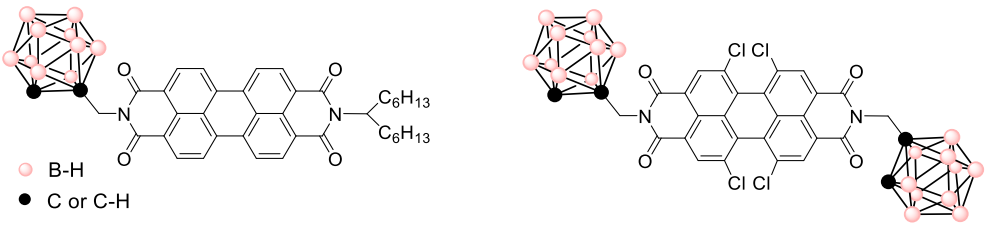

Figure 5.1 Aim of the work

5.2. Results and discussion

5.2.1. Synthesis and derivatization of perylendiimides

The synthesis of perylendiimide derivatives was performed in collaboration with Dr. Jordi Hernando from UAB. The synthesis and derivatization of PDIs are commonly performed through two different transformations of the commercially available perylenetetracarboxylic dianhydride, **PTCDA**. The first strategy described in Scheme 5.1 is the most general one. It deals with the introduction of imide groups by a quantitative condensation reaction between **PTCDA** and amines to yield symmetric perylene tetracarboxydiimides, $\mathbf{PDI_{sym}}$.[16] Nevertheless, asymmetric PDIs have also been synthesized along the years for different purposes. Those can be obtained by partial hydrolysis of the easily prepared symmetric PDIs to produce the corresponding perylene monoimides **PMI**, which can then be condensed with another primary amine to give rise to the desired asymmetric perylene tetracarboxdiimides, $\mathbf{PDI_{asym}}$(Scheme 5.1).[17]

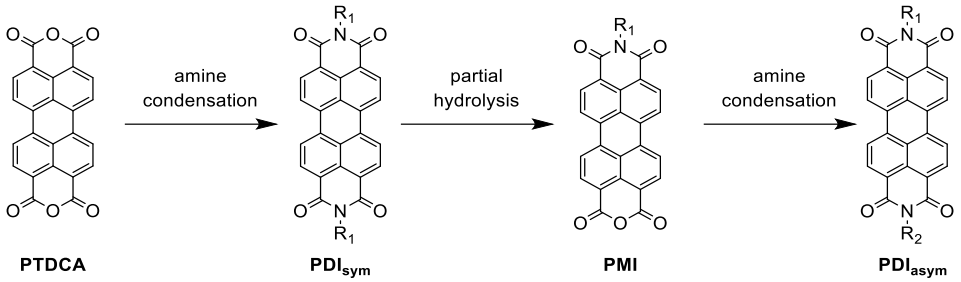

Scheme 5.1. General procedure for the preparation of *N*,*N*′-disubstituted symmetric and asymmetric PDIs.

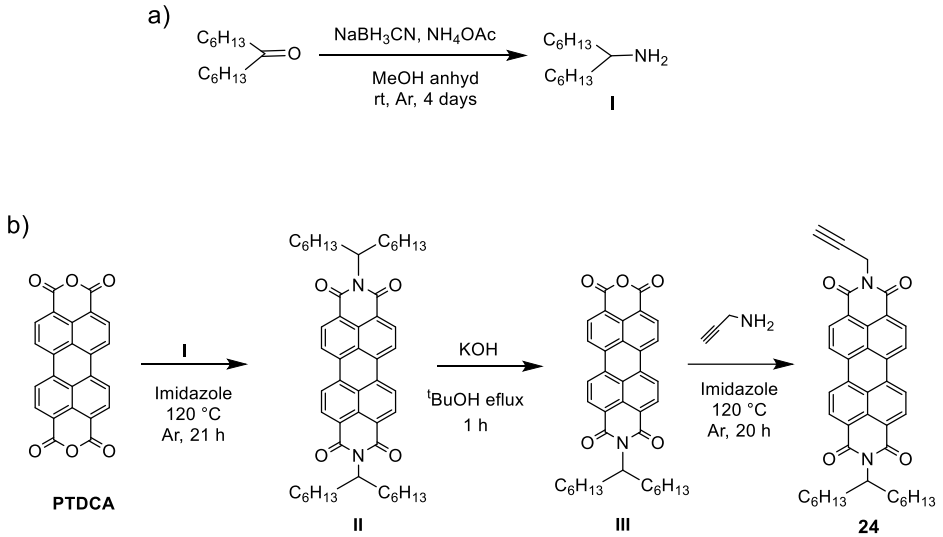

Scheme 5.2. (a) Synthesis of 7-tridecanamine (**I**). (b) Synthesis of the asymmetric precursor **24** from **PTCDA**

To obtain the first PDI-carborane tether, we first synthesized precursor **24** following the methodology in Scheme 5.1, which required the preparation of the asymmetric PDI derivative bearing the desired propargylgroup (HC≡C–CH_2–) and a branched alkyl chain at its *N*-imide positions. The branched 1-hexylheptyl chain was selected for this purpose, as it is known to give good solubility to PDIs.[16] For this reason, we had to first carry out the preparation of 7-tridecanamine (**I**) through

the reductive amination described by Borch *et al.*[18] of commercially available dihexyl ketone using ammonium acetate and sodium cyanoborohydride as a reducing agent. In thisway, 7-tridecanamine was isolated in 85% yield (Scheme 5.2a).

Then, we employed amine **I** for the preparation of the perylene monoimide (**III**) (Scheme 5.2b), using the methodology described by Langhals *et al*. First, direct condensation between 7-tridecanamine **I** and commercially available dianhydride **PTCDA** yielded quantitatively the symmetrically functionalized PDI (**II**).[16] This reaction was performed using molten imidazole as a solvent because of the low solubility of **PTCDA** in most media. Then, compound **II** was subjected to partial hydrolysis in basic media to obtain the carboximide anhydride **III**.[17] The reaction time of this step had to be carefully monitored by TLC and we stopped it when the desired monoanhydride **III** was the major compound compared to both the starting material **II** and **PTCDA** resulting from full hydrolysis. The resulting mixture of these three compounds could not be resolved by flash chromatography because of the low solubility of **III** and **PTCDA**. Instead, it was treated with different basic solutions to produce the corresponding perylene tetracarboxylate (from **PTCDA**) and dicarboxylate (from **III**) that could be separated from each other and diimide **II** thanks to their differential solubility in aqueous media. After acid treatment, perylene monoimide **III** was isolated in 55% yield.

The final step of the synthetic path to obtain PDI precursor **24** was a direct condensation of commercially available propargylamine with previously synthesized mono-anhydride **III** (Scheme 5.2b). In a first attempt, we followed the same purification process as for the synthesis of **II**, which involves the treatment of the reaction with acid and subsequent

filtration to give rise to the desired compound in 79% yield. In a second attempt, we applied the procedure described by Shanks *et al.* for the synthesis of the same compound,[19] which consists in concentrating the reaction mixture under vacuum and further purification by flash column chromatography without treatment with acid. In this way, the final asymmetrically functionalized diimide **24** was obtained in 94 % yield.

Apart from the functionalization of *imide* positions, PDIs can also be modified by the introduction of other groups on the *bay* positions, as described in Scheme 5.3. This is typically achieved by halogenation of the *bay* positions in **PTCDA** to obtain, for instance, the tetrahalogenated derivative **PTCDA$_{X4}$** (X = halogen). However, depending on the conditions of the reaction, the number of halogen substituents introduced to the PDI core can change. Subsequent condensation with primary amines can transform **PTCDA$_{X4}$** to symmetric *bay*-substituted perylenediimides **PDI$_{X4}$**. In a last step, halogens are replaced from the *bay* positions by nucleophiles via nucleophilic aromatic substitution reactions to obtain **PDI$_{R'4}$** (Scheme 5.3).[3]

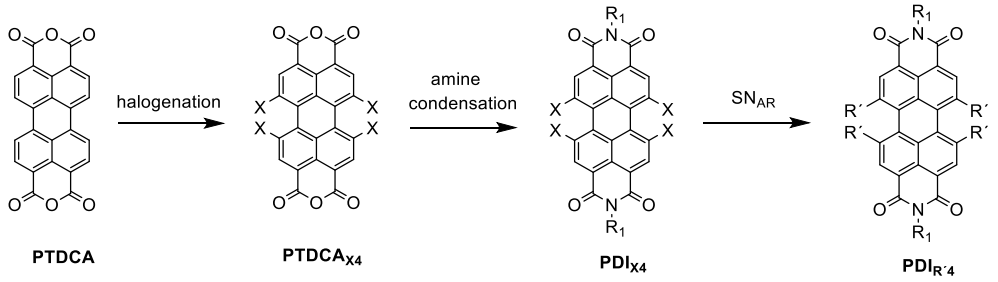

Scheme 5.3. General procedure for the preparation of *bay* substituted PDIs.

We followed this strategy for the preparation of the PDI unit needed for the synthesis of the second of our PDI-carborane target compounds. In particular, we aimed to prepare PDI precursor **25**, for which we started with chlorination of **PTCDA** using chlorosulfonic acid and iodine as reported by Sadrai *et al.* (Scheme 5.4).[20] As described by Würthner *et al.*,[21] different chlorinated products with similar polarities could be formed in this process, which means that the reaction time had to be carefully monitored. We did this by regularly taking aliquots and analysing them by ^{1}H NMR until observing that the aromatic signal corresponding to the desired tetrachlorinated derivative **IV** was predominant. This occurred after six hours of reaction. Subsequent purification by Soxhlet extraction yieldeda 9:1 mixture of the desired PDI **IV** with the corresponding penta-chlorinated derivative (46% yield). Unfortunately, this mixture could not be separated because of the low solubility of the two products, and it was subjected to next reaction without further purification. It must be noted that, by increasing the reaction time up to 22 hours, a 1:1 mixture of the tetra- and pentachlorinated compounds could be obtained.

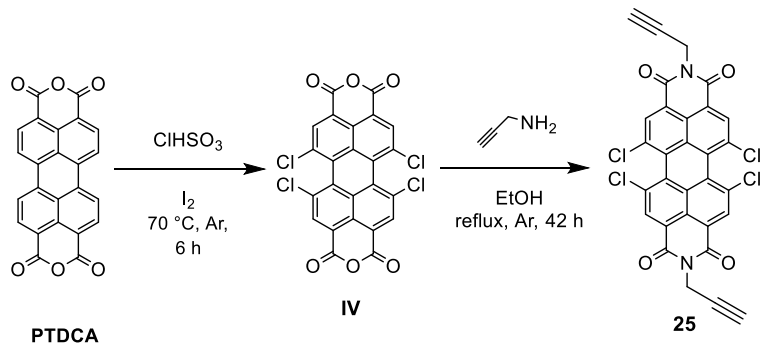

Scheme 5.4. Synthesis of the symmetric precursor **25** from **PTCDA**

The final step of the synthetic path to obtain the symmetrically functionalized PDI asymmetric precursor **25** wasa direct condensation of

commercially available propargylamine and previously prepared tetrachlorinated perylene **IV** (Scheme 5.4). The first experimental procedure tried for this reaction was extrapolated from our previous reactions with **PTCDA** and amines, which involved the use of imidazole as a solvent. In this way, a dried black solid was obtainedin 72% yield despite of the tedious filtrations required during the work-up. Alternatively, we also attempted the procedure described by Sun *et al.* for the synthesis of **25**,[22] which uses EtOH instead of imidazole as a solvent and applies a simplified treatment ofthe reaction mixture consisting in concentration under vacuum and washing the resulting crude with Et_2O. Applying this procedure, symmetrically functionalized diimide **25** was obtained as a black solid in 98% yield. It must be noted that when analysing this solid by ^1H NMR, no trace of the diimide by-product formed from the pentachlorinated starting material was found, which suggests that it is more soluble than **25** and as a consequence, it was removed during the digestion with Et_2O.

5.2.2. Synthesis and characterization of perylendiimide-carborane conjugates

For the synthesis of the final asymmetric perylendiimide-carborane dyad **26** (R = H) and the symmetric conjugate **27** (R = Cl), the synthetic strategy shown in Scheme 5.5 was devised. It consists in tethering the PDI and carborane (CB) units together by direct reaction between the *N*-propargyl group of the corresponding perylendiimide and decaborane ($B_{10}H_{14}$) to construct the carborane moiety through insertion reaction which also requires a Lewis base.

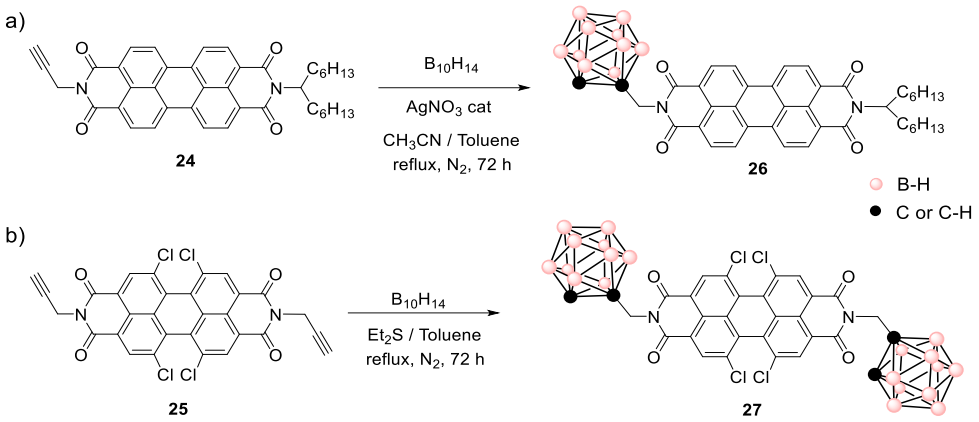

Scheme 5.5. Insertion reaction to prepare asymmetric carborane-containing PDI **26** (a) and symmetric carborane-containing PDI **27** (b).

As shown in Scheme 5.5a, the insertion reaction of $B_{10}H_{14}$ to the acetylene group of **24** to afford **26** was conducted with $AgNO_3$ as a catalyst and acetonitrile as a Lewis base.[23] After optimization of the reaction procedure, this led to the target **26** conjugate in 43% yield. By contrast, these conditions failed to produce **27** from **25** and $B_{10}H_{14}$; instead, we had to apply a different approach for the construction of the *o*-carborane scaffold,[24] where no silver salts were employed as catalysts and SEt_2 was used as a Lewis base instead of acetonitrile (Scheme 5.5b). In this way, target compound **27** was obtained in only 26% yield.

Structures of precursors **24** and **25** as well as of *o*-carboranyl derivatives **26** and **27** were characterized by ^{1}H, $^{13}C\{^{1}H\}$ NMR and FT-IR spectroscopies and Mass Spectrometry (MS). Moreover, structures of **26** and **27** were also confirmed by ^{11}B NMR spectroscopy. All the spectra and information can be found in Annex of Chapter 5.

In the ^{1}H NMR of **26** and **27** (Figure 5.2b), we observed the disappearance of the narrow resonance at 2.23 ppm corresponding to the alkyne proton

of the starting compounds **24** and **25** (Figure 5.2a), and the appearance of a broad peak around 4.21 ppm due to the proton bonded to the $C_{cluster}$ atom (C_c-H) of the final compounds. In addition, a very broad ^{1}H NMR resonance between 2.5-0.5 ppm was also found for **26** and **27**, which corresponds to the B-H protons of the *o*-carborane unit that cannot be well resolved because of boron-proton coupling.

It must be mentioned that in the ^{13}C NMR spectrum of **27**, the signals of the C=O group and some of the aromatic carbons were split into two, a feature that has been previously observed for symmetric PDIs bearing very bulky groups at the *N*-imide positions that hinder free rotation of the C-N bond.[25]

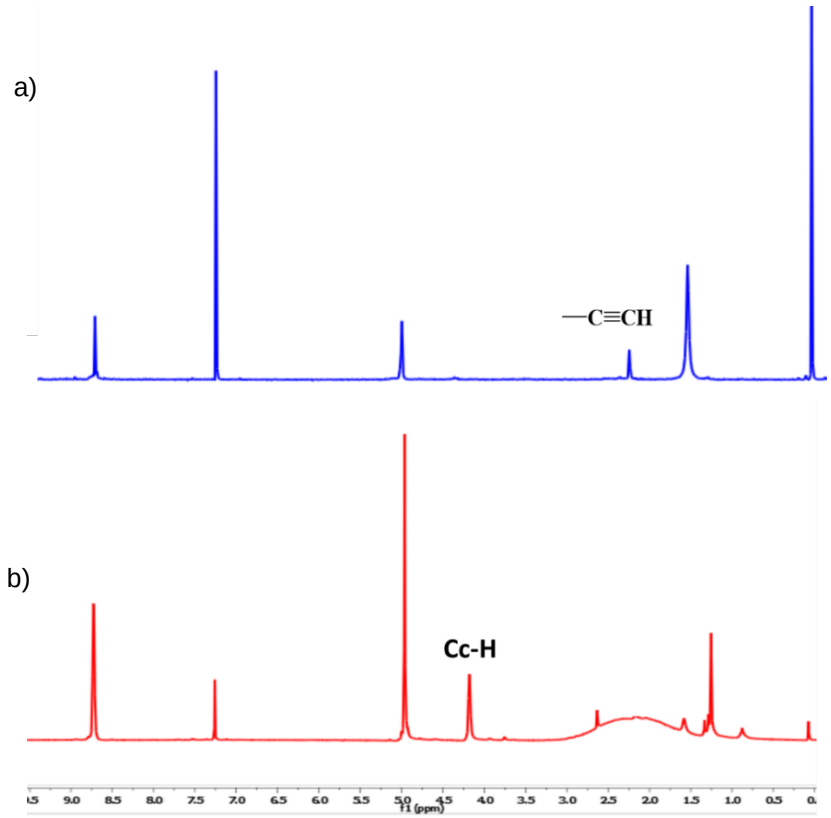

Figure 5.2. ^{1}H NMR spectra of (a) **25** and (b) **27** in $CHCl_3$.

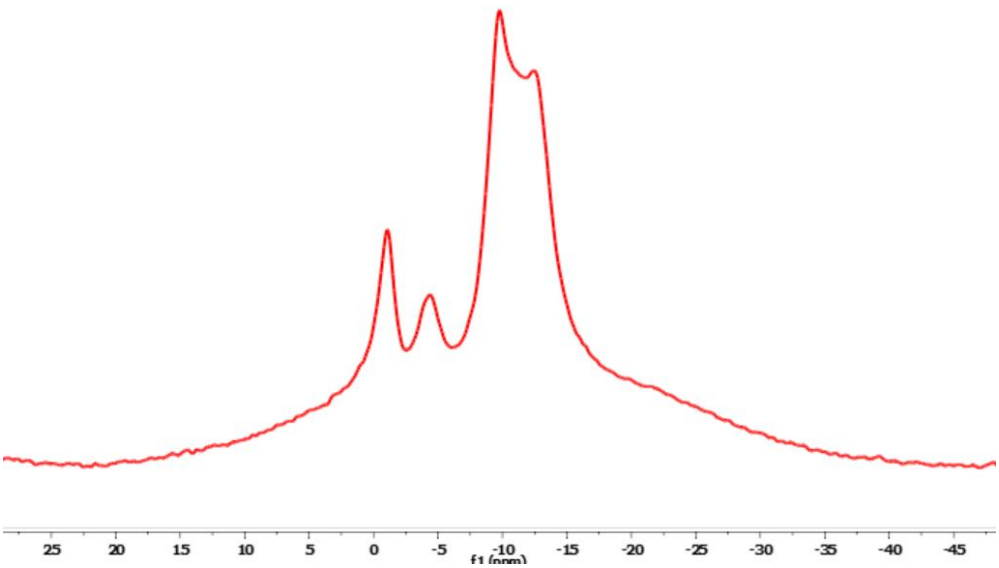

Figure 5.3. $^{1}B\{^{1}H\}$ NMR spectra of **27** in CH_3Cl.

The formation of PDI-carborane derivatives **26** and **27** was ultimately confirmed by ^{11}B NMR spectroscopy. In Figure 5.3 the $^{11}B\{^{1}H\}$ NMR spectrum of compound **27** is shown, which exhibits a 1:1:8 signal pattern that is characteristic for monosubstituted *o*-carborane derivatives. Therefore, this is a clear evidence about the achievement of the insertion reaction between acetylene and the $B_{10}H_{14}$. A similar $^{11}B\{^{1}H\}$ NMR spectrum was obtained for **26** (Annex Chapter 5). All these data together confirmed the successful formation of the expected perylendiimide-carborane conjugates **26** and **27**.

Furthermore, the IR-ATR spectrum of **26** showed the broad band characteristic of B-H stretching at 2577 cm^{-1}, whereas the B-H stretching for **27** appears at 2584 cm^{-1}, further indicating that the insertion reaction into PDI **24** and **25** with $B_{10}H_{14}$ had been produced. The MS data for **26** is as follows: calculated $[C_{40}H_{47}B_{10}N_2O_4]^+$: 729.5, which matched well with

found: 729.9 (M-H) and similarly for **27**: calculated $[C_{30}H_{30}B_{20}Cl_4N_2O_4]^+$: 842.3 matched well with found: 842.3.

5.2.3. Photophysical studies of perylendiimide-carborane conjugates in solution

The UV-Vis absorption and fluorescence spectroscopic properties of the newly designed compounds **26** and **27** were first evaluated in solution. The absorption spectra of these compounds and carboranyl-free perylendiimide reference fluorophores **24** and **25** were recorded in acetonitrile at low concentrations (c < 1.0 10^{-5} M, Figure 5.4a and Table 5.1). All of them showed similar absorption bands, exhibiting several peaks in the visible range from 400 to 525 nm that correspond to different vibronic transitions between the ground electronic state (S_0) and the first excited state (S_1) of their PDI core.[26] No absorption signals were observed for the *o*-carborane units of **26** and **27**, as they do not absorb in the UV-Vis. In fact, the introduction of these boron clusters did not cause any significant change with respect to the PDI absorption spectra of reference compounds **24** and **25**. This can be understood by the fact that the HOMO and LUMO orbitals of PDI chromophores have nodes at the imide nitrogen atoms. As a consequence, derivatization at the *N*-imide positions does not modify their electronic structure.[27,28] However, changes can occur by functionalization at the bay positions. This is the reason why we observed that the absorption bands for the chlorinated PDI derivatives (**27** and **25**) were broader than for the non-chlorinated compounds (**26** and **24**).

The emission spectra for all the compounds were also measured in acetonitrile (Figure 5.4b and Table 5.1). The characteristic PDI emission

bands were observed in the range from 500 to 700 nm, which correspond to different vibronic transitions for the $S_1 \rightarrow S_0$ transition of the PDI unit. Again, very minor differences were observed between the spectra of **26**, **27** and those of reference compounds **24** and **25**. Therefore, the introduction of *o*-carborane clusters at the *N*-imide positions did not change the emission bands from the nearby PDI fluorophores significantly, except for a small spectral red-shift.

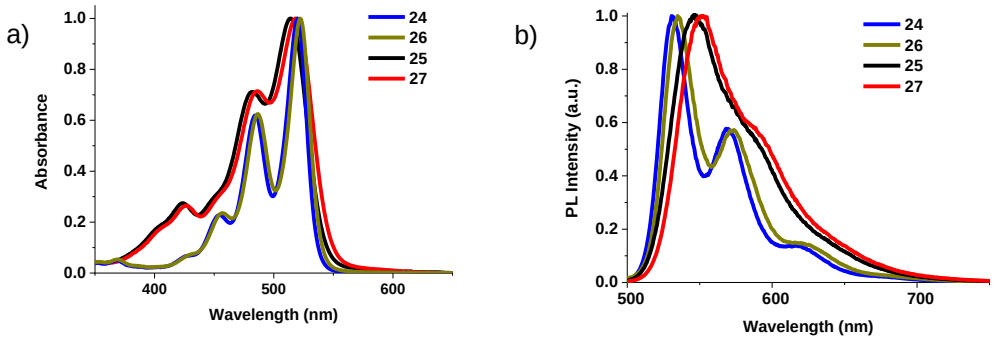

Figure 5.4. (a) Absorption and (b) emission spectra (λ_{exc} = 445 nm) of **26**, **27** and their respective precursors **24** and **25** in acetonitrile. They were all normalized with respect to their spectral maximum.

From the absorbance and fluorescence values measured, fluorescence quantum yield (Φ_F) values could be calculated for each sample (**24**, **25**, **26** and **27**) as shown in Table 5.1. To determine the Φ_F, we used compound **II** from Scheme 5.2 as the reference compound with a Φ_F = 1 in acetonitrile [29]

Table 5.1. Optical properties in acetonitrile solution of **24**, **25**, **26**and **27**.

Compound	λ_{abs}^{max} (nm)	λ_{fl}^{max} (nm)	Ɛ (L mol^{-1} cm^{-1})[a]	Φ_F
24	520	530	67 351	1.00 ± 0.04
26	522	535	64 295	1.00 ± 0.04
25	514	546	35 384	0.89 ± 0.02
27	519	552	33 011	0.93 ± 0.02

[a]Molar absorption coefficients at the spectral maximum.

By comparing the fluorescence quantum yields of final carboranyl-containing compounds with their corresponding starting PDI precursors in solution, we can conclude that no quenching of fluorescence was observed. We noticed a rather similar emission behaviour and Φ_F values, which indicates that the electronic interaction between the *o*-carborane clusters and PDI units in the excited state is negligible. As a result, all the compounds have 89% to 100% fluorescence quantum yield values (Φ_F), as expected for PDI fluorophores in solution.[3] This is a striking difference with respect to other conjugates where *o*-carborane units are directly attached to fluorophores, where intramolecular charge transfer occurs from the dye (donor unit) to *o*-carborane clusters (acceptor unit) and lead to significant fluorescence emission quenching.[14] This is for instance the case of the fluorene-carborane derivatives reported in Chapter 3 of this thesis.[30] Two main factors should account for the absence of ICT in our PDI-carborane conjugates **26** and **27**: a) the introduction of a CH_2 linker between the dye and boron cluster units; b) the electron-deficient nature of PDIs, which make them poor donors in charge transfer processes.

A clear advantage of the introduction of bulky carboranyl groups on the *N*-imide positions of **26** and **27** is that it rendered these compounds fairly

soluble in a high range of organic solvents, ranging from cyclohexane to DMSO. In addition, they preserved the high Φ_F values of their PDI cores in most of these media, as shown in Table 5.2.

Table 5.2. Fluorescence quantum yield Φ_F values of **26** in different organic solvents

No.	Solvent	Φ_F
1	Cyclohexane	0.98
2	Dioxane	1.0
3	Toluene	1.0
4	Chloroform	1.0
5	Tetrahydrofuran	1.0
6	Acetonitrile	1.0
7	Methanol	0.78
8	Dimethoxysulfoxide	0.25

Actually, only for highly polar solvents such as methanol and DMSO we observed a clear decrease of fluorescence quantum yield. This is a significant improvement relative to previously reported conjugates between PDIs and carboranes, which showed moderate emission efficiencies in solution ($\Phi_F \sim 0.1 - 0.8$).[31] Most probably, this effect was caused by a combination of factors that we managed to prevent for tethers **26** and **27**: a) enhanced intra- and intermolecular PDI-PDI interactions, which are very sensitive to concentration and solvent conditions; and b) partial intramolecular charge transfer between the PDI and *o*-carborane units, which is favored by the use of π-conjugated linkers (e.g., phenyl and phenylacetylene groups).

5.2.4. Studies of aggregation of 26 and 27 in different solvents.

As mentioned above, the introduction of bulky carboranyl groups enhances the solubility of the PDI units of **26** and **27** and, therefore, should modify their capacity to aggregate in solution. For this reason, we performed aggregation studies for **26** and **27** and their precursors **24** and **25** by adding increasing amounts of these compounds in media that are known to be poor solvents for PDI dyes. This method should in principle favour aggregation of the molecules, which often leads to spectral changes in absorption and emission.

With this idea, hexane was first chosen as an insoluble solvent in this experiment because PDI dyes are generally poorly soluble in hexane. For reference PDI compounds **24** and **25**, we observed that the addition of very little amounts of chloroform stock solutions to hexane led to monomer-like absorption spectra similar to those measured in acetonitrile (Figure 5.5a). But for increasing concentrations of these compounds in hexane, clear spectral changes were observed (Figure 5.5b). First, new absorption bands were found at longer wavelengths: two bands at 542 and 569 nm in the case of **24**, and a band at 555 nm for **25**. In addition, broadening and relative intensity variation of the monomeric PDI absorption bands were also observed. This behaviour is characteristic of PDI aggregation, mainly via π-π interactions in a co-facial configuration.[7,32] As a result, increasingly larger aggregates were formed on increasing the concentration of **24** and **25**, which explains why large broadening of their absorption spectra was measured.

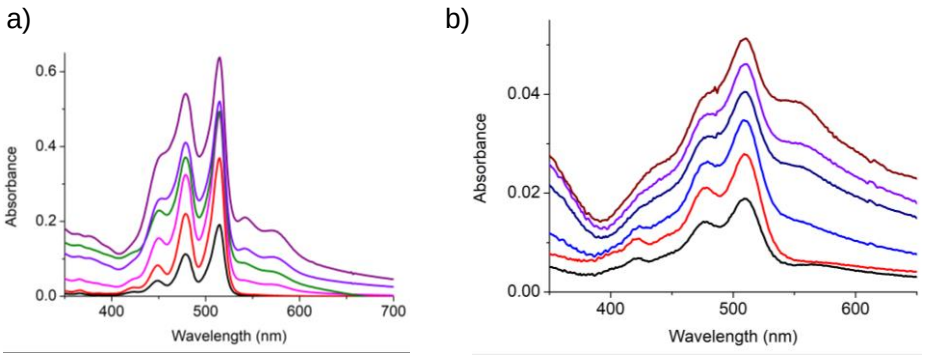

Figure 5.5. Variation of the absorption spectra of PDI reference compounds **24** and **25** when increasing their concentration in hexane. (a) Consecutive additions of 5 μL of a stock solution of **24** in $CHCl_3$ (c = 1.1 10^{-3} M) to 2 mL of hexane in a 1 cm-thick cuvette. (b) Consecutive additions of 10 μL of a stock solution of **25** (c = 0.5 10^{-3} M) to 60 µL of hexane in a 1 mm-thick cuvette.

Interestingly, when the same procedure was applied for the formation of aggregates of **26** and **27**, no changes in the absorption spectra were observed. Instead, an increase in the monomeric absorption intensity that followed the Lambert-Beer law was observed for increased concentration of these compounds. This clearly supports the evidence of the enhancement of the compound's solubility by the introduction of bulky groups such as carboranes on the *N*-imide positions. As explained by Wurthner and co-workers, this hinders molecular π-π stacking and aggregation.[33,34]

Since **26** and **27** were found to be highly soluble in hexane, different media was chosen for the aggregation studies: dioxane:water mixtures. When applying these conditions to reference compounds **24** and **25**, spectral changes in absorption proving chromophore aggregation were observed even for very diluted solutions. This indicates that they are even more insoluble in dioxane:water mixtures than in hexane. Compound **26** was then investigated. After some preliminary studies, we found that the

use of dioxane:water in a 3:2 mixture gave the best results. When adding increasing amounts of **26** to this medium, the transition from a monomer-type to an aggregate absorption spectrum was clearly observed (Figure 5.6a). Thus, the appearance of a red-shifted band from reference compound **24** and the broadening and relative intensity variation of the monomer bands was clearly measured.

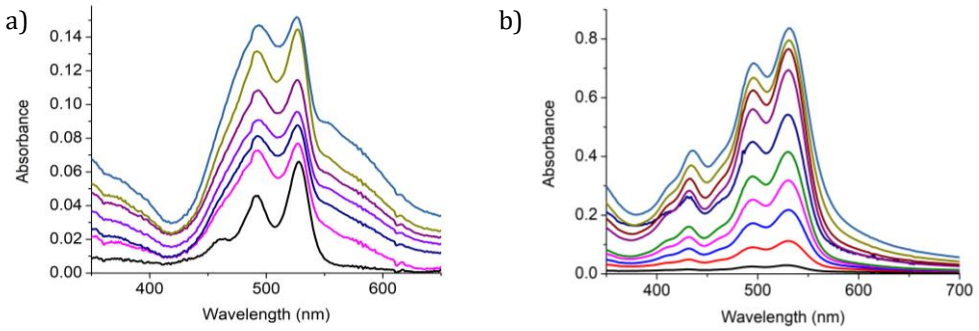

Figure 5.6. Variation of the absorption spectrum of **26** and **27** upon consecutive additions of 6 μL of a stock solution of **26** (a) and 20 μL of a stock solution of **27** (b) in dioxane (c=0.4 10^{-3} M) into 2 mL of dioxane:water (3:2 and 2:3 v/v mixture respectively).

The same procedure as for **26** was followed to find the optimal dioxane:water mixture to observe the aggregation evolution for **27**. Surprisingly, a new band did not appear at a longer wavelength and we only observed a slight broadening of the overall absorption spectrum in all the media assayed, even when using 100% water (Figure 5.6b). Although this may suggest that no aggregation took place for **27**, the lack of fluorescence when irradiated with a UV lamp proved that this compound had indeed aggregated. It must be taken into account that clear changes in absorption due to chromophore aggregation are only observed for very tight and ordered molecular packing that led to what are called strong excitonic effects.[35] However, aggregates can also be

formed with larger interchromophoric distances and higher disorder that do not exhibit defined absorption changes but do affect fluorescence emission. This is what probably occurs for **27** due to the presence of two bulky carboranes side groups as well as the four chlorine bay substituents.

In light of this, we decided to investigate **26** and **27** aggregation in dioxane:water mixtures using emission measurements. In particular, a 3:2 dioxane:water mixture was considered for **26** and 2:3 solvent ratio for **27**. In both cases, we mainly observed the appearance of a new broad and red-shifted emission band at around 650 nm upon aggregation (Figure 5.7), which was especially visible for **27**. This type of emission is typical for the so-called PDI excimers, which are low-emissive excited dimers formed in π-stacks of PDI fluorophores.[15] It must be noted that, for all these samples, excimer emission co-exists with monomer emission from the molecules that have not been aggregated yet. This, together with the lower fluorescence quantum yield expected for excimers and the occurrence of other interchromophoric interactions in the aggregates (e.g., emission quenching by photoinduced electron transfer), explains why the monomer emission bands are still predominant in the spectra shown in Figure 5.7 even for high **26** and **27** concentrations.

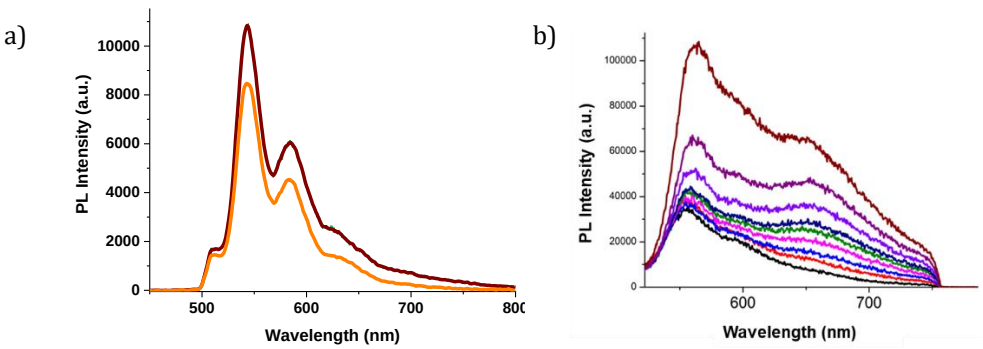

Figure 5.7. Variation of the emission spectra (λ_{exc} = 400 nm) of (a) **26** upon adding 500 μL of stock solution (10^{-3} M) and (b) (λ_{exc} = 532 nm) **27** upon consecutive additions of 20 μL of a stock solution (10^{-3} M) of this compounds in dioxane to 2 mL of a dioxane:water 3:2 and 2:3 mixture respectively

Actually, the formation of red-emitting excimers could also be observed by naked eye for the aggregates of **24**, **25**, **26** and **27**. This is clearly observed in Figure 5.8 showing images of the emission from non-aggregated and aggregated samples of these compounds. In all the cases, strong lime green emission is observed for the non-aggregated solutions, which corresponds to monomer fluorescence. Upon aggregation, less intense red emission is observed arising from the excimer species formed after photoexcitation.

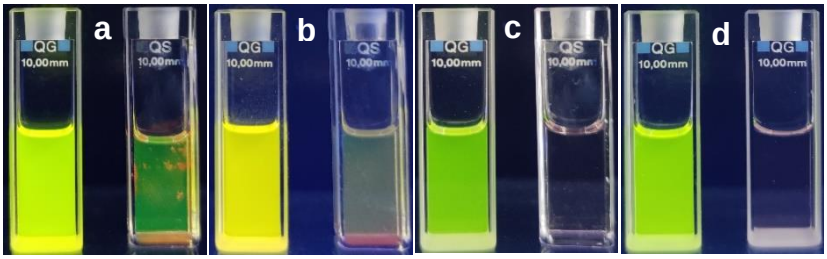

Figure 5.8. Images of the emission (λ_{exc} = 365 nm) from non-aggregated and aggregated samples of: (a) **24** in $CHCl_3$ and hexane, (b) **25** in $CHCl_3$ and hexane, (c) **26** in dioxane and water, (d) **27** in dioxane and water.

5.2.5. Photophysical properties in solid state

We also measured the absorption and emission spectra of solids **26** and **27** obtained from the synthesis (Figure 5.9). Compounds **26** and **27** produce vividly colored solutions in organic solvents with intense fluorescence. By contrast, a red-shift of the fluorescence emission was observed with maxima at around 650 nm in the solid state together with a dramatic decay of the fluorescence efficiency. In general, this is usually due to the stacking of PDI cores, which gives rise to interchromophoric interactions that lead to the formation of excimers, among other types of low- (or non) emissive species. As a consequence, the optical properties of PDI derivatives in the solid state are very dependent of molecular packing and there is strong interest to develop compounds of this type that preserve the strong monomeric emission when aggregated.

From these results it can be concluded that the introduction of *o*-carboranes in the *N*-imide positions of PDIs does not prevent the formation of excimers due to π-π stacking upon aggregation and the loss of the emissive properties of these fluorophores in the solid state. In fact, the fluorescence behavior for both compounds **26** and **27** in solid state is very similar with the observation of red excimer emission and very low quantum yields: **26** (Φ_F = 0.045 ± 0.004) and **27** (Φ_F =0.010 ± 0.006).

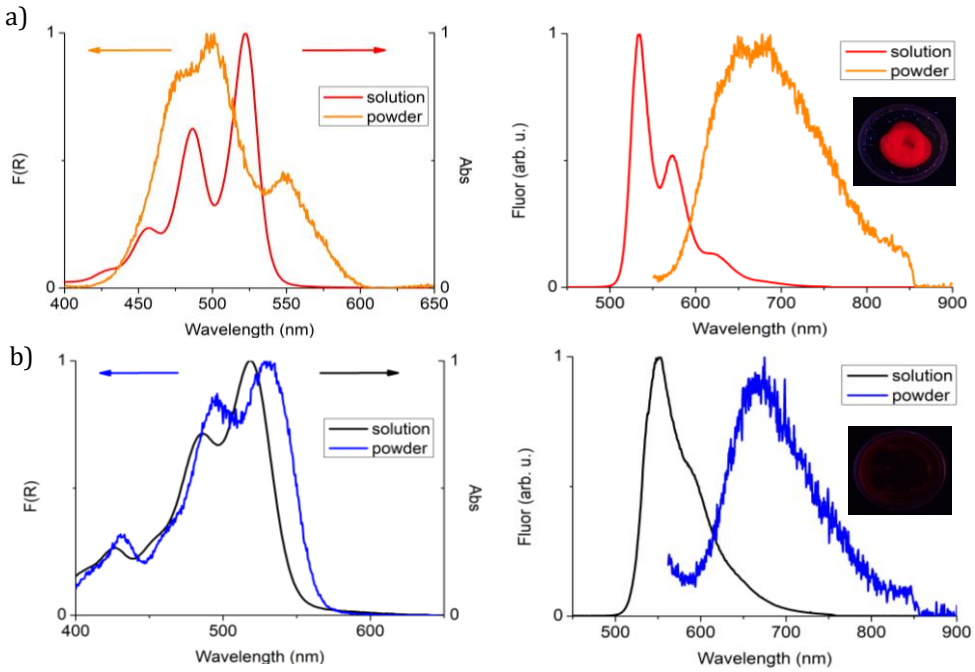

Figure 5.9. Absorption (left) and emission (right) (λ_{exc}=532 nm) spectra of the solids from (a) **26** and (b) **27**, which are compared to those measured in acetonitrile solution for both compounds. In the case of absorption in solid, the Kubelka-Munk function (F(R)) determined from the diffuse reflectance absorption spectrum is given, as indicated by the arrows. For sake of comparison, all the spectra are normalized. The insets in (a) and (b) show a photograph of the emission from powders under irradiation at λ_{exc} =365 nm.

5.2.6. Preparation of water-dispersible nanoparticles and photophysical studies

In light of the poor fluorescent properties of **26** and **27** in the solid state, we explored whether this behavior could be improved upon micro- and nanostructuration. If so, the resulting miniaturized structures could be of use for biological studies. With this aim, we first prepared water-dispersed nanoparticles of **26** and **27** using the precipitation method, followed by purification through dialysis (i.e., following the same

procedure shown in Chapter 3; Figure 5.10 and Table 5.3 [30]. Due to the challenges faced with respect to the solubility of PDI derivatives in aqueous media, the idea of preparing homogeneous and water-dispersible NPs could be of high interest.

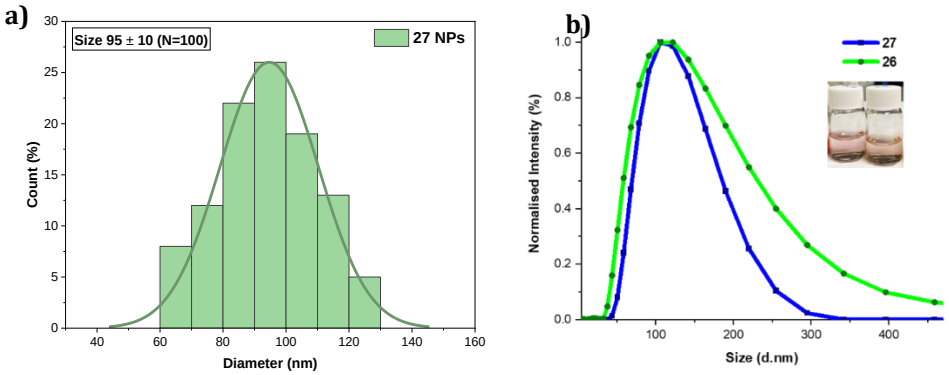

Figure 5.10. (a) Size distribution histogram for NPs of **27** (size 95 ± 10; N = 100) (b) Size distributions of **26** and **27** NPs obtained by DLS.

Table 5.3 Average Size and PD of **26** and **27** NPs

Compound	Concentration (M)	Average Size (nm)	PdI
26	1×10^{-4}	112	0.12
27	1×10^{-4}	108	0.10

Table 5.2 shows that the average sizes of **26** and **27** NPs determined by DLS are in the range of 108 to 112 nm with almost 0.1 polydispersity index (PdI). These results align well with those obtained from TEM images, where the average size of **26** and **27** NPs seems to be between 90 to 120 nm; for instance, the average size of **27** NPs was determined to be 95 ± 10 nm from TEM measurements (Figure 5.11). A Z-potential value around -41.2 mV was measured for these NPs, thus suggesting colloidal

stability. Actually, after storage at 4 ºC for two weeks, no changes in UV-Vis absorption, TEM and DLS measurements were observed for the NP dispersions.

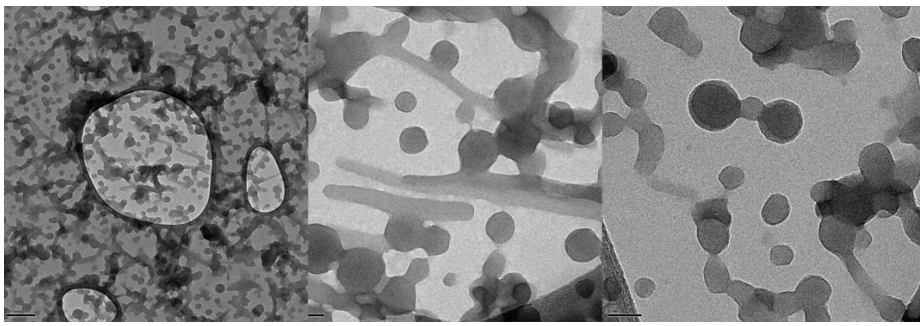

Figure 5.11 TEM image of NPs of **27**.

When comparing the fluorescence emission spectra of **26** and **27** in organic solution and in the NPs dispersed in water, larger differences were found (Figure 5.12). No monomer fluorescence was observed for the NPs; instead, only red-shifted excimer emission at λ_{max} around 650 nm and with very low quantum yield values was registered: Φ_F = 0.02 and < 0.01 for **26** and **27** NPs, respectively. This demonstrated that all the absorbed excitation energy is funneled towards excimer sites in the NPs that eventually emit. Actually, this is the same behavior previously measured for **26** and **27** in solid powder.

We also performed temperature dependence fluorescence emission studies for the NPs of **26** and **27**, but we did not observe any changes within the range from 8 °C to 55 °C.[36] Therefore, though we were able to prepare water-dispersible nanoparticles from **26** and **27**, a significant fluorescence quenching was observed in comparison to the solution state because of the formation of poorly emitting excimer species.

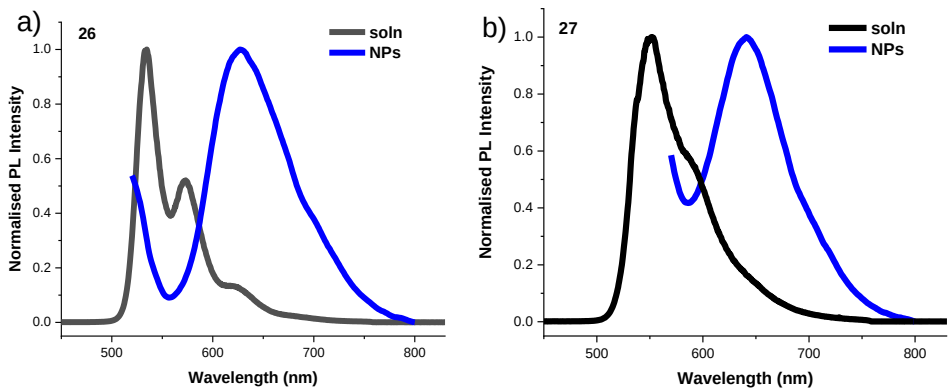

Figure 5.12. Comparison of the emission spectra (λ_{exc} = 532 nm) of (a) **26** and (b) **27** in solution (ACN) and NPs in water at low concentrations.

5.2.7 Preparation and characterization of microstructures

During NP formation by the precipitation method, fast molecular aggregation takes place that may hinder ordered packing and leads to quasi-spherical structures. For this reason, we also explored other methods for the structuration of **26** and **27** that could favor molecular ordering in the final materials, as this is a parameter known to dramatically affect their optical properties. For this purpose, we applied a slow solvent-induced precipitation method: the so-called solvent exchange by phase transfer (PT). In this method, the assembly of molecules to form supramolecular structures takes place in the absence of stirring at the interface between a good solvent, where the molecule is dissolved, and a poor solvent, which induces the aggregation.[37] To do so, we dropped an excess of the bad solvent (~ 5 mL) into a vial that contained a smaller amount of solution of interest in the good solvent (~ 1 mL, ~10^{-3} M); then, we let the two phases initially formed to mix by slow

solvent diffusion (~ 24 h). Selection of those solvents was done from the results obtained in our previous study of aggregation in solution. For sake of comparison, we also applied the same structuration method for reference compounds **24** and **25**.

In the case of **24**, hexane was used as a poor solvent that was added to the stock solution in chloroform. After 24 hours, a thin layer of red wires was observed to be formed in the interface between both solvents. The same exact procedure was followed for **26**, where two different solvent pairs were considered: chloroform and hexane, and dioxane and water. In both cases, the apparition of small red lumps was observed after 24 hours.

Scanning electron microscopy (SEM) images of the resulting aggregates were recorded. In Figure 5.13a and 5.13b, the structures formed for **24** are shown, which are long and flexible microfibers with a rather uniform 3 μm in width. In contrast, two different kinds of supramolecular structures were observed for the two strategies followed for **26**. Using hexane as bad solvent led to round microstructures growing narrower wires on their surface (Figure 5.13c). The formation of those structures could be probably explained because of a too fast addition of the poor solvent, which may lead to faster mixing with the good solvent and fast precipitation of the compound into poorly organized micromaterials. In the second case where water was used to induce aggregation of the stock solution of **26** in dioxane, a supramolecular gel made of hundreds of well-defined and flexible nanofibers was formed (thickness ~ 150 nm, Figure 5.13d).

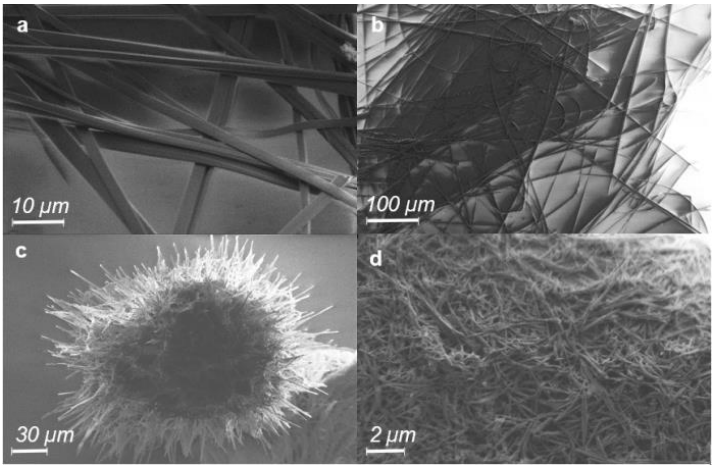

Figure 5.13. SEM images of: (a-b) **24** microstructures formed by PT using hexane as bad solvent; (c) **26** microstructures formed by PT using hexane as bad solvent; (d) **26** nanostructures formed by PT using water as a bad solvent.

The formation of nanostructures and gel-like materials had already been reported in other PDI derivative dyes.[37,38] Since the aromatic PDI core of **24** and **26** is planar, slow solvent diffusion in PT processes should induce an organized π-π packing of these molecules. It is worth to mention that such self-assembly capacity was not lost by the introduction of a carborane unit in the *N*-imide position of **26**, which can form well-defined nanostructures if the proper solvents are selected.

The PT methodology was also used to prepare micro- and nanostructures of **25** and **27**. When using hexane as bad solvent over stock solutions of **25** and **27** in chloroform, the formation of solid structures was only observed for **25** after 24 h. By contrast, small solid grains were obtained for **27** when using water as poor solvent. Unfortunately, when analyzing by SEM the structures obtained for both compounds, the formation of well-defined micro- or nanomaterials could not be observed in either case (Figure 5.14). This demonstrates that **25** and **27** have much lower

tendency to self-assemble in an organized fashion, which we attribute to two different factors: a) the introduction of chlorines on the bay positions of their PDI units, which must hinder ordered π-π stacking probably due to the twisting of the aromatic perylene core; b), this effect should be worsened for **27** because of the presence of two voluminous carborane groups at the *N*-imide positions.

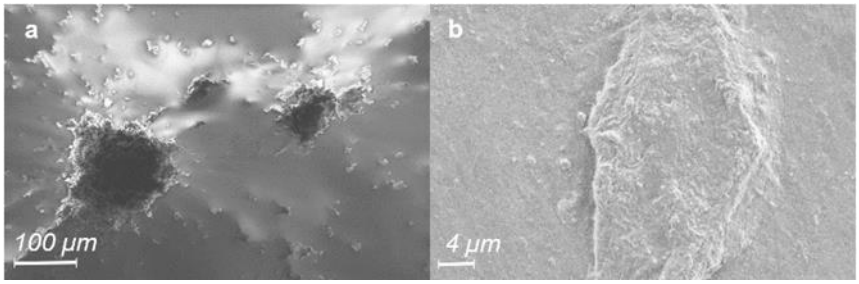

Figure 5.14. SEM images of: (a) **25** solid formed by PT using hexane as a poor solvent; (b) **27** solid formed by PT using water as a poor solvent.

The fluorescence emission of the microstructures for **26** were measured but we only observed poorly efficient excimer emission. So, even in this case, where the aggregates were formed in a much regular fashion, the fluorescence of the system was similar to that of the solid powder and water-dispersible nanoparticles.

5.2.8. Preliminary biological studies

The cell viability test was performed by XTT-assay and for that the protocol followed was, first seeding of 100µl cells in DMEM+10%FBS (SKBR3, 1000/well, density of 2.2x10 ^{4} cells/ml) was done with 24h incubation. Then, media was removed and 100µl of compound was added later diluted in DMEM+10%FBS. (50µg/ml, 25µg/ml and 10µg/ml) with

24-48h incubation. Finally, removed media, washed cells with PBS to remove excess compound and added 100ul of fresh media also added 70µl of CyQUANT™ XTT cell viability assay. Incubated for 4h and read with UV-Vis at 450 and 660 nm (Figure 5.15).[39]

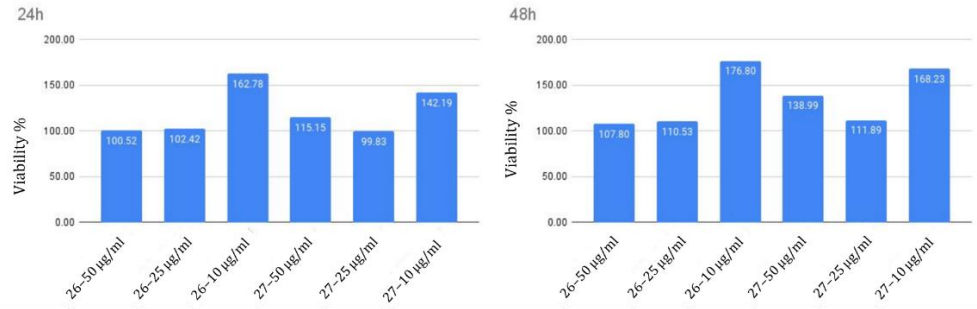

Figure 5.15. XTT Cell Viability Assay of **26** and **27**

As observed for XTT cell viability assay, the % of cell viability was abnormal for **26** and **27** in DMEM+10%FBS with greater than 100 % results for some concentrations. Therefore, we performed another cell viability test, where the cells have been incubated in a 48-well plate at a density of 2.2x10 ^{4} cells/ml. 24h later, the medium was aspirated and 200 µl of sample were added in dilutions of 100, 50, 25 and 10 µg/ml. The sample has been diluted in 100 µl of DMSO, in turn dissolved in 9.9ml of DMEM. 24 hours later, the cells were counted with a Neubauer chamber adding Trypan Blue as indicator. (Figure 5.16).

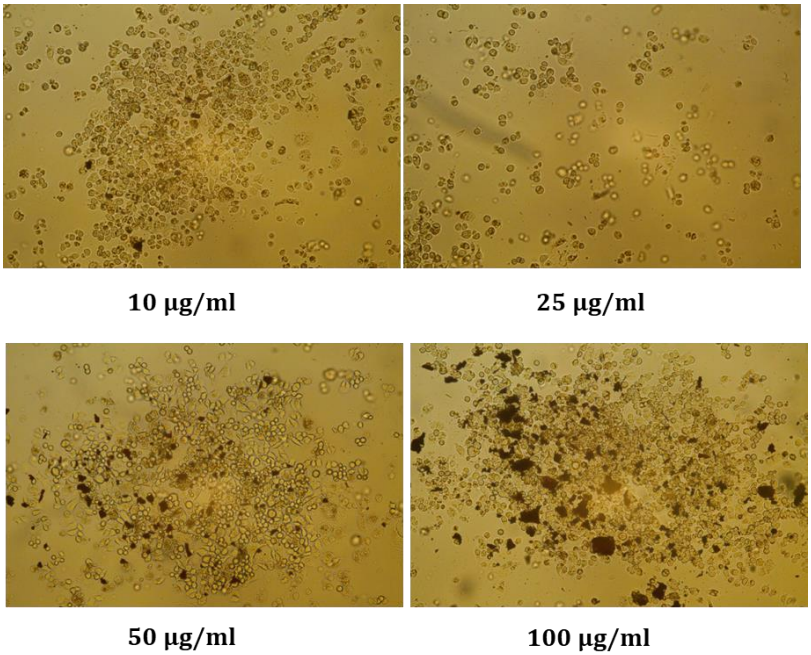

Figure 5.16. Microscope images of cells containing compounds **26** in DMEM+10%FBS using different concentrations before adding Trypan blue dye for the cell counts

In Figure 5.16, in order to count the live cells containing compounds in DMEM+10%FBS of different concentrations, we obtained these images from microscope. From the images it has been observed that the cells grow in clusters of similar size, the clusters are pronounced with increase in concentration of the compound **26** in DMEM+10%FBS and these clusters observed were aggregates of the compounds and were only seen around the areas with many cells and not throughout the well. In some of the images it has been observed that there was some contamination while preparing the samples (compounds in DMEM+10%FBS) in a non-sterile environment, but it was not seen that it had affected cell viability (Table 5.4).

Table 5.4. Cell viability experiment with Trypan blue cell lines for compounds **26** and **27** in DMEM+10%FBS using different concentrations

Sample	No. of cells per mL	Percentage of live cells
Control	39.64 x10^4	99.97
27 -100 µg/ml	38.56 x10^4	99.82
27 – 50 µg/ml	39.24 x10^4	99.87
27 – 25 µg/ml	38.97 x10^4	99.91
27- 10 µg/ml	39.12 x10^4	99.90
26 – 100 µg/ml	38.75 x10^4	99.82
26 – 50 µg/ml	39.45 x10^4	99.84
26 – 25 µg/ml	39.21 x10^4	99.88
26 – 10 µg/ml	39.52 x10^4	99.92

Later after the cell counting, Trypan blue dye was added to these cells and from Table 5.3. it can be concluded that, 99% of the cells were alive in all the different concentrations of compound **26** and **27** in DMEM+10%FBS despite of formation of aggregates in certain cases. Since, we obtained good cell viability results we moved to study the internalization of these compounds by cancer cell lines. Similar protocol was followed, where first seeding of 100µl cells in DMEM+10%FBS (SKBR3, 1000/well) was done with 24h incubation. Then, the media was removed and 100µl of compound was added and diluted in DMEM+10%FBS to make different concentrations of 50ug/ml, 25µg/ml and 10µg/ml with 4 hours of incubation. Then, after adding cell marker, these cells were observed under the confocal microscope with an irradiation in the range of λ_{exc} = 525-545 nm, we observed strong fluorescence from these cells as shown in Figure 5.17. To further confirm the fluorescence, we performed two more sets of experiments using samples and cell control. Due to an autofluorescence of the cell control, we were not able to confirm that

fluorescence (as shown in Figure 5.17) comes from our compounds, but form the cells.

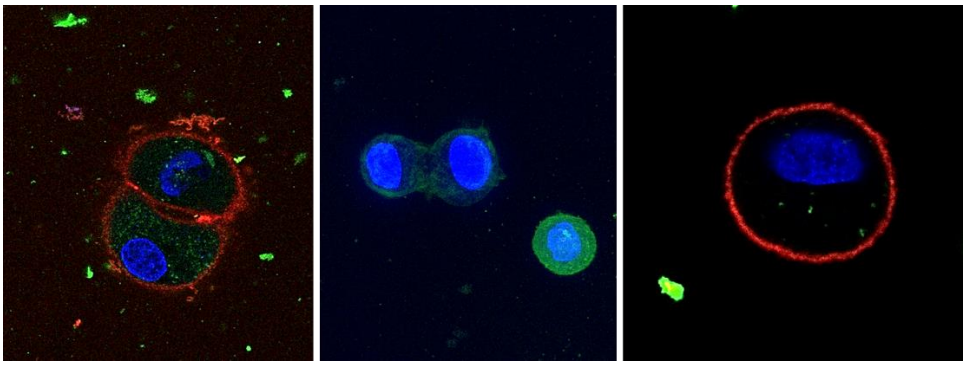

Figure 5.17. Confocal images of SKBR3 cells after 4h incubation with **27**

Therefore, these were the preliminary biological studies to check the internalization of our compounds by SKBR3 cancer cells. We can conclude that probably due to formation of aggregates in the cells culture medium, they were not internalized by cells, which was confirmed by confocal microscopy, where only autofluorescence of cells was observed. Further biological assays will be performed with NPs due to their water dispersability.

5.3. Conclusions

Two PDI based *o*-carborane derivatives **26** and **27** were successfully synthesized by the insertion reaction of $B_{10}H_{14}$ with corresponding alkyne-terminated PDIs **24** and **25**, after optimization of conditions to construct the carborane scaffold, which proceeded in low yields (26-45% yields).

The introduction of *o*-carborane side groups in **26** and **27** did not affect the optical properties of their PDI units in solution relative to reference carborane-free compounds. No changes in absorption and emission patterns were observed and, therefore, the PDI-carborane conjugates prepared preserved the high fluorescence quantum yields ($\Phi_F \sim 1$) of PDI fluorophores.

A noteworthy enhancement of the solubility and dispersibility of **26** and **27** both in apolar organic solvents (hexane) and aqueous media (dioxane:water mixtures) was observed by means of aggregation studies. This is attributed to the introduction of the bulky carboranes on the *N*-imide positions of the PDI units, which hinder their aggregation by π-π stacking. The high fluorescent quantum yields ($\Phi_F \sim 1$) were preserved in most organic solvents, in contrast to PDI-carborane aggregates.

The formation of water-dispersible nanoparticles (NPs) of **26** and **27** showed longer λ_{max} emission wavelengths in water indicating an important red-shift from the solution state. The fluorescence emission for NPs in water matched quite well with the emission in solid state. Nevertheless, no enhancement of the emission properties was found for **26** and **27** neither in solid state nor for NPs in water. In all the cases, strong fluorescence quenching was observed (quantum yields of fluorescence < 5%) compared to the solutions, and only red-shifted excimer emission could be observed, but with low fluorescence efficiency. This demonstrates that the introduction of the bulky *o*-carborane groups in the *bay* PDI positions in **26** and **27** does not prevent the formation of low or non-emissive states by interchromophoric interactions between the PDI groups of neighbouring molecules in the solid state.

Well-defined supramolecular nanofibers could be obtained for **26**, while it was not possible to achieve the same for **27**. By comparison with carborane-free precursors **24** and **25**, this behavior can be explained by the functionalization of the *bay* PDI positions and the presence of two bulky carborane groups in **27**, which hinder the organized self-assembly of the PDI groups by π-π stacking. In fact, the microstructures of **26** showed poor emission from excimers resembling similar emission behavior as observed for solid and NPs of **26** and **27**.

Preliminary biological studies of compounds **26** and **27** showed no cytotoxicity for SKBR3 cancer cells. However, after cellular uptake studies by confocal microscopy, we observed that compounds were not internalized by cells, due to the formation of aggregates in the cell medium.

5.4. References

[1] (a) F. Graser, E. Hädicke, *Justus L*iebigs *Ann. Chem*., 1980, 1994–2011; (b) F. Graser. E. Hädicke, *Justus Liebigs Ann. Chem*., 1984, 483–494; (c) E. Hädicke, F. Graser, *Acta Crystallogr., Sect. C*, 1986, 42, 189–195; (d) E. Hädicke, F. Graser, *Acta Crystallogr., Sect. C*, 1986, 42, 195–198; (e) G. Klebe, F. Graser, E. Hädicke, J. Berndt, *Acta Crystallogr., Sect*. B, 1989, 45, 69–77.

[2] P. Zugenmaier, J. Duff, T. L. Bluhm, *Cryst. Res. Technol*., 2000, 35, 1095–1115

[3] F. Würthner, *Chem. Commun*. 2004, 1564

[4] H. Zollinger, *Color Chemistry, 3rd edn*., *VCH*, Weinheim, 2003.

[5] W. Herbst, K. Hunger, Industrial Organic Pigments: Production, Properties, Applications*, 2nd Edn., Wiley-Vch*, Weinheim, 1997.

[6] P. Singh, A. Hirsc, S. Kumar, Trends *Analyt. Chem*. 2021,138, 116237

[7] F. Würthner, *Angew. Chem., Int. Ed*, 2001, 40, 1037–1039.

[8] (a) L. Schmidt-Mende, A. Fechtenkötter, K. Müllen, E. Moons, R. H. Friend, J. D. MacKenzie*, Science,* 2001, 293, 1119–1122; b) A. Yakimov, S. R. Forrest, *Appl. Phys. Lett*., 2002, 80, 1667–1669.

[9] M. P. O'Neil, M. P. Niemczyk, W. A. Svec, D. Gosztda, G. L. Gaines III, M. R. Wasielewski, *Science*, 1992, 257, 63–66.

[10] S. Prathapan, S. I. Yang, J. Seth, M. A. Miller, D. F. Bocian, D. Holten, J. S. Lindsey, *J. Phys. Chem. B.*, 2001, 105, 8237–8248.

[11] (a) Hayes, R. T.; Wasielewski, M. R.; Gosztola, D*. J. Am. Chem. Soc.* 2000, 122, 5563-5567; (b) Davis, W. B.; Svec, W. A.; Ratner, M. A.; Wasielewski, M. R. *Nature* 1998, 396, 60-63.

[12] (a) Gregg, B. A.; Cormier, R. A*. J. Am. Chem. Soc*. 2001, 123, 7959-7960; (b) Breeze, A. J.; Salomon, A.; Ginley, D. S.; Gregg, B. A.; Tillmann, H.; Horhold, H. H. *Appl. Phys. Lett.* 2002, 81, 3085-3087.

[13] (a) M. J. Fuller, M. R. Wasielewski, *J. Phys. Chem*. B 2001, 105, 7216-7219; (b) M. J. Fuller, C. J. Walsh, Y. Zhao, Wasielewski, *Chem. Mater*. 2002, 14, 952-953.

[14] R. Núñez, I. Romero, F. Teixidor, C. Viñas, *Chem. Soc. Rev.,* 2016,45, 5147-5173.

[15] L. Parejo, M. Chaari, S. Santiago, G. Guirado, F. Teixidor, R. Nuñez, J. Hernando, *Chem. Eur. J.* 2021, 27, 270 – 280.

[16] S. Demmig, H. Langhals, *Chem. Ber*. 1988, 121, 225-230.

[17] H. Kaiser, J. Lindner, H. Langdales, *Chem. Ber*. 1991, *124*, 529-535.

[18] R. F. Borch, M. D. Bernstein, H. D. Durst, *J. Am. Chem. Soc*. 1971, 93, 2897-2904.

[19]D. Shanks, S. Preus, K. Qvortrup, T. Hassenkam, M. B. Nielsen, K. Kilså, *New J. Chem*. 2009, 33, 507–516.

[20] M. Sadrai, L. Hadel, R. R. Sauers, S. Husain, K. Krogh-Jespersen, *J. Phys. Chem.* 1992, 96, 7988-7996.

[21] A. Nowak-Król, F. Würthner, *Org. Chem. Front*. 2019, 6, 1272–1318.

[22] K. Sun, C. Xiao, C. Liu, W. Fu, Z. Wang, Li, *Langmuir*, 2014, 30, 11040–11045.

[23] A. Toppino, A. R. Genady, M. E. El-Zaria, J. Reeve, F. Mostofian, J. Kent, J. F. Valliant, *Inorg. Chem.*, 2013, 52, 8743–8749.

[24] N. Shin, S. Yu, J. H. Lee, H. Hwang, K. M. Lee, *Organometallics*, 2017,

36, 1522–1529.

[25] L. D. Wescott, D. L. Mattern, *J. Org. Chem.*, 2003, 68, 10058–10066.

[26] H. Langhals, *Science*. 2000, 56, 2207–2210.

[27] P. M. Kazmaier, R. Hoffmann, *J. Am. Chem. Soc*. 1994, 116, 9684–9691.

[28] H. Langhals, *Heterocycles* 1995, *40*, 477–500.

[29] T. Kircher, H.-G. Löhmannsröben, *Phys. Chem. Chem. Phys*. 1999, 1, 3987–3992

[30] S. Sinha, Z. Kelemen, E. Hümpfner, I. Ratera, J. P. Marval, J. P. Jurado, C. Viñas, F. Teixidor, R. Núñez, *Chem. Commun.*, 2022, 58, 4016–4019.

[31] C. Sang, G. Wang, Y.-C. Wei, Q. Jiang, K. Liu, M. Zhang, Y.-Y. Chen, X. Chang, F. Liu, S. Yin, P.-T. Chou, Y. Fang, *CCS Chem.*, 2022, 4, 1949–1960; K. Liu, Z. Wang, C. Shang, X. Li, H. Peng, R. Miao, L. Ding, J. Liu, T. Liu, Y. Fang, *Adv. Mater. Technol.*, 2019, 4, 1800644; W. Feng, K. Liu, J. Zang, J. Xu, H. Peng, L. Ding, T. Liu, Y. Fang, *J. Phys. Chem. B*, 2021, 125, 11540-11547.

[32] K. Balakrishnan, A. Datar, T. Naddo, J. Huang, R. Oitker, M. Yen, J. Zhao, L. Zang, *J. Am. Chem. Soc.* 2006, *128*, 7390–7398.

[33] M. M. Safont-Sempere, P. Osswald, K. Radacki, F. Würthner, *Chem. – Eur. J*., 2010, 16, 7380–7384

[34] M. M. Safont-Sempere, P. Osswald, M. Stolte, M. Grune, M. Renz, M. Kaupp, K. Radacki, H. Braunschweig, F. Würthner, *J. Am. Chem. Soc*., 2011, 133, 9580–9591.

[35] M. Kasha, H. R. Rawls, M. A. El-Bayoumi, *Pure Appl. Chem*. 1965, 11, 371– 392

[36] J. Liu, Y. Zhang, C. Zhang, P. Zhang, R. Zeng, J. Cui, J. Chen, *Mater. Adv*., 2020, 1, 1330-1336

[37] F. Zhang, Y. Ma, Y. Chi, H. Yu, Y. Li, T. Jiang, X. Wei, Shi, *J. Sci. Rep.* 2018, *8*, 1–11.

[38] E. Krieg, E. Shirman, H. Weissman, E. Shimoni, S. G. Wolf, I. Pinkas, B.

Rybtchinski, *J. Am. Chem. Soc.* 2009, *131*, 14365–14373.

[39] C. Bellomo, M. Chaari, J. Cabrera-González, M. Blangetti, C. Lombardi, A. M. Deagostino, C. Viñas, N. Gaztelumendi, C. Nogues, Rosario Nuñez, C. Prandi, *Chem. Eur. J.* 2018, 24, 15622–15630

Chapter 6

Synthesis, characterization and photophysical properties of new tri-branched fluorene & truxene systems bearing o-carborane clusters

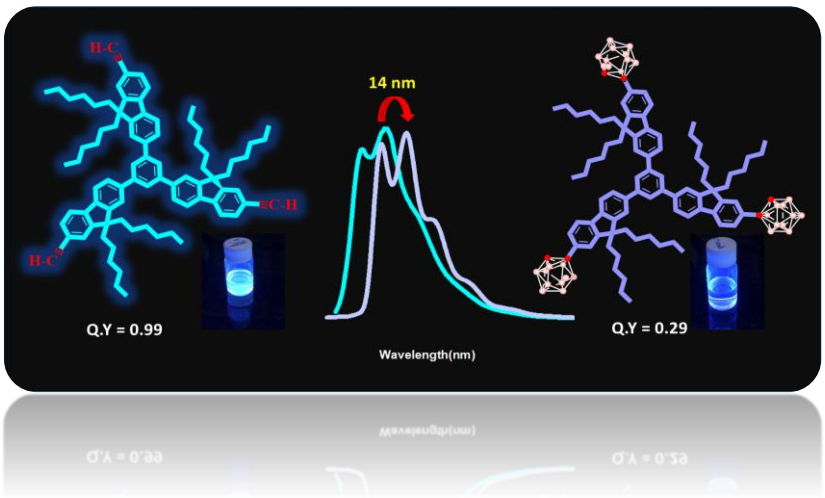

CONTENTS

6.1. Introduction

6.2. Results and discussion

6.2.1. Synthesis of *o*-carborane containing tri-branched fluorene and truxene derivatives

6.2.2. Characterization of *o*-carborane containing tri-branched fluorene and triene derivatives

6.2.3. Photophysical properties in solution, aggregation and thin films

6.2.4. Electrochemical analysis (Cyclic Voltammetry)

6.5.5. Theoretical calculations (DFT)

6.5.6. Two-photon absorption (TPA) spectroscopy

6.3. Conclusions

6.4. References

6.1. Introduction

Organic electronic devices and fluorescent probes containing *o*-carboranes have been a subject of investigation for decades and thus is extensively used in light-emitting diodes, thin film transistors, optical sensors, and biomedicine in recent years.[1] As evidence of the 3D σ-aromaticity and unique electronic attributes of *o*-carborane clusters on π-conjugated systems, there has been many recent works.[1,2] One of the main components in these reports is an observable enhancement of luminescence in solid state or thin films due to the effect of *o*-carborane directly attached to π-conjugated fluorophores exhibiting aggregation-induced emission (AIE).[3,4] The influence of *o*-carborane units on the backbone of various fluorophores shows unique optical properties not just in one-arm systems (*o*-carborane attached to one-arm π-conjugated fluorophores) but also in tri-branched systems (*o*-carborane attached to three-arm π-conjugated fluorophores).[5]

On the other hand, tri-branched fluorophore systems or star-shaped π-conjugated fluorophores have attracted a prominent attention for two-photon absorption applications such as in optical materials, bioimaging and two-photon dynamic therapy.[5]

Two photon absorption is a phenomenon in which a molecule can simultaneously absorb two photons of same energy to reach a stable excited state via virtual state (of very short lifetime). Continuous laser waves are avoided, and instead pulsed laser is used in the spectral range from 690 nm to 960 nm.[6] Thus, in comparison to one-photon microscopy,

two-photon microscopy is useful in terms of non-invasive cell imaging due to higher spatial resolution, less photo-damaging and bleaching.

In this chapter, we will focus on synthesis and characterization of novel tri-branched π-conjugated fluorene and truxene based acetylene precursors and the tri-branched systems directly attached to *o*-carborane clusters at the terminals of the structures. Then we will focus on their unique photophysical properties in solution, aggregation, thin films and their future prospects in the field of opto-electronics and two-photon absorption spectroscopy. The electron-withdrawing nature of *o*-carborane units when attached to various fluorophores is quite popular among many investigations[7, 8] done so far hence with the help of cyclic voltammetry, DFT calculations and TPA measurements, the HOMO LUMO energy levels, transitions and band gaps have been studied in detail.

6.2. Results and discussion

6.2.1. Synthesis of *o*-carborane containing tri-branched fluorene and truxene derivatives

The synthesis of starting tri-branched fluorene and truxene was performed in collaboration with Dr. Norberto Farfan's group at UNAM (Mexico). To synthesize o-carborane containing tri-branched fluorene and truxene derivatives, The preparation of π-conjugated aromatic group assembled 1,2-dicarba-*closo*-dodecacarborane (or *o*-carborane) fluorophores can be explained in three parts: (a) synthesis of the tri-branched fluorene-based acetylene precursor (b) synthesis of the tri-branched truxene-based acetylene precursor and (c) synthesis of *o*-carborane-functionalized tri-branched fluorene and truxene derivative.

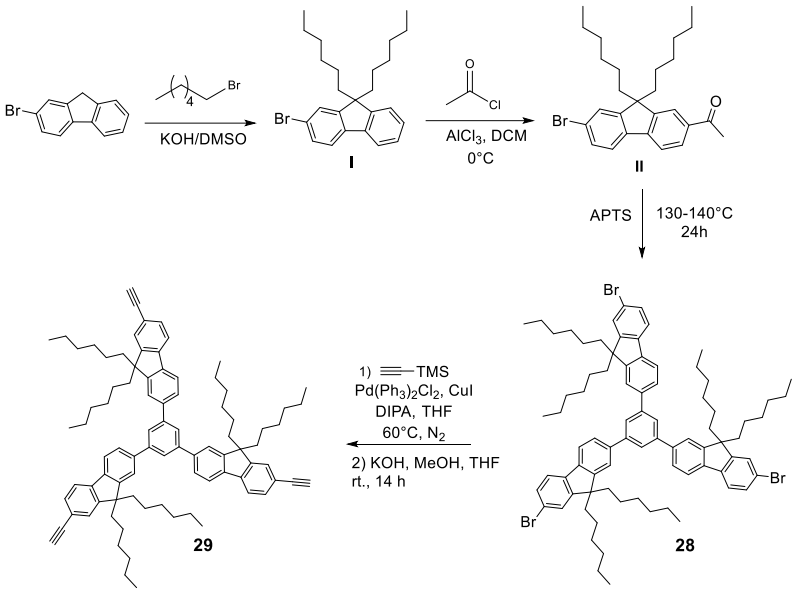

Scheme 6.1. Synthesis of the tri-branched fluorene-based acetylene precursor.

(a) Synthesis of the tri-branched fluorene-based acetylene precursor: as it is shown in Scheme 6.1, first dialkylation was performed using commercially available 7-bromofluorene and n-hexyl bromide in basic medium to obtain **I**. Compound **I** was reacted with acid chloride and a Lewis acid ($AlCl_3$) to undergo Friedel Craft´s acylation reaction to give **II**, where the hydrogen atom bonded to the free aromatic ring of structure **II** was substituted by acyl group. Then compound **28** was formed by trimerization condensation of **II** in the presence of ethyl orthoformate and dry gaseous HCl at 25 °C for 4 hours followed by the previously reported work of Kovalev and co-workers.[9] Finally, Pd-catalyzed Sonogashira cross-coupling reaction was performed using **28**, trimethylsilyl acetylene and $Pd(PPh_3)_2Cl_2$ as a catalyst, and CuI as co-catalyst followed by formation of **29** by substitution reaction. After the purification and isolation of **29**, the final yield obtained was 65%.

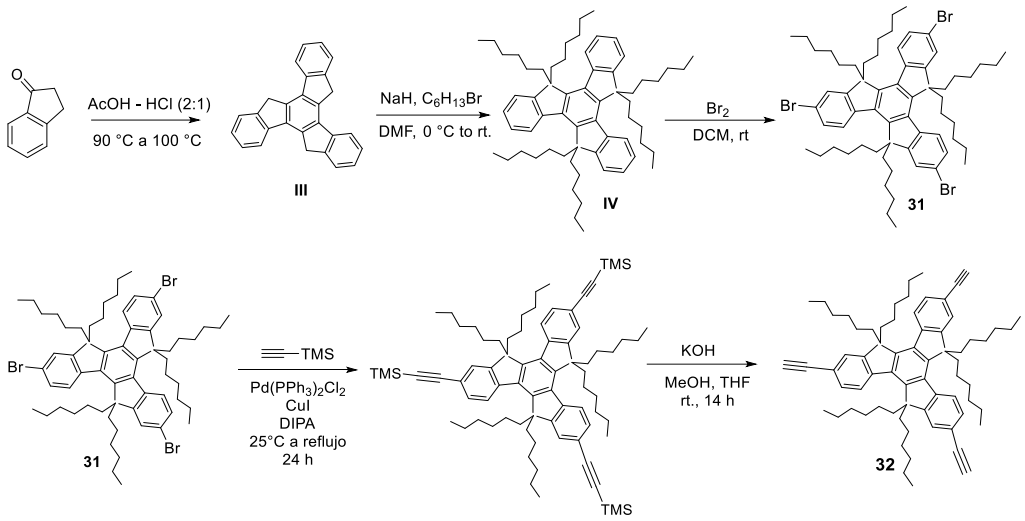

Scheme 6.2. Synthesis of the tri-branched truxene-based acetylene precursor.

(b) Synthesis of tri-branched truxene-based acetylene precursor: in Scheme 6.2, compound **III** was obtained by cyclization of 1-indanone in presence of acetic acid and conc. aqueous HCl in 2:1 ratio.[10] Dialkylation was performed by using *n*-hexyl bromide and NaH as base for the formation of **IV,** which was then brominated in the absence of light to accelerate the radical pathway.[11] Tribromohexahexyltruxene (**31**), trimethylsilyl acetylene and $Pd(PPh_3)_2Cl_2$ as a catalyst, and CuI as co-catalyst were used for Pd-catalyzed Sonogashira cross-coupling followed by reaction in basic medium to obtain **32**. After the purification and isolation of **32**, the final yield obtained was 62%.

(c) Synthesis of *o*-carborane functionalized tri-branched fluorene and truxene derivatives: in this part of the synthesis, insertion reaction was performed using decaborane, $B_{10}H_{14}$ and corresponding acetylene precursors in one-pot reaction conditions to obtain the final compounds

containing *o*-carborane units. Usually, this reaction requires a proper selection of Lewis base in order to obtain better yield and in this case, we used 5 equivalents of diethyl sulfide (Et_2S) for each acetylene unit present in the tri-branched fluorene and truxene systems in the presence of toluene as solvent. The main role of the Lewis base as explained in previous chapters is to form an adduct which then reacts with the corresponding tri-branched acetylene precursors **29** and **32** to give the final compounds **30** and **33** (Scheme 6.3). After proper extraction, purification, and isolation of **29** and **32**, we obtained 40 to 45 % as pure acetylene compounds, respectively.

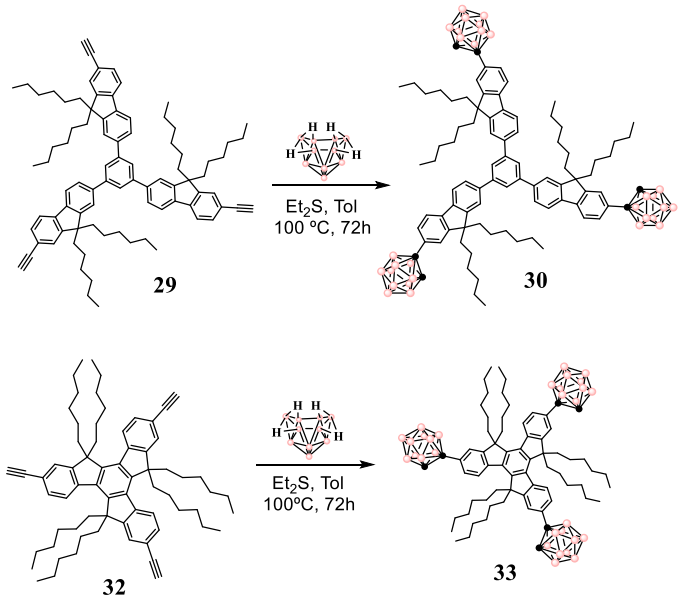

Scheme 6.3. Synthesis of *o*-carborane containing tri-branched fluorene and truxene derivatives

6.2.2. Characterization of tri-branched fluorene and truxene derivatives

The structures from **28** to **33** were established and easily monitored by FT-IR, ^{1}H, $^{13}C\{^{1}H\}$ spectroscopy techniques. Additionally, the structures of

30 and **33** were also confirmed by $^{11}B\{^{1}H\}$ spectroscopy and elemental analyses.

The FT-IR spectra of acetylene precursors **29** (Figure 6.1) and **32** show a narrow υ(C-H) stretching band of -C≡C-H at 3305 cm^{-1}, whereas the υ(C-H) bend of -C≡C-H appears around 700-610 cm^{-1}. The FT-IR spectra of **30** and **33** typically show υ(B-H) strong bands around 2546 cm^{-1}, where *closo* clusters usually appear (Figure 6.1). From this spectrum, we also observe that this typical strong and broad υ(B-H) band is missing in case of decaborane ($B_{10}H_{14}$), instead a weak band appears in the range of 2529 to 2575 cm^{-1}. This could be considered as a preliminary confirmation of the formation of *o*-carborane units at the terminal of the core structure for both **30** and **33**.

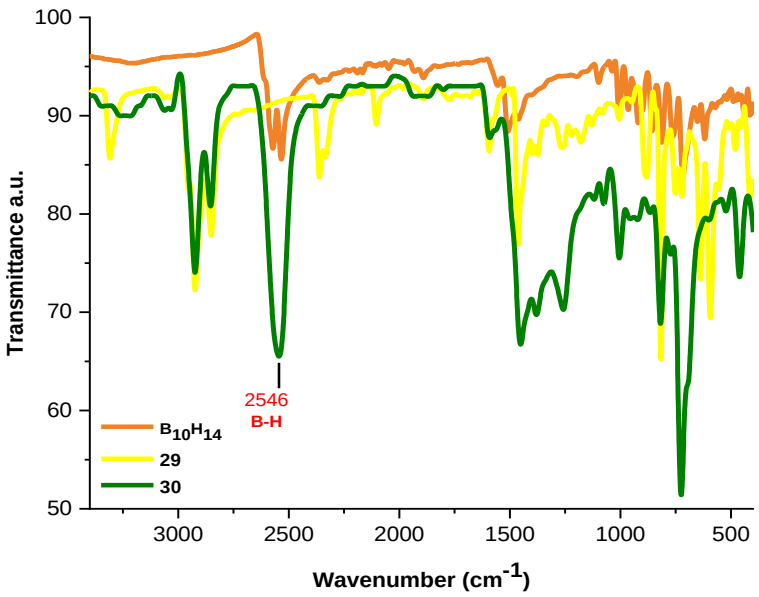

Figure 6.1. FT-IR spectrum of **$B_{10}H_{14}$** (orange), **29** (yellow) and **30** (green). The last one shows typical υ(B-H) band for *o*-carboranyl derivatives.

On the other hand, the conversion of **28** to **29** in Scheme 6.1 was monitored and confirmed by ^{1}H NMR spectra (Figure 6.2), in which the acetylenic protons of **29** appear at δ 3.16 ppm along with the proton resonances in the aromatic region δ 7.92-7.51 ppm. In the aromatic region, no shift in resonance was observed after the structural conversion to **29**, neither in the aliphatic region any significant shift was observed and the presence of dihexyl chain was confirmed by the presence of resonances from δ 1.06 to 1.15 ppm (see Annex of Chapter 6). We have observed a similar trend for the conversion of **31** to **32** in the ^{1}H NMR spectra. The three acetylenic protons of **32** appear at δ 3.20 ppm, however in this case there was an upfield shift in the aromatic region of tri-branched truxene based acetylene precursor approximately by 0.14 ppm for the interior aromatic protons that show multiplicity of doublet nature (more details in Annex of Chapter 6). Clearly, we see a structural difference between **29** and **32** through ^{1}H NMR spectra because in case of the truxene acetylene precursor **32** not only the aromatic protons but also the aliphatic protons have experienced a slight upfield shift by 0.06 ppm from **31**, which was not the case of tri-branched fluorene-based acetylene precursor **29**.

The insertion reaction of $B_{10}H_{14}$ was monitored by ^{1}H NMR, where we noticed the acetylenic protons of **29** at δ 3.16 ppm disappeared and protons attributed to C_c-H in **30** at δ 4.06 ppm appeared (Figure 6.2). Usually, the monosubstituted *o*-carborane shows the proton resonances in this region, along with that we were able to observe a very less intense, but broad signal for proton attached to boron atoms (B-H) of the 1,2-$C_2B_{10}H_{10}$ cluster from δ 1.75 to 3.20 ppm (Figure 6.2). This is a distinct

property of *o*-carborane containing compounds, which is absent in case of their corresponding tri-branched acetylene precursors. Interestingly, no dramatic change in aromatic protons were observed after the final conversion from **29** to **30**, that appeared in the same region, around δ 7.51 to 7.89 ppm, as well as the protons of dihexyl chains that appeared around the same range as the acetylene precursor (see Figure 6.2).

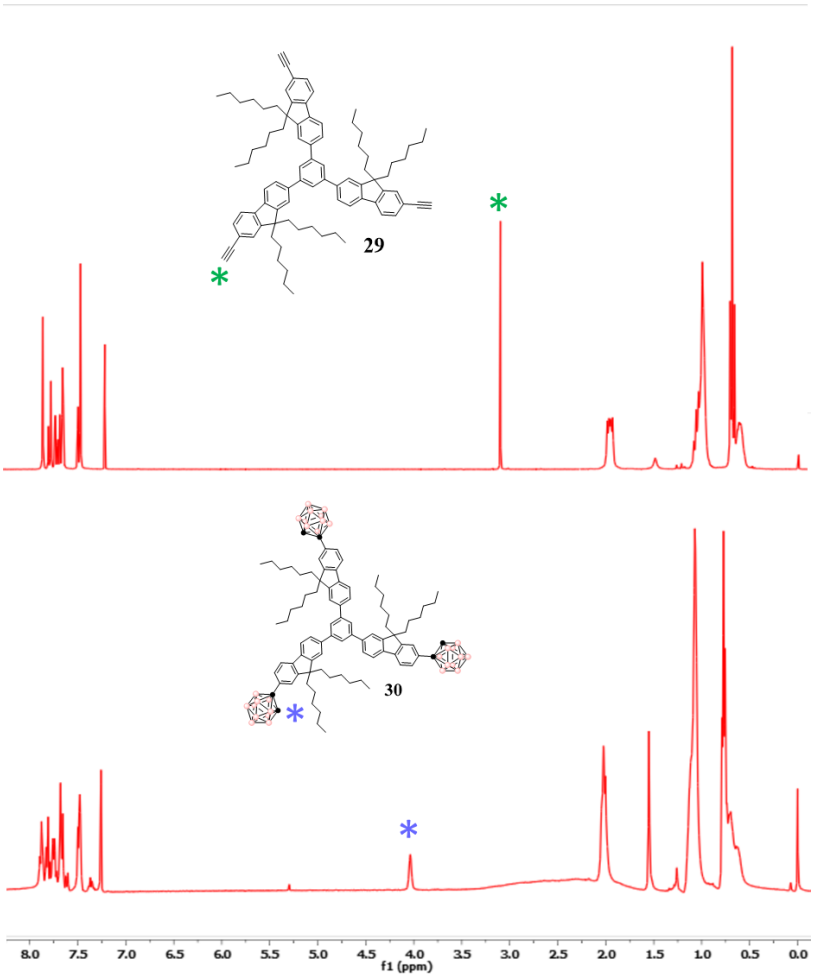

Figure 6.2. Comparison of ^{1}H NMR spectra of **29** and **30** in $CDCl_3$

Similar characteristic proton resonances attributed to the C_c-H of **33** were observed at δ 4.09 ppm along with broad signal for proton attached to boron atoms (B-H) of the *o*-carborane cluster from δ 1.75 to 3.20 ppm (Figure 6.3). In fact, the aromatic protons and dihexyl chain protons showed peaks in the same region as **32**, from δ 7.54 to 8.31 ppm and δ 0.90 ppm, respectively.

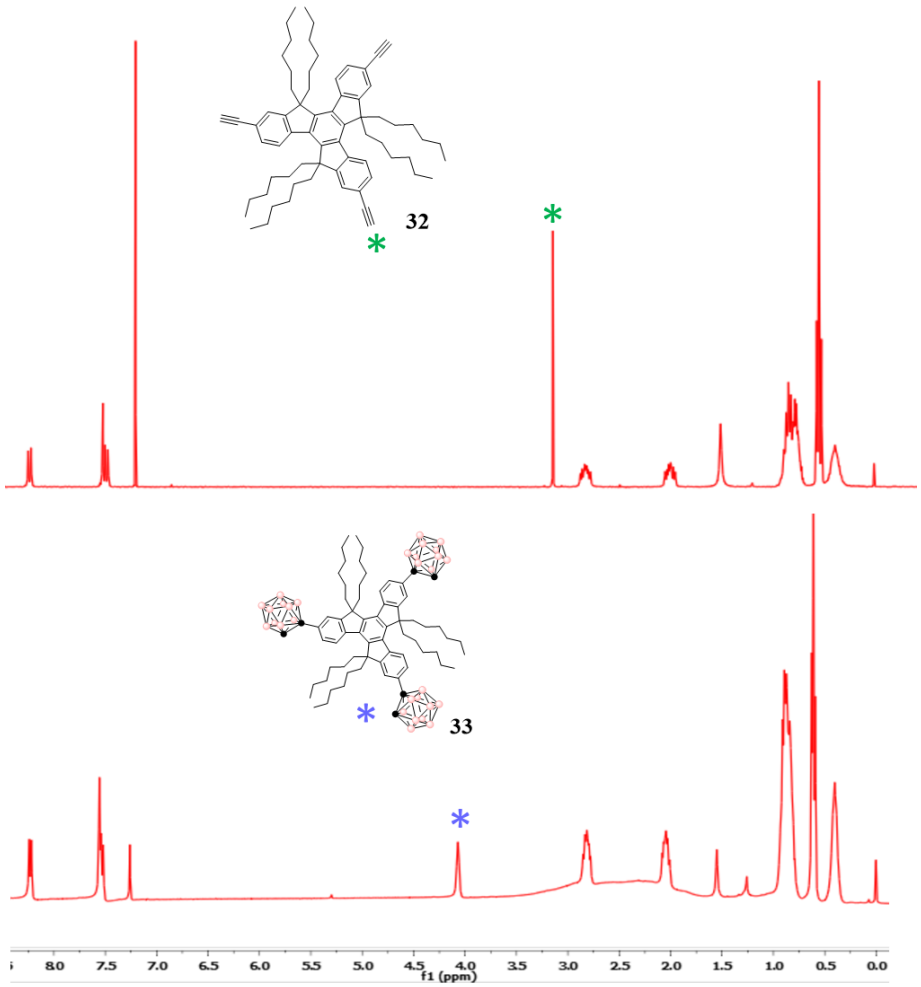

Figure 6.3. Comparison of ^{1}H NMR spectra of **32** and **33** in $CDCl_3$

Therefore, other than the disappearance of resonances from acetylenic proton, the appearance of peaks due to protons attached to the C_c atoms and the broad band due to the B-H protons, we do not see any other significant change in the chemical shift of ^1H NMR spectra for **30** and **33** with respect to their precursors. Thus, we can conclude that insertion of *o*-carborane clusters does not have a distinct effect on aromatic or aliphatic protons of the core tri-branched fluorene and truxene structures.

Furthermore, the $^{13}C\{^1H\}$ NMR spectra of **29** shows $C{\equiv}CH_3$ resonance at δ 84.67 ppm and for **32** the peaks appear at δ 83.45 ppm and 84.37 ppm (see spectra in Annex of Chapter 6). These compounds show aromatic resonances in a similar range from δ 119.95 to 153.63 ppm, wherein the number of aromatic carbon peaks is higher in **29** than in **32**. Just as the aromatic region, the aliphatic carbon atoms in both acetylene precursors appear in the region δ 13.81 - 55.89 ppm, with slight upfield shift in case of **29** by 0.35 ppm. In Figure 6.4, the $^{13}C\{^1H\}$ NMR spectra for carboranyl derivatives **30** and **33** are represented. In the spectra we have indicated resonances assigned to the *C*c-H carbon atoms from the *o*-carborane clusters at around 60 ppm. On the other hand, the disappearance of resonances from the $C{\equiv}CH_3$ also confirms the formation of the *o*-carborane clusters. No other differences in resonances from the other carbon atoms with respect to the precursors are observed.

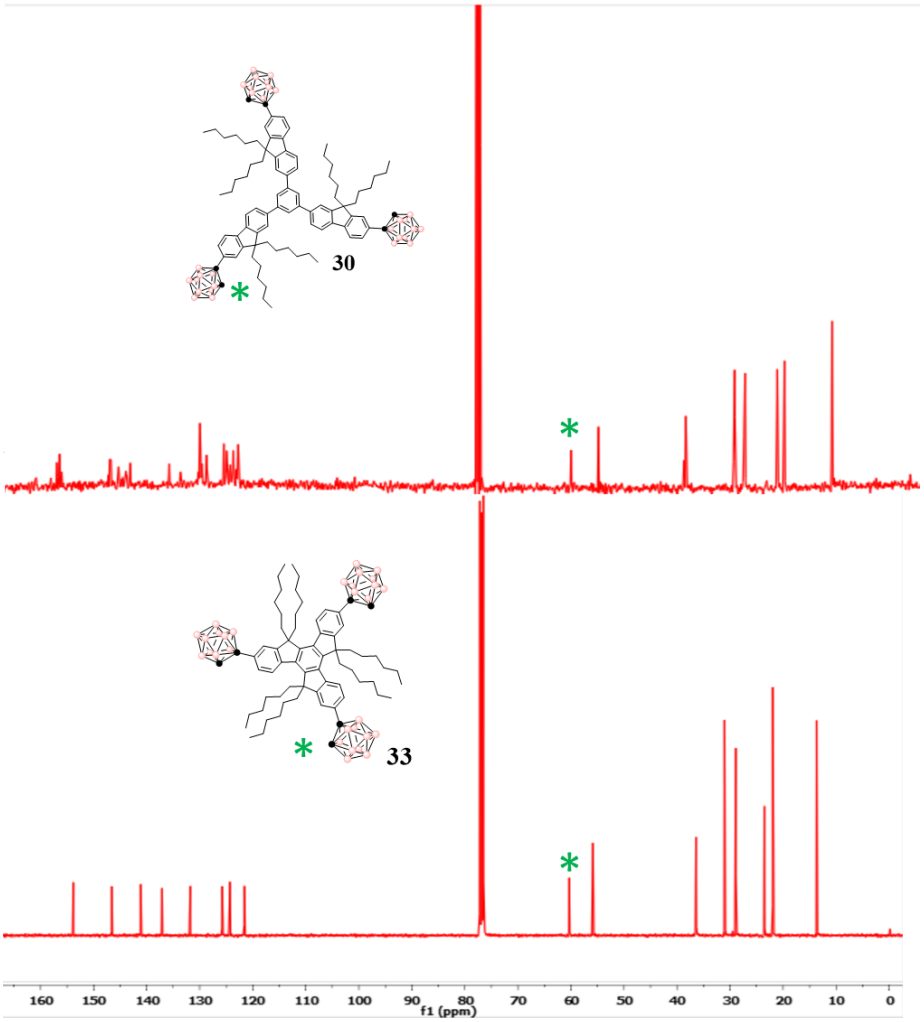

Figure 6.4. $^{13}C\{^{1}H\}$ NMR of *o*-carborane containing 1,3,5-tris(7-ethynyl-9,9-dihexyl-9H-fluoren-2-yl) benzene **30** and *o*-carborane containing triethynylhexahexyltruxene **33**

Finally, to confirm the incorporation of *o*-carborane clusters at the terminals of tri-branched structures **30** and **33**, we performed and analysed the final *o*-carborane containing compounds by $^{11}B\{^{1}H\}$ NMR. The resonances of characteristic *closo* region appeared from δ -1.89 to -10.55 ppm for **30** (Figure 6.5) and δ -1.84 to -10.62 ppm for **33** (annex

chapter 6), showing a general pattern of 2:4:4, which is usually for mono-substituted *o*-carborane units. Notably, one of the key confirmations for this kind of reactions that involves the formation of *o*-carborane derivatives is $^{11}B\{^{1}H\}$ NMR spectra and these observations clearly indicate the presence of *o*-carborane clusters at the terminal of the molecules.

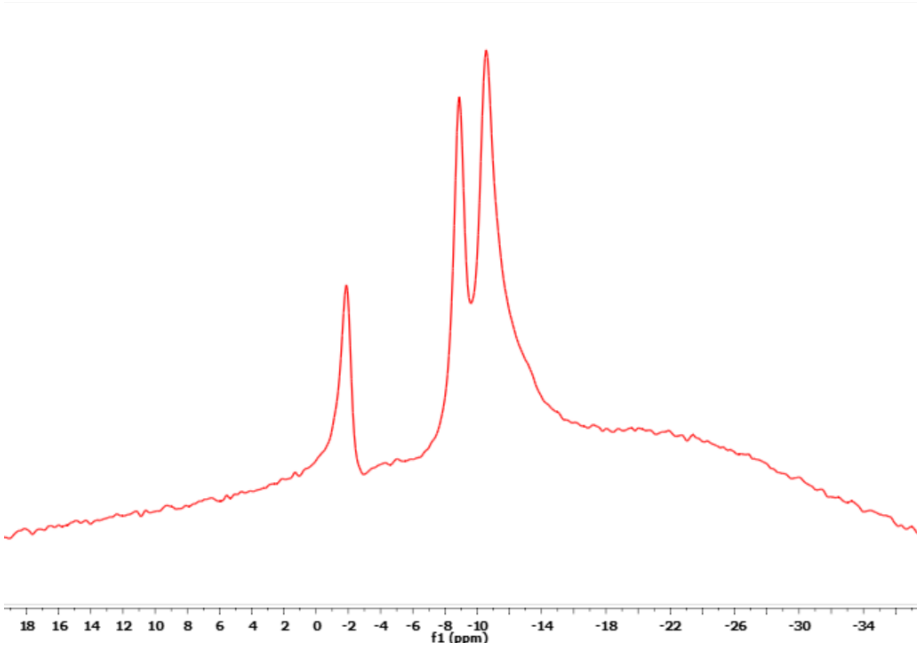

Figure 6.5. $^{11}B\{^{1}H\}$ NMR of *o*-carborane containing 1,3,5-tris(7-ethynyl-9,9-dihexyl-9H-fluoren-2-yl)benzene **30**

6.2.3. Photophysical properties in solution, aggregation and thin films

Since there is a limited investigation on the photo-physics and donor-acceptor behaviour of *o*-carborane containing tri-branched fluorene and truxene systems, a more detailed investigation was carried out starting from the photophysical properties of compounds **29**, **30**, **32** and **33** in

different states: solution, aggregation, solid and thin films. Further, the study of energy levels (HOMO and LUMO) were performed, which was also supported by cyclic-voltammetry analysis (Section 6.2.4) and DFT calculations (Section 6.2.5).

The UV-vis absorption of **29**, **30**, **32** and **33** shown in Figure 6.6 clearly depicts that incorporating *o*-carborane clusters into the backbone of π-conjugated tri-branched system leads to a hypsochromic shift (or blue-shift) with lower absorption values (by ~5-9 nm), molar extinction coefficient values (ε) (Table 6.1) and absorption onset values (λ_{onset}). Although not a very dramatic blue-shift but still this is indicative of the fact that there is a characteristic decrease in conjugation of the final compounds **30** and **33** from their starting acetylene precursors. To validate this argument, we calculated the HOMO and LUMO energy levels from onset of electrochemical oxidation or E_{ox} of the acetylene precursors (**29** and **32**) and *o*-carborane derivatives (**30** and **33**) *(vide infra).*

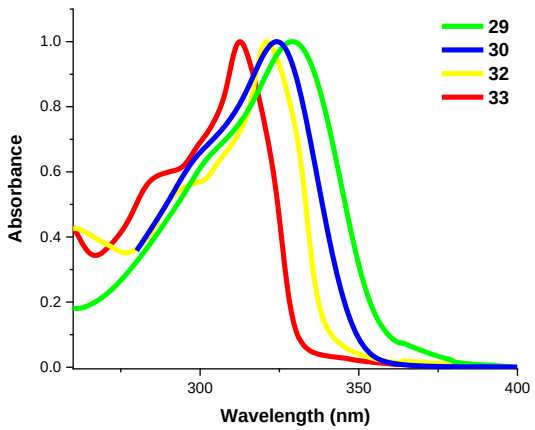

Figure 6.6. Normalised absorption spectra of acetylene precursors (**29** and **32**) and *o*-carborane containing compounds (**30** and **33**)

Table 6.1. Photophysical study of compounds **29,30,32** and **33**

S. No.	Abs		λ_{em}[a] (nm)	Φ_{PL}[a]	λ_{em}[b] (nm)	Φ_{PL}[b]	λ_{em}[c,d] (nm)	Φ_{PL}[c,d]
	λ_{abs}[a](nm)	$\varepsilon/10^6$*						
29	330	0.929	370	0.84	370, 386	0.55	408, 430	0.15
30	325	0.629	363, 590	0.09	375, 512	0.04	410, 493	0.05
32	321	1.189	370, 387	0.36	369, 387	0.29	387, 468	0.14
33	312	0.988	361, 376, 560	<0.02	363, 518	0.04	518	0.05

[a]THF solutions (3.0 x 10^{-5} M for **30** and **33** and 1 x 10^{-7} M for **29** and **32**), [b]in aggregate state (THF/H_2O = 1/99 (v/v)), [c]thin films prepared by spin-coating of THF solutions on Spectrosil B quartz substrates, [d]absolute Φ_{PL} from the integrating sphere. *$M^{-1}\cdot cm^{-1}$.

Photoluminescence (PL) studies in solution (THF) has been carried out for all the compounds, where we can observe a slight blue-shift of fluorescence emission maxima in case of *o*-carborane derivatives **30** compared to **29**, and for compound **33** with respect to **32** (Figure 6.7 and Table 6.1).

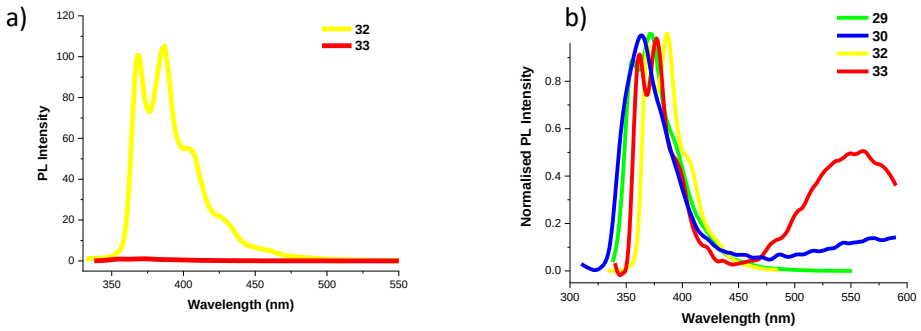

Figure 6.7. (a) PL emission spectra of **32** and **33**; (b) Normalised PL emission spectra of acetylene precursors (**29** and **32**) and *o*-carborane containing compounds (**30** and **33**) in THF

9,10 diphenylanthracene in cyclohexane was considered as the standard to calculate the Φ_{PL} values of all the compounds. As expected, a severe quenching in fluorescence emission for *o*-carborane derivatives ($\Phi_{PL} \leq$ 0.10) takes place as it is observed in Figure 6.7a. As seen earlier, the fluorescence quenching in solution is a common phenomenon when *o*-carborane units are directly attached to the fluorophores without any spacer.[12] Apart from quenching in fluorescence, a small gaussian curve was observed (Figure 6.7b) due to the intramolecular charge transfer (ICT) character of *o*-carborane units which is usually predominant in these types of systems. Although, majorly observed charge-transfer process was local emission (LE) in solution at room temperature with a trace amount of ICT in **30** and **33**.

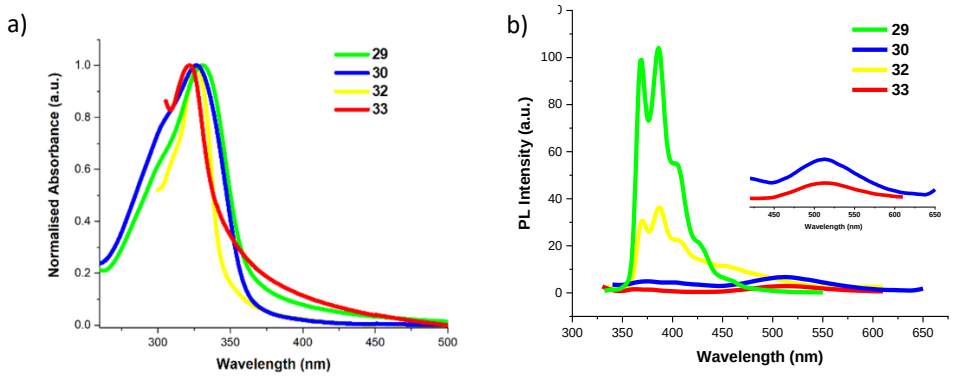

Figure 6.8. (a) Normalised absorption spectra of **29, 30, 32** to **33** in THF:H_2O (1/99, v/v). (b) PL emission spectra of acetylene precursors **29, 30, 32** to **33** in THF:H_2O (1/99, v/v)

Then we moved to photophysical studies in aggregation state, where the solution of compounds **29, 30, 32** and **33** were prepared considering a good solvent (THF) and a poor solvent (H_2O) which were miscible. A mixture of THF:H_2O (1/99, v/v) was selected and the observed maxima

absorption values (Figure 6.8a) of all the compounds were in a similar range starting from 322 nm to 330 nm.

As shown in Figure 6.8b, the fluorescence emission spectra of *o*-carborane based compounds (**30** and **33**) showed a second emission band in the 450-700 nm range. The fluorescence emission values (LE type emission bands) for aggregation state of all the compounds either remained the same or experienced a slight red-shift from that of the solution state. However, this large gaussian shape band at around 512 and 518 nm for **30** and **33** respectively, whose contribution is more significant than their locally excited (LE) type emission bands, appears sensitive towards formation of aggregation and solvent polarity. Thereby, this suggests an intramolecular-charge transfer (ICT) type behavior, which is commonly observed when *o*-carborane is involved in a system. In this case, we observe an ICT behavior predominantly in **30** and **33**, giving us a clue about the electron-withdrawing nature of *o*-carborane and its contribution at the LUMO energy level (see section 6.2.5, Tables 6.5 and 6.6). Unfortunately, the Φ_{PL} values (0.04) for *o*-carborane containing final compounds **30** and **33** are almost negligible in aggregation state suggesting that the aggregation-induced emission (AIE) phenomenon is not relevant. For their corresponding tri-branched acetylene precursors **29** and **32** (Table 6.1), decreased Φ values have been observed with regards to the solution state, which as we know suggests the general idea of fluorophores directly attached to an electron-withdrawing group (acetylene), undergoes rapid charge transfer from fluorophore to electron-withdrawing fragment exhibiting a quenching in fluorescence emission in aggregation.[13,14]

Figure 6.9. (a) Preparation of thin-films by spin-coating technique on Spectrosil B quartz substrates using compounds in THF, conc. 10^{-3} M. (b) PL emission spectra of acetylene precursors (**29** and **32**) and *o*-carborane containing compounds (**30** and **33**) in thin-films.

Finally, thin-films were prepared by using spin-coating technique of THF solutions (10^{-3} M) on Spectrosil B quartz substrates for all the compounds (Figure 6.9a). Taking a clue from the aggregation state of fluorescence emission values (λ_{em}), which were seen to be slightly red-shifted (in some cases) we can say that the λ_{em} values have considerably red-shifted from that of solution and aggregation state, whereas the λ_{abs} values remained the same as aggregation state (322 nm to 330 nm) (Table 6.1). Due to the absence of AIE effect, the compounds exhibited low to negligible Φ_{PL} values (0.03 to 0.14). Out of all, **29** and **32** appear to be comparatively more fluorescent than their *o*-carborane derivatives **30** and **33** (Figure 6.9b) due to the usual vibronic structures of star-shaped fluorene and truxene based acetylene derivatives in thin films.[11]

One interesting fact observed for fluorescence emission spectra of **30** and **33** in aggregation and thin films is the presence of broader gaussian bands in the longer wavelength region which was majorly observed unlike in solution phase where a trace amount of ICT was observed.

6.2.4. Electrochemical analysis (cyclic voltammetry)

The electrochemical properties of tri-branched fluorene and truxene systems (**29, 30**, **32** and **33**) were investigated by cyclic voltammetry (CV) (Figure 6.10). This method was used to calculate HOMO energies from E_{onset} (Table 6.2) and LUMO energy levels were then derived from the optical band gap (in eV) determined from the UV-Vis results.

Table 6.2. Onset redox potentials, HOMO/LUMO energies and band gaps of **29** to **30** and **32** to **33**

Sample	λ_{onset} (nm)	Band gap (eV)	E_{ox} (V)	HOMO/LUMO (-eV)
29	346	3.58	1.25	6.05/2.47
30	336	3.69	1.29	6.09/2.40
32	358	3.46	1.28	6.08/2.62
33	348	3.56	1.33	6.13/2.57

[a] CV determined from onset of E_{ox} relative to (Fc^+/Fc) with known HOMO energy level = 4.8 eV. Onset potentials (V vs Ag/AgCl) from E_{red} and E_{ox} .

Therefore, estimated equations: HOMO energy level = -[E_{ox} + 4.8(vs Ag/AgCl)-E_{ox}(Fc)]eV or HOMO = -4.8- E_{ox} (eV), where F_c is ferrocene and LUMO energy level has been derived from optical band gap (Table 6.2).

The four compounds **29**, **30**, **32** and **33** showed a similar oxidation characteristic with quasi reversible oxidation wave at +1.25, +1.29, +1.28, +1.33 V, respectively (Figure 6.10). Also, the oxidation of *o*-carborane derivatives shifted towards positive potentials by 40 to 50 mV, this could be due to the slightly higher electron-withdrawing character of covalently bonded *o*-carborane clusters in **30** and **33** than their corresponding precursors **29** and **32**.

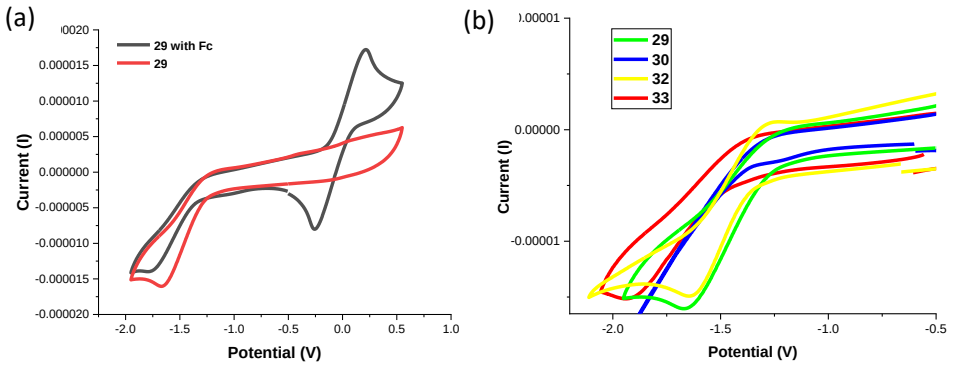

Figure. 6.10. (a) Cyclic voltammetry of **29** and **29** with Fc (1x10^{-3} M), Fc is used as an internal reference for all the compounds. (b) Comparative CV of acetylene precursors (**29** and **32**) and *o*-carborane containing compounds (**30** and **33**) using DCM:ACN (0.5:1), 0.1 M Bu_4NPF_6 supporting electrode with scan rate 100 mV s-1 at r.t.

In fact, as observed earlier from the UV-Vis absorption spectra in solution, there has been a blue-shift in the absorption values from **29** to **30** and **32** to **33**, suggesting shorter conjugation length. Further, values in Table 6.2 support the fact that a slight increase in the band gaps of *o*-carborane derivatives have been noticed experimentally from CV. Therefore, a comparison of HOMO and LUMO energy levels of **30** and **33** derived from CV further supports the argument of decrease in effective π-conjugation along with increase in energy of π-π^* transition of molecules. This is also in accordance with the well-established simple relation of Kohler and Woehl[15] which is:

$$E_g = a + b/l_c$$

Where, a = energy gap for infinite l_c, b = fit parameter, l_c = corresponding to number of phenyl rings.

So far, we have appreciated that the introduction of *o*-carborane moieties have not affected the tri-branched core fluorene and truxene systems to a great extent, but nevertheless it acts as an electron-acceptor group and thus we expected a higher percentage contribution of these clusters in LUMO energy levels (see Section 6.2.5) than HOMO energy levels. DFT calculations, in particular Table 6.5 to 6.8 reaffirms these experimental values along with TPA measurements shown in Table 6.9 (Section 6.2.6).

6.2.5. Theoretical calculations (DFT)

Our initial approach was to consider one arm of these tri-branched systems (**29** and **30**) and optimize as well as compute their UV spectrum both at ground state and first excited state where CAM-B3LYP/6-31G*[16] function was employed using THF as solvent. We also investigated the Stoke shift of the one arm systems containing *o*-carborane based π-conjugated systems as well as their precursors using above-mentioned computation and these values were then compared to experimental tri-branched systems (obtained from UV-Vis spectra).

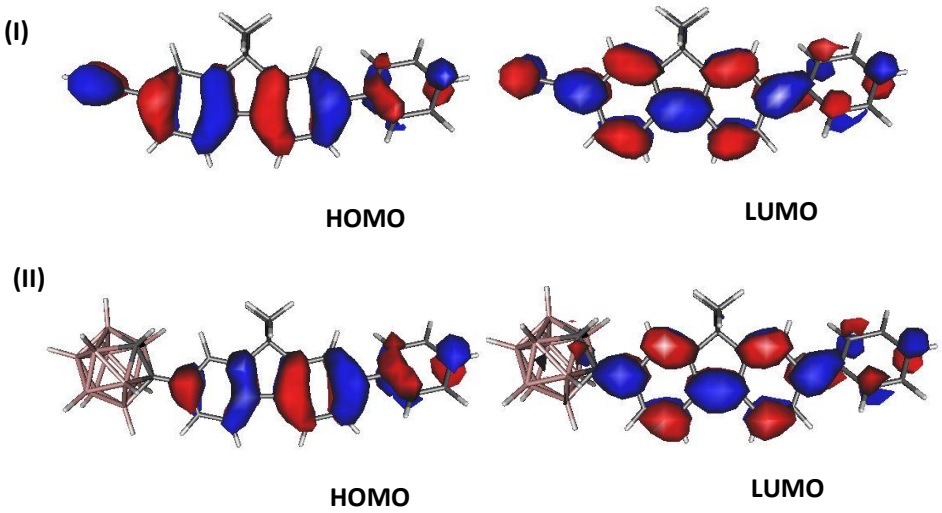

Figure 6.11. Electron-density distribution of first excited state frontier molecular orbitals of the structures, **I** and **II** computed by CAM-B3LYP/6-31G*[16] functions using THF

Since, it was difficult to compute the UV-Vis spectra of tri-branched systems and transition between HOMO and LUMO therefore we considered the computation of one-arm systems. First, we noticed the experimental Stoke shift values from acetylene precursors (**29** and **32**) to the systems containing *o*-carborane (**30** and **33**) were almost similar, which was also proved to be correct using Born-Oppenheimer approximation and DFT calculations, in Figure 6.12 and Table. 6.3. For instance, the experimental Stoke shift for tri-branched systems i.e., **30** is equivalent to 39 nm or 3276.08 cm^{-1} and for **33** it is 40 nm or 3296.46 cm^{-1}, whereas the theoretical values were calculated for (**I** and **II**) as 81 nm or 7088.97 cm^{-1} and 7189.79 cm^{-1} respectively (Table 6.3). So, the Stoke shift values in theoretical calculations were much higher for one-arm systems than in experimental values for tri-branched systems.

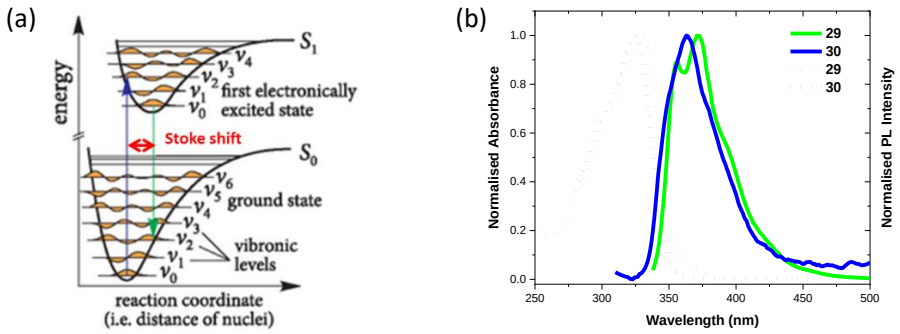

Figure. 6.12. (a) Born-Oppenheimer approximation; (b) Experimental Stoke shift using normalized absorption and emission spectra of **29** and **30**

Table 6.3. Computed λ_{max} values in nm from DFT calculations using CAM-B3LYP/6-31G* geometries at their ground state (S_0) and first excited state (S_1) fully optimised in THF to calculate theoretical Stoke shift values of (a) and (b), comparing with the experimental Stoke shift values of **29** and **30**

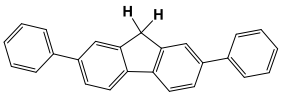

(I)

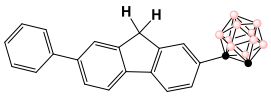

(II)

Optimised structures	**λ_{max} (nm) G. state**	**λ_{max} (nm) Ex. state**	**Stoke shift (nm)**	**Stoke shift (eV)**	**Stoke shift (cm^{-1})**
(I)	301	382	81	0.8789	7088.97
(II)	298	379	81	0.8914	7189.79
Exp. Structures	**λ_{max} (nm) abs**	**λ_{max} (nm) em**	**Stoke shift (nm)**	**Stoke shift (eV)**	**Stoke shift (cm^{-1})**
29	330	370	39	0.4061	3276.08
30	325	363	40	0.4087	3296.46

Using one-arm systems (I and II) we can try to assume a probable reason for the quenching of the fluorescence in solution state in case of **30** and

33 is the direct linkage of *o*-carborane clusters to the fluorophore, also see annex S.6.2.

Therefore, due to inaccuracy in comparison of calculated one-arm based to experimental values of tri-branched systems, finally we moved to optimising the latter systems in the ground state and calculated HOMO and LUMO energy levels of tri-branched system using CAM-B3LYP/6-31G* in THF. The theoretical band gap values were compared to the experimental band gap values from cyclic voltammetry as shown in Figure 6.13 and Table 6.4 (optimised structures of tri-branched systems are mentioned in S.6.6 to S.6.10 of annex).

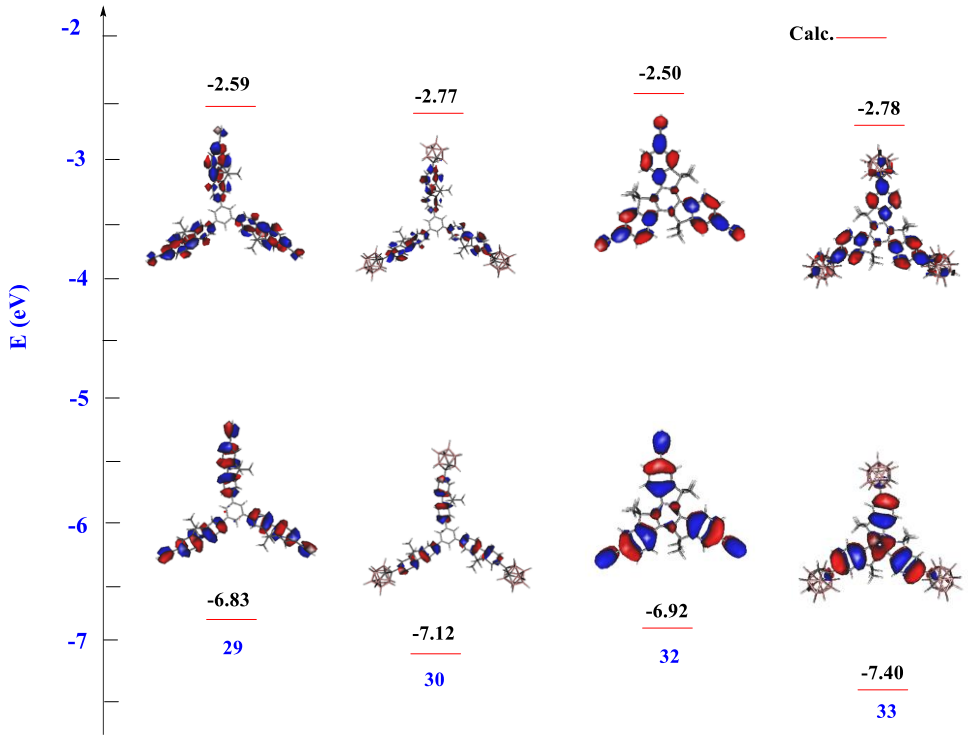

Figure. 6.13. Frontier molecular orbitals derived from DFT calculations and their energy levels for **29**, **30**, **32** and **33** of the calculated HOMO/LUMO energy levels acquired by using CAM-B3LYP/6-31G*

From the Figure 6.13, it can be suggested that the calculated HOMO and LUMO energy gap slightly increases on incorporating *o*-carborane units (at **30** and **33,** Table 6.4) from their corresponding precursors (**29** and **32**). The HOMO density distribution was mainly delocalised over fluorene and truxene core of the systems for all the compounds, whereas LUMO density distribution was located over the central fluorene and truxene with also some contribution from C atoms of *o*-carborane cages. The calculated energy levels of HOMO for all the compounds were observed from -6.83 eV to -7.40 eV. A slight decrease in LUMO energy levels from acetylene precursors to their corresponding *o*-carborane moieties was observed (decreased by 0.18-0.28 eV) due to participation of the cluster units. Therefore, the LUMO is more energetically stabilised for **30** and **33** as shown in the FMO energy diagram in Figure 6.13. A larger HOMO and LUMO gap indicates a blue shift in λ_{abs} values of 30 and 33, which is in accordance with the UV-Vis spectra, Figure 6.8 a) and Table 6.1. Thus, it can be said that introduction of *o*-carborane might lower the HOMO and LUMO energy levels in the tri-branched fluorene and truxene systems.

Now, despite of the similar pattern and behaviour observed for all the compounds experimentally matched well with theoretical studies, in the Table 6.4, it is evident that the calculated energy gap and experimental energy gap values acquired from CV measurements are different from each other. Technically, TD-DFT computations have an accuracy around 0.5 eV for big molecules with long range delocalization, therefore accurate values were not expected for these kinds of tri-branched systems.

Table 6.4. Theoretical and experimental (CV and TPA) band gap values in eV

Structures	Calculated values (eV)	Experimental values (eV)	
		CV	TPA
29	4.24	3.58	3.55
30	4.35	3.69	3.58
32	4.45	3.46	3.37
33	4.62	3.56	3.44

From the theoretical point of view, we can say that although the HOMO levels must be accessible by electrochemistry i.e., HOMO energy level values but it is difficult to predict overall band gaps values from DFT calculations and therefore cannot resemble accurately with the band gap values measured from CV for these kinds of tri-branched systems. However, the experimental band gap values obtained from CV and TPA matches well, as seen in Table 6.4.

On the other hand, using Density Functional Theory (DFT), specifically GaussSum 3.0 program [17]computational quantum mechanical modelling method, the investigation of % contribution of each fragment of the entire tri-branched systems containing *o*-carborane units were performed. C_3 symmetry was chosen for the DFT computation.

From the Tables 6.5 to 6.8, it can be observed that the HOMO, H-1 and H-2 of compounds **29** and **30** is mainly located on the 9,9'-dioctylfluorene fragment with minor % contribution of phenyl ring and for **32** and **33** on the truxene unit. The main contribution at the LUMO, L+1 and L+2 comes from these fragments (core of the fluorophore) with small contribution from *o*-carborane units for **30** and **33** i.e., 12% and 25% respectively from

L+2 energy orbitals (in this case, due to symmetrical reasons the major % contribution of each fragment was observed at H-2 and L+2 energy orbitals). Anyways, the contribution of phenyl ring at the centre of the tri-branched structure of **29** and **30** has been limited to 2% for L+2 energy orbitals.

Table 6.5. Theoretical calculation for % contribution of each fragments using GaussSum 3.0 program for the molecular orbitals of **29**

Orbitals	**phenyl(%)**	**9,9'-dioctylfluorene (%)**	**C≡C (%)**	**eV**
L+2	2	86	12	-0.07
L+1	18	74	8	-0.30
LUMO	18	74	8	-0.30
HOMO	17	73	10	-6.83
H-1	17	73	10	-6.83
H-2	2	83	15	-6.98

Table 6.6. Theoretical calculation for % contribution of each fragments using GaussSum 3.0 program for the molecular orbitals of **30**

Orbitals	**phenyl(%)**	**9,9'-dioctylfluorene (%)**	***o*-carborane(%)**	**eV**
L+2	2	86	12	-0.44
L+1	18	74	7	-0.67
LUMO	18	74	7	-0.67
HOMO	24	73	2	-7.38
H-1	24	73	2	-7.38
H-2	3	93	4	-7.61

Table 6.7. Theoretical calculation for % contribution of each fragments using GaussSum 3.0 program for the molecular orbitals of **32**

Orbitals	truxene(%)	C≡C (%)	eV
L+2	80	20	0.32
L+1	89	11	-0.27
LUMO	89	11	--0.27
HOMO	87	13	-6.92
H-1	87	13	-6.92
H-2	68	32	-7.62

Table 6.8. Theoretical calculation for % contribution of each fragments using GaussSum 3.0 program for the molecular orbitals of **33**

Orbitals	truxene(%)	*o*-carborane (%)	eV
L+2	75	25	-0.14
L+1	91	9	--0.74
LUMO	91	9	--0.74
HOMO	96	4	-7.66
H-1	96	4	-7.66
H-2	89	11	-8.66

In conclusion, the % contribution of *o*-carborane cluster is similar as for the acetylene precursor in case of **30**, however it acts as a slightly better electron-withdrawing group in case of **33** showing 25% contribution at the L+2 energy orbital level whereas in case of acetylene unit in **32** is

20%. This difference in %contribution from **30, 32** to **32** can be attempted to be explained from the optimised structures of all the compounds, shown below in Figure 6.14.

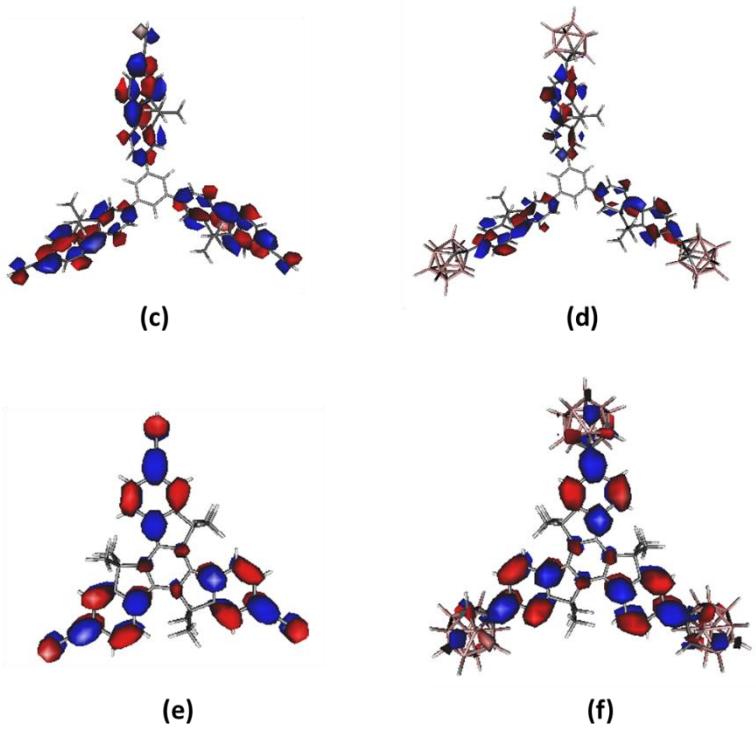

Figure 6.14. Optimised LUMO energy orbitals of the tri-branched compounds in the form of (c) to (f) using CAM-B3LYP/6-31G* in THF (refer Annex for detailed molecular orbitals at different energy levels, S.6.3 to S.6.6)

As observed in Table 6.1, the Φ_{PL} value for **33** is much lower than **30**, giving a clue that the participation of *o*-carborane is much significant in case of **33**, and in support of this DFT calculations also align well through the % contribution of *o*-carborane cluster (Table 6.8). In fact, Figure 6.7 b) the normalised fluorescence emission spectra in solution shows a higher and broader gaussion band i.e., above 500 nm indicating slightly more pronounced ICT behaviour in **33**, also confirms a higher participation of *o*-carborane units. We also tried to investigate the torsion

angle between C-C bond of cluster and directly attached fluorophore, in one arm systems (annex S.6.2) in the optimised ground state and first excited state.

Therefore, in summary we first optimised and computed one-arm systems with and without *o*-carborane units (**I** and **II**) and tried to compare the calculated Stoke shift values with the experimental Stoke shift values where we observed that the values (in cm^{-1}) from precursor derivatives (**I** and **29**) to final *o*-carborane containing derivatives (**II** and **30**) was slightly increased due to blue shift λ_{max} values in **(II)** and **30**. However, the magnitude of this energy difference in case of theoretical studies was too high and inaccurate perhaps due to two different choice of branched systems were considered (Table 6.3). Then, tri-branched systems were optimised at the ground state and HOMO/LUMO energy orbitals were derived (refer annex Figure S.6.6 to S.6.10) as well as the energy band gaps were calculated. and compared to the experimental energy band gaps (Table 6.4). Here, we observed a similar pattern in theoretical as well as experimental studies, that on incorporating *o*-carborane units, specially the LUMO energy orbitals reaches a slightly energetically stabilised level (i.e., decreased energy level), leading to an increased band gap in comparison to their corresponding precursors. Clearly, here we see the influence of *o*-carborane cluster and to reaffirm this, percentage contribution of each fragment of the tri-branched systems were investigated and we observed a relatively higher % contribution of *o*-carborane cluster in case of **33** than **30**.

6.2.6. Studies of two-photon absorption (TPA) spectroscopy

The tri-branched fluorophore systems or star-shaped π-conjugated fluorophores have drawn a special attention towards two-photon absorption applications, such as in optical materials, bioimaging and two-photon dynamic therap.[5] This prompted us to study the TPA properties of tri-branched acetylene and *o*-carborane containing compounds **29, 30, 32** to **33**. Initially, the absorption and fluorescence emission studies were done considering DCM as a solvent (Figure 6.15).

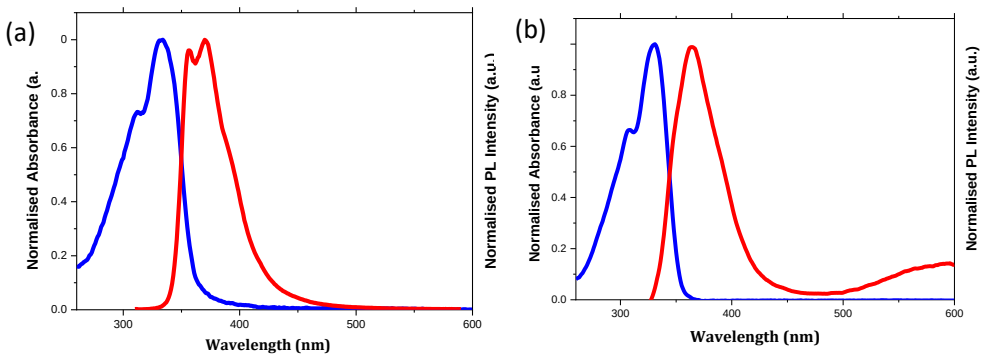

Fig. 6.15. Normalised absorption (blue) and fluorescence emission (red) spectra of **29** (a) and **30** (b)

The absorption spectrum of **29** is relatively unstructured with a λ_{max} at 334 nm and a shoulder in the high energy side of the longest wavelength absorption band. By contrast the fluorescence band is vibronically structured in DCM, which suggests a photoinduced planarization of the emitting species. Such a photophysical effect which is quite similar to that observed for oligothiophene derivatives should stem from the twist angle decrease between the central phenyl and a fluorenyl moiety. In parallel, the absorption band of **30** globally displays the same shape as that of its non-substituted homologue with a very slight blue-shift. The fluorescence band of **30** was also located at the same spectral range as that of **29** but this new band does not show any vibronic behaviour. Compound **29** is

highly emissive with Φ value of 0.64 in DCM (Table 6.9). This fluorescence quantum yield collapses by three orders of magnitude with the introduction of *o*-carborane groups at the rim of the structure.

Table 6.9. Spectroscopic data in DCM of **29, 30, 32** to **33**

Compound	λ_{abs} (nm)	λ_{fluo} (nm)	E_{gap} (eV)	Φ_{fluo}	δ_{2PA}(GM)	λ_{2PA} (nm)
29	334	370	3.55	0.64	25 ± 4	680
30	328	364,593	3.58	0.002	-	-
32	331	368	3.37	0.33	14 ± 3	700
33	320	361,571	3.44	0.0012	-	-

Due to the rigidity of its expanded aromatic core, both absorption and fluorescence spectra of **32** are strongly structured with maxima located at 331 nm and 368 nm respectively (Table 6.9). Interestingly, the fluorescence band exhibits a clear mirror image relationship with a weakly intensive absorption band located at the red edge of the absorption spectrum (Figure 6.16). This very weak absorption band should correspond to the S_0-S_1 transition. Compound **32** is emissive with Φ of 0.33 in DCM and, like the compound **30**, the introduction of *o*-carborane moieties lead to a severe loss in emission with a Φ of about 10^{-3}. Consequently, presence of *o*-carborane allows the new non-radiative deactivation channels at singlet excited state.

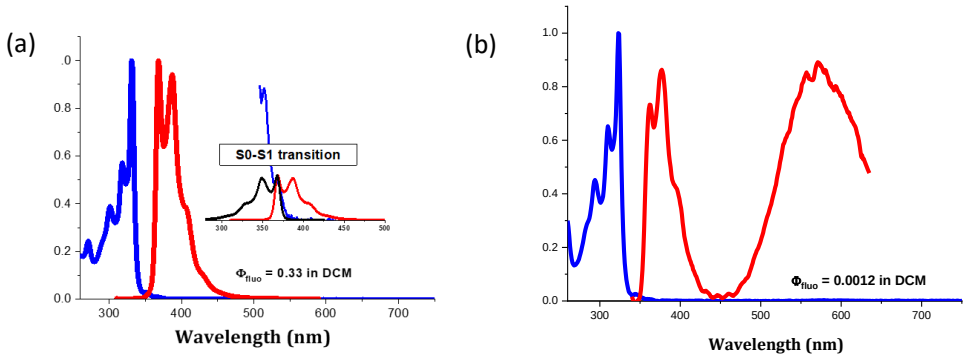

Figure 6.16. Normalised absorption (blue) and fluorescence emission (red) spectra of **32** (a) and **33** (b) in DCM.

As seen earlier, in the case of fluorescence emission spectra of aggregation state, both carborane-based derivatives show a second emission band in the 450-750 nm range, which resembles gaussian shape and thus we might be able to confirm that this is due to sensitivity towards solvent polarity (Figure 6.17). This large gaussian shape band whose weighted contribution is more significant for compound **33** seems sensitive to solvent polarity which thereby suggests an emission process from a charge transfer species. These results also match well with theoretical calculations.

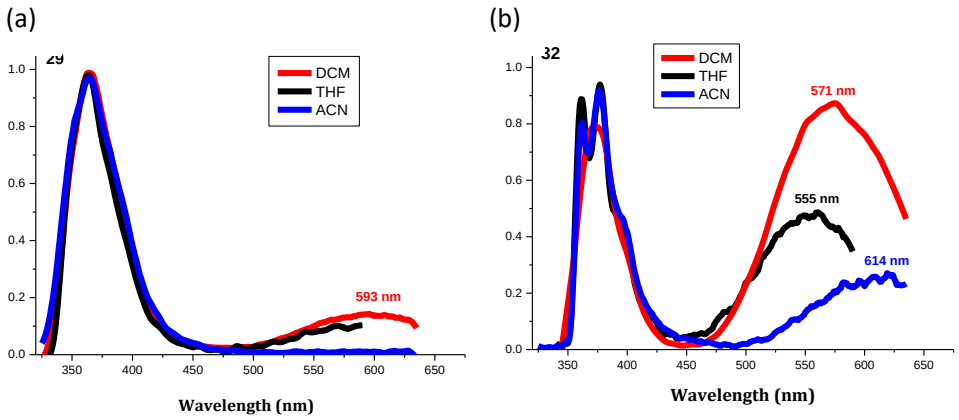

Figure. 6.17. Normalised fluorescence emission spectra of **30** (a) and **33** (b) in DCM, THF and ACN

Unfortunately, due to the very weak emissivity of **30** and **33** in DCM, it was not possible to record any TPA spectra. The TPA spectra of compounds **29** and **32** are presented in Table 6.6 (note that the λ axis of TPA spectra are divided by two in order to allow a direct comparison with the 1PA spectra). The TPA band reasonably matches the 1PA one (Figure 6.18). For compound **29**, the main 1PA band should mainly correspond to the S_0-S_1 transition which is TPA allowed. For compound **32**, we also confirm that the S_0-S_1 transition corresponds to the red-edge of the 1PA band. For both derivatives, the TPA cross-sections are relatively low with values of ~ 25 GM for **29** and ~ 14 GM for **32**.

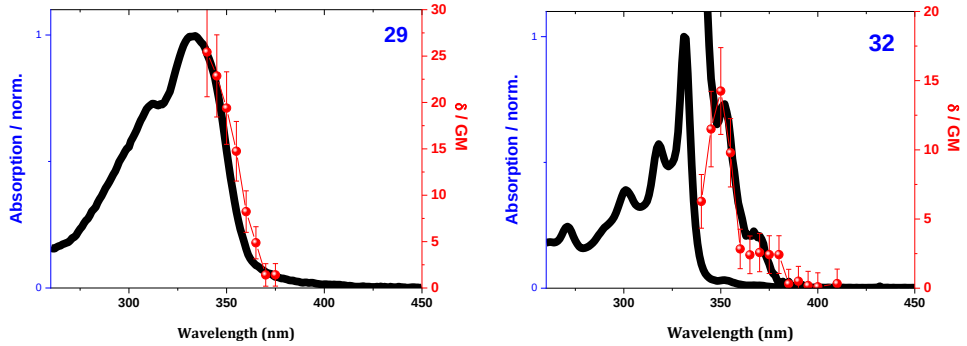

Figure 6.18. Two-photon absorption spectra of **29** and **32** in DCM

6.3. Conclusions

Synthesis of truxene and tri-branched 9,9´-dioctylfluorene based acetylene fluorophores and their *o*-carboranyl derivatives, as well as their characterization (FT-IR, ^{1}H, ^{11}B{^{1}H} and ^{13}C{^{1}H} NMR spectroscopic techniques) were performed. The final new compounds were obtained by insertion reaction using decaborane, a Lewis base and by optimising reaction conditions. Finally, the optical properties were studied in solution, aggregation state and thin films. The photophysical results showed a significant quenching in fluorescence quantum yields in solution due to direct linkage of three *o*-carborane units to the highly luminescent fluorophores, which was also supported by theoretical calculations. Having said that, in aggregation and thin films we did not see AIE in final compounds (**30** and **33**), however we saw the presence of broad gaussian emission bands in a longer wavelength region, which could be due to ICT behaviour and changes in dipole moment with solvent polarity and formation of aggregates. Slightly higher band gap values were obtained on incorporation of *o*-carborane units as observed

experimentally through cyclic voltammetry analysis. This proves an influence of carborane clusters in the tri-branched systems.

Further, the % contribution of clusters in LUMO was confirmed by DFT calculation, where the *o*-carborane participation in L+2 energy orbitals was greater in **33** than **30**. This slightly higher % contribution could also explain the increased fluorescence quenching in solution of **33**.

The *o*-carborane compounds did not show TPA, whereas the precursors **29** and **32** showed weak TPA properties, probably due to the structural arrangement of the star shaped fluorophore system in our case.

6.4. References

[1] (a) A. R. Davis, J. J. Peterson, K. R. Carter, *ACS Macro Lett.*, 2012, 1, 4, 469–472; (b) T. O B Olusanya, G. Calabrese, D. G Fatouros, J. Tsibouklis, J. R Smith, *Biophys Chem* 2019, 247, 25-33; (c) A. F.-Ugalde, A. G.-Campo, C. Viñas, J. R.-Romero, R. Santillan, N. Farfan, R. Sillanpää, A. S.-Pedrares, R. Nuñez, F. Teixidor, Chem. *Eur. J.* 20, 32, 9940-9951.

[2] J. Ochi, K. Tanaka, Y.Chujo, *Dalton Trans.,* 2021, 50, 1025

[3] X. Wu, J. Guo, Y. Lv, D. Jia, J. Zhao, H. Shan, X. Jina Y. Maa, *Mater. Chem. Front*., 2020, 4, 257-267.

[4] J. Ochi, K. Tanaka, Y. Chujo, *Angew. Chem. Int. Ed.* 2020, 59, 9841–9855.

[5] L. Zhu, W. Lv, S. Liu, H. Yan, Q. Zhao, W. Huang, *Chem. Commun*., 2013**,** 49**,** 10638-10640.

[6] M. A. Albota, C. Xu, W. W. Webb, *Applied Optics*, 1998, 37, 7352-7356.

[7] F. Teixidor, G. Barberà, A. Vaca, R. Kivekäs, R. Sillanpää, J. Oliva, C. Viñas *J. Am. Chem. Soc.* 2005, 127, 29, 10158–10159

[8] A. V. Puga, F. Teixidor, R. Sillanp, R. Kiveks, M. Arca, G. Barber, C. Viñas, *Chem. Eur. J.* 2009, 15, 9755 – 9763.

[9] A. I. Kovalev, A. V. Shapovalov, E. V. Sukhorukova, A. M. Sergeev, A. S. Peregudov, A. L. Rusanova, I. A. Khotinaa, *Mendeleev Commun.,* 2011, 21, 9–11.

[10] (a) A. H. Abdourazak, Z. Marcinow, A. Sygula, R. Sygula, P. W. Rabideau, *J. Am. Chem. Soc.* 1995, 117, 6410– 6411; (b) E. V. Demlow, T. Kelle, *Synth. Commun.* 1997, 27, 2021–2031; (c) M. J. Plater, M. Praveen, A. R. Howie, *J. Chem. Res.* (S) 1997, 46–47; *J. Chem. Res.* (M) 1997, 0430–0436; (d) B. G.-Lor, Ó. Frutos, A. M. Echavarren, *Chem. Commun.* 1999, 2431–2432; (e) B. G. Lor, E. G. Cantalapiedra, M. Ruiz, Ó. Frutos, D. J. Cárdenas, A. Santos, A. M. Echavarren, *Chem. Eur. J.* 2004, 10, 2601–2608.

[11] A. L. Kanibolotsky, R. Berridge, P. J. Skabara, I. F. Perepichka, D. D. C. Bradley, M. Koeberg, *J. Am. Chem. Soc.*, 2004, 126, 13695–13702.

[12] S. Sinha, Z. Kelemen, E. Hümpfner, I. Ratera, J. P. Marval, J. P. Jurado, C. Viñas, F. Teixidor, R. Núñez, *Chem. Commun.*, 2022, **58**, 4016–4019

[13] Y. Hong, JWY. Lam, BZ. Tang, *Chem Soc Rev* 2011, 40, 5361-88

[14] S.W. Thomas, G.D. Joly, TM. Swager, *Chem Rev* 2007, 107, 1339-86

[15] B. E. Kohler, J. C. Woehl*, J. Chem. Phys.* 103, 14, 1995

[16] T. Yanai; D. P. Tew, N. C. Handy, *Chem. Phys. Lett.* 2004, 393, 51–57.

[17] N. M. O'Boyle, A. L. Tenderholt, K. M. Langer, *J. Comput. Chem*., 2008,29, 839.

Chapter 7

Conclusions

The present study increases the diversity of carborane-based fluorphores in which the carborane is linked π-aromatic groups. Thanks to the unique properties of *o*-carborane cluster, a diversified photo-physics of this kind of systems in different states was observed, which could trigger important applications in the field of biomedicine and optoelectronics.

In Chapter 3, a well-engineered architecture based on *o*-carborane-containing fluorophores as good light emitters both in solid state and in aqueous medium as nanoparticles have been prepared.. As a proof of concepts, a preliminary study was performed by using one of the high luminescent fluorene derivatives in thin films for inkjet printing. Further, the nanoparticles when deposited on thin films retained the quantum yield efficiency, suggesting its fluorescent tunable properties in solid state and thin films. This could enable different opportunities for this kind of system in biomedicine and optoelectronic devices.

In Chapter 4, the work highlights the significance of styrene-containing carboranyl-BODIPY systems synthesized by Pd-catalyzed Heck coupling reaction. All the final compounds were fully characterized, further the photophysical study where the absorption and emission patterns were contemplated with the help of DFT studies, these were in accordance with experimental values with regards to energy transitions (S_0 and S_1 states) from HOMO to LUMO and coplanarity. Therefore, these systems have the ability to highlight their fluorescence properties, which is useful for bioimaging applications.

In Chapter 5, it can be concluded that the incorporation of *o*-carborane units did not affect the excellent fluorescence quantum yield of PDI derivatives in solution. In fact, the incorporation of clusters improved the solubility in organic solvents to a great extent. This led to further photophysical studies in aggregation, solid and micro/nanostructures, but due to excimer formation, a fluorescence quenching was observed. However, this work allows solution state and nanoparticles of *o*-carborane appended compounds to further explore in confocal imaging due to the high water-dispersibility, respectively.

In the Chapter 6, the synthesis, characterization and in details photophysical studies of newly developed *o*-carborane directly attached to tri-branched donor acceptor systems enabled a new pathway for these kind of C_3 symmetric systems containing carborane clusters (without spacer), which has not been investigated enough. The two-photon absorption (TPA) properties was unfortunately negligible for the final *o*-carborane systems but further research will be done in order to improve the structural configuration of these tri-branched system for them to be active TPA candidates.

Annex

Annex- Chapter 3

1. Experimental section:

Instrumentation. Elemental analyses were performed using a Carlo Erba EA1108 microanalyzer. ATR-IR spectra were recorded on JASCO FT/IR-4700 spectrometer on a high-resolution. ^{1}H NMR, ^{11}B NMR, $^{11}B\{^{1}H\}$ NMR and $^{13}C\{^{1}H\}$ NMR spectra were recorded on a NMR-FT Bruker 400 MHz spectrometer using deuterated acetonitrile (CD_3CN) at 25 ºC. Chemical shifts are reported in ppm and referenced to the residual solvent peak for ^{1}H and $^{13}C\{^{1}H\}$ NMR or to $BF_3{\cdot}OEt_2$ as an external standard for ^{11}B and $^{11}B\{^{1}H\}$ NMR. Chemical shifts are reported in ppm and coupling constants in Hertz. Multiplets nomenclature is as follows: s, singlet; d, doublet; t, triplet; br, broad; m, multiplet.

The UV-Vis spectra were recorded on a JASCO V-780 UV-Visible/NIR spectrophotometers, using spectroscopic grade THF (Sigma-Aldrich), in normal quartz cuvette having 1 cm path length, for different solutions for each compound in the range 10^{-4} to 10^{-5} M in order to calculate the molar extinction coefficients (Φ) were run on a with a quartz cell having a path length of 1 cm in the range of 190-600 nm. Solid-state electronic spectra were run on a JASCO V-780 UV-Visible/NIR spectrophotometer equipped with a 60 mm integrating sphere model ISN-901i/A001461872. The fluorescence emission and excitation spectra for all samples in solution were recorded in a VARIANT Cary Eclipse Fluorescence spectrometer. No fluorescent contaminants were detected on excitation in the wavelength region of experimental interest. The fluorescence quantum yields were determined by the “single point method” and repeated three times with

similar optical density for reproducibility, against quinine sulfate in 0.5 M aqueous sulfuric acid with Φ_F = 0.54 as a standard. For the aggregates in THF/water (1/99, v/v) the refractive index was assumed to be that of pure water (1.33). Thin films were prepared by spin coating solutions of **9** and **11** in THF at a concentration of 15 mg·mL^{-1} on Spectrosil B quartz substrates at 3200 rpm Solid state emission and excitation spectra were run on a Nanologt Horib Jobin Yvon IHR320 fluorimeter. Quantum yields for compounds **8-13** in the solid state were measured on a Hammatsu Absolute PL Quantum Yield Spectometer C9920-02G. Images of nanoparticles were obtained from a Transmission Electron Microscope (TEM) 120 KV JEOL 1210, using ultrathin carbon film on lacey carbon support film, 400 mesh, Copper. Fluorescence images were obtained using an inverted Olympus IX70 microscope coupled with a TRITC filter cube. Particle size distribution were determined using a Zetasizer Nano ZS; Malvern Instruments.

Materials. All reactions were performed under atmosphere of nitrogen employing standard Schlenk techniques. Toluene was purchased from Merck and distilled from sodium benzophenone prior to use. Commercial grade diethyl ether, hexane, petroleum ether, *n*-heptane, chloroform and dichloromethane were used without further purification. $B_{10}H_{14}$ was supplied from KatChem Ltd. (Prague) and used as received. Di-bromo-fluorene was purchased from TCI chemicals, diiodothiophene, phenylacetylene, bis(triphenylphosphine) palladium(II)dichloride ($Pd(PPh_3)_2Cl_2$), CuI, triethyl amine, trimethylsilylacetylene were purchased from Sigma-Aldrich, diethyl sulfide and 4-butylphenylacetylene were purchased from Alfa Aesar.

General synthesis of acetylene precursors for fluorene derivatives:

The acetylene precursors for fluorene derivatives were prepared with the appropriate stoichiometric amounts of starting materials. A dry 10ml round-bottomed flask equipped with a condenser and a magnetic stirring bar was charged under nitrogen with a mixture of di-bromo fluorene derivatives, $Pd(PPh_3)_2Cl_2$ and copper iodide, toluene and TEA (v/v 1/9) were added at room temperature. The reaction mixture was allowed to stir for 30 minutes then 1.2 equivalent of 4-butylphenylacetylene was added to the resulting dark brown slurry. After the reaction was refluxed for 24 h, the volatiles were removed with rotary evaporator. The dark brown residue was washed with MeOH followed by hexane, the resultant solids were finally purified by preparative thin layer chromatography (preparative TLC), obtaining the corresponding acetylene precursors.

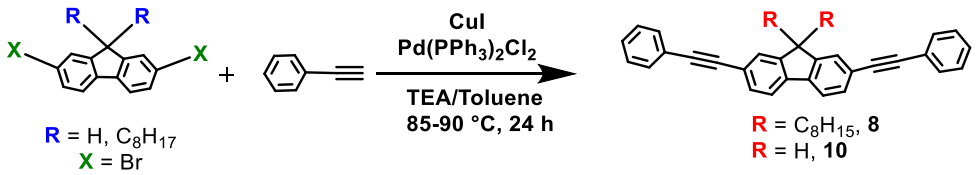

Synthesis of 9,9-dioctyl-2,7-bis(phenylethynyl)-9H-fluorene (8)

2,7-dibromo-9,9-dioctylfluorene (270 mg, 0.49 mmol), $Pd(PPh_3)_2Cl_2$ (10 mg, 0.014 mmol), CuI (6 mg, 0.032 mmol) and phenylacetylene (131 mg, 1.28 mmol) afford compound **8** as pale white solid after purification with preparative TLC (hexane/dichloromethane, 1:1). Yield: 61%. ^1H NMR ($CDCl_3$): δ 7.72 (d, J = 8 Hz, 2H), 7.65 (d, J = 8 Hz, 4H), 7.59 (d, J = 8 Hz, 5H), 7.41 (m, 7H), 2.05 (t, J = 16 Hz, 4H), 1.2 (m, 22 H), 0.89 (t, J = 18 MHz, 6H). ^{13}C NMR ($CDCL_3$): δ151.07, 140.70, 131.77, 130.77, 128.45, 126.12, 123.04, 122.03, 120.27, 90.68, 89.88, 55.42, 40.04, 31.25, 30.27, 29.33,

23.87, 22.50, 14.13. FT-IR: 2924 (str, C_{aryl}-H). Elemental analysis calcd. (%) for $C_{45}H_{50}$: C, 91.47; H, 8.52. Found: C, 90.98; H, 8.16.

Synthesis of 2,7-bis(phenylethynyl)-9H-fluorene (10)

2, 7-dibromofluorene (100 mg, 0.48 mmol), $Pd(PPh_3)_2Cl_2$ (10 mg, 0.014 mmol), copper iodide (6mg, 0.032 mmol) and phenylacetylene (90.4 mg, 0.57 mmol) afford compound **10** as pale white solid after purification with preparative TLC (eluent used 1:1 hexane and dichloromethane). Yield: 64%. ^{1}H NMR ($CDCl_3$) δ 7.78 (d, J = 8 Hz, 2H), 7.74 (s, 2H), 7.61 (s, 1H), 7.58 (d, J = 8 Hz, 4H), 7.38 (m, 5H), 3.95 (s, 2H). ^{13}C NMR ($CDCL_3$): δ 143.46, 141.14, 131.57, 130.49, 128.47, 123.32, 121.76, 120.33, 29.88, 89.59, 36.61. FT-IR: **3**056 (str, C_{aryl}-H). Elemental analysis calcd. (%) for $C_{29}H_{18}$: C, 95.05; H, 4.95. Found: C, 94.98; H, 4.86.

General Synthesis of *o*-carborane- functionalized fluorene derivatives:

The fluorene derivatives containing two *o*-carborane clusters were afforded in two steps, first adding an excess amount of diethyl sulfide (Et_2S, 5 equiv per acetylene precursor) to a toluene solution (6-8ml) of decaborane ($B_{10}H_{14}$) and a second step by adding the corresponding acetylene precursors (**8** and **10**) at room temperature. The reaction mixture was heated to reflux and the further stirred for 3 days.

Synthesis of [9,9-dioctyl-2,7-bis(phenyl)-1-o-carboran-1-yl]-9H-fluorene (9)

Decaborane (0.59 g, 4.8 mmol), Et_2S (1.2 mL, 11 mmol) and precursor **8** (1.03 g, 2.2 mmol) in toluene afforded compound **9** as a white solid. Yield: 34%. ^{1}H NMR ($CDCl_3$) δ (ppm): 7.45 (d, J = 8Hz, 6H), 7.37 (d, J = 8Hz, 2H),

7.32 (s, 2H), 7.17 (t, J = 18Hz, 2H), 7.09 (t, J = 18 Hz, 4H), 1.72 (m, 4H), 1.22 (m, 12 H), 0.97 (m, 6H), 0.90 (t, J = 18 Hz, 6H). ^{11}B NMR ($CDCl_3$, $BF_3{\cdot}Et_2O$), δ (ppm): -3.14 (br s, 2H), -10.79 (br s, 8H). ^{11}B{^{1}H} NMR ($CDCl_3$, $BF_3{\cdot}Et_2O$), δ (ppm): -2.62 (br s, 2H), -10.30 (br s, 8H) ^{13}C NMR ($CDCl_3$): δ 151.14, 141.30, 130.55, 130.12, 130.07, 128.14, 125.00, 119.91, 85.84, 85.49, 55.19. FT-IR: 3210 (str, C_{aryl}-H), 2576 (str, B-H). Elemental analysis calcd. (%) for $C_{40}B_{20}H_{70}$: C, 65.33; H, 8.53. Found: C, 65.31; H, 8.59.

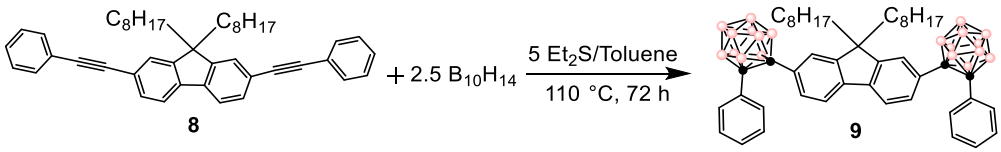

Synthesis of [2,7-bis(phenyl)-1-o-carboran-1-yl]-9H-fluorene (11)

Decaborane (0.59 g, 4.8 mmol), Et_2S (1.2 mL, 11 mmol), and precursor **10** (1.03 g, 2.2 mmol) in toluene afforded compound **11** as a white solid. Yield: 38%. ^{1}H NMR ($CDCl_3$) δ 7.59 (s, 2H), 7.45 (m, 8H), 7.21 (t, J = 18 Hz, 2H), 7.13 (t, J = 18 Hz, 3H), 3.65 (s, 2H). ^{11}B NMR ($CDCl_3$, $BF_3{\cdot}Et_2O$), δ (ppm): 1.76 (br s, 2H), -9.80 (br s, 8H). ^{11}B{^{1}H} NMR ($CDCl_3$, $BF_3{\cdot}Et_2O$), δ (ppm): -2.65 (br s, 2H), -10.68 (br s, 8H). ^{13}C NMR δ 143.63, 141.96, 130.63, 129.76, 128.30, 119.97, 85.84, 85.50, 36.62, FT-IR: 2952 (str, C_{aryl}-H), 2590 (str, B-H). Elemental analysis calcd. (%) for $C_{29}B_{20}H_{38}$: C, 57.78; H, 6.35. Found: C, 57.72; H, 6.31.

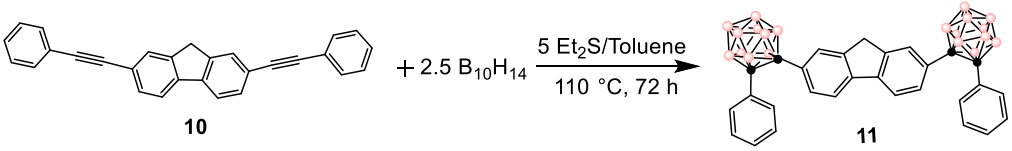

General Synthesis of acetylene precursors for thiophene derivatives:

The acetylene precursors for thiophene derivatives were prepared with the proper stoichiometric amounts of starting materials respectively. A dry 10ml round-bottomed flask equipped with a condenser and a magnetic stirring bar was charged under nitrogen with a mixture of mono-iodo or di-iodo thiophene compounds, $Pd(PPh_3)_2Cl_2$ and copper iodide, toluene and triethylamine (TEA) (v/v 1/99) at room temperature. The reaction mixture was allowed to stir for 30 minutes, then 1.3 to 2.3 equivalents of the 4-butylphenylacetylene derivatives was added to the resulting dark brown slurry containing mono-iodo or di-iodo thiophene, respectively. After, the reaction was refluxed for 24 h, the volatiles were removed with rotary evaporator. The dark brown residue was washed with MeOH followed by hexane, the resultant solids were finally purified by preparative thin layer chromatography (preparative TLC), obtaining the corresponding acetylene precursors.

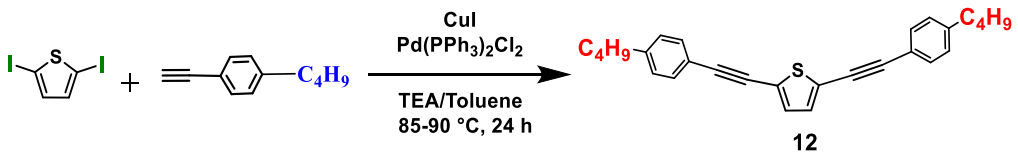

Synthesis of 2,5-bis((4-butylphenyl)ethynyl)thiophene (12)

2,5-diiodothiophene (200 mg, 0.595 mmol), $Pd(PPh_3)_2Cl_2$ (18 mg, 0.026 mmol), copper iodide (12 mg, 0.063 mmol) and 4-butylphenylacetylene (222 mg, 1.403 mmol) in 5 ml toluene/TEA mixture afforded compound **12** as pale white solid after purification with preparative TLC (eluent used 1:1 hexane and dichloromethane). Yield: 62%. ^{1}H NMR ($CDCl_3$): δ 7.48 (d, J= 8 Hz, 4H), 7.21 (d, J = 8Hz, 4H), 7.17 (s, 2H), 2.67 (t, J = 8Hz, 4H), 1.65 (m, 4H), 1.405 (m, 4H), 0.98 (t, J = 4Hz, 6H). ^{13}C NMR ($CDCl_3$): δ

144.52, 144.07, 94.11, 81.22, 35.71, 33.27, 22.44, 13.87. FT-IR: 2956 (str, C_{aryl}-H). Elemental analysis calcd. (%) for $C_{28}H_{28}S$: C, 84.79; H, 7.12. Found: C, 84.75; H, 7.16.

Synthesis of 2,5-bis((4-butylphenyl)-*o*-carboran-1-yl)thiophene (13).

To a toluene (5 mL) solution of $B_{10}H_{14}$ (200 mg, 1.636 mmol), an excess amount (Et_2S, 5 equiv per acetylene precursor, 0.4 mL, 3.725 mmol), and precursor **12** (296 mg, 0.745 mmol) at room temperature. The reaction mixture was refluxed for 3 days to afford compound **13** as white solid. Yield: 46% ^{1}H NMR ($CDCl_3$): δ ^{1}H NMR (CDCl3): δ 7.29 (d, J = 8 Hz, 4H), 7.02 (d, J = 8 Hz, 4H), 6.59 (s, 2H), 2.59 (t, J = 8Hz, 4H), 1.57 (m, 5H), 1.31 (m, 4H), 0.93 (t, J = 8Hz, 6H). ^{11}B NMR ($CDCl_3$): δ -1.88 (s, 2H), -9.78 (s, 8H). ^{11}B {^{1}H} NMR ($CDCl_3$): δ -2.46 (s, 2H), -10.34 (s, 8H). **^{13}C NMR ($CDCl_3$):** δ 145.98, 137.77, 130.86, 128.43, 127.47, 85.95, 85.94, 35.10, 35.17, 22.23, 13.91 **FT-IR:** 3191 (str, C_{aryl}-H), 2514 (str, B-H). Elemental analysis calcd. (%) for $C_{28}B_{20}H_{48}S$: C, 53.13; H, 7.64. Found: C, 53.22; H, 7.16.

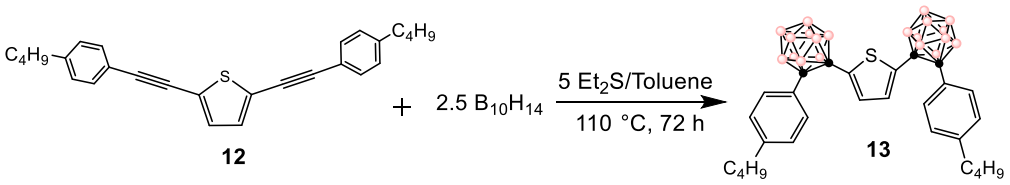

2. NMR Spectra

9,9-dioctyl-2,7-bis(phenylethynyl)-9H-fluorene (8)

Figure S1. ^{1}H NMR (400 MHz, $CDCl_3$) of **8**

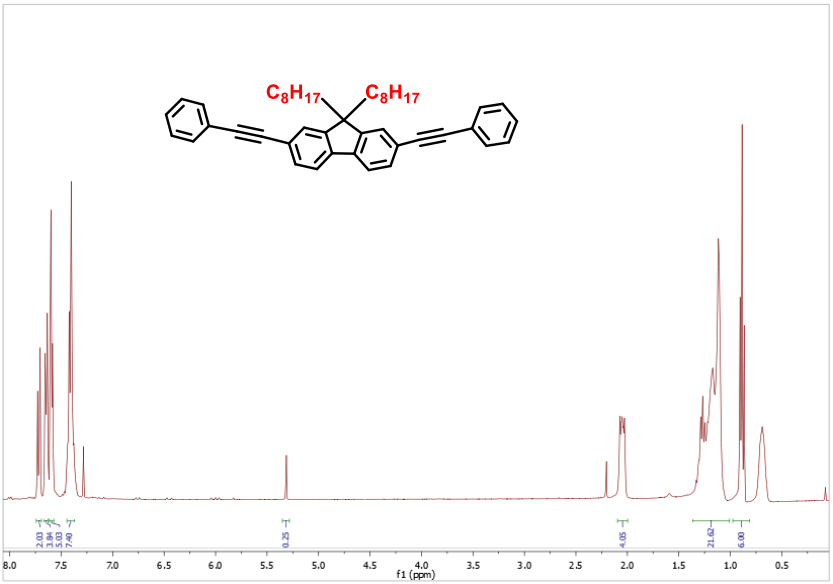

Figure S2. ^{13}C NMR (400 MHz, $CDCl_3$) of **8**

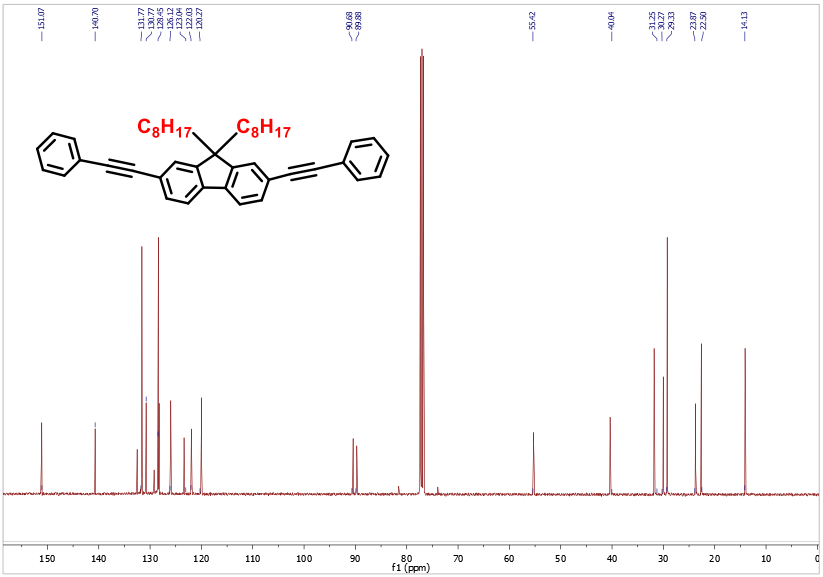

[9,9-dioctyl-2,7-bis(phenyl)-1-o-carboran-1-yl]-9H-fluorene (9)

Figure S3. ^{1}H NMR (400 MHz, $CDCl_3$) of **9**

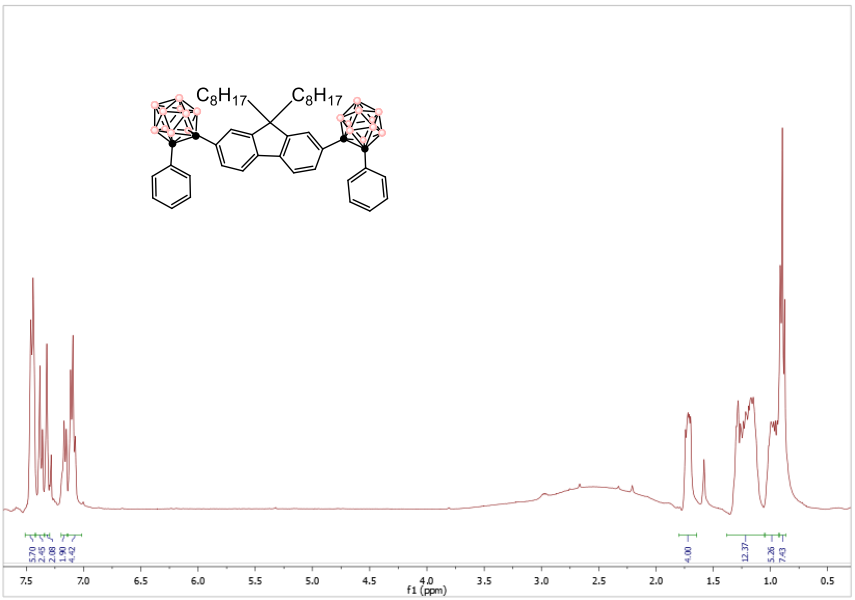

Figure S4. ^{13}C NMR (400 MHz, $CDCl_3$) of **9**

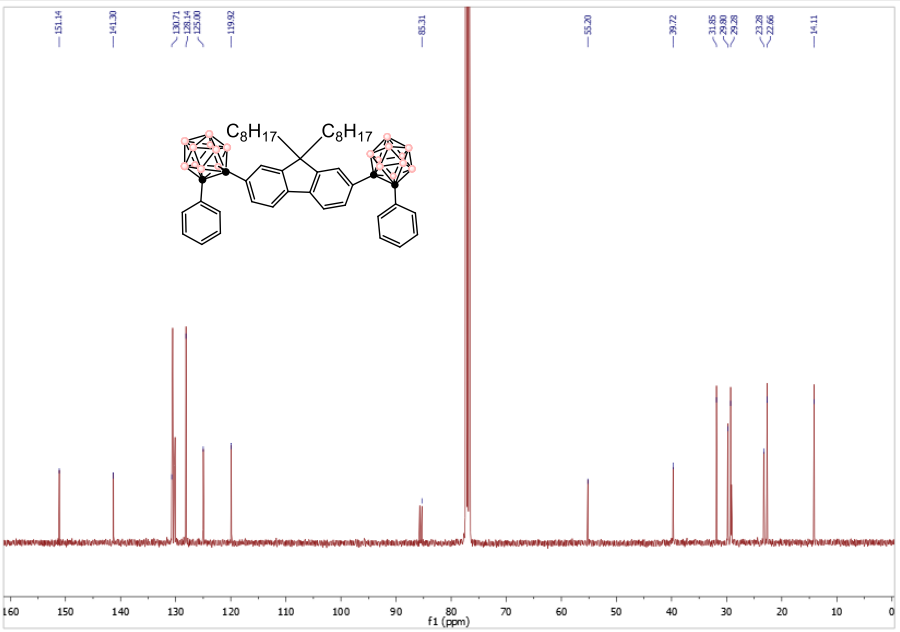

Figure S5. $^{11}B\{^{1}H\}$ NMR (400 MHz, $CDCl_3$) of **9**

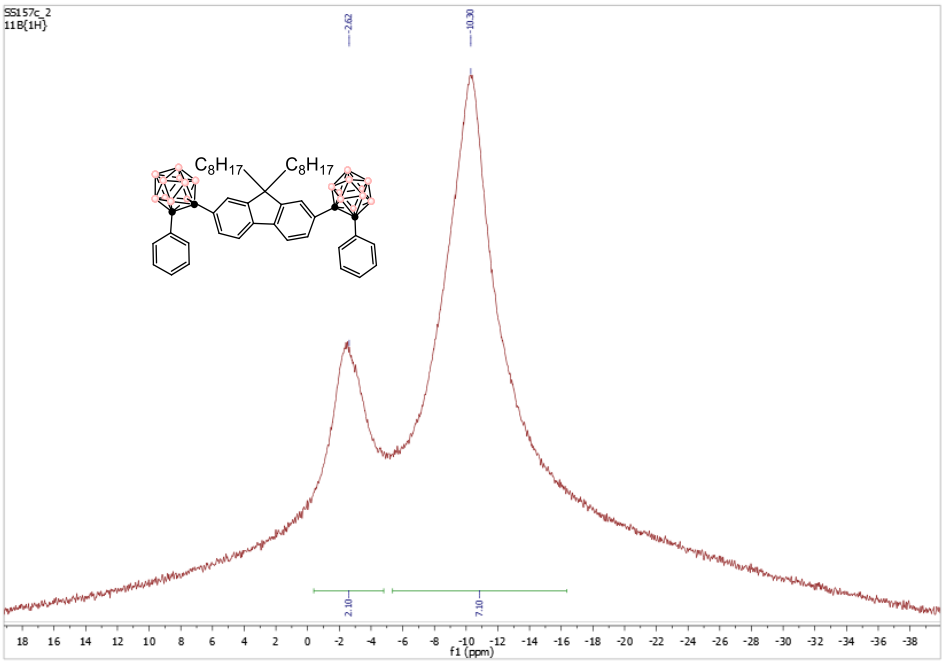

2,7-bis(phenylethynyl)-9H-fluorene (10)

Figure S6. ^{1}H NMR (400 MHz, $CDCl_3$) of **10**

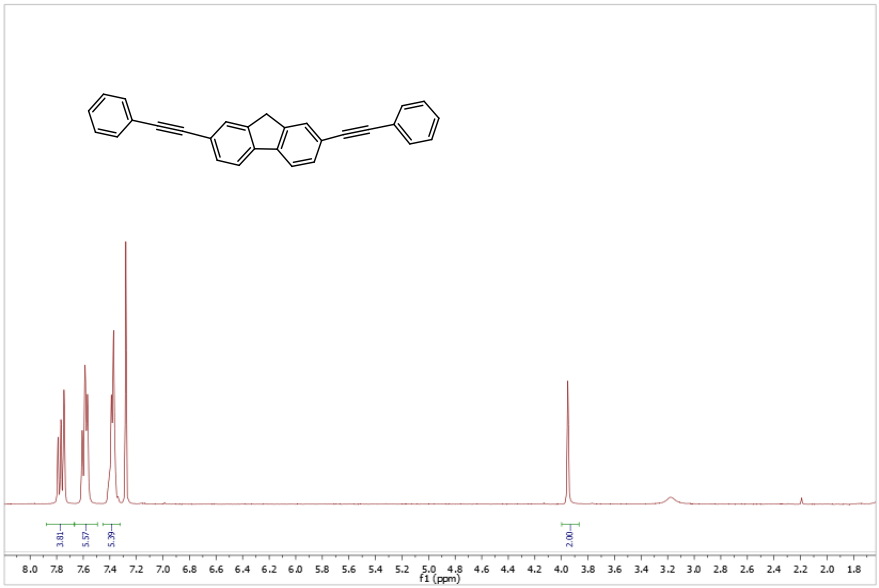

Figure S7 ^{13}C NMR (400 MHz, $CDCl_3$) of **10**

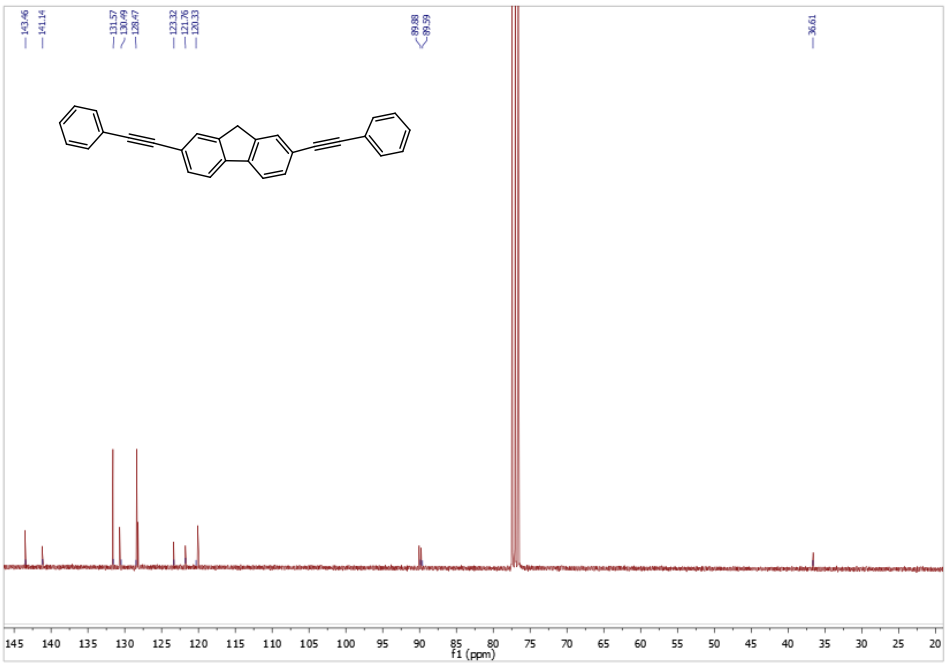

[2,7-bis(phenyl)-1-o-carboran-1-yl]-9H-fluorene (11)

Figure S8. ^{1}H NMR (400 MHz, $CDCl_3$) of **11**

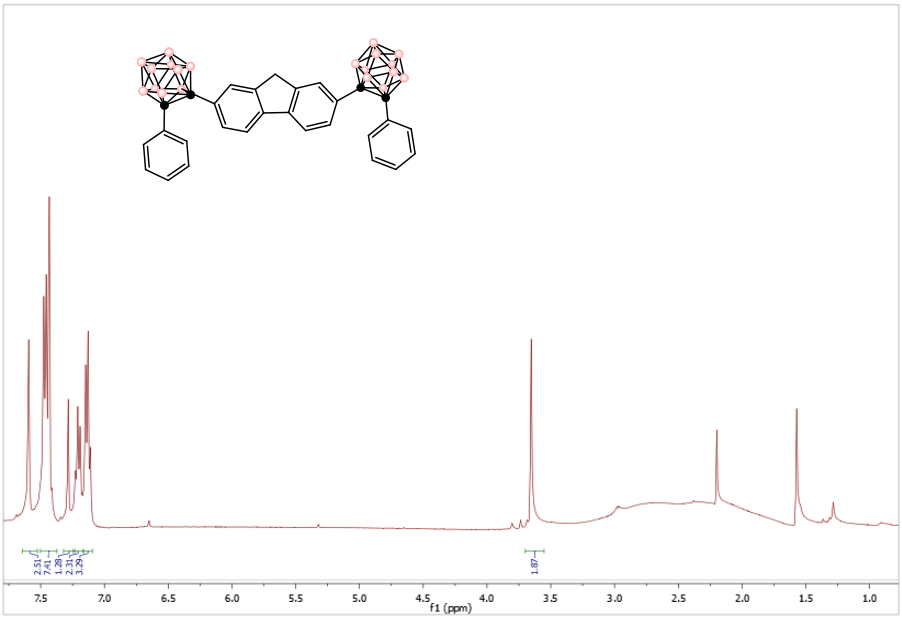

Figure S9. n^{13}C NMR (400 MHz, $CDCl_3$) of **11**

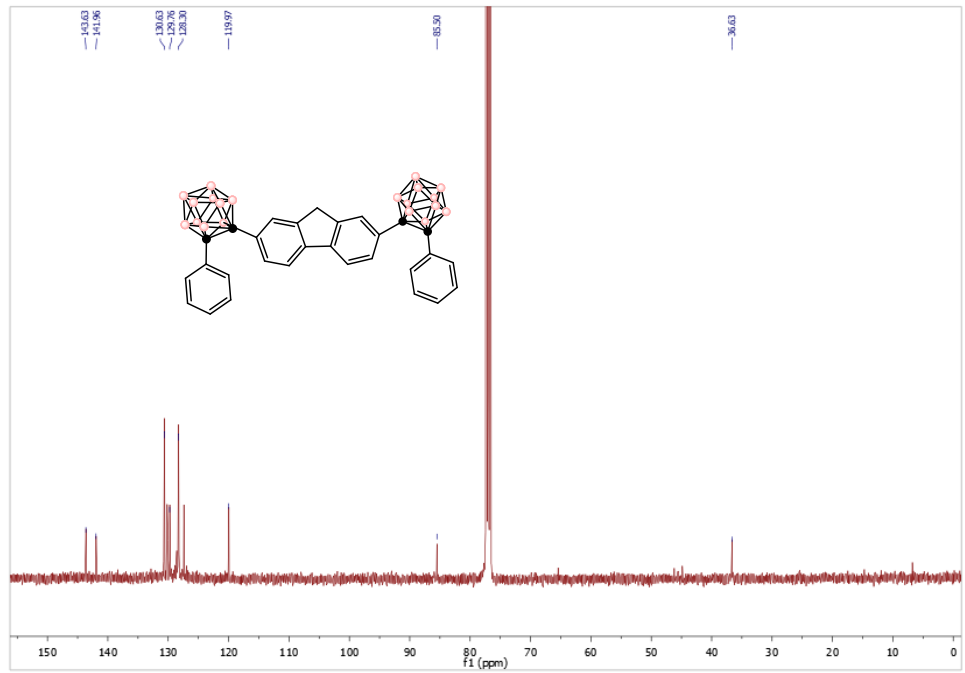

Figure S10. $^{11}B\{^{1}H\}$ NMR (400 MHz, $CDCl_3$) of **11**

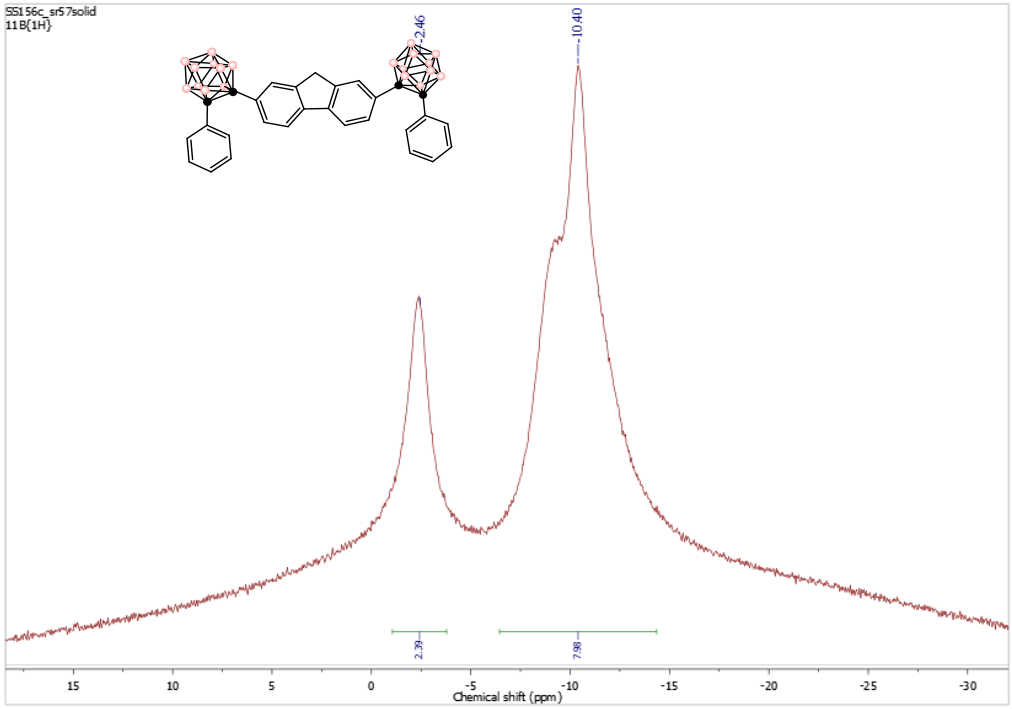

2,5-bis((4-butylphenyl)ethynyl)thiophene (12)

Figure S11. ^{1}H NMR (400 MHz, $CDCl_3$) of **12**

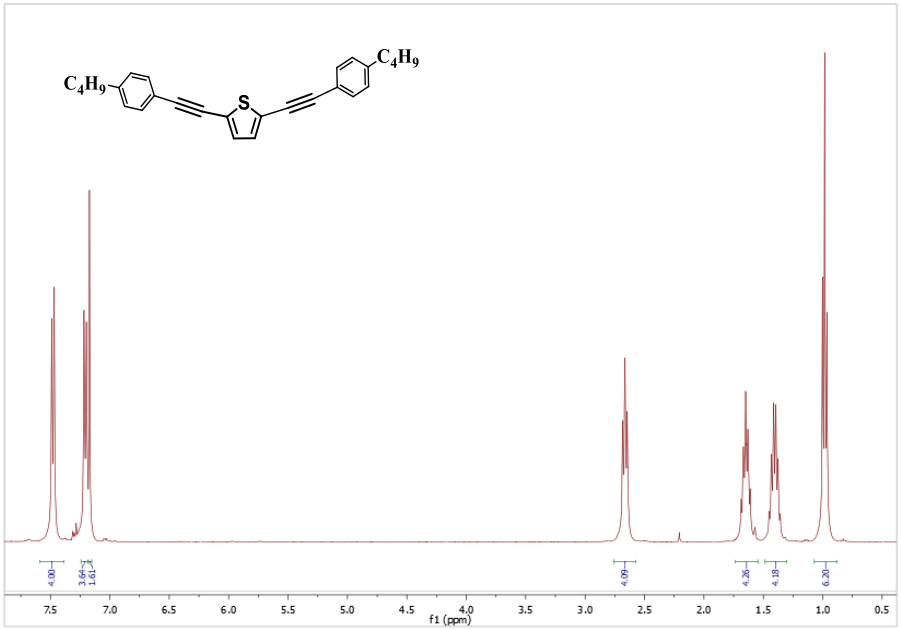

Figure S12. ^{13}C NMR (400 MHz, $CDCl_3$) of **12**

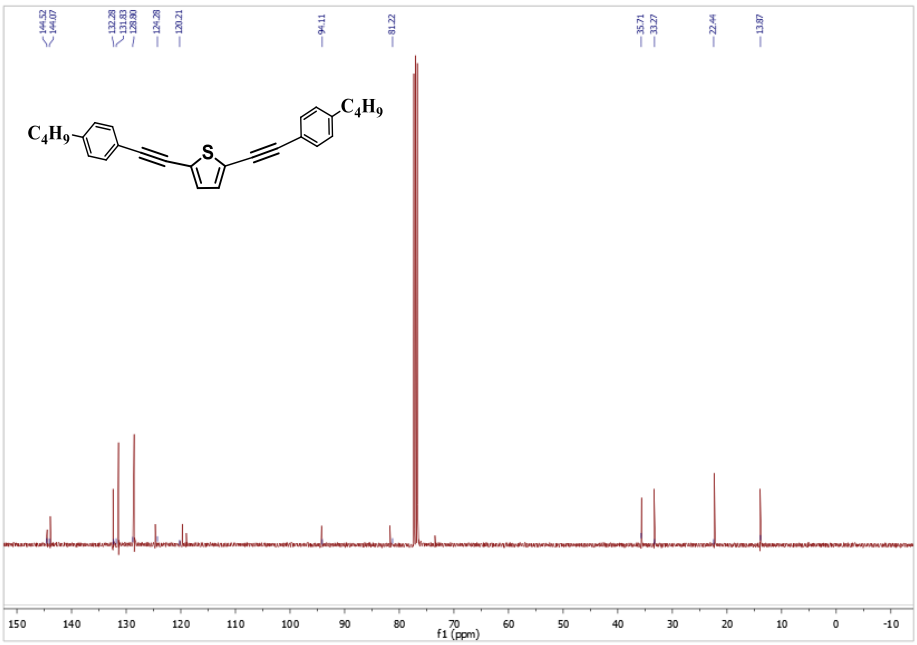

2,5-bis((4-butylphenyl)-*o*-carboran-1-yl)thiophene (13)

Figure S13. ^{1}H NMR (400 MHz, $CDCl_3$) of **13**

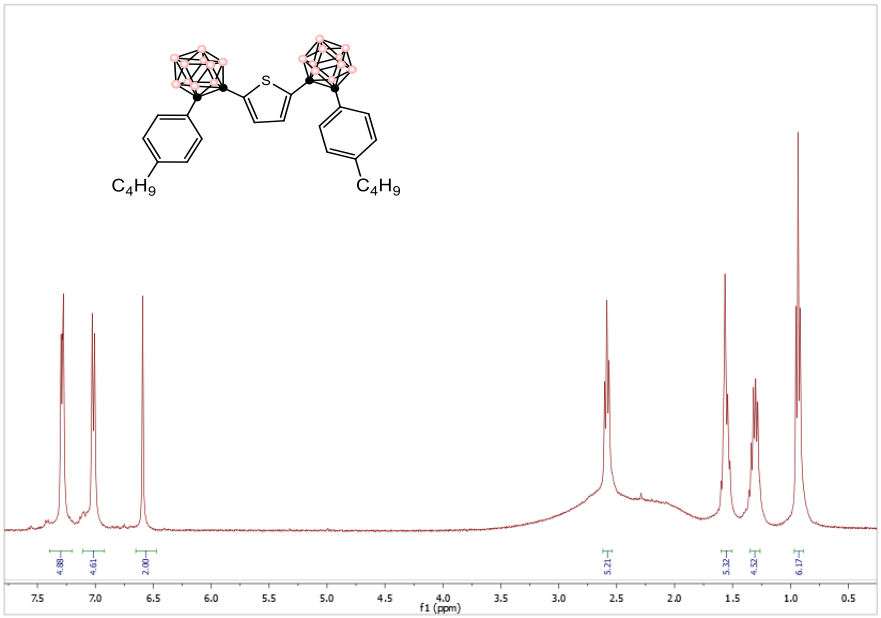

Figure S14. ^{13}C NMR (400 MHz, $CDCl_3$) of **13**

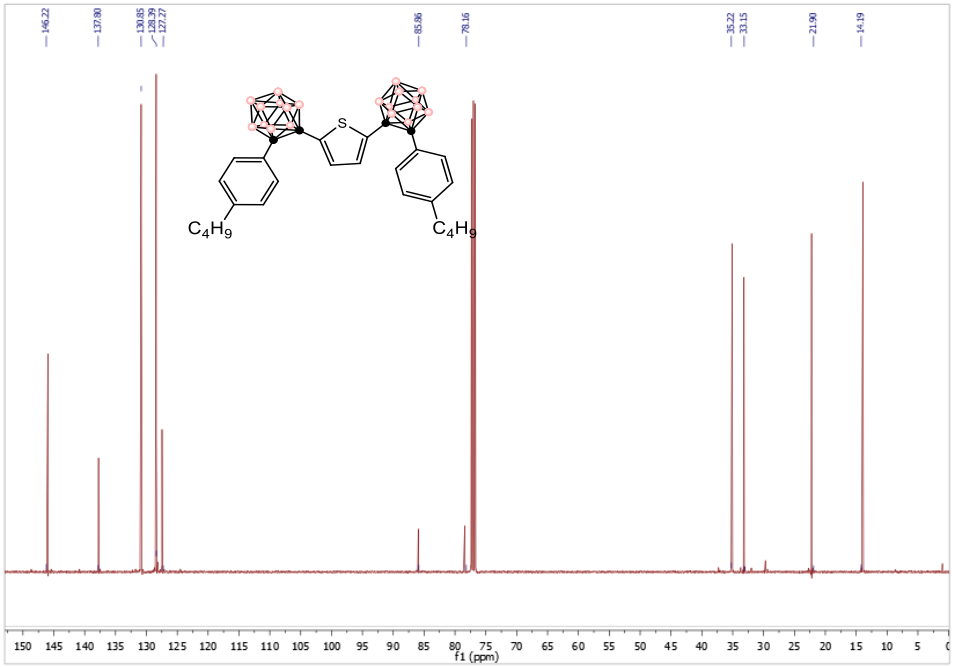

Figure S15. $^{11}B\{^{1}H\}$ NMR (400 MHz, $CDCl_3$) of **13**

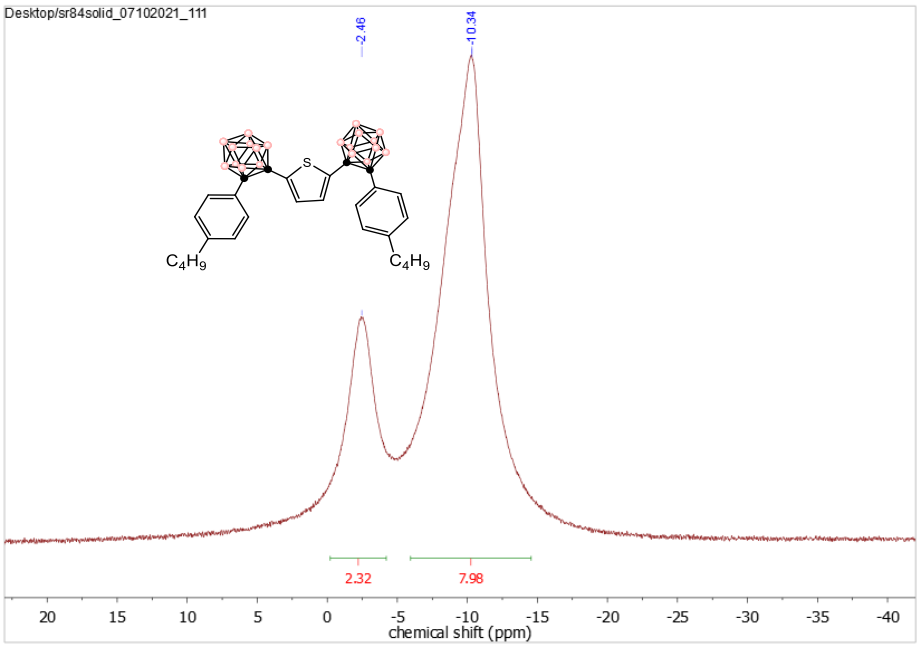

Preparation of nanoparticles.

The reprecipitation method is a single-step self-assembly method for obtaining organic nanoparticles. It is the most popular solvent-exchange process that has been developed over a decade by several groups such as Nakanishi´s, Majima´s, Yao´s, Park´s, Barbara´s, Horn and coworkers. These groups have successfully studied the preparation, size dependency of the luminescence and emission enhancement of various nanoparticles.[1,2] The precipitation method generally consists of dropping a concentrated solution of a water miscible organic solvent solution of an hydrophobic compound in a large amount of an anti-solvent, usually water, under vigorous stirring. The fast mixing of the two solvents induces the precipitation of the organic compound in micro/nano

aggregates since the organic molecule is no more soluble in the new solvent mixture. The experimental parameters involved in the preparation technique to control the particle size are temperature, concentrations, volume and velocity of the injection, nature and volume of the miscible solvent, and composition and time and agitation speed (rpm) of the non-solvent. Therefore, both kinetics and thermodynamics processes are considered for the growth of organic nanoparticles.[3]

In our experiment, carborane-containing compounds **9**, **11** and **13** were dissolved in THF in a 10^{-3} M concentration. Then, 1 ml of this solution was taken in a Hamilton microsyringe and added with a rate of 1 ml/ hour using a 4.61 mm diameter of the syringe to a volume of 9 ml milliQ water under vigorous stirring (400 rpm) at room temperature for 1 hour. The mixture was kept stirring for an hour after the addition of THF and over a duration of time, the precipitation in the mixture appeared and the solubility of the organic material decreases homogeneously thus these molecules aggregate and form nanoparticles.[4] Therefore, the final concentration was 10^{-4} M. In order to obtain a NP suspension in pure water for biological applications, the THF is remove with a dialysis procedure using a D9652-100FT dialysis tubing cellulose membrane purchased from Sigma Aldrich. Samples were dialyzed in 500 mL of milliQ water, and water was changed every 6 hours during 72 hours. Later, the NPs in water suspension were diluted from 10^{-4} M to 10^{-6} M concentration and further characterized with DLS, TEM, UV-Vis and fluorescence spectroscopy techniques. To our knowledge, this is the first time that NPs of carborane-based fluorophores have been prepared following this methodology.

4. Theoretical Calculations (DFT)

To elucidate the origin of these photophysical properties, DFT calculations were performed. The Gaussian 09 program package[5] was used for all calculations, while Molden 4.0[6] and IQmol 2.15.0[7] were used for the visualization of the computed structures and orbitals. In order to reduce computational time, the long alkyl chains were replaced by methyl substituents for **8-13** (the notation ′ stands for using Me substituents instead of the alkyl branch). Geometry optimizations were carried out at the B3LYP/6-31G* level of theory. The results of these calculations were compared with the calculations at ω-B97XD/6-311+G**, however, the application of the higher level resulted in only marginal structural changes. During the investigation of the photophysical properties, the two levels of theory were compared for the *ortho*-carboranes (Table S1) and the largest deviation between the functionals and basis sets was only 14 nm. Due to the marginal differences in the structures and absorption maxima, B3LYP/6-31G* was chosen for optimization, in order to reduce computational demand. The B3LYP functional with 6-31G* basis set was utilized for **9**, **11** and **13'**, as it has been successfully applied for the investigation of related carborane based fluorophores.[8] However, for the purely organic systems (**8**, **10** and **12**) the CAM-B3LYP functional was used, as the hybrid, long-range corrected CAM-B3LYP functional provided better results for extended conjugate organic systems, which was verified by test calculations as well (Table S2). Several rotamers have been investigated (Tables S3-S5), nonetheless, the differences proved to be small in all investigated cases, both in energy (ΔE_{max}=1.42 kcal/mol) and in the absorption maxima (ΔABS_{max}=7 nm) (Table S6). TD-DFT calculations have demonstrated that the HOMO-LUMO transitions have the highest contribution, and while **8**, **10** and **12** possess a conjugation

that expands over the entire structure, in case of the **9**, **11**, **13** the carborane cages interrupt the conjugation (Tables S7-S9). Upon the investigation of the Kohm-Sham orbitals, all *ortho*-carboranes exhibit some CT characteristics, but for **13** it is much more significant than **9** and **11**, which exhibit stronger LE excitation character (Tables S10-S13). It should be highlighted that in case of **13** the charge transfer occurs from the phenyl substituents towards the thiophene unit and the participation of the carborane units are marginal. Indeed, the lack of the AIE of in contrast of **9** or 11 could be attributed to the lower participation of the carborane units in the charge transfer process. In order to further support this idea, the corresponding excited states (S_1) of **9**, **11**, **13** were optimized. Investigating the geometry of these structures (S_1 states) it could be established that in case of **9** and **11** the $C_{cluster}$ - $C_{cluster}$ (C_c-C_c) distance elongated to 2.48 Å (similar values were reported recently),[9] which was in agreement with the postulated charge transfer towards the carborane units. These results indicate that the bond elongation proceeds when the compounds **9** and **11** are depicted as single molecules and no strong fluorescence could be expected in diluted solution. On the other hand, in the S_1 state of **13** the $C_{cluster}$ - $C_{cluster}$ distance is significantly shorter (2.26 Å), which was in agreement with the different nature of the CT process and the lack of the AIE.

Table S1: Comparison of the two functional and basis sets through the calculation of absorption maxima

	9	**9-rot**	**11**	**11-rot**	**13**	**13-rot**
Experimental values	**286, 314**		**293, 308**		**274**	
B3LYP/6-31G*	**305**	**306**	**301**	**302**	**286**	**279**
ωB97X-D/6-311+G**	**269**	**-**	**266**	**272**	**-**	**-**
B3LYP/6-31G*// ωB97X-D/6-311+G**	**294**	**297**	**289**	**291**	**276**	**265**

Table S2: The calculated absorption maxima at different levels of theory

	8	**9**	**10**	**11**	**12**	**13**
Experimental values	**349**	**286, 314**	**346**	**293, 308**	**348**	**274**
CAM-B3LYP/6-31G*	**339**	-	**336**	**276**	**359**	-
CAM-B3LYP/6-31G* PCM=THF	**346**	**284**	**343**	**280**	**370**	**259**
B3LYP/6-31+G*	**392**	**309**	-	-	**403**	-
B3LYP/6-31+G* PCM=THF	**401**	**315**	**398**	**311**	**418**	**292**
B3LYP/6-31G*	**385**	**305**	**382**	**301**	**397**	**285**
B3LYP/6-31G* PCM=THF	-	-	**392**	**308**	**413**	**291**
PBE1PBE/6-31G*	**373**	**298**	**371**	**294**	**387**	-

Table S3: Kohn-Sham canonical orbitals and their energies of the investigated rotamers of 9 at B3LYP/6-31G* level of theory

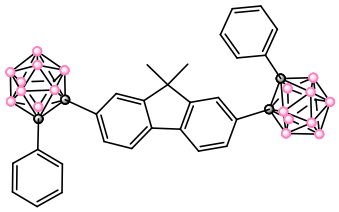

9

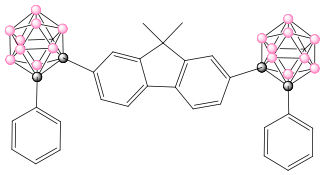

9-rot

LUMO +1

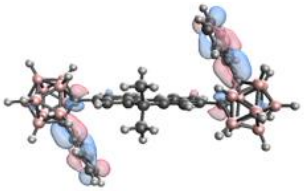

-1.34 eV

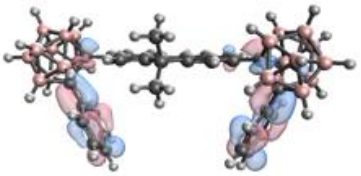

-1.36 eV

LUMO

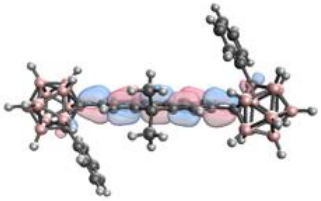

-2.02 eV

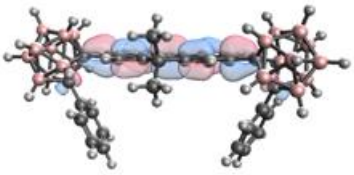

-2.02 eV

HOMO

-6.51 eV

-6.51 eV

HOMO -1

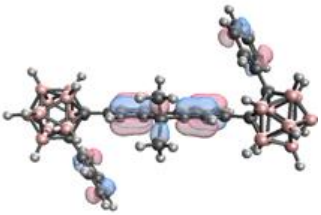

-7.24 eV

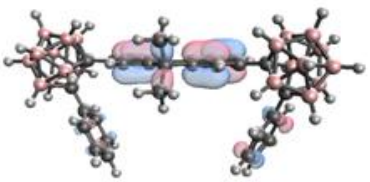

-7.25 eV

Table S4 Kohn-Sham canonical orbitals and their energies of the investigated rotamers of 11 at B3LYP/6-31G* level of theory

	11	**11-rot**
	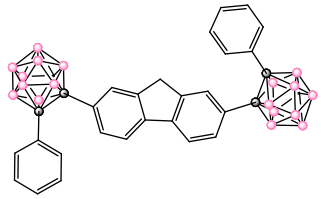	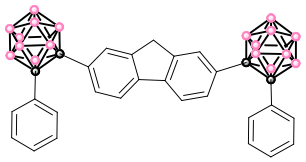
LUMO +1	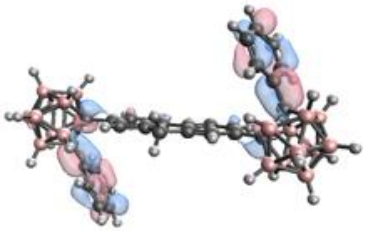	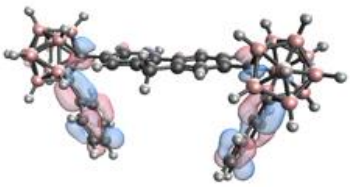
	-1.34 eV	**-1.37 eV**
LUMO	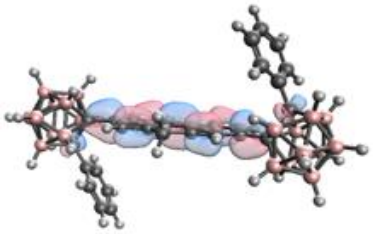	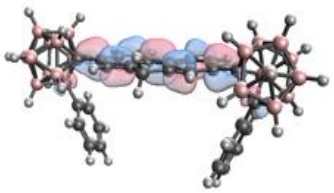
	-2.01 eV	**-2.02 eV**
HOMO	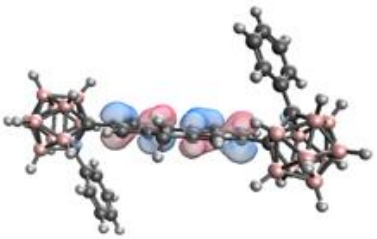	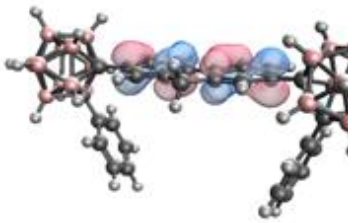
	-6.54 eV	**-6.54 eV**

HOMO -1	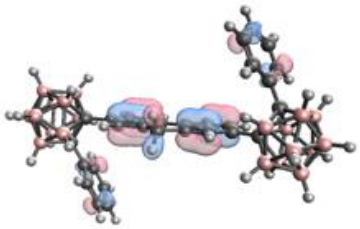	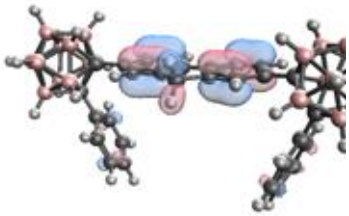
	-7.23 eV	**-7.25 eV**

Table S5: Kohn-Sham canonical orbitals and their energies of the investigated rotamers of 13 at B3LYP/6-31G* level of theory

	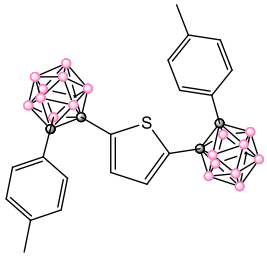	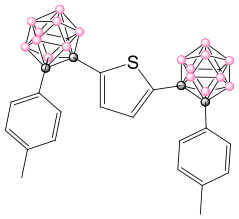
	13	**13-rot**
LUMO +1	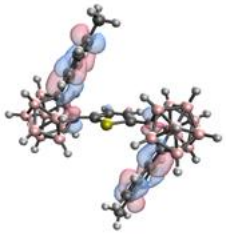	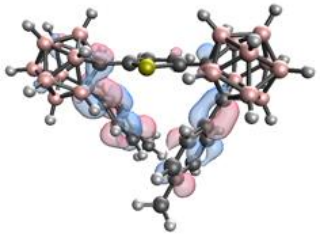
	-1.29 eV	**-1.39 eV**
LUMO	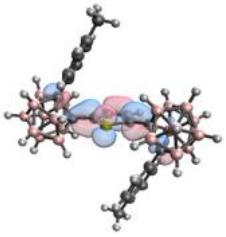	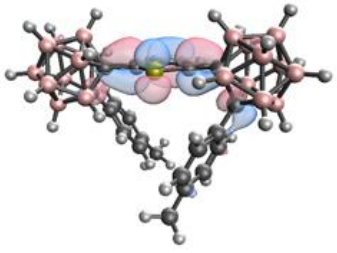
	-2.08 eV	**-2.04 eV**

HOMO

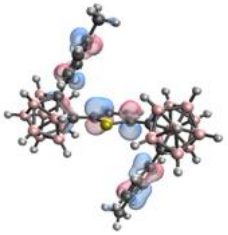

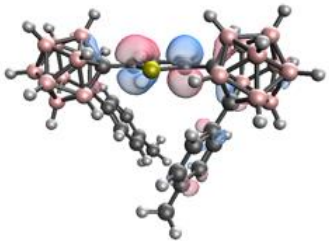

-6.99 eV **-7.01 eV**

HOMO -1

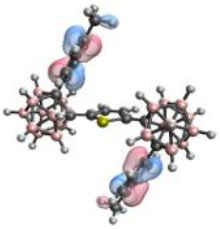

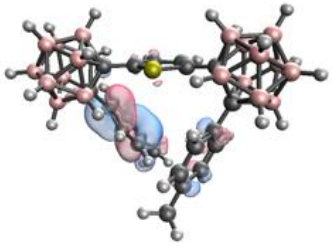

-7.05 eV **-7.15 eV**

Table S6: Total energy and absorption maxima difference between different rotamers of the investigated systems

	Compound	**Energy (E) [Hartree]**	**ΔE [kcal/mol]**	**Absorption maxima (ABS) [nm]**	**ΔABS [nm]**
	9	-1703.953120	0.39	305	1
	9-rot	-1703.952499		306	
	11	-1625.324857	0.32	301	1
	11-rot	-1625.324344		302	
	13	-1755.542797	1.42	286	7
	13-rot	-1755.540540		279	

Table S7: Kohn-Sham orbitals for compound 8 **(**CAM-B3LYP/6-31G*) and the most stable rotamer of 9 (B3LYP/6-31G*)

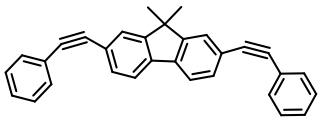

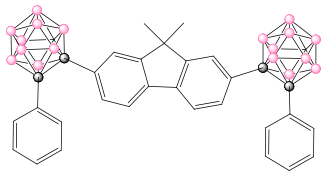

LUMO +1

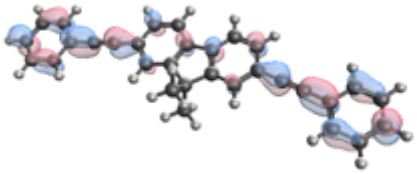

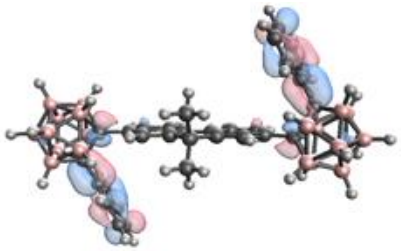

0.27 eV **-1.34 eV**

LUMO

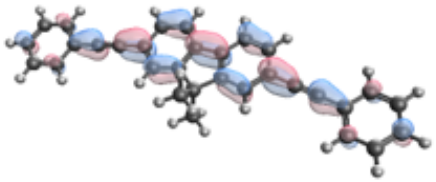

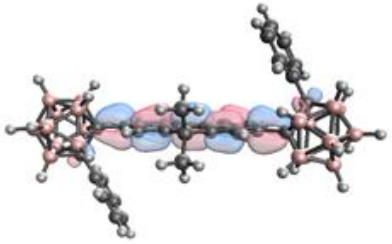

-0.66 eV **-2.02 eV**

HOMO

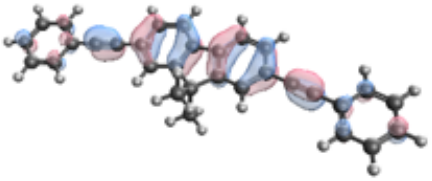

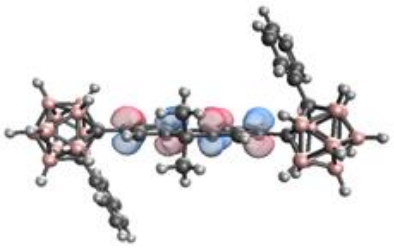

-6.45 eV **-6.51 eV**

HOMO -1

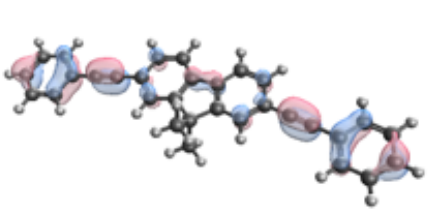

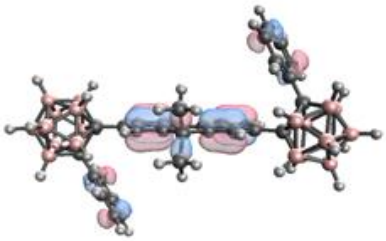

-7.27 **-7.24 eV**

Table S8: Kohn-Sham orbitals for compound 10 **(**CAM-B3LYP/6-31G*) and the most stable rotamer of 11 (B3LYP/6-31G*)

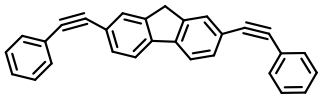

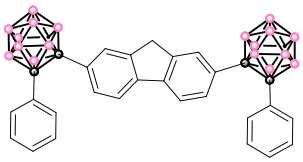

LUMO +1

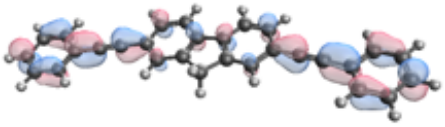

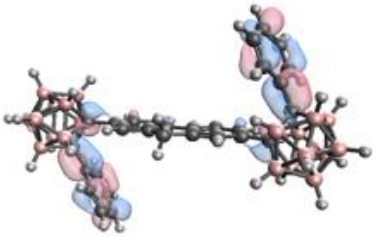

0.26 eV **-1.34 eV**

LUMO

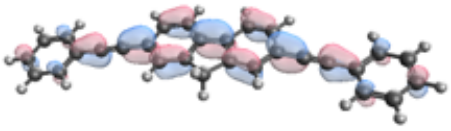

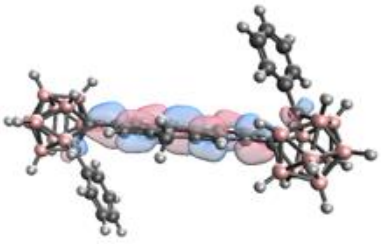

-0.65 eV **-2.01 eV**

HOMO

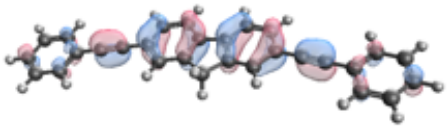

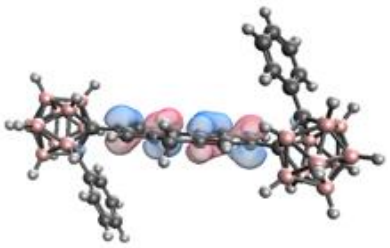

-6.46 eV **-6.54 eV**

HOMO -1

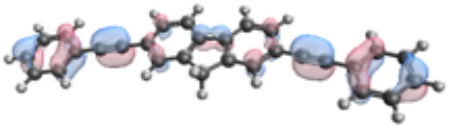

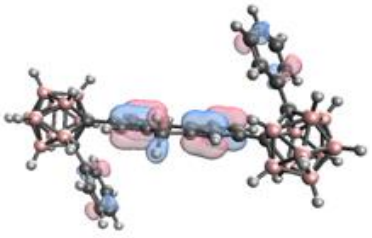

-7.27 eV **-7.23 eV**

Table S9: Kohn-Sham orbitals for compound 12 (CAM-B3LYP/6-31G*) and the most stable rotamer of 13 (B3LYP/6-31G*)

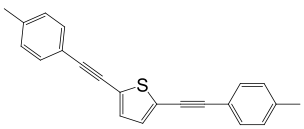

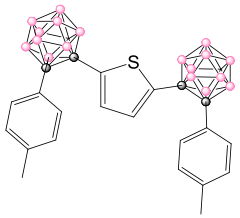

LUMO +1

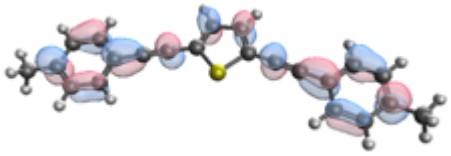

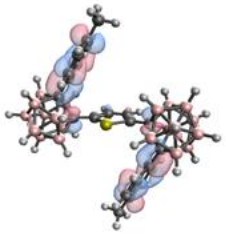

0.57 eV **-1.29 eV**

LUMO

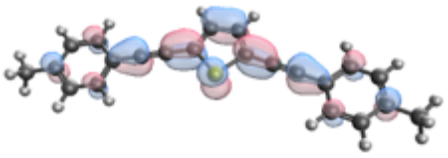

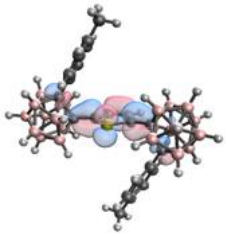

-0.72 eV **-2.08 eV**

HOMO

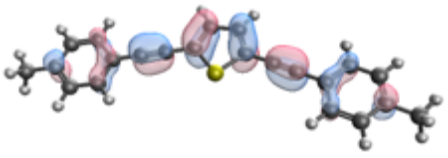

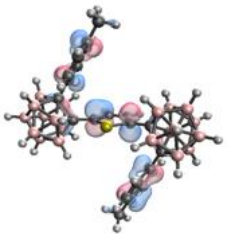

-6.34 eV **-6.99 eV**

HOMO -1

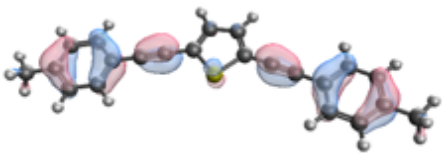

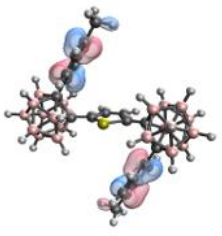

-7.56 eV **-7.05 eV**

Table S10: Charge-density difference map. he blue and red parts correspond to the regions in which electron density is decreased and increased after electron excitation, respectively. Isosurface value: 0.0015 (8, 10 **, 12** were calculated at CAM-B3LYP/6-31G* and 9, 11, 13 were calculated at B3LYP/6-31G*)

1’

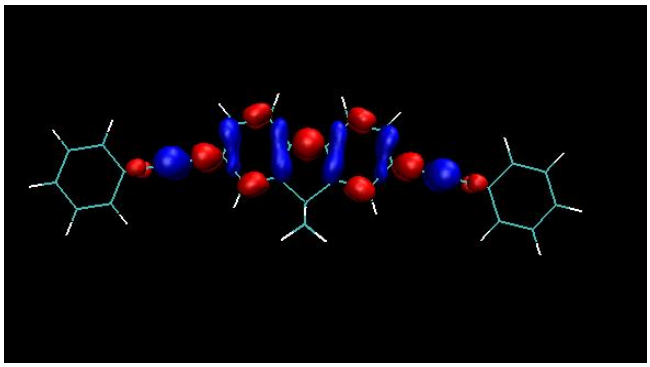

9

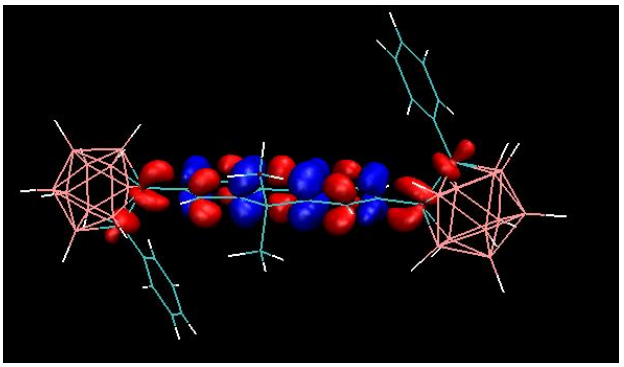

3

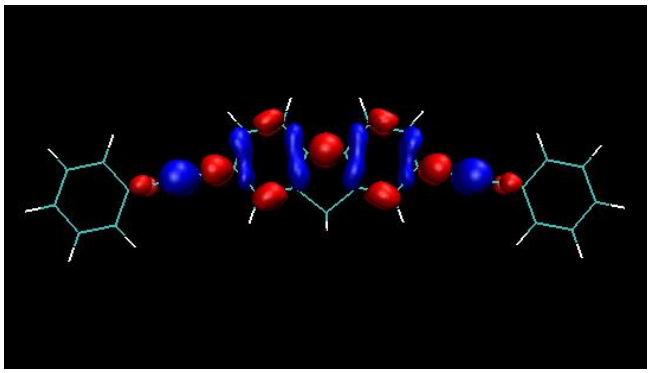

11

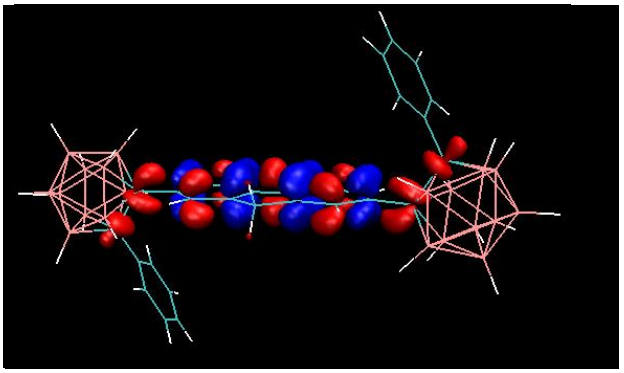

5’

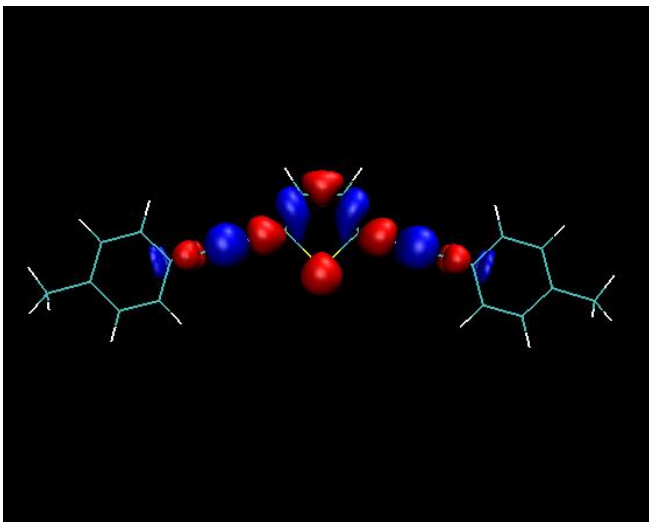

13

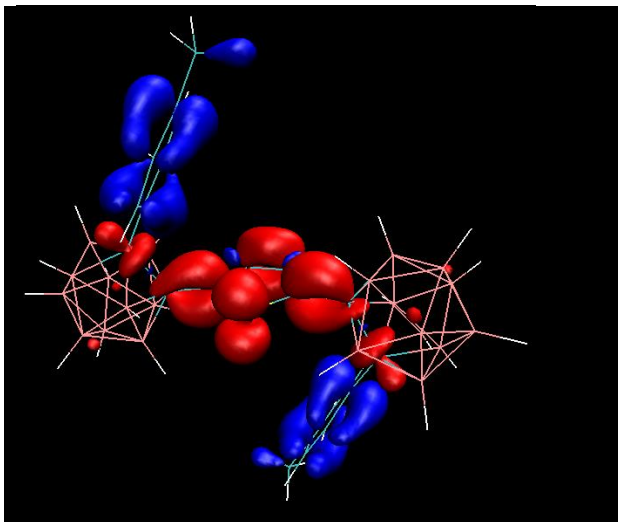

Table S11: HOMO-LUMO orbitals (at B3LYP/6-31G*) in S_0 and S_1 states for compound 9, S_1 shows a lengthening of one C_c-C_c bond.

LUMO	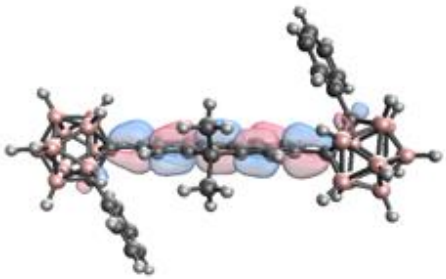	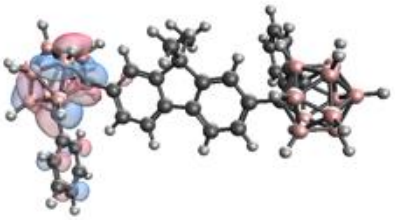
	-2.02 eV	**-3.83 eV**
HOMO	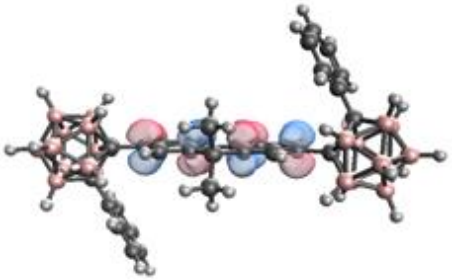	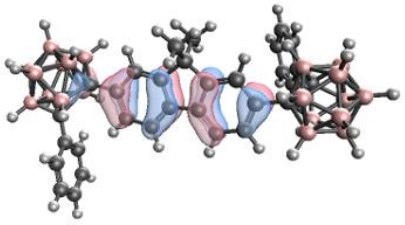
	-6.51 eV	**-5.96 eV**
	S_0	**S_1**
C_c-C_c bond	**1.76 Å**	**2.48 Å**

Table S12: HOMO-LUMO orbitals (at B3LYP/6-31G*) in S_0 and S_1 states for compound 11, S_1 shows a lengthening of one C_c-C_c bond.

LUMO	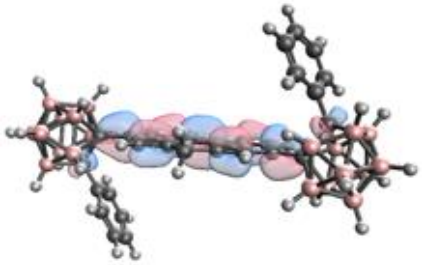	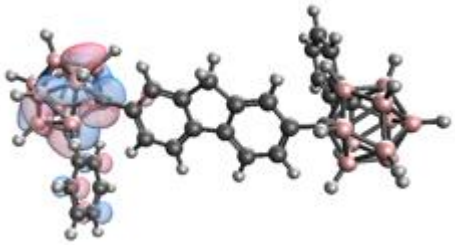
	-2.01 eV	**-3.86 eV**
HOMO	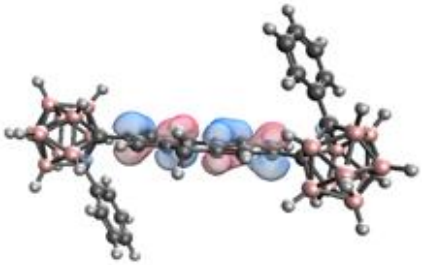	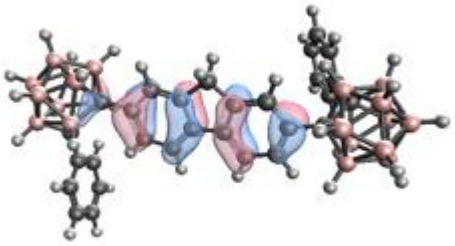
	-6.54 eV	**-6.00 eV**
	S_0	**S_1**
C_c-C_c bond	**1.76 Å**	**2.48 Å**

Table S13: HOMO-LUMO orbitals (at B3LYP/6-31G*) in S_0 and S_1 states for compound 13, S_1 shows a lengthening of both C_c-C_c bonds.

LUMO	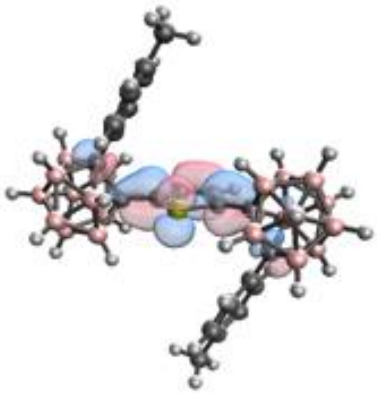	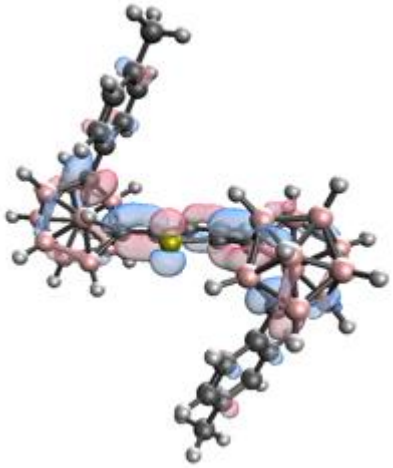
	-2.08 eV	**-3.59 eV**
HOMO	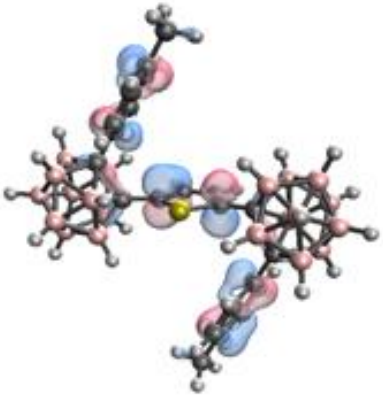	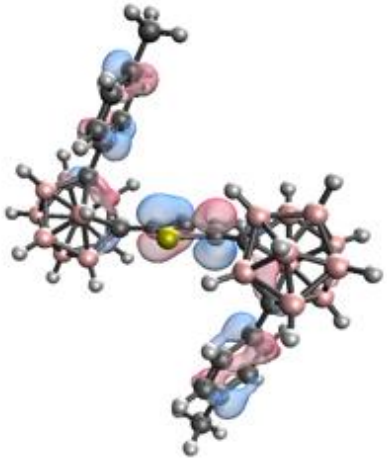
	-6.99 eV	**-6.66 eV**
	S_0	**S_1**
C_c-C_c bond	**1.77 Å**	**2.26 Å**

1 D. Xiao, L. Xi, W. Yang, H. Fu, Z. Shuai, Y. Fang and J. Yao *J. Am. Chem. Soc.* 2003, **125**, 22, 6740–6745.

2 S. J. Lim, B. K. An, S. D. Jung, M. A. Chung, and S. Y. Park, *Angew. Chem. Int. Ed.* 2004, **43**, 6346–6350

3 S. F. Forgues, *Nanoscale,* 2013, **5**, 8428

4 D. Blasi, D. M. Nikolaidou, F. Terenziani, I. Ratera and J. Veciana, *Phys. Chem. Chem. Phys*., 2017, **19**, 9313.

5 Gaussian 09, Revision E.01, M. J. Frisch, G. W. Trucks, H. B. Schlegel, G. E. Scuseria, M. A. Robb, J. R. Cheeseman, G. Scalmani, V. Barone, B. Mennucci, G. A. Petersson, H. Nakatsuji, M. Caricato, X. Li, H. P. Hratchian, A. F. Izmaylov, J. Bloino, G. Zheng, J. L. Sonnenberg, M. Hada, M. Ehara, K. Toyota, R. Fukuda, J. Hasegawa, M. Ishida, T. Nakajima, Y. Honda, O. Kitao, H. Nakai, T. Vreven, J. A. Montgomery, Jr., J. E. Peralta, F. Ogliaro, M. Bearpark, J. J. Heyd, E. Brothers, K. N. Kudin, V. N. Staroverov, T. Keith, R. Kobayashi, J. Normand, K. Raghavachari, A. Rendell, J. C. Burant, S. S. Iyengar, J. Tomasi, M. Cossi, N. Rega, J. M. Millam, M. Klene, J. E. Knox, J. B. Cross, V. Bakken, C. Adamo, J. Jaramillo, R. Gomperts, R. E. Stratmann, O. Yazyev, A. J. Austin, R. Cammi, C. Pomelli, J. W. Ochterski, R. L. Martin, K. Morokuma, V. G. Zakrzewski, G. A. Voth, P. Salvador, J. J. Dannenberg, S. Dapprich, A. D. Daniels, O. Farkas, J. B. Foresman, J. V. Ortiz, J. Cioslowski, D. J. Fox, *Gaussian, Inc., Wallingford CT,* 2013.

6 G. Schaftenaar, J. H. Nordik *J. Comput. Aided Mol. Des.* 2000, **14**, 123–134.

7 A. T. B. Gilbert, IQmol molecular viewer. Available at: http://iqmol.org (Accessed October, **2012**).

8 M. Chaari, Z. Kelemen, D. Choquesillo-Lazarte, F. Teixidor, C. Viñas and R. Núñez, *Inorg. Chem. Front.*, 2020, **7**, 2370 —2380

9 J. Ochi, K. Tanaka, Y. Chujo, *Dalton Trans., 2021, **50**, 1025*

Annex- Chapter 4

Experimental Section

Materials and methods

Unless specified, all reagents were used as received without further purifications. [$Pd_2(dba)_3$], [Pd(*t*-$Bu_3P)_2$] and Cy_2*N*Me were purchased from Aldrich. All reactions involving air-sensitive reagents were performed under nitrogen in oven-dried glassware using the syringe septum cap technique. Anhydrous CH_2Cl_2 was obtained by distillation over CaH_2. Anhydrous THF was obtained by distillation over $LiAlH_4$, followed by distillation over Na-benzophenone. Et_3N was distilled over CaH_2 and dry 1,4-dioxane was purchased from Merck-SigmaAldrich and used as received. Reactions were monitored using thin layer chromatography on silica gel coated aluminium plates. Chromatographic separations were performed under pressure on silica gel (40–63 μm, 230–400 mesh). R_f values refer to TLC carried out on silica gel plates with UV light (254 nm and/or 366 nm) as visualizing agent.

Instrumentation

^1H NMR (600 MHz) and $^{13}C\{^1H\}$ (150 MHz) NMR spectra were recorded in $CDCl_3$ on a Jeol ECZR 600 spectrometer at RT using residual solvent peak as an internal standard. $^{11}B\{^1H\}$ (128.38 MHz) NMR spectra were recorded on a Bruker ARX 400 spectrometer in $CDCl_3$. Chemical shift values for $^{11}B\{^1H\}$ NMR spectra were referenced to external $BF_3{\cdot}OEt_2$, those for ^1H and $^{13}C\{^1H\}$ NMR were referenced to [$Si(CH_3)_4$] (TMS). Chemical shifts (δ) are given in parts per million (ppm) and coupling constants (J) in Hertz (Hz). Multiplicities are reported as follows: *s* (singlet), *d*(doublet), *t*(triplet), *q* (quartet), *m* (multiplet). Low-resolution

mass spectra were recorded on a Micromass Quattro microTM API (Waters Corporation, Milford, MA, USA) or at an ionizing voltage of 70 eV on a HP 5989B mass selective detector connected to an HP 5890 GC with a methyl silicone capillary column (EI). The MS flow-injection analyses were run on a high resolving power hybrid mass spectrometer (HRMS) Orbitrap Fusion (Thermo Scientific, Rodano, Italy), equipped with an ESI ion source. The samples were analyzed in acetonitrile solution using a syringe pump at a flow rate of 5 μL/min. The tuning parameters adopted for the ESI source were: source voltage 4.0 kV. The heated capillary temperature was maintained at 275 C. The mass accuracy of the recorded ions (vs. the calculated ones) was ±2.5 mmu (milli-mass units). Analyses were run using both full MS (150–2000 *m/z* range) and MS/MS acquisition, at 500000 resolutions (200 *m/z*).

Synthesis and analysis of compound **14b**

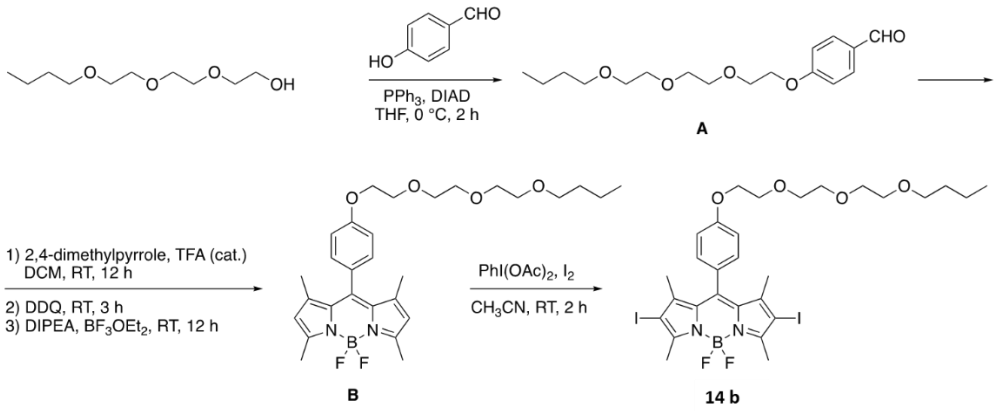

4-(2-(2-(2-Butoxyethoxy)ethoxy)ethoxy)benzaldehyde (A). The triethylene glycol monobutyl ether (1 g, 5.0 mmol) was dissolved in dry THF (10 mL) under a positive N_2 atmosphere, and the resulting solution was cooled to 0 °C. 4-Hydroxybenzaldehyde (610 mg, 5.0 mmol, 1 eq.),

triphenylphosphine (1.57 g, 6.0 mmol, 1.2 eq.) and diisopropylazodicarboxylate (DIAD, 1.21 g, 6.0 mmol, 1.2 eq.) were sequentially added. The reaction was stirred at 0 °C for 2 h. Dichlorometane (30 mL) was added, the mixture was washed with water, and the combined organic layers were dried over Na_2SO_4 and concentrated to dryness. Purification by flash column chromatography on silica gel (PE/Acetone 8/2 v/v) gave **A** as a colourless oil (66%, R_f = 0.6 PE/Acetone 8/2 v/v). ^{1}H NMR (600 MHz, $CDCl_3$): δ 9.91 (s, 1H), 7.85 (d, *J* = 8.9 Hz, 2H), 7.06 (d, *J* = 8.8 Hz, 2H), 4.26-4.22 (m, 2H), 3.93-3.90 (m, 2H), 3.77-3.74 (m, 2H), 3.73-3.70 (m, 2H), 3.69-3.65 (m, 2H), 3.61-3.58 (m, 2H), 3.50-3.46 (m, 2H), 1.62-1.55 (m, 2H), 1.44-1.36 (m, 2H), 0.95 (t, *J* = 7.5 Hz, 3H). ^{13}C{^{1}H} NMR (150 MHz, $CDCl_3$): δ 190.4, 163.6, 131.6, 129.7, 114.6, 70.8, 70.6, 70.4, 70.3, 69.7, 69.1, 67.5, 31.4, 19.0, 13.6. EI-MS *m/z* (%): 310 (M^+, 17), 210 (33), 148 (81), 121 (50), 77 (38), 57 (100).

***Meso*-(4-(2-(2-(2-butoxyethoxy)ethoxy)ethoxy)phenyl)-1,3,5,7-tetramethyl BODIPY (B).** To a stirred solution of aldehyde **A** (961 mg, 3.1 mmol) and 2,4-dimethylpyrrole (589 mg, 6.2 mmol, 2 eq.) in dry CH_2Cl_2 (30 mL) under a positive N_2 atmosphere was added a catalytic amount of TFA (5 drops), and the reaction mixture was stirred at RT overnight until complete consumption of the aldehyde, as monitored by TLC analysis. DDQ (704 mg, 3.1 mmol, 1 eq.) was added, and the mixture was stirred at RT for 3 h. The reaction mixture was then washed with water, dried over Na_2SO_4 and concentrated to dryness. The crude residue was dissolved in dry CH_2Cl_2 (20 mL), DIPEA (5.40 mL, 31.0 mmol, 10 eq.) was added at 0 °C and the mixture was stirred for 10 min. $BF_3{\cdot}OEt_2$ (25.0 mmol) was slowly added and the resulting mixture was stirred at RT overnight. The reaction mixture was concentrated to dryness and the

crude was purified by flash column chromatography on silica gel (R_f = 0.35 PE/EtOAc 6/4 v/v) to give **B** as an orange bright semisolid (18%, R_f = 0.35 PE/EtOAc 6/4 v/v). ^{1}H NMR (600 MHz, $CDCl_3$): δ 7.10 (d, *J* = 8.7 Hz, 2H), 6.97 (d, *J* = 8.7 Hz, 2H), 5.93 (s, 2H), 4.26-4.22 (m, 2H), 3.93-3.90 (m, 2H), 3.77-3.74 (m, 2H), 3.73-3.70 (m, 2H), 3.69-3.65 (m, 2H), 3.61-3.58 (m, 2H), 3.43 (t, *J* = 6.7 Hz, 2H), 2.49 (s, 6H), 1.56-1.51 (m, 2H), 1.37 (s, 6H), 1.34-1.30 (m, 2H), 0.87 (t, *J* = 7.4 Hz, 3H). ^{13}C {^{1}H} NMR (150 MHz, $CDCl_3$): δ 159.5, 155.4, 143.3, 141.9, 131.9, 129.3, 127.3, 121.2, 115.3, 71.3, 71.0, 70.8, 70.8, 70.2, 69.8, 67.6, 31.8, 19.4, 14.7, 14.7, 14.0.

2,6-Diiodo-*meso*-(4-(2-(2-(2-butoxyethoxy)ethoxy)ethoxy)phenyl)-1,3,5,7-tetramethyl BODIPY (14b). A solution of compound **B** (264 mg, 0.5 mmol) in ACN (60 mL) was treated with iodine (317 mg, 1.25 mmol, 2.5 eq.) followed by (diacetoxy)iodobenzene (322 mg, 1.00 mmol, 2 eq.). The reaction mixture was stirred at RT for 2 h and the solvent removed under reduced pressure. Purification by flash column chromatography on silica gel (DCM/EtOAc 96/4 v/v) gave **1b** as a bright red semisolid (70%, R_f = 0.6 DCM/EtOAc 96/4 v/v). ^{1}H NMR (600 MHz, $CDCl_3$): δ 7.12-7.09 (m, 2H), 7.05-7.02 (m, 2H), 4.20-4.17 (m, 2H), 3.93-3.89 (m, 2H), 3.77-3.74 (m, 2H), 3.73-3.69 (m, 2H), 3.68-3.65 (m, 2H), 3.62-3.57 (m, 2H), 3.46 (t, *J* = 6.8 Hz, 2H), 2.62 (s, 6H), 1.59-1.53 (m, 2H), 1.42 (s, 6H), 1.39-1.32 (m, 2H), 0.90 (t, *J* = 7.4 Hz, 3H). ^{13}C {^{1}H} NMR (150 MHz, $CDCl_3$): δ 159.9, 156.7, 145.5, 141.7, 131.8, 129.1, 126.9, 115.6, 85.6, 71.3, 71.0, 70.8, 70.8, 70.2, 69.8, 67.7, 31.8, 19.4, 17.3, 16.1, 14.1. ESI-HRMS $[M+Na]^+$: *m/z* 803.0800; $C_{29}H_{37}BF_2I_2N_2O_4Na^+$ requires 803.0796.

4-(2-(2-(2-Butoxyethoxy)ethoxy)ethoxy)benzaldehyde (A)

^{1}H NMR (600 MHz, $CDCl_3$)

^{13}C NMR (150 MHz, $CDCl_3$)

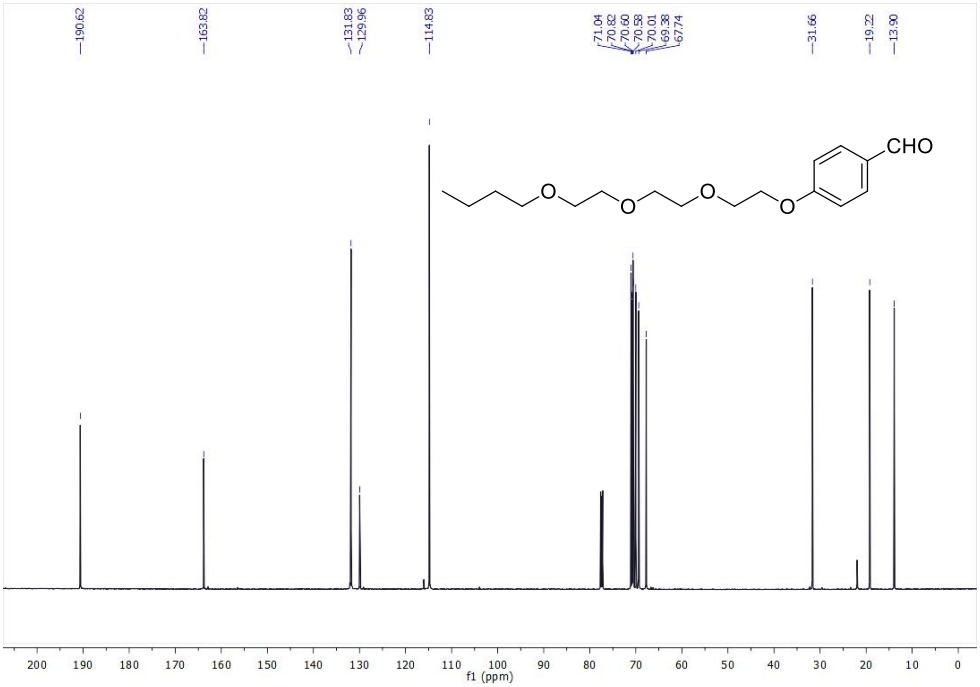

***Meso*-(4-(2-(2-(2-butoxyethoxy)ethoxy)ethoxy)phenyl)-1,3,5,7-tetramethyl BODIPY (B)**

^{1}H NMR (600 MHz, $CDCl_3$)

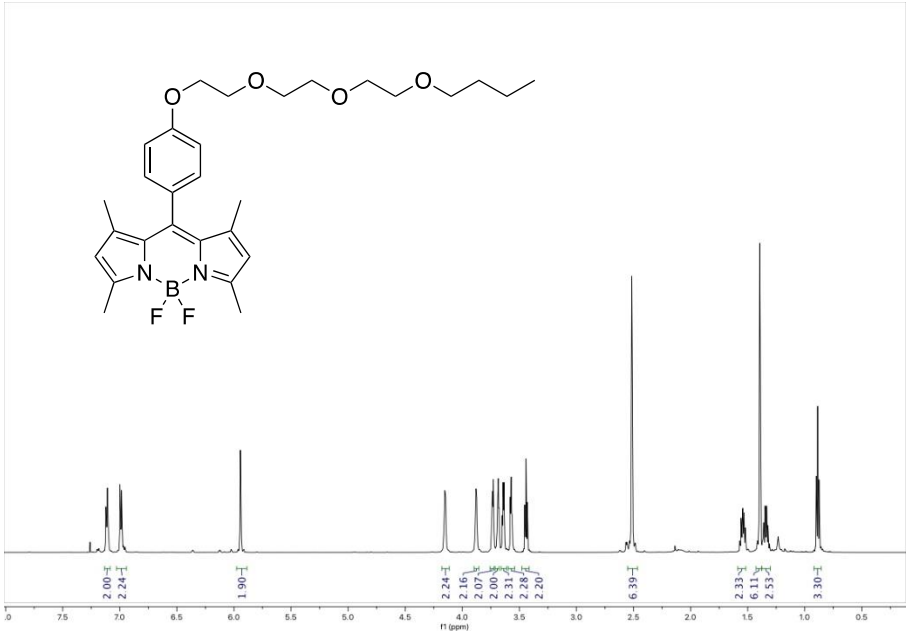

^{13}C NMR (150 MHz, $CDCl_3$)

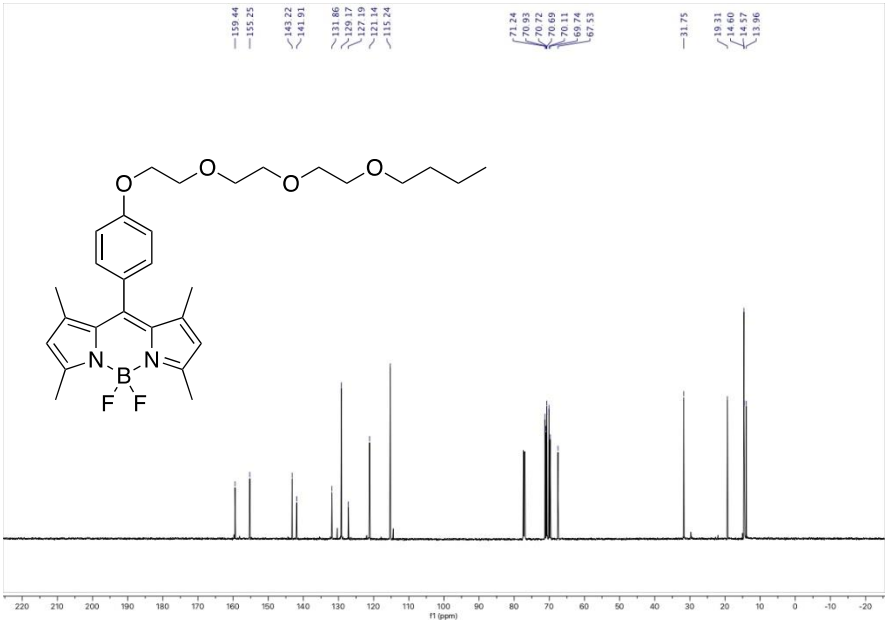

2,6-Diiodo-*meso*-(4-(2-(2-(2-butoxyethoxy)ethoxy)ethoxy)phenyl)-1,3,5,7-tetramethyl BODIPY (14b)

^{1}H NMR (600 MHz, $CDCl_3$)

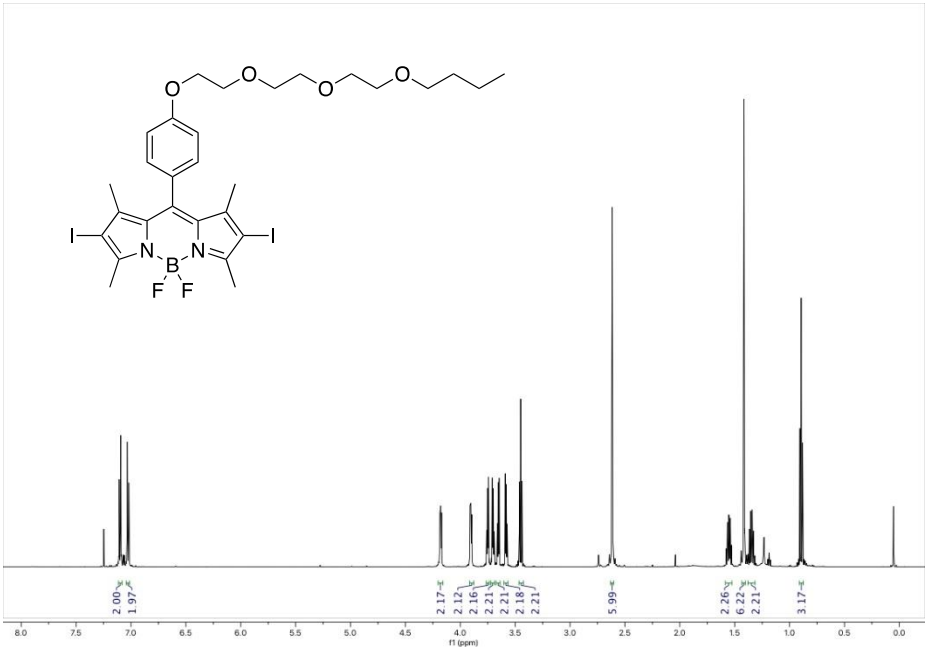

^{13}C NMR (150 MHz, $CDCl_3$)

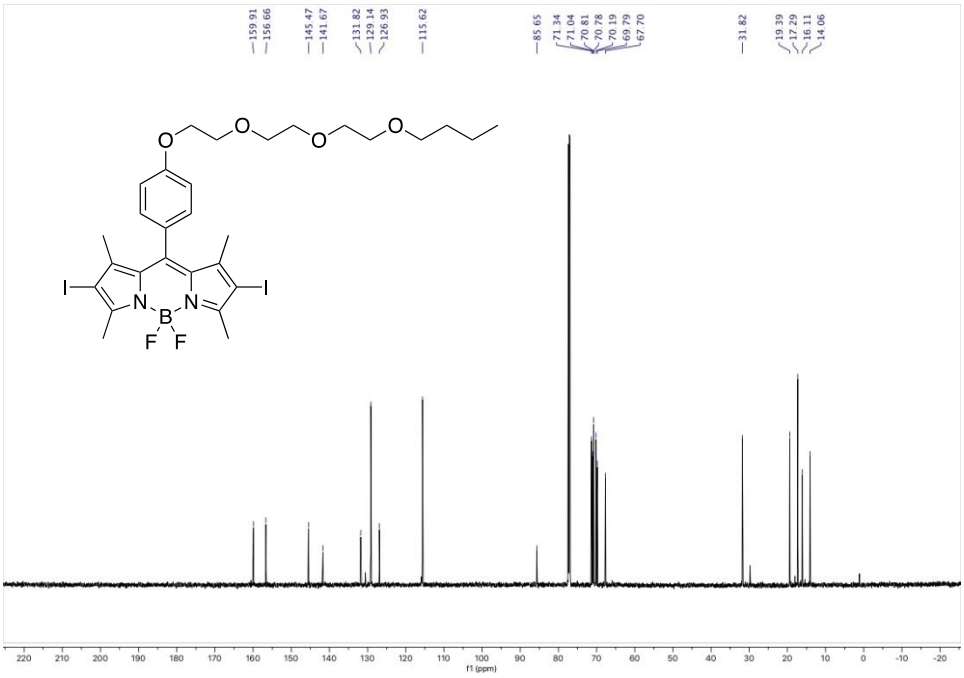

Synthesis and characterization of compound 15. General procedure (A) starting from 14a and m-Me-CB. Purification by flash column chromatography on silica gel (PE/DCM 6/4 v/v) gave 15 as a bright blue solid. (43%, Rf = 0.5 PE/DCM 6/4 v/v). 1 H NMR (600 MHz, $CDCl_3$): δ 7.54–7.52 (m, 3H), 7.37 (d, J = 8.2 Hz, 4H), 7.34–7.33 (m, 2H), 7.07 (d, J = 8.2 Hz, 4H), 6.87 (d, J = 16.5 Hz, 2H), 6.63 (d, J = 16.5 Hz, 2H), 3.18 (s, 4H), 2.74 (s, 6H), 1.64 (s, 6H), 1.47 (s, 6H). $^{13}C\{1\ H\}$ NMR (150 MHz, $CDCl_3$) δ: 155.4, 141.6, 138.9, 137.1, 136.4, 135.4, 131.6, 131.0, 130.4, 129.4, 129.3, 129.0, 128.4, 128.2, 126.2, 120.0, 70.9, 42.8, 24.7, 14.2, 13.1. 11B{1 H} NMR (128.38 MHz, $CDCl_3$) δ: 0.99 (s, 1B, BF2) − 6.17 (s, 2B), − 7.88 (s, 2B), − 10.50 (br s, 12B), − 13.04 (s, 4B). ESIHRMS [M+Na]+: m/z 891.6674; $C_{43}H_{59}B_{21}F_2N_2Na$ + requires 891.6638.

Synthesis and characterization of compound 16. Isolated by flash column chromatography on silica gel (PE/DCM 6/4 v/v) from the crude reaction mixture giving compound 16 (6%, Rf = 0.6 PE/DCM 6:4 v/v). 1 H NMR (600 MHz, $CDCl_3$): δ 7.50–7.49 (m, 3H), 7.38 (d, J = 8.2 Hz, 2H), 7.35–7.33 (m, 2H), 7.23 (d, J = 8.3 Hz, 2H), 7.07 (d, J = 8.2 Hz, 2H), 7.02 (d, J = 8.3 Hz, 2H), 6.88 (d, J = 16.5 Hz, 1H), 6.63 (d, J = 16.5, 1H), 5.84 (s, 1H), 5.10 (s, 1H), 3.18 (s, 2H), 3.16 (s, 2H), 2.73 (s, 3H), 2.37 (s, 3H), 1.64 (s, 3H), 1.63 (s, 3H), 1.48 (s, 3H), 1.22 (s, 3H). 13C {1 H} NMR (150 MHz, $CDCl_3$): δ 155.2, 155.0, 140.7, 140.5, 139.4, 138.8, 136.7, 136.3, 135.3, 131.5, 130.8, 130.3, 130.1, 129.3, 129.2, 128.7, 128.2, 126.5, 126.2, 120.1, 117.6, 80.4, 70.8, 42.7, 42.6, 29.8, 24.6, 14.1, 13.5, 13.0, 12.9. 11B{1 H} NMR (128.38 MHz, $CDCl_3$) δ: 1.01 (s, 1B, BF2), − 6.24 (s, 2B), − 7.91 (s, 2B), − 10.50 (br s, 12B), − 13.04 (s, 4B). ESI-HRMS [M+Na]+: m/z 891.6618; C43H59B21F2N2Na + requires 891.6638

Synthesis and characterization of compound 17. General procedure (A) starting from 14a and m-Ph-CB. Purification by flash column chromatography on silica gel (PE/DCM 6/4 v/v) gave 17 as a bright blue solid (57%, Rf = 0.4 PE/DCM 6/4 v/v). 1 H NMR (600 MHz, CDCl3): δ 7.49–7.40 (m, 4H), 7.33–7.24 (m, 11H), 7.15 (d, J = 7.9 Hz, 4H), 7.02 129.2, 128.9, 128.6, 128.3, 127.8, 126.2, 120.0, 78.2, 76.3, 42.9, 14.1, 13.0. 11B{1 H} NMR (128.38 MHz, CDCl3) δ: 0.95 (s, 1B, BF2), − 5,90 (s, 4B), − 10.66 (br s, 12B), − 13.51 (s, 4B). ESI-HRMS [M+Na]+: m/z 1015.6956; C53H63B21F2N2Na + requires 1015.6951.

Synthesis and characterization of compound 18. General procedure (A) starting from 14b and m-Ph-CB. Purification by flash column chromatography on silica gel (DCM) gave 18 as a bright blue solid (52%, Rf = 0.55 DCM). ^{1} H NMR (600 MHz, CDCl3): δ 7.38 (d, J = 8.2 Hz, 4H), 7.35 (d, J = 8.6 Hz, 4H), 7.26–7.18 (m, 8H), 7.10 (d, J = 8.1 Hz, 4H), 7.06 (d, J = 8.7 Hz, 2H), 6.88 (d, J = 16.5 Hz, 2H), 6.62 (d, J = 16.5 Hz, 2H), 4.23–4.20 (m, 2H), 3.95–3.92 (m, 2H), 3.79–3.76 (m, 2H), 3.75–3.70 (m, 2H), 3.70–3.66 (m, 2H), 3.62–3.58 (m, 2H), 3.47 (t, J = 6.8 Hz, 2H), 3.26 (s, 4H), 2.72 (s, 6H), 1.58–1.54 (m, 2H), 1.52 (s, 6H), 1.40–1.33 (m, 2H), 0.91 (t, J = 7.4 Hz, 3H). ^{13}C{^{1} H} NMR (150 MHz, CDCl3): δ 155.2, 139.0, 137.2, 136.3, 135.4, 132.0, 130.9, 130.4, 129.6, 129.4, 128.9, 128.7, 128.4, 127.9, 127.6, 127.2, 126.3, 120.2, 115.5, 78.3, 76.4, 71.4, 71.1, 70.9, 70.8, 70.2, 69.9, 67.7, 43.0, 31.8, 29.8, 19.4, 14.1, 13.4. ^{11}B {^{1} H} NMR (128.38 MHz, CDCl3) δ:0.93 (s, 1B, BF2), − 5.92 (s, 4B), − 10.64 (br s, 12B), − 13.48 (s, 4B). ESI-HRMS [M+Na]+: m/z 1219.8335; $C_{63}H_{83}B_{21}F_2N_2O_4Na$ + requires 1219.8318.

Synthesis and characterization of compound 19. A round -bottomed flask equipped with a reflux condenser was charged with 3 mL of dry 1,4-dioxane, and the solvent was degassed with nitrogen for 15 min. The carborane m-Me-CB (1 equiv.) and mono-iodinated BODIPY derivative 14c (1.1 equiv.) were

added, followed by [$Pd_2(dba)_3$] (1.2 mol%), [$Pd(tBu_3P)_2$] (1.6 mol%) and Cy_2NMe (1.34 equiv.). The reaction mixture was heated at reflux overnight. After complete conversion of the starting material (as monitored by TLC analysis), the mixture was filtered over celite, washed with THF and concentrated to dryness. The crude residue was purified by flash column chromatography on silica gel (PE/DCM 7/ 3 v/v) to give 19 as a bright purple solid (72%, R_f = 0.4 PE/DCM 7/3 v/v). ^{1} H NMR (600 MHz, CDCl3): δ 7.53–7.46 (m, 3H), 7.36 (d, J = 8.1 Hz, 2H), 7.31–7.27 (m, 2H), 7.05 (d, J = 8.2 Hz, 2H), 6.86 (d, J = 16.5 Hz, 1H), 6.60 (d, J = 16.5 Hz, 1H), 6.00 (s, 1H), 3.16 (s, 2H), 2.71 (s, 3H), 2.57 (s, 3H), 1.46 (s, 3H), 1.37 (s, 3H). 13C{1 H} NMR (150 MHz, CDCl3): δ 156.1, 154.8, 143.6, 141.8, 138.7, 137.1, 136.4, 135.2, 131.9, 131.2, 130.7, 130.3, 129.3, 129.2, 128.6, 128.2, 126.2, 121.7, 120.1, 76.8, 70.8, 42.8, 24.6, 14.8, 14.6, 14.1, 13.0.

Synthesis and characterization of compound 21. To a stirred solution of 20 (0.13 mmol) in dry DCM (30 mL) under a positive N_2 atmosphere was added N-iodosuccinimide (NIS, 0.26 mmol, 2 eq.), and the reaction mixture was stirred at RT overnight. The mixture was then washed with water, dried over Na_2SO_4 and purified by flash column chromatography on silica gel (PE/DCM 75/25 v/v) to give 6 as purple solid (84%, Rf = 0.55 PE/DCM 75/25 v/v). 1 H NMR (600 MHz, $CDCl_3$): δ 7.48–7.43 (m, 3H), 7.30 (d, J = 8.3 Hz, 2H), 7.24–7.20 (m, 2H), 6.99 (d, J = 8.1 Hz, 2H), 6.77 (d, J = 16.5 Hz, 1H), 6.55 (d, J = 16.5 Hz, 1H), 3.10 (s, 2H), 2.65 (s, 3H), 2.58 (s, 3H), 1.56 (s, 3H), 1.34 (s, 3H), 1.31 (s, 3H). ^{13}C {^{1} H} NMR (150 MHz, CDCl3): δ 157.2, 155.0, 143.6, 141.4, 140.3, 136.8, 136.6, 135.1, 131.5, 131.3, 130.3, 129.7, 129.4, 128.1, 126.2, 119.6, 84.8, 76.6, 70.8, 42.7, 29.8, 24.6, 16.9, 16.0, 14.3, 13.1.

Synthesis and characterization of compound 20. General procedure (B) starting from 20 and *o*-Ph-CB. Purification by flash column chromatography on silica gel (PE/DCM 6/4 v/v) gave 20 as a bright blue solid (55%, Rf = 0.35

PE/DCM 75/25 v/v). ^{1}H NMR (600 MHz, $CDCl_3$): δ 7.72 (d, J = 7.7 Hz, 2H), 7.57–7.50 (m, 4H), 7.49–7.43 (m, 2H), 7.38 (d, J = 8.1 Hz, 2H), 7.34–7.32 (m, 2H), 7.29 (d, J = 8.1 Hz, 2H), 7.07 (d, J = 8.0 Hz, 2H), 6.87 (d, J = 16.3 Hz, 1H), 6.85 (d, J = 16.3 Hz, 1H), 6.78 (d, J = 8.1 Hz, 2H), 6.62 (d, J = 16.5 Hz, 1H), 6.58 (d, J = 16.5 Hz, 1H), 3.18 (s, 2H), 3.07 (s, 2H), 2.73 (s, 3H), 2.72 (s, 3H), 1.64 (s, 3H), 1.47 (s, 3H), 1.46 (s, 3H). $^{13}C\{^{1}H\}$ NMR (150 MHz, $CDCl_3$): δ 155.4, 155.3, 141.6, 138.9, 137.4, 137.1, 136.4, 135.4, 134.5, 131.6, 131.6, 131.0, 130.9, 130.7, 130.5, 130.4, 129.4, 129.3, 129.2, 129.0, 128.9, 128.4, 126.2, 126.1, 120.3, 120.0, 83.8, 82.1, 70.8, 42.8, 40.8, 32.1, 24.7, 22.8, 14.2, 13.1. $^{11}B\{^{1}H\}$ NMR (128.38 MHz, CDCl3) δ: 1.08 (s, 1B, BF_2), − 3.17 (s, 2B), − 6.22 (s, 1B), − 7.98 (s, 1B), − 10.24 (br s, 14B), − 12.93 (s, 2B). ESI HRMS [M+Na]+: m/z 953.6817; $C_{48}H_{61}B_{21}F_2N_2Na$ + requires 953.6794.

Synthesis and characterization of compound 22. General procedure (B) starting from 20 and m-Ph-CB. Purification by flash column chromatography on silica gel (PE/DCM 7/3 v/v) gave 22 as a bright blue solid. (35%, Rf = 0.21 PE/DCM 7/3 v/v). ^{1}H NMR (600 MHz, $CDCl_3$): δ 7.53 (m, 3H), 7.38–7.33 (m, 9H), 7.23–7.21 (m, 2H), 7.10–7.06 (m, 4H), 6.87 (d, J = 16.5 Hz, 2H), 6.62 (d, J = 16.5 Hz, 2H), 3.26 (s, 2H), 3.18 (s, 2H), 2.74 (s, 6H), 1.64 (s, 3H), 1.47 (s, 6H). $^{13}C\{^{1}H\}$ NMR (150 MHz, $CDCl_3$): δ 155.4, 141.6, 138.9, 137.1, 137.1, 136.4, 136.3. 135.4, 132.0, 131.0, 130.9, 130.4, 129.4, 129.3, 129.0, 128.7, 128.4, 127.9, 126.3, 126.2, 121.0, 120.0, 78.3, 76.8, 76.3, 70.9, 43.0, 42.8, 24.7, 14.2, 13.1. $^{11}B\{^{1}H\}$ NMR (128.38 MHz, $CDCl_3$) δ: 1.01 (br s, 1B, BF_2), − 6.05 (s, 3B), − 7.85 (s, 1B), − 10.46 (s, 12B), − 13.01 (s, 4B). ESI-HRMS [M+Na]+: m/ z 953.6824; C48H61B21F2N2Na + requires 953.6794.
Synthesis and characterization of compound 23. General procedure (A) starting from 14d and m-Ph-CB. Purification by flash column chromatography on silica gel (PE/DCM 7/3 v/v) gave 23 as a bright blue solid. (30%, Rf = 0.33

PE/DCM 7/3 v/v). [1] H NMR (600 MHz, CDCl3): δ 7.79 (d, J = 16.3 Hz, 2H), 7.62 (d, J = 8.1 Hz, 4H), 7.56–7.50 (m, 6H), 7.37–7.36 (m, 4H), 7.32 (d, J = 16.3 Hz, 2H), 7.25–7.21 (m, 5H), 7.19 (d, J = 8.1 Hz, 4H), 6.93 (d, J = 4.5 Hz, 2H), 6.82 (d, J = 4.4 Hz, 2H), 3.30 (s, 4H). ^{13}C{1 H} NMR (150 MHz, CDCl3): δ 154.8, 139.8, 138.0, 136.4, 136.2, 135.9, 135.3, 134.4, 130.6, 130.5, 130.0, 129.9, 128.7, 128.4, 127.9, 129.9, 119.7, 116.5, 78.4, 76.1, 43.1. ESI-MS [M+H]+: m/ z 939.16.

Compound 15

^{1}H NMR (600 MHz, $CDCl_3$)

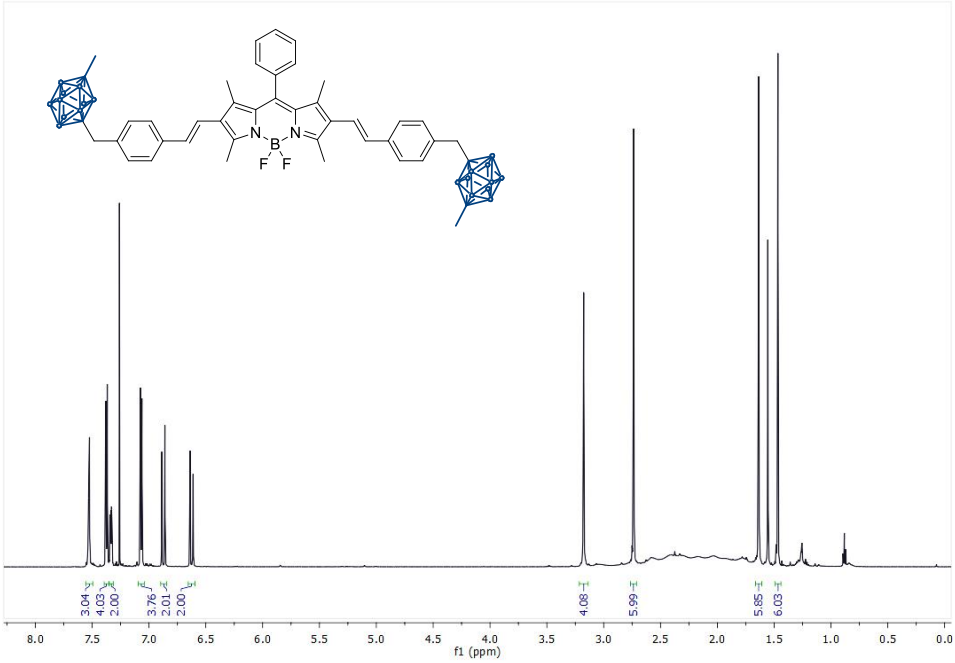

^{13}C NMR (150 MHz, $CDCl_3$)

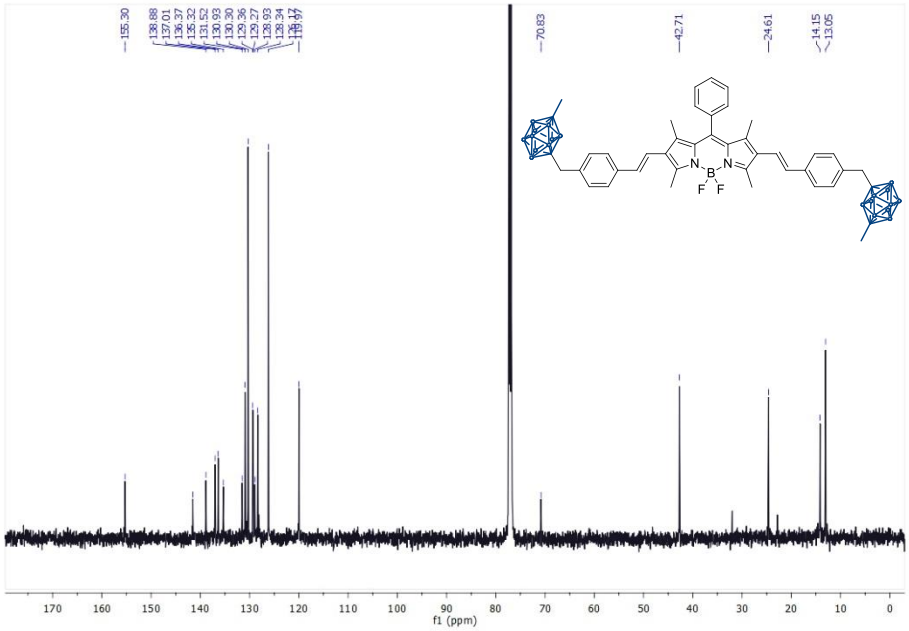

$^{11}B\{^{1}H\}$ NMR (128.38 MHz, $CDCl_3$)

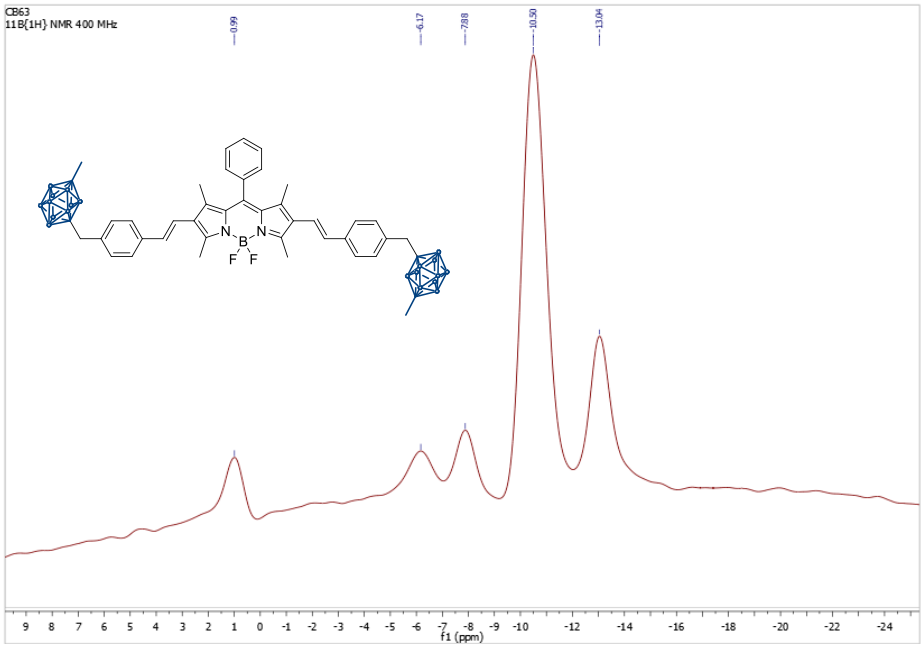

ESI(+)-HRMS

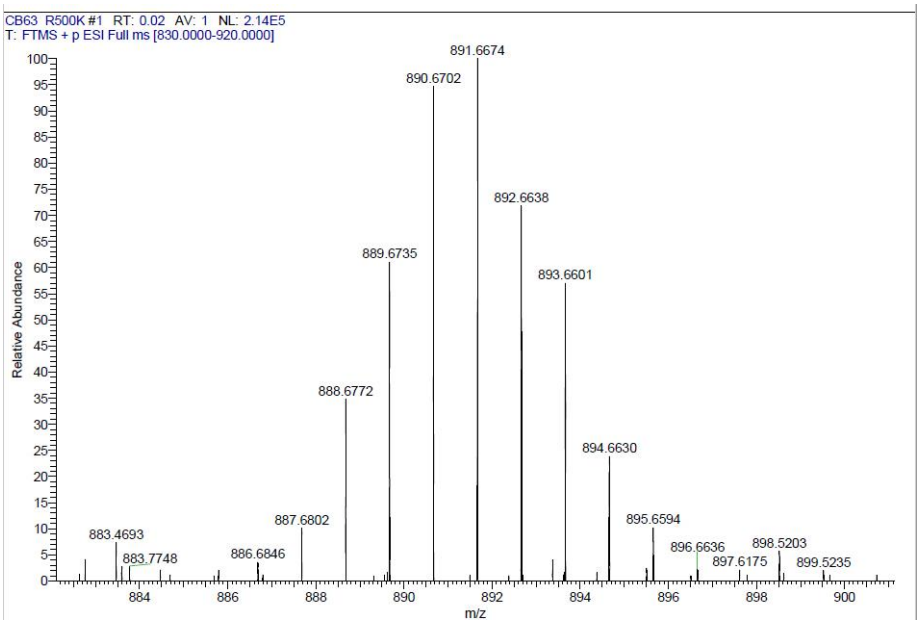

Compound 16

^{1}H NMR (600 MHz, $CDCl_3$)

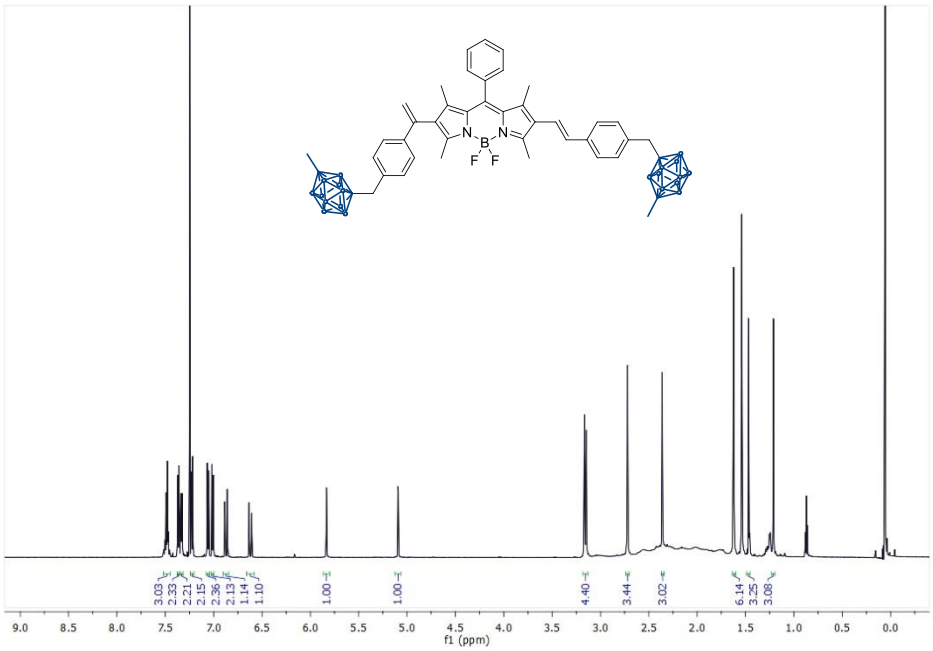

^{13}C NMR (150 MHz, $CDCl_3$)

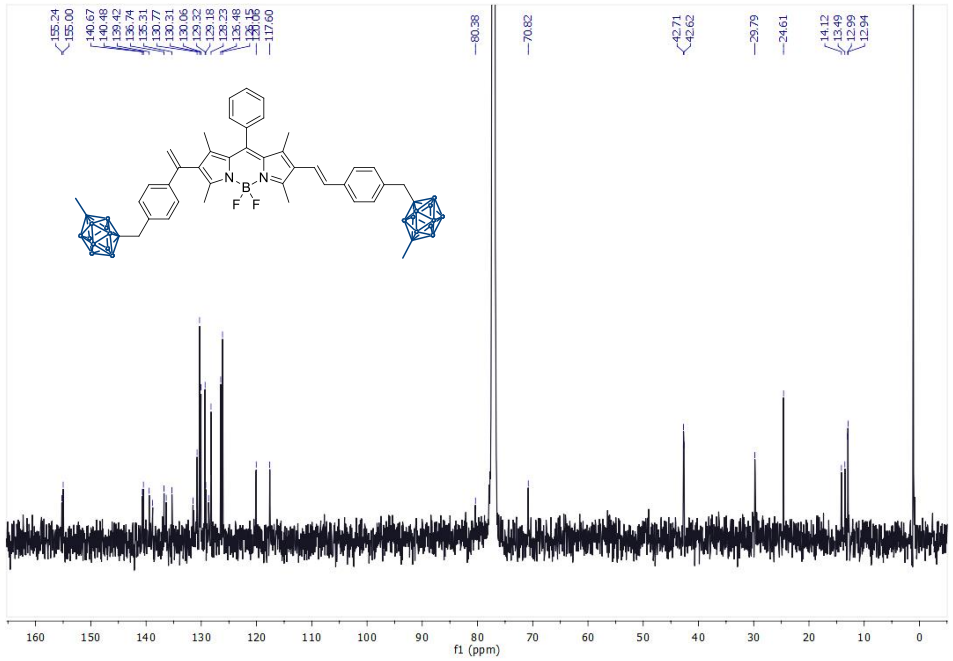

$^{11}B\{^{1}H\}$ NMR (128.38 MHz, $CDCl_3$)

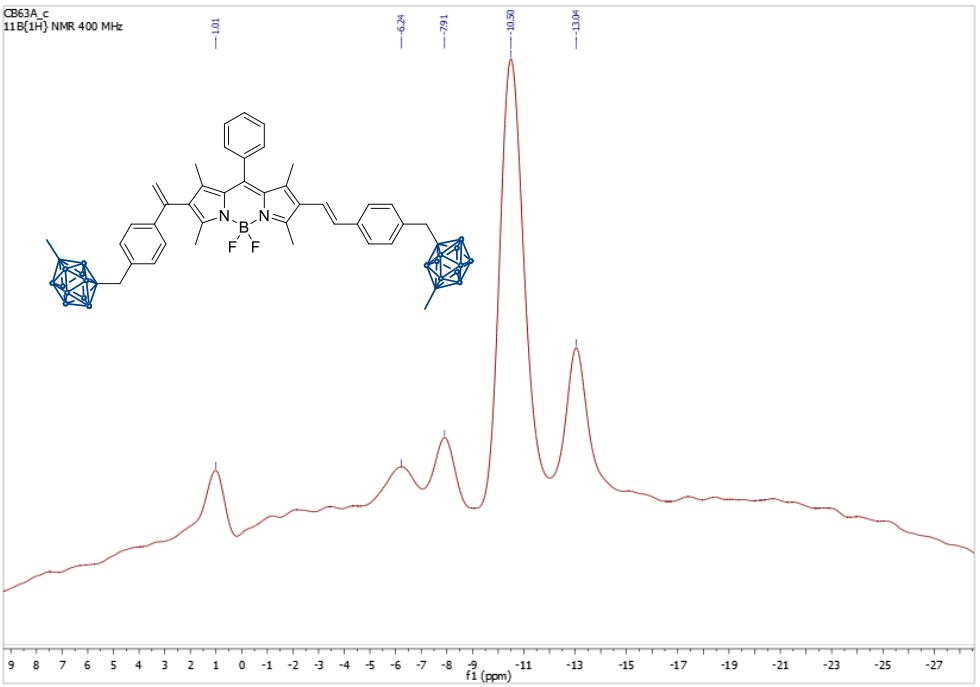

ESI(+)-HRMS

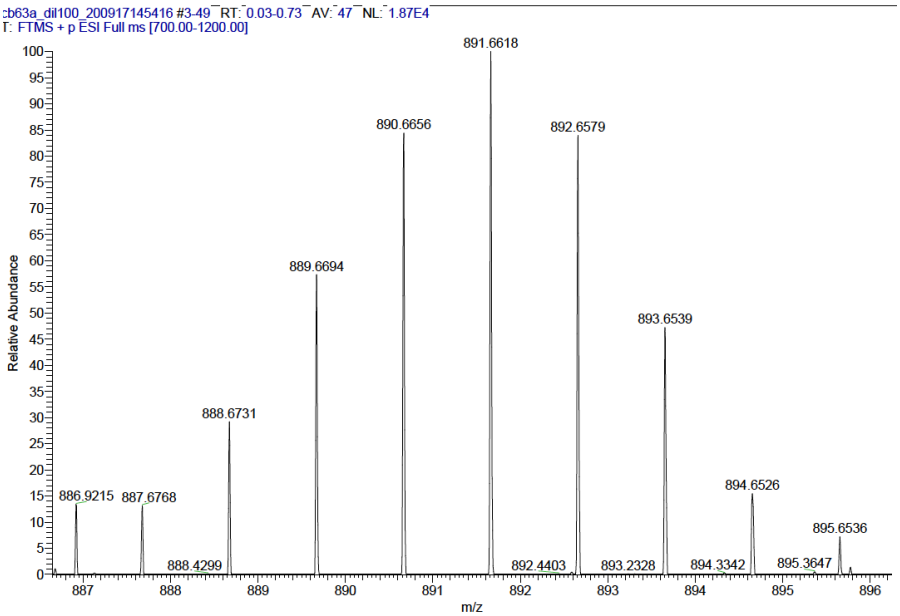

Compound 17

^{1}H NMR (600 MHz, $CDCl_3$)

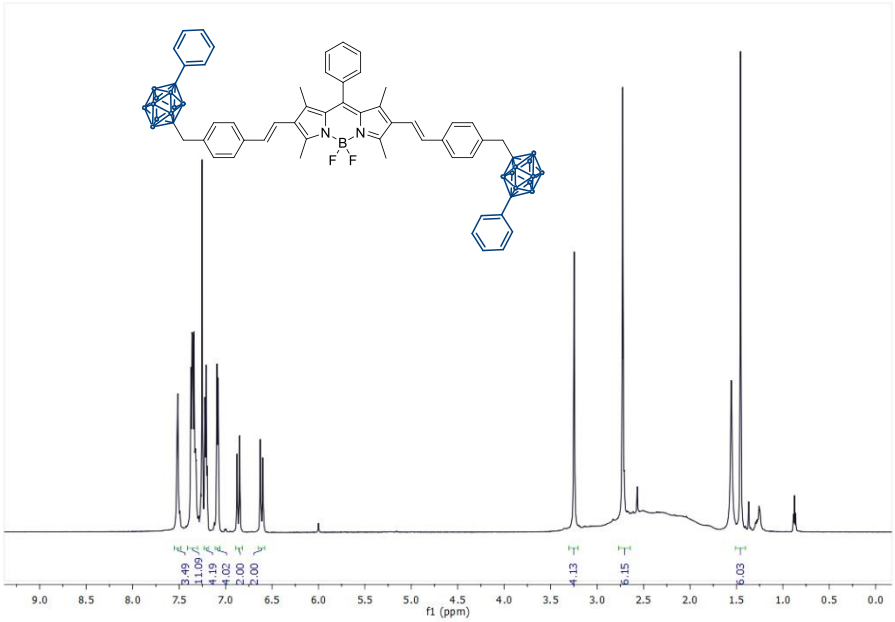

^{13}C NMR (150 MHz, $CDCl_3$)

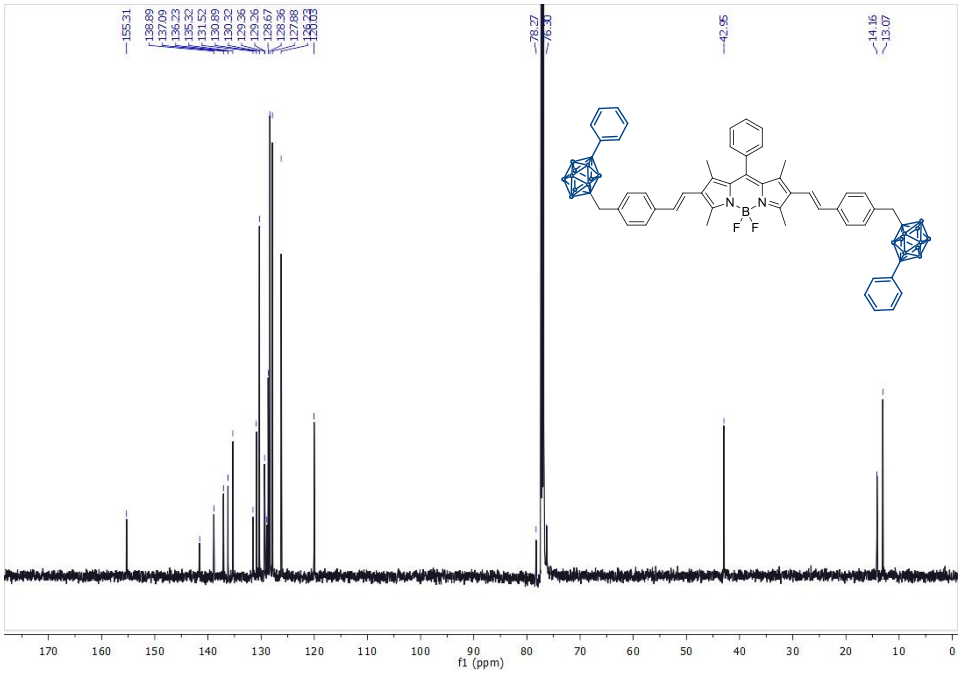

$^{11}B\{^{1}H\}$ NMR (128.38 MHz, $CDCl_3$)

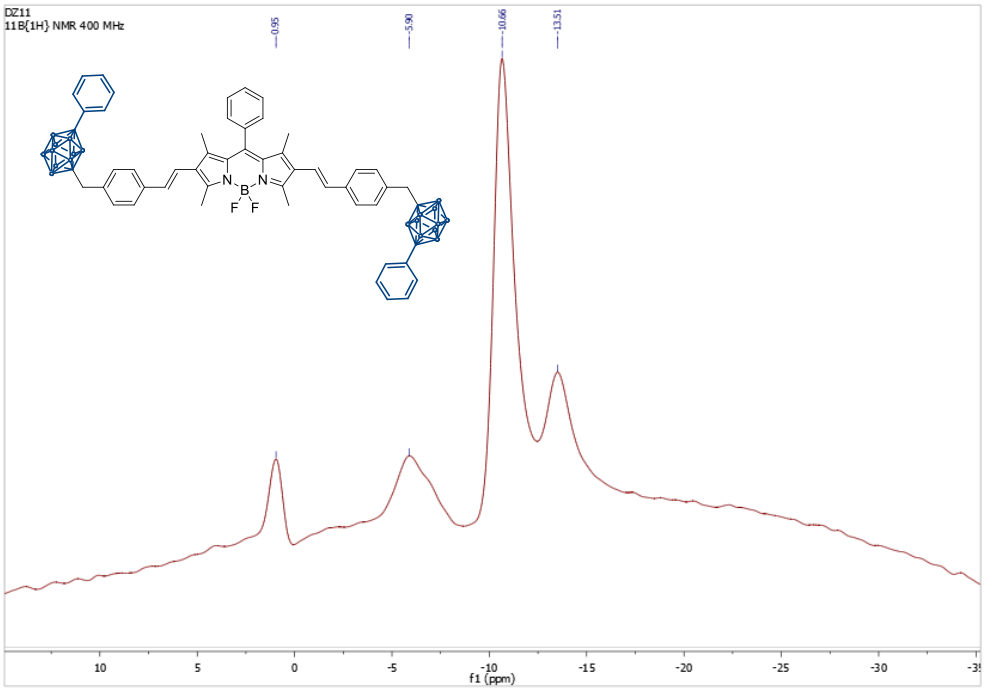

ESI(+)-HRMS

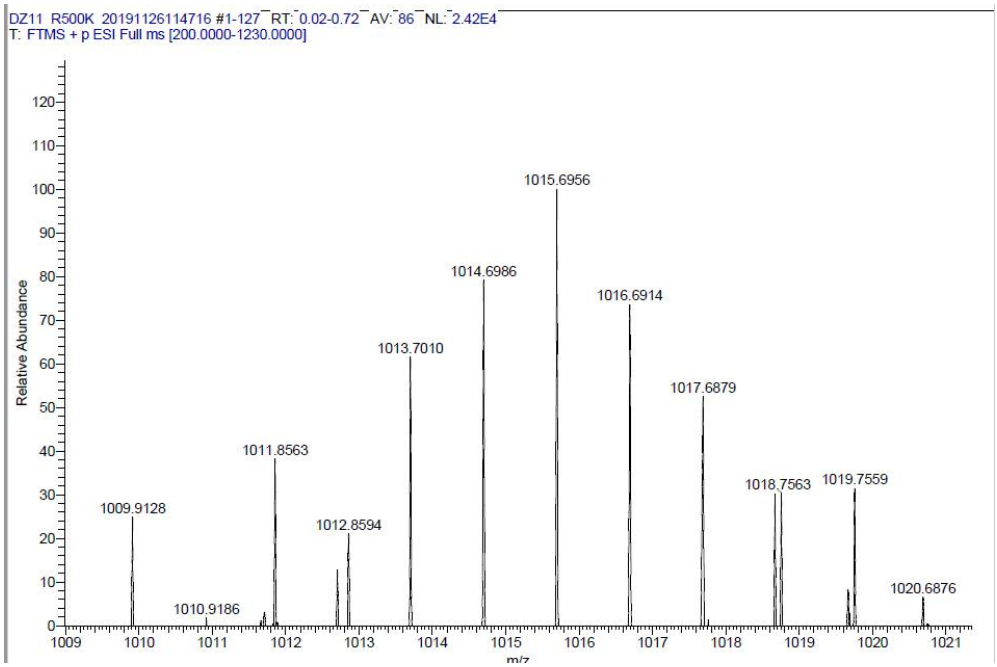
DZ11 R500K 20191126114716 #1-127 RT: 0.02-0.72 AV: 86 NL: 2.42E4
T: FTMS + p ESI Full ms [200.0000-1230.0000]
Relative Abundance
m/z
1009.9128
1010.9186
1011.8563
1012.8594
1013.7010
1014.6986
1015.6956
1016.6914
1017.6879
1018.7563
1019.7559
1020.6876

Compound 18

^{1}H NMR (600 MHz, $CDCl_3$)

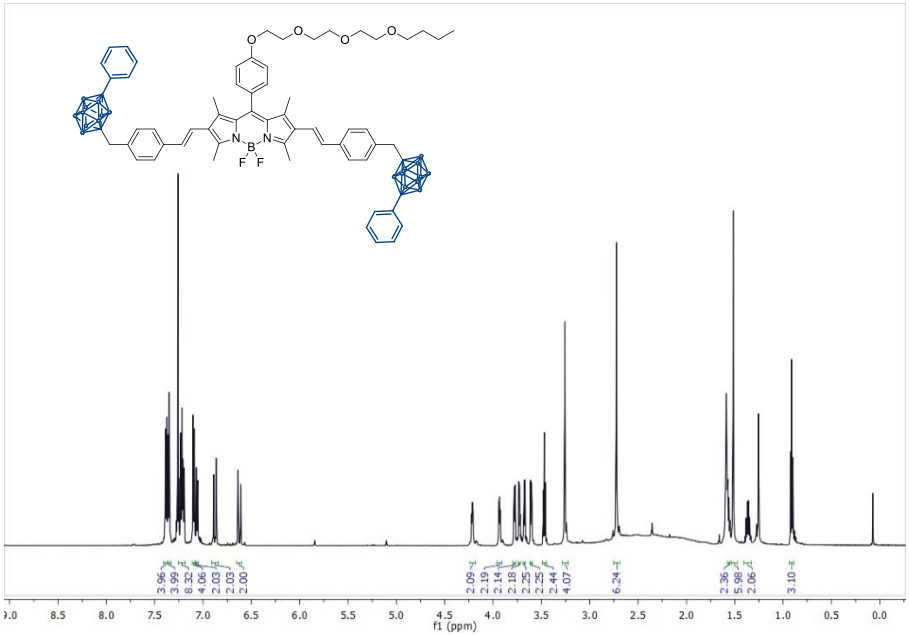

^{13}C NMR (150 MHz, $CDCl_3$)

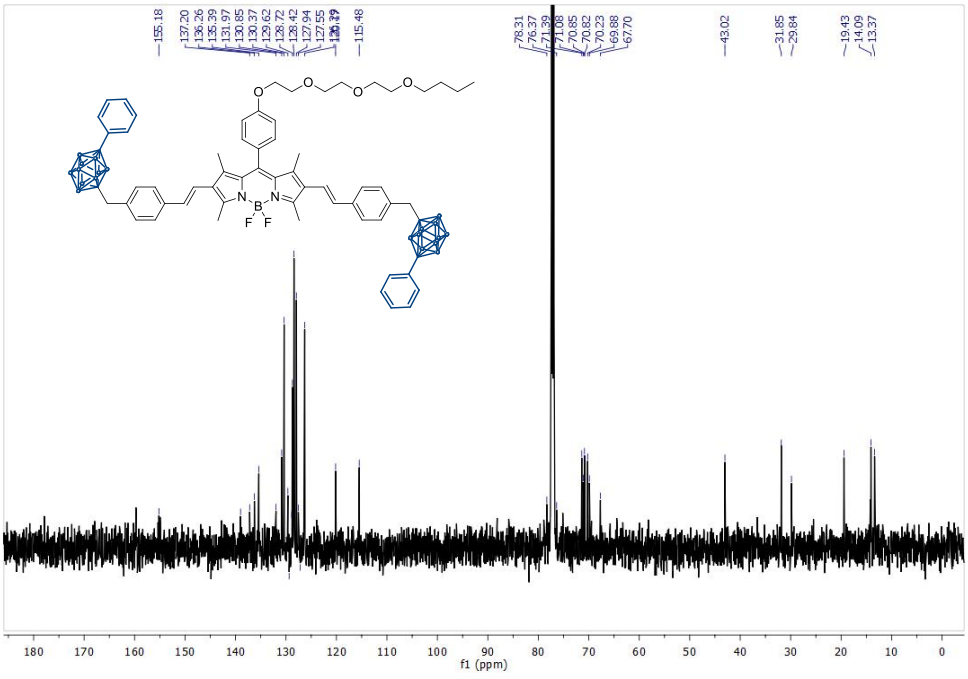

$^{11}B\{^{1}H\}$ NMR (128.38 MHz, $CDCl_3$)

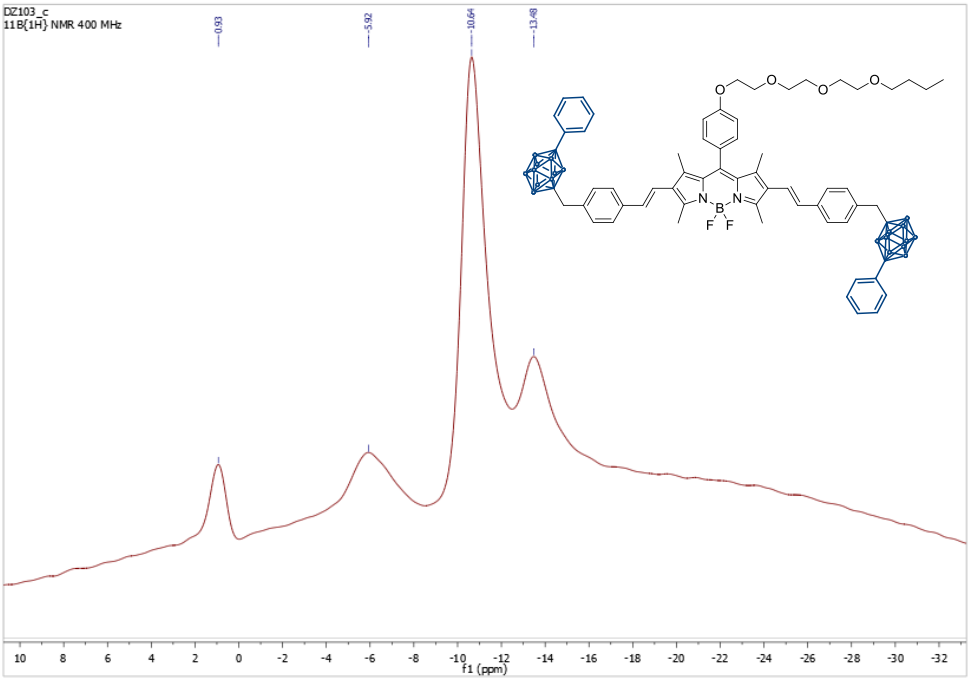

ESI(+)-HRMS

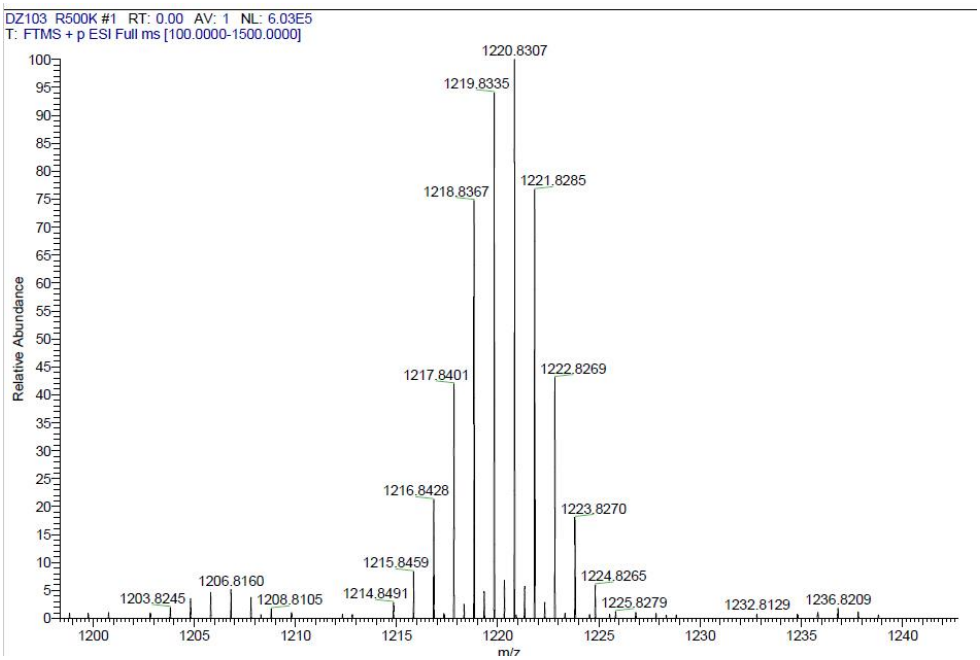

Compound 19

^{1}H NMR (600 MHz, $CDCl_3$)

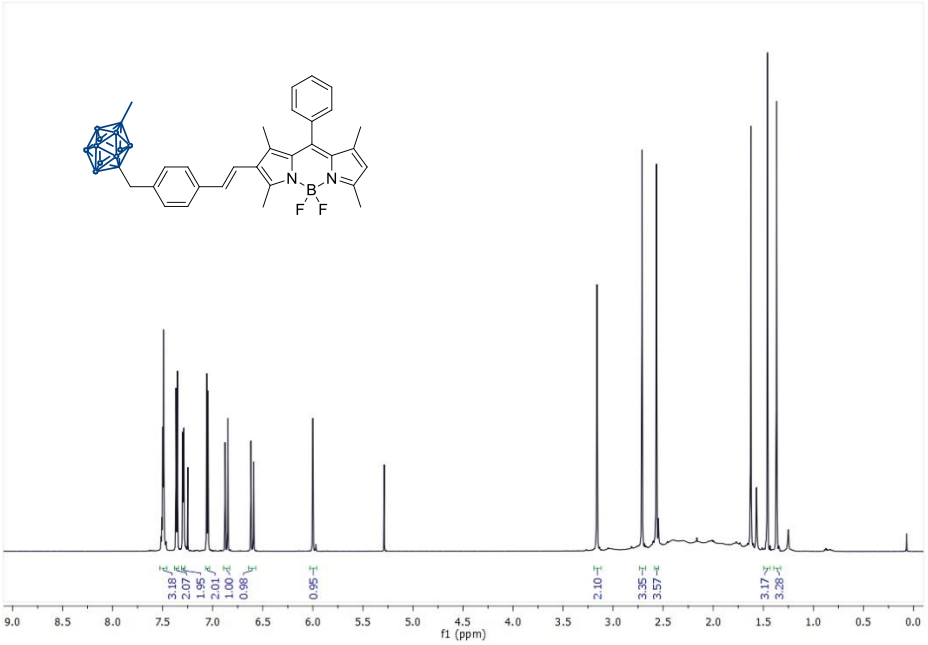

^{13}C NMR (150 MHz, $CDCl_3$)

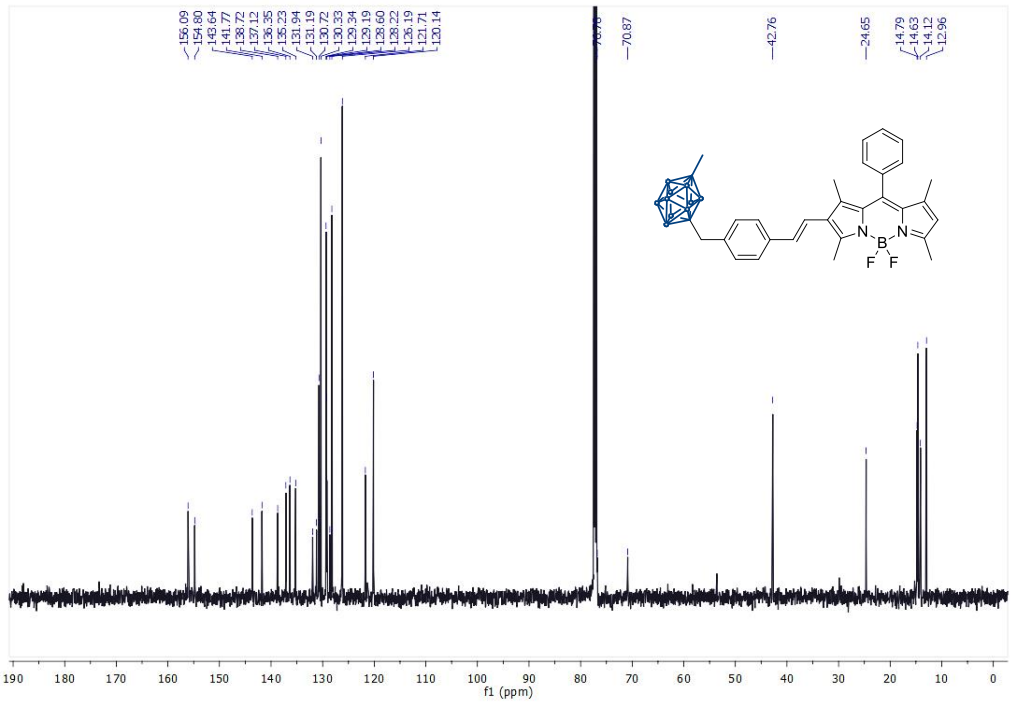

Compound 20

^{1}H NMR (600 MHz, $CDCl_3$)

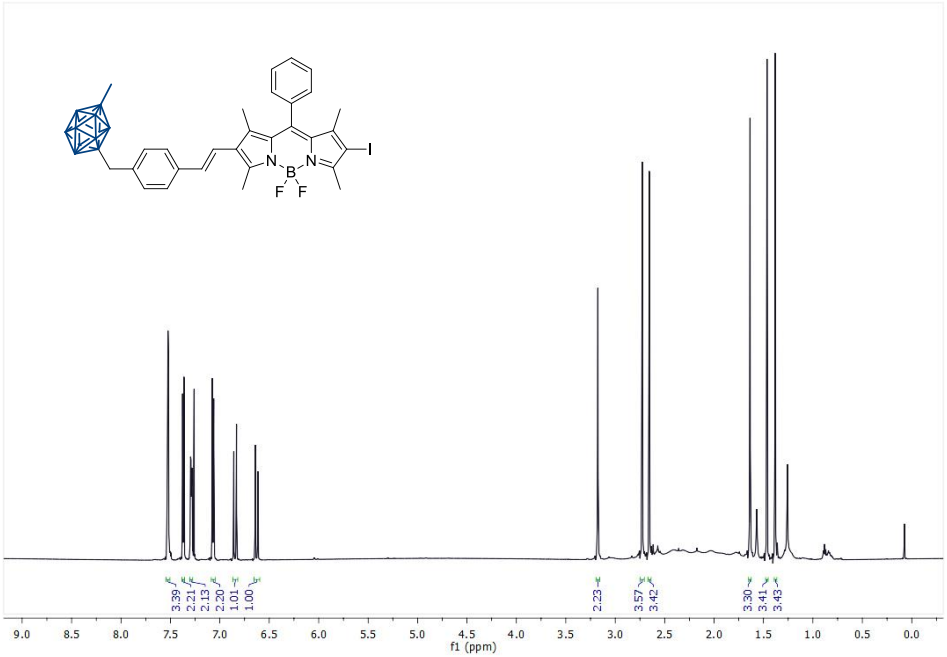

^{13}C NMR (150 MHz, $CDCl_3$)

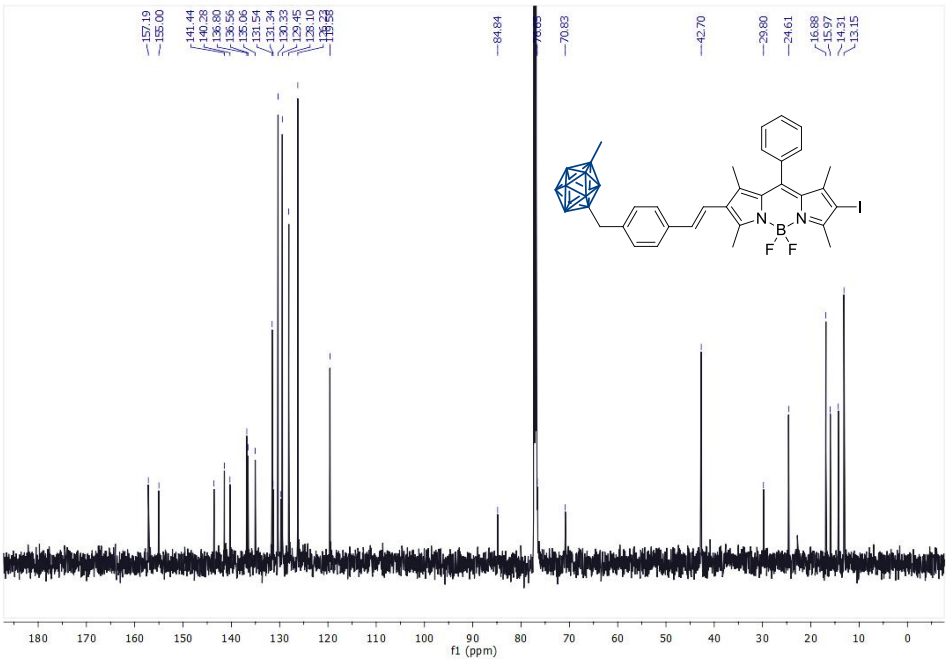

Compound 21

^{1}H NMR (600 MHz, $CDCl_3$)

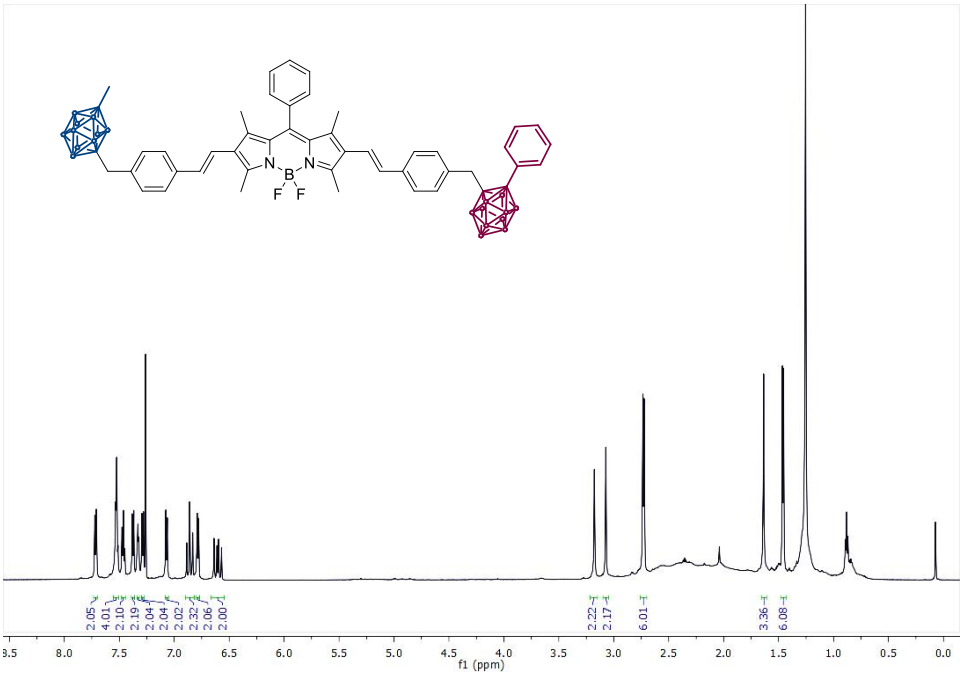

^{13}C NMR (150 MHz, $CDCl_3$)

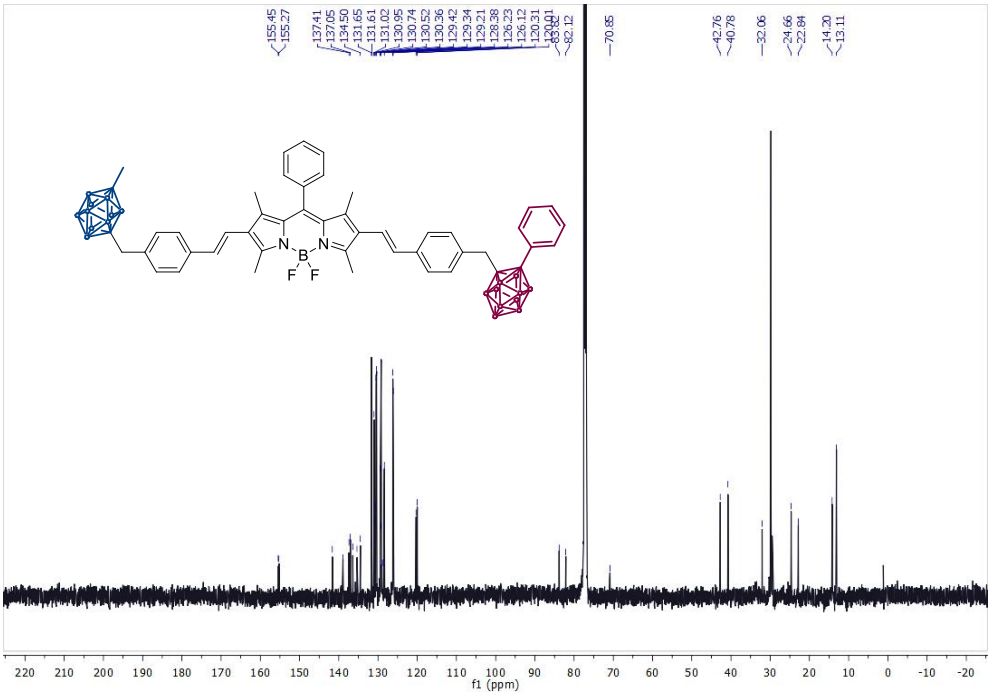

^{11}B{^{1}H} NMR (128.38 MHz, $CDCl_3$)

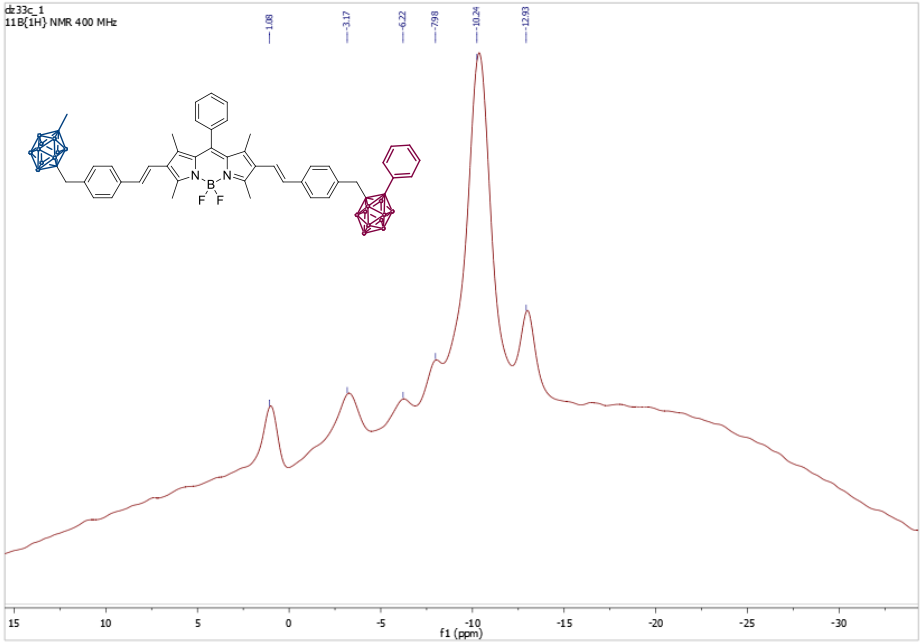
dz33c_1
11B{1H} NMR 400 MHz
1.08
-3.17
-6.22
-7.98
-10.24
-12.93
15
10
5
0
-5
-10
-15
-20
-25
-30
f1 (ppm)

ESI(+)-HRMS

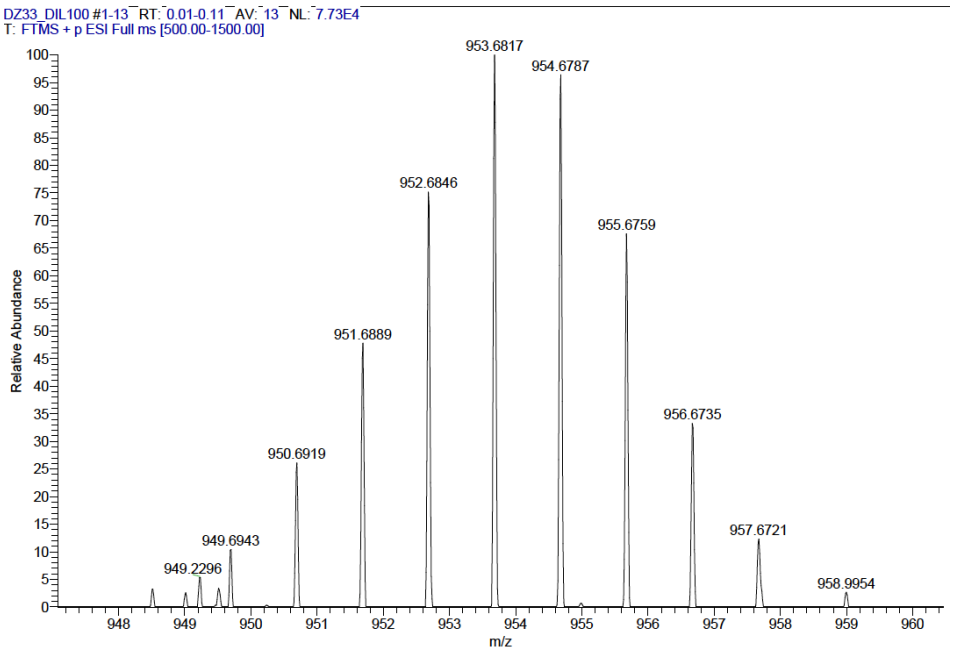
DZ33_DIL100 #1-13 RT: 0.01-0.11 AV: 13 NL: 7.73E4
T: FTMS + p ESI Full ms [500.00-1500.00]
Relative Abundance
m/z
953.6817
954.6787
952.6846
955.6759
951.6889
956.6735
950.6919
957.6721
949.6943
958.9954
949.2296

Compound 22

^{1}H NMR (600 MHz, $CDCl_3$)

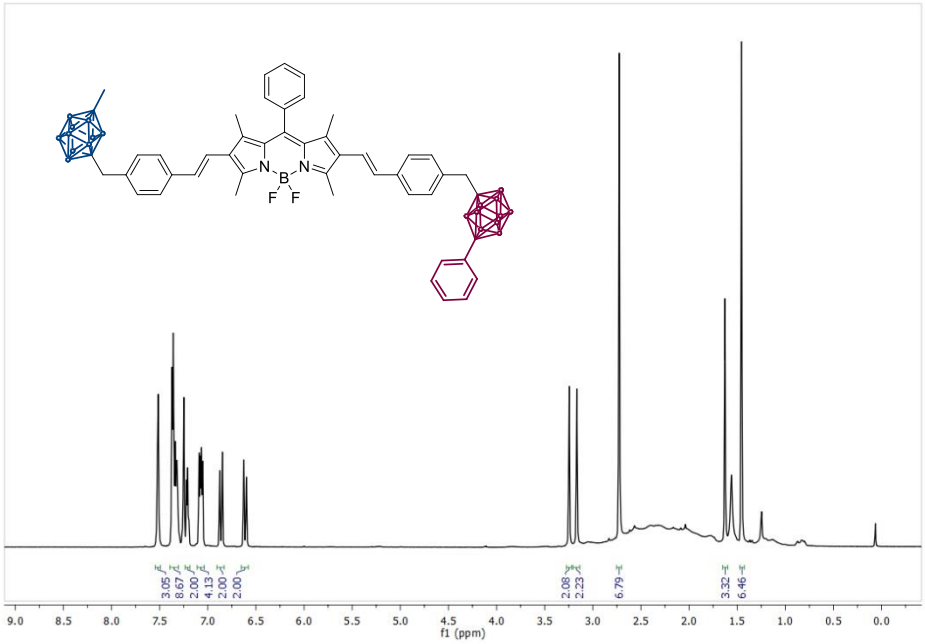

^{13}C NMR (150 MHz, $CDCl_3$)

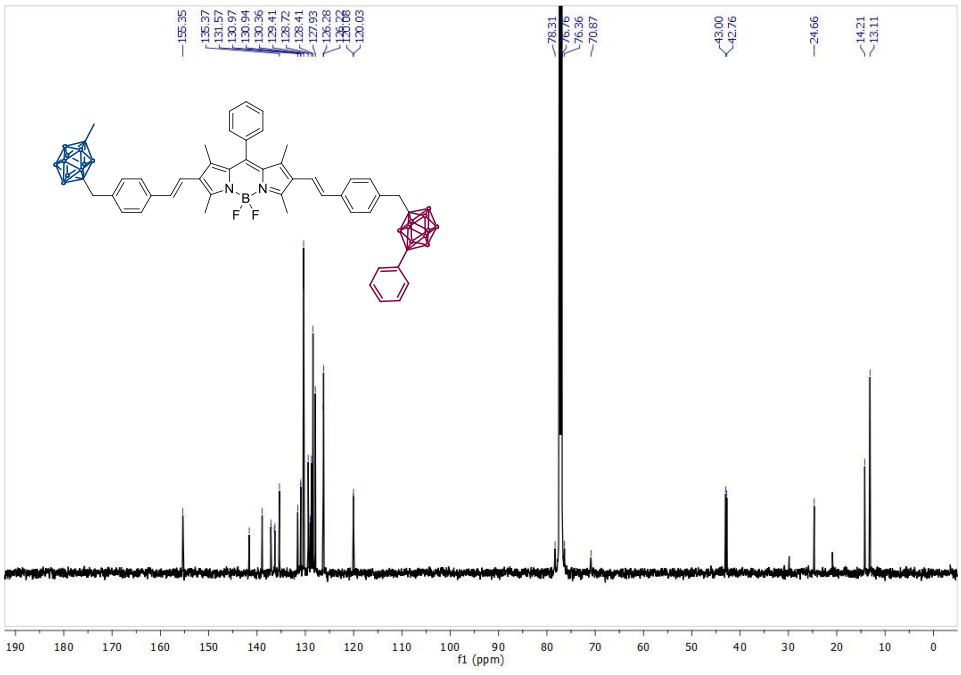

$^{11}B\{^{1}H\}$ NMR (128.38 MHz, $CDCl_3$)

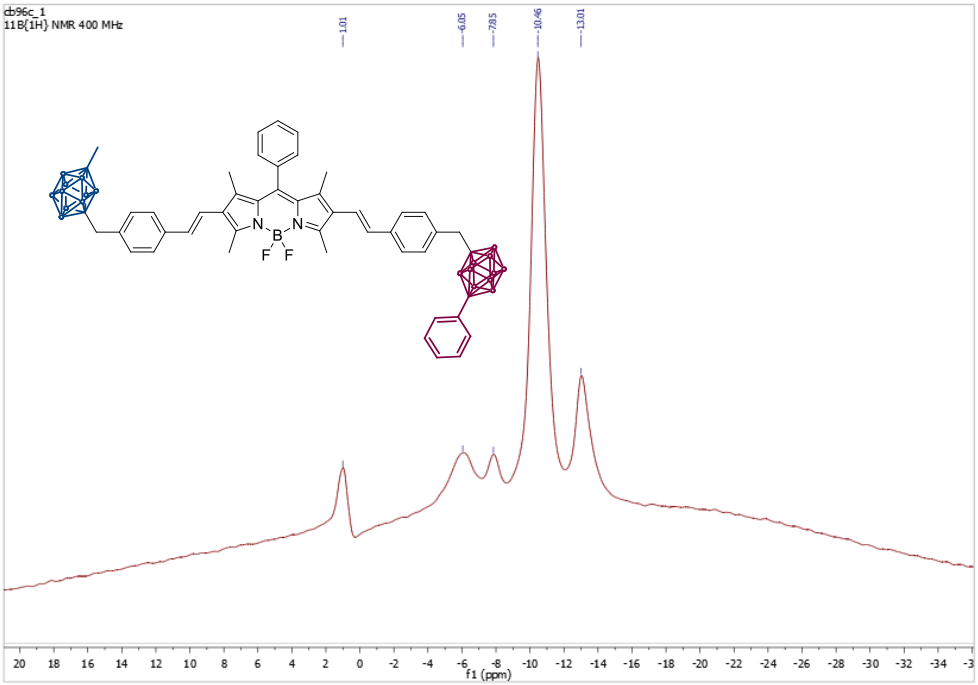

ESI(+)-HRMS

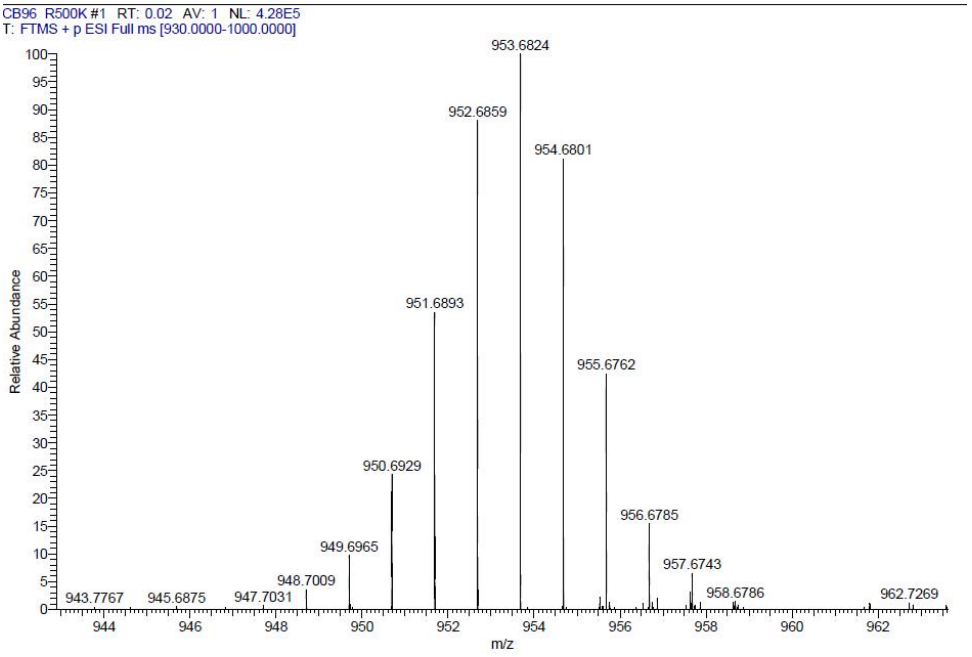

Compound 23

^{1}H NMR (600 MHz, $CDCl_3$)

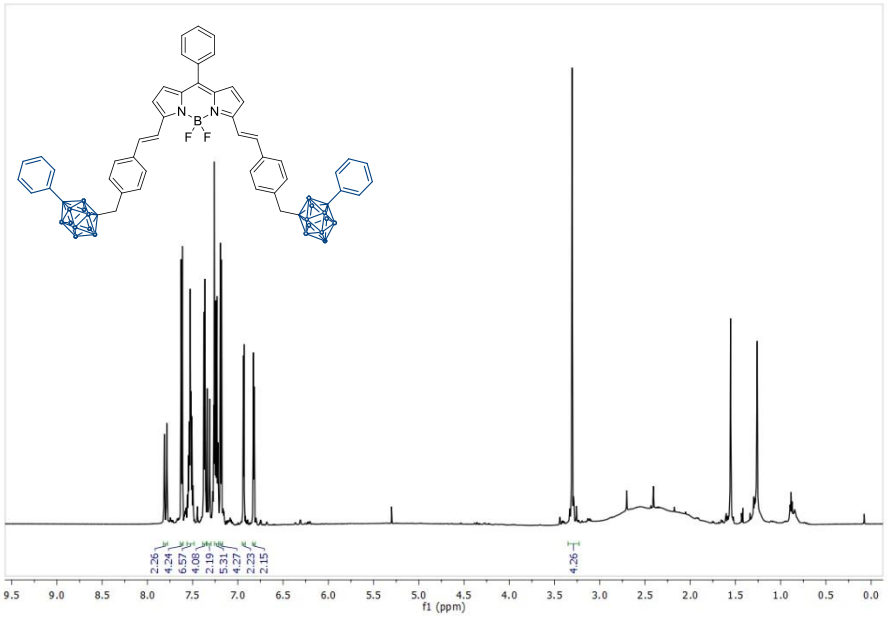

^{13}C NMR (150 MHz, $CDCl_3$)

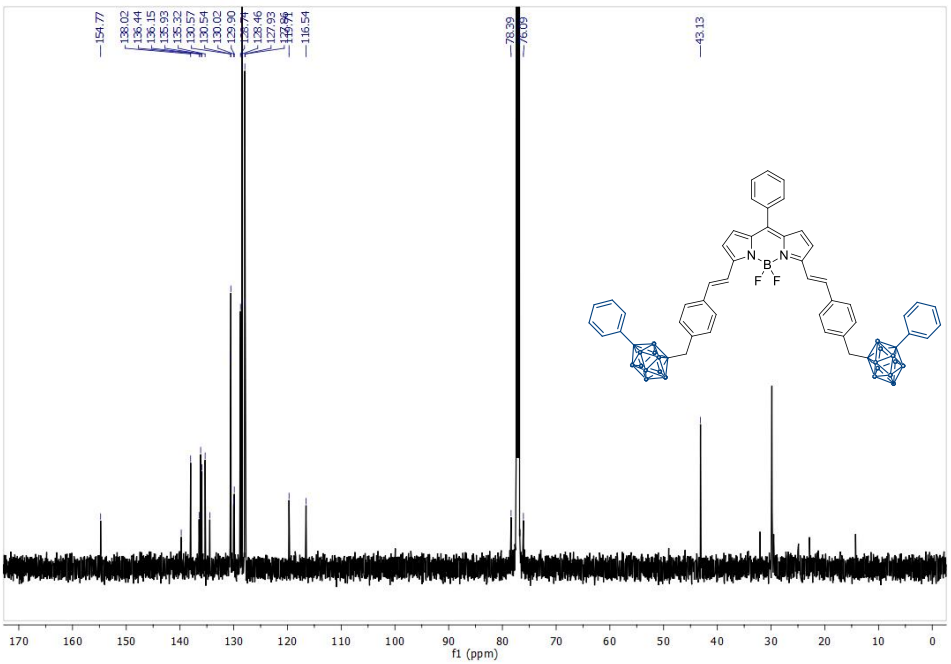

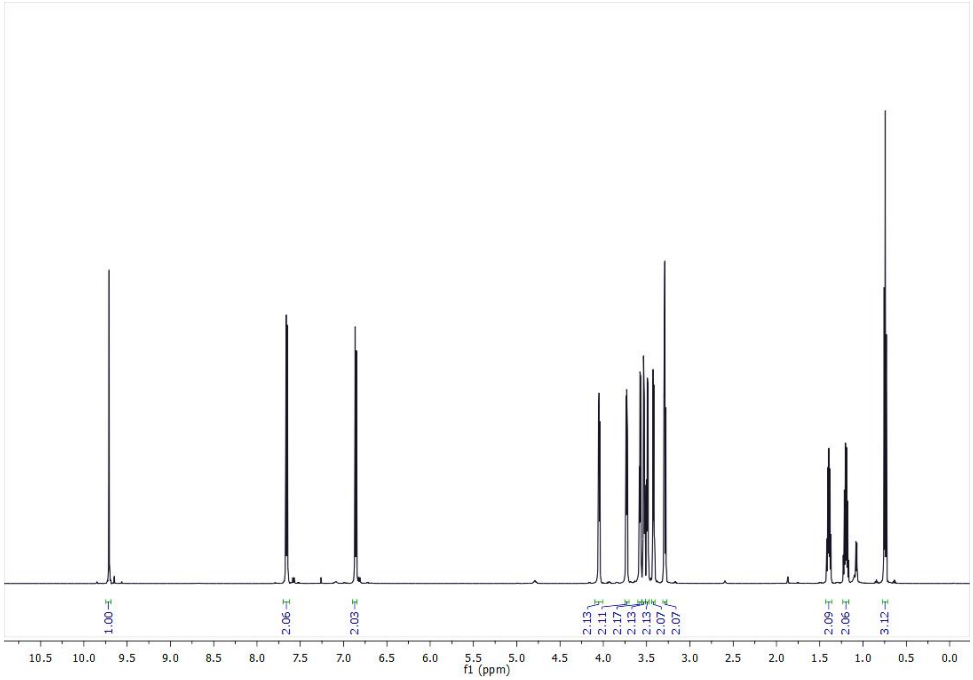
1.00
2.06
2.03
2.13
2.11
2.17
2.13
2.07
2.07
2.09
2.06
3.12
10.5 10.0 9.5 9.0 8.5 8.0 7.5 7.0 6.5 6.0 5.5 5.0 4.5 4.0 3.5 3.0 2.5 2.0 1.5 1.0 0.5 0.0
f1 (ppm)

Annex- Chapter 5

Experimental section

Materials and methods

Commercial reagents were used as received from suppliers. Anhydrous MeOH was prepared by treatment with molecular sieves (3 Å). Thin layer chromatography (TLC) was performed on pre-coated aluminum layers of silica gel 60 F254 (0.20 mm thick): MACHEREY-NAGEL Alugram® silica plates SIL G/UV254. Preparative TLC was performed on Pre-coated TLC-plates SIL HD; 0.25 mm thick silica gel 60. Flash columnchromatography was performed by using silica gel (SiO_2) with 0.04 - 0.06 mm in particle size and 60 Å in pore size.

Instrumentation

Infrared spectra were recorded using a Bruker Tensor 27 spectrometer equipped with aGolden Gate Single Reflection Diamond ATR at the "Servei d'Anàlisi Química" of the UAB. Nuclear magnetic resonance (NMR) spectra were recorded at "Servei de Ressonància Magnètica Nuclear" of the UAB with Bruker DPX-250, DPX-360 and DPX-400 spectrometers. Chemical shifts are reported in ppm using the signal of the residual nondeuterated solvent molecules as a reference for ^{1}H NMR and ^{13}C NMR. Chemical shift values for $^{11}B\{1H\}$ and ^{11}B NMR spectra were referenced to external $BF_3 \cdot Et_2O$. MALDI-TOF mass spectra using dithranol (DIT) as a matrix were measured at the Universidad de Zaragoza. Absorbance spectra in solution were recorded on an Agilent 8453 spectrophotometer using 1 cm- or 1 mm-thick quartz cuvettes. Emission spectra insolution

were measured in a custom-made spectrofluorometer by using cw laser at λ_{exc}

= 445 or 532 nm as an excitation source and detecting the emitted photons in an AndorICCD camera coupled to an Andor spectrograph. To avoid self-absorption effects, emission measurements were taken in highly diluted solutions (absorbance < 0.05 at theexcitation wavelength for 1 cm-thick quartz cuvettes) or, for aggregation experiments, in1 mm-thick cuvettes and working in reflection mode. HPLC quality solvents were used inall the cases and, to prevent the effect of impurities in fluorescence quantum yield measurements, all samples were further purified by preparative TLC. Absorption spectraand fluorescence quantum yields in the solid state were recorded on a Cary 60 spectrophotometer and a Hamamatsu spectrofluorometer at the "Institut Català de Nanociència i Nanotecnologia", respectively. Scanning electron microscopy images of the micro- and nanostructures obtained were performed in a MERLIN FE-SEM microscope from "Servei de Microscòpia" of the UAB.

Synthesis of 7-tridecanamine, I

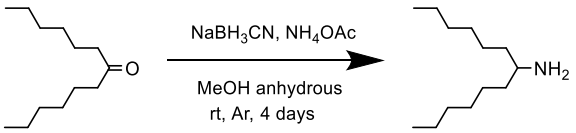

Compound **a** (4.808 g, 24.24 mmol), NH_4OAc (19.638 g, 254.74 mmol) and $NaBH_3CN$ (1.477 g, 23.50 mmol) were dissolved in 60 mL of anhydrous methanol in a 100 mL Schlenk. The mixture was stirred at room temperature under argon atmosphere for 4 days. The evolution of the

reaction was monitored by TLC using chloroform as an eluent. A *p*-anisaldehyde solution was used as a staining reagent. After 4 days, basification of the reaction mixture - from pH 7 to pH 10 - was done by addition of a saturated solution of NaOH in methanol. The resulting mixture was extracted with chloroform and the organic phase was concentrated under vacuum. The resulting oil was purified by flash column chromatography ($CHCl_3$ with 2% NEt_3 followed by an increasing gradient of MeOH:$CHCl_3$ up to 5:95 v/v). Pure 7-tridecanamine **I** was isolated as a yellow oil (4.044 g, 84 % yield). **^{1}H NMR** (360 MHz, $CDCl_3$) δ (ppm) 2.70 (s, 1H), 1.46 – 1.19 (m, 20H), 0.90 (t, 6H).

Synthesis of N,N'-bis(1-hexylheptyl)perylene-3,4:9,10-tetracarboxidiimide, II.

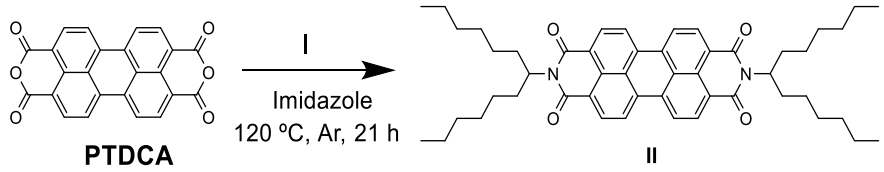

PTCDA (0.867 g, 2.21 mmol), compound **I** (2.695 g, 13.5 mmol) and imidazole (8.5 g) were heated at 120 ºC for 20 hours under argon atmosphere. The reaction was stopped when the starting material was consumed according to TLC. The reaction was cooled down to room temperature and acidified – from pH 9 to pH 2 – by adding a 2 M HCl solution in ethanol. The mixture turned from a dark red to a brownish-dark maroon colour and it was filtered under vacuum – for 1 hour by using a 0.2 μm Nylon filter. The filtered light red solid was dried under vacuum at 120 ºC for 3 h to obtain compound **II** as a dark red solid (1.668 g, 100% yield). **^{1}H NMR** (360 MHz, $CDCl_3$) δ (ppm) 8.75 – 8.61 (m, 8H),

5.19 (m, 2H), 2.31 – 2.18 (m, 4H), 1.92 – 1.80 (m, 4H), 1.44 – 1.12 (m, 36H), 0.82 (t, *J* = 6.5 Hz, 12H).

Synthesis of N-(1-hexylheptyl)perylene-3,4:9,10-tetracarboxil-3,4-anhidride-9,10-imide, III.

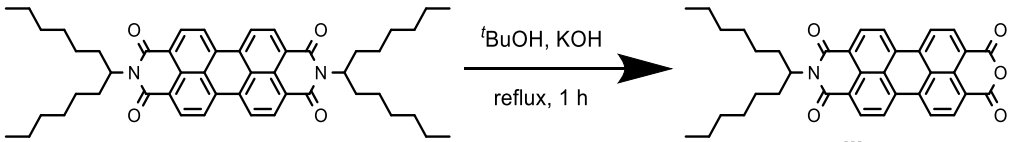

II III

The symmetrically functionalized PDI **II** (1.805 g, 2.39 mmol) and KOH (0.485 g, 8.65 mmol) were dissolved in 48 mL of *tert*-butanol in a three-necked flask. The dark red mixture was stirred and heated under reflux for 1 hour while following the reaction by TLC. The reaction mixture was cooled down to room temperature and acidified to pH 3 by the addition of 40 mL of concentrated acetic acid and 20 mL of a 2 M aqueous HCl solution causing the appearance of a reddish-brownish clay. The mixture was filtered under vacuum by using a 0.4 μm Nylon filter. The filtered brown solid was dried under vacuum at 120 ºC for 3 hours. The solid was added to 60 mL of a 10 % aqueous solution of K_2CO_3 and heated under reflux for 50 min. The resulting dark-green solution was filtered under vacuum by using a 0.45 μm Nylon filter. The filtered brown-red solid was washed with a hot 10 % aqueous solution of K_2CO_3 until the green colour of the filtrate disappeared. Straightaway, it was acidified by the addition of a 2 M aqueous HCl solution – from pH 12 to pH 2. The solid was washed thoroughly with distilled water and finally dried under vacuum at 130 ºC for 5 hours. A dark red-brown solid was obtained. The dried solid was then suspended in 62 mL of distilled boiling water and 2.45 mL of NEt_3.

The mixture was stirred until the solution turned red. A hot filtration under vacuum – by using paper filter for some hours – was carried out. The filtered solid was washed with a 6 M aqueous HCl solution – to pH 1 – followed by rinsing with distilled water – to pH 5-6. The filtered solid was dried under vacuum at 120 ºC for 4 hours to obtain a dark red solid (0.754 g, 55% yield). **^{1}H NMR** (360 MHz, $CDCl_3$): δ (ppm) 8.81 - 8.60 (m, 8H), 5.20 (m, 1H), 2.25 (m, 2H), 1.88 (m, 2H), 1.40 - 1.10 (m, 18H), 0.87 (t, *J* = 6.8 Hz, 6H).

Synthesis of *N*-(1-hexylheptyl)-*N'*-propargylperylene-3,4:9,10-tetracarboxdiimide, 1.

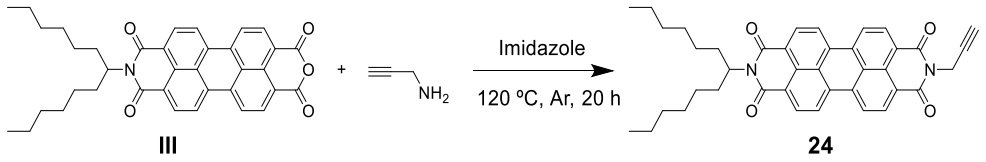

III 24

The asymmetrically functionalized monoimide **III** (0.101 g, 0.18 mmol) and imidazole (0.314 g) were dried in the Schlenk line. Prop-2-yn-1-amine (100 μL, 1.57 mmol) was added with a syringe under argon atmosphere and the resulting mixture was heated at 120 ºC for 20 hours. The reaction mixture was cooled down to room temperature and dissolved in $CHCl_3$. The solution was moved into a round-bottom flask where Celite (0.5 g) was added. The mixture was concentrated under vacuum getting the dry loading that was purified by flash column chromatography (CH_2Cl_2, followed by an increasing gradient of CH_2Cl_2/MeOH up to 95:5 v/v). Pure asymmetrically functionalized PDI **24** was isolated as a red solid (0.103 g, 94% yield). **^{1}H NMR** (360 MHz, $CDCl_3$) δ (ppm) 8.72 – 8.34 (m, 8H), 5.18 (m, 1H), 4.96 (d, *J* = 2.1 Hz, 2H), 2.34 –

2.15 (overlapping m and t, 3H), 1.98 – 1.79 (m, 2H), 1.42 – 1.16 (m, 18H), 0.83 (t, *J* = 6.7 Hz, 6H).

Synthesis of PDI-CB.

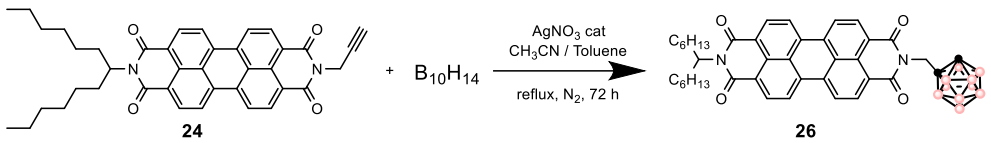

Decaborane ($B_{10}H_{14}$) (44 mg, 0.36 mmol) was dissolved in CH_3CN (8.0 mL, 152 mmol) and heated under reflux for 2 hours. Then, diimide **24** (63 mg, 0.12 mmol) dissolved in 12 mL of anhydrous toluene in the presence of $AgNO_3$ (8.3 mg, 0.05 mmol) was added to the $B_{10}H_{12}\cdot(CH_3CN)_2$ adduct mixture with a syringe and heated under reflux for 72 hours under nitrogen atmosphere. The reaction mixture was cooled down to room temperature, diluted with 15 mL of toluene and filtered through Celite. The resulting orange fluorescent solution was concentrated under reduced pressure and purified by flash column chromatography ($CHCl_3$) to obtain pure **26** (32 mg, 43% yield) as a red solid. **^{1}H NMR** (250 MHz, $CDCl_3$) δ (ppm) 8.82 – 8.43 (m, 8H), 5.18 (m, 1H), 4.96 (s, 2H), 4.21 (s, C_{CB}-H), 2.36 – 2.09 (m, 2H), 1.98 – 1.73 (m, 2H), 1.47 – 1.04 (m, 16H), 0.85 (t, *J* = 9.1 Hz, 6H). **^{13}C NMR** (400 MHz, $CDCl_3$) δ (ppm) 163.11, 135.70, 133.79, 132.26, 129.56, 129.44, 126.53, 126.23, 123.60, 123.00, 121.74, 73.46, 61.12, 54.96, 44.28, 31.78, 29.24, 26.98, 22.60, 14.05, 1.03. **^{11}B NMR** (400 MHz, $CDCl_3$) δ (ppm) -2.04, -5.00, -10.75. **^{11}B{^{1}H} NMR** (400 MHz, $CDCl_3$) δ (ppm) -1.18 (s, 2B), -4.59 (s, 2B), -10.11 (s,4B), -12.17(s, 2B). **IR** (ATR) ν (cm^{-1}) 3085, 2924, 2855, 2583 (B-H), 1698 (C=O imide), 1652 (C=O imide), 1593, 1578, 1436, 1403, 1337, 1250, 1177, 1108, 1066, 1017, 852,

809, 746, 725, 675, 645. **MS** (MALDI) m/z: Calculated for $[C_{40}H_{47}B_{10}N_2O_4]^+$: 729.5; found: 729.9 (M-H).

^1H, ^{13}C, ^{11}B, $^{11}B\{^1H\}$ NMR and IR-ATR spectra of target compounds 26

^1H NMR (250 MHz, $CDCl_3$)

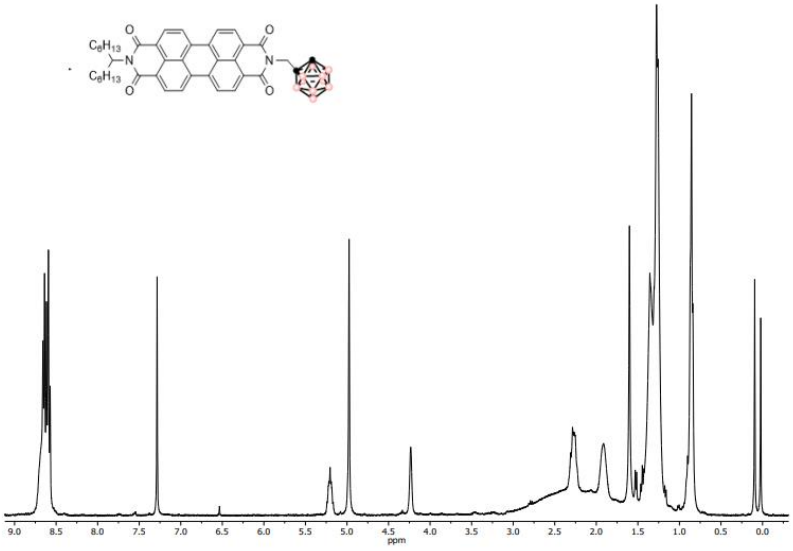

IR (ATR)

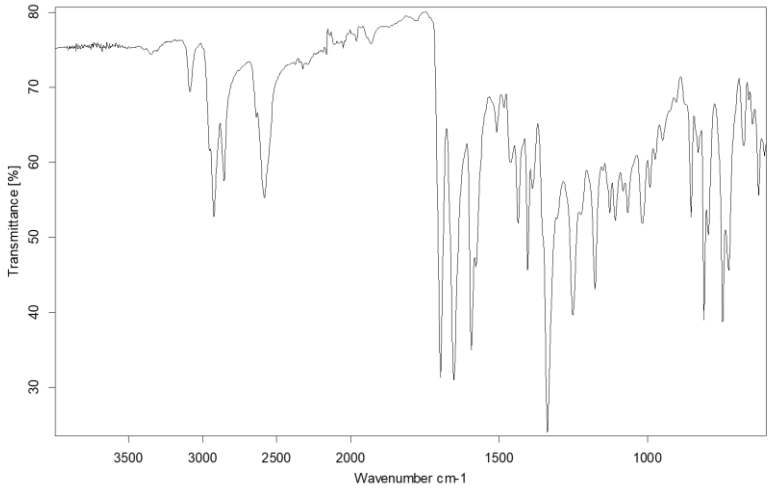

^{13}C NMR (100 MHz, $CDCl_3$)

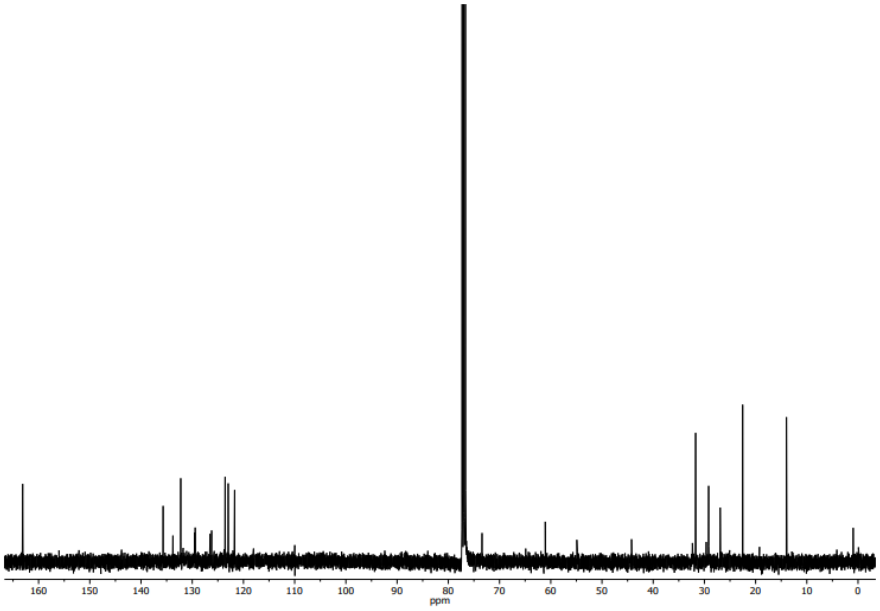

^{11}B NMR (128 MHz, $CDCl_3$)

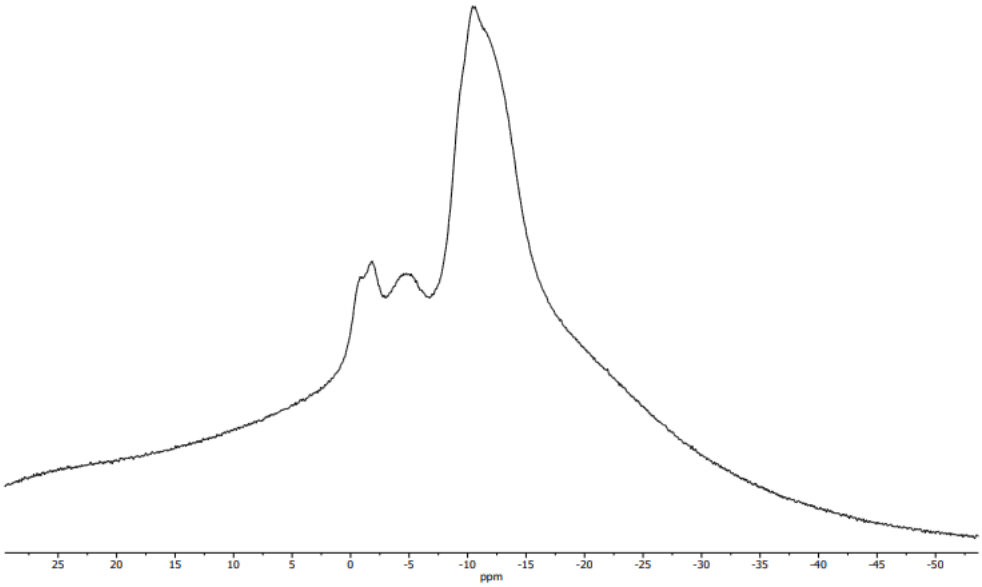

$^{11}B\{^{1}H\}$ NMR (128 MHz, $CDCl_3$)

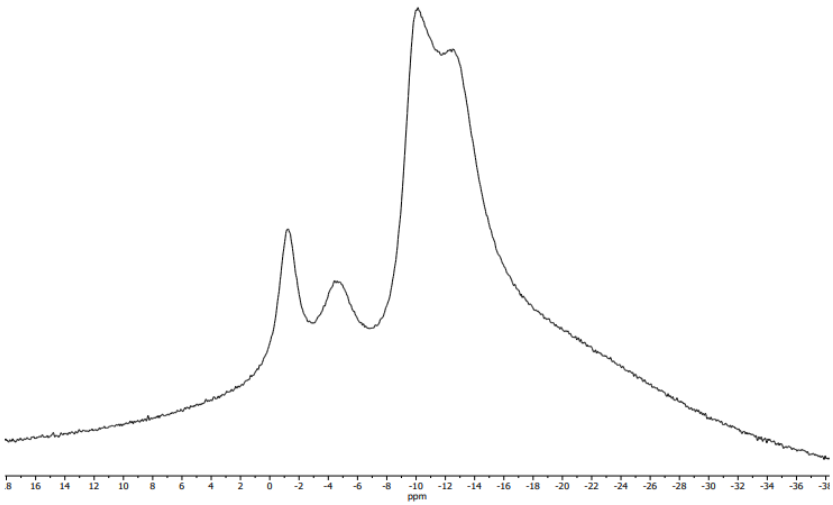

Synthesis of 1,6,7,12-tetrachloroperylene-3,4,9,10-tetracarboxylic, IV

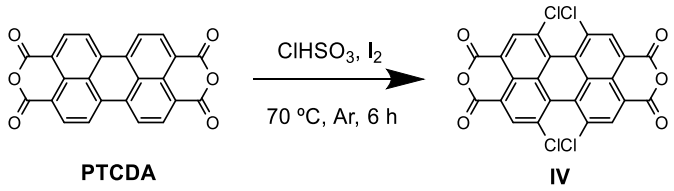

PTDCA (5.000 g, 12.75 mmol), I_2 (0.967 g, 3.8 mmol) and $ClHSO_3$ (34 mL, 511.52 mmol) were heated at 70 ºC for 6 hours under argon atmosphere. The reaction was followed by ^1H NMR spectroscopy. The resulting black mixture was cooled down to room temperature and poured on 200 mL of ice. The resulting red sample was filtered under vacuum and purified by consecutive Soxhlet extractions with refluxing CH_2Cl_2. The filtered organic solvent was concentrated under vacuum to obtain an orange solid (3.444 g) that we found to be composed of an insoluble 9:1 mixture of the desired compound **IV** (46% yield) and of the tetrachlorinated derivative of **PTCDA**. **^{1}H NMR** (360 MHz, $CDCl_3$) δ (ppm) 8.8 (s).

Synthesis of N,N'-bispropargyl-1,6,7,12-tetrachloroperylene-3,4,9,10-tetracarboxylic diimide, 25

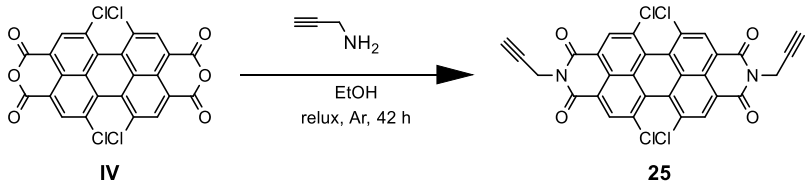

The tetrachlorinated perylene core **IV** (0.330 g, 0.62 mmol) and prop-2-yn-1-amine (0.6 μL, 9.42 mmol) were dissolved in 10 mL of EtOH and heated under reflux for 42 hours under argon atmosphere. The reaction

mixture was cooled down to room temperature and the solvent was removed under vacuum. The remaining precipitate was stirred with diethyl ether and filtered. The filtered solid was dried under vacuum at 120 ºC for 4 hours to obtain **25** as a dark solid (0.367 g, 98% yield). **^{1}H NMR** (360 MHz, $CDCl_3$) δ (ppm) 8.73 (s, 4H), 5.00 (s, 4H), 2.23 (s, 2H).

Synthesis of 27

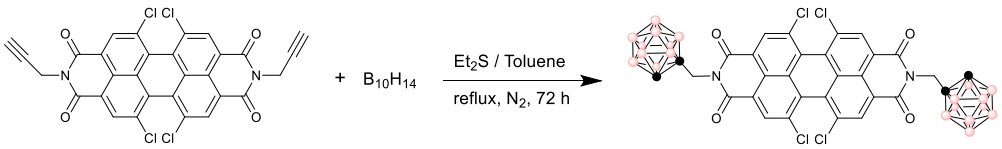

Et_2S (0.2 mL, 1.86 mmol) was added to a 2.2 mL of anhydrous toluene solution of $B_{10}H_{14}$ (116 mg, 0.95 mmol) and the mixture was stirred at room temperature for 30 min. Then, diimide **25** (101 mg, 0.17 mmol) was dissolved in 8.6 mL of anhydrous toluene and was added to the decaborane solution mixture with a syringe. The resulting mixture was heated under reflux for 72 hours under nitrogen atmosphere. Afterwards, it was cooled down to room temperature and the solvent was removed under vacuum. The resulting black solid was dissolved in 25 mL of MeOH, filtered and washed with toluene. The resulting orange-greenish fluorescent filtered solution was concentrated under reduced pressure and purified by flash column chromatography ($CHCl_3$) to obtain pure **27** (37.1 mg, 26 % yield) as a red solid.

^{1}H NMR (400 MHz, $CDCl_3$) δ (ppm) 8.73 (m, 4H), 4.96 (s, 4H), 4.18 (s, 2H). **^{13}C NMR** (400 MHz, $CDCl_3$) δ (ppm) 162.10, 161.95, 136.00, 135.93, 135.90, 135.83, 133.90, 133.87, 133.82, 133.78, 131.51, 129.32, 129.24,

123.34, 122.19, 122.15, 73.02, 61.25, 44.46, 29.29. **^{11}B NMR** (400 MHz, $CDCl_3$) δ (ppm) -1.76, --4.61, -10.49, -12.01. **^{11}B{^{1}H} NMR** (400 MHz, $CDCl_3$) δ (ppm) -1.17 (s, 4B), -4.46 (s, 4B), -9.83 (br s,6B), -12.66 (br s, 6B). **IR** (ATR) ν (cm^{-1}) 3068, 2923, 2853, 2577 (B-H), 1708, 1668, 1587, 1420, 1390 1360, 1288, 1239, 1185, 1115, 1077, 1017, 904, 871, 824, 802, 749, 726, 686. **MS** (MALDI) m/z: Calculated for $[C_{30}H_{30}B_{20}Cl_4N_2O_4]^+$: 842.3; found: 842.3

^{1}H, ^{13}C, ^{11}B, ^{11}B{^{1}H} NMR and IR-ATR spectra of target compounds 27

^{1}H NMR (250 MHz, CDCl3)

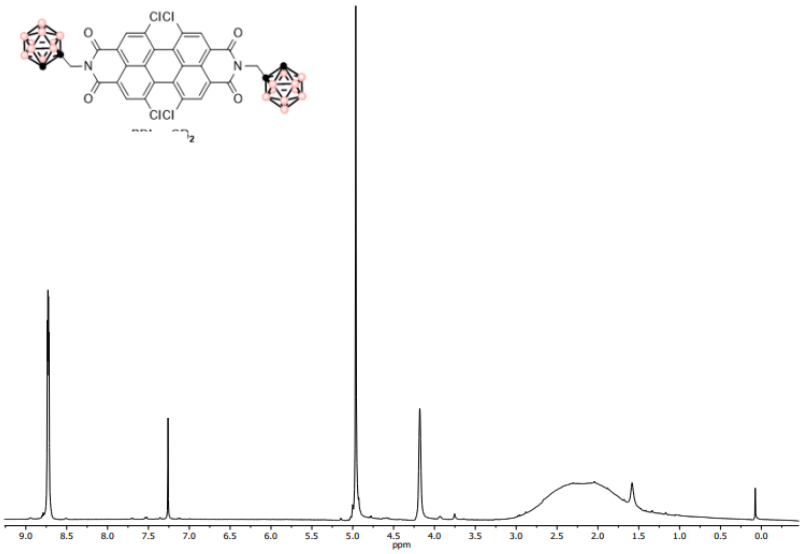

^{13}C NMR (100 MHz, $CDCl_3$)

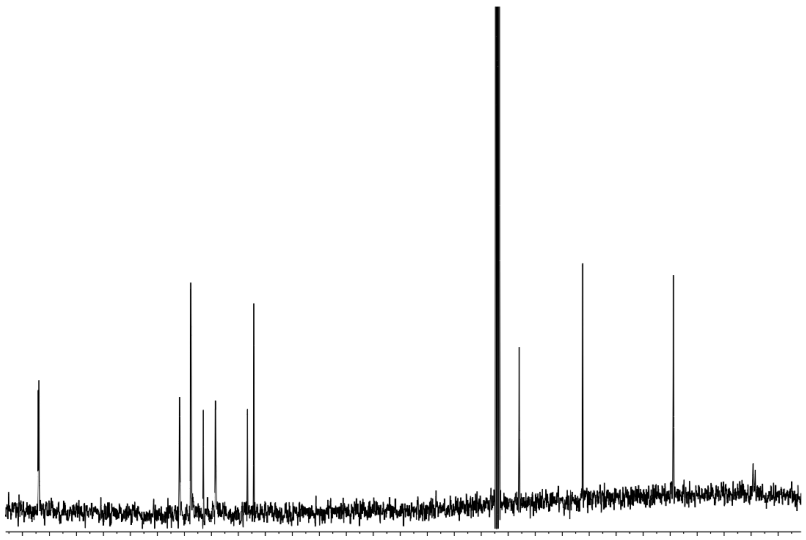

^{11}B NMR (128 MHz, $CDCl_3$)

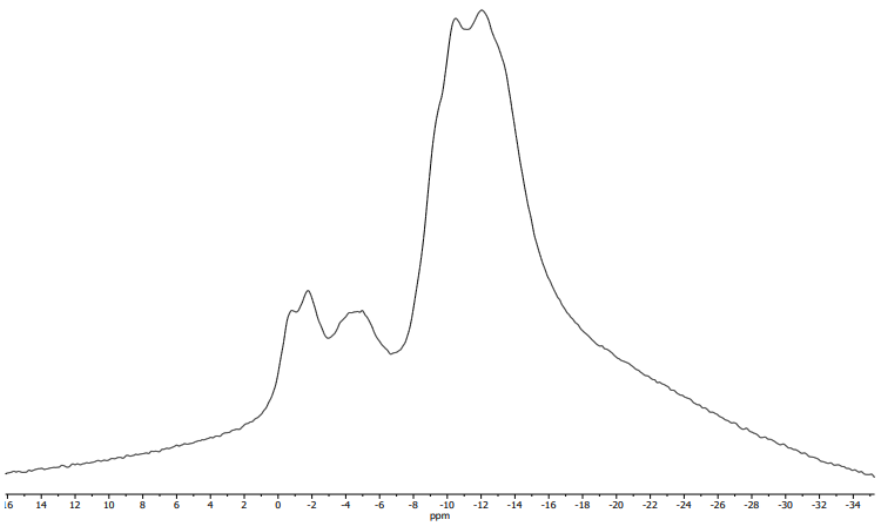

$^{11}B\{^{1}H\}$ NMR (128 MHz, $CDCl_3$)

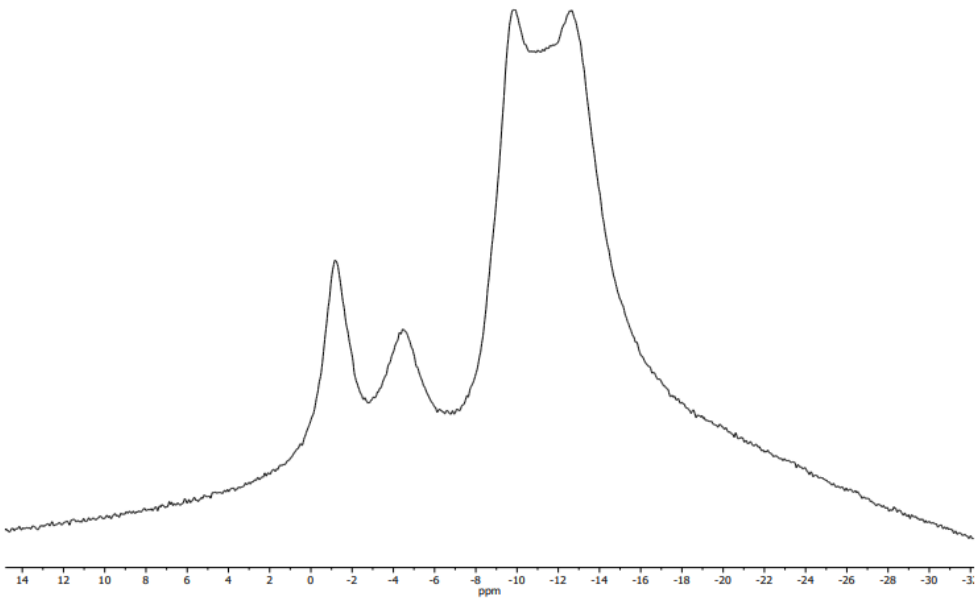

IR (ATR)

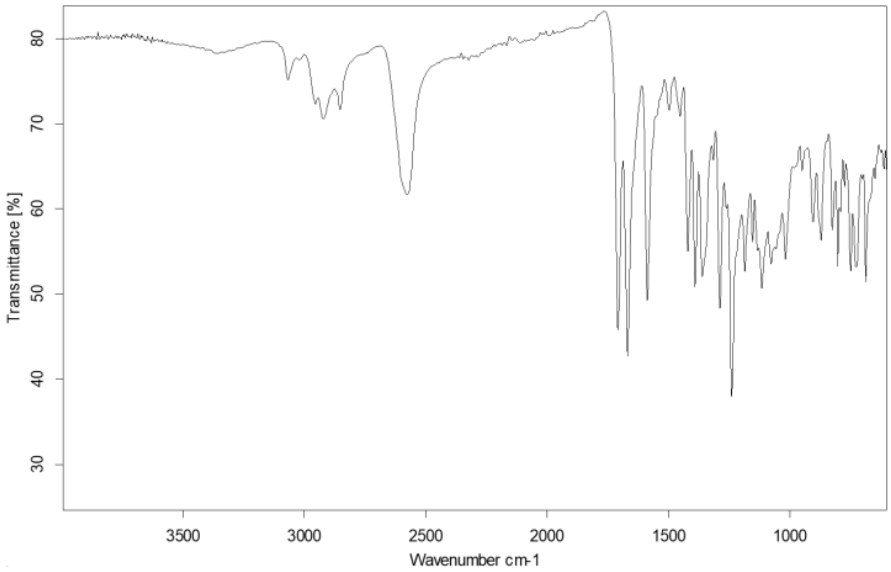

Preparation nanostructures

1 mL of a solution of the compound of interest in chloroform/dioxane (c ~ 10^{-3} M) was introduced in a test tube. Hexane (or water) was added dropwise, carefully allowing the drops to slide down the walls of the tube and without stirring. We added it until observing the formation of two phases. The sample was left overnight to allow phase mixing by diffusion of the two solvents. The precipitate formed was redispersed in hexane (or water) after removing the supernatant.

Annex- Chapter 6

Experimental section:

Instrumentation.

Elemental analyses were performed using a Carlo Erba EA1108 microanalyzer. ATR-IR spectra were recorded on JASCO FT/IR-4700 spectrometer on a high-resolution. ^{1}H NMR, ^{11}B NMR, $^{11}B\{^{1}H\}$ NMR and $^{13}C\{^{1}H\}$ NMR spectra were recorded on NMR-FT Bruker 400 MHz spectrometer using deuterated acetonitrile ($CDCl_3$) at 25 ºC. Chemical shifts are reported in ppm and referenced to the residual solvent peak for ^{1}H and $^{13}C\{^{1}H\}$ NMR or to $BF_3{\cdot}OEt_2$ as an external standard for ^{11}B and $^{11}B\{^{1}H\}$ NMR. Chemical shifts are reported in ppm and coupling constants in Hertz. Multiplets nomenclature is as follows: s, singlet; d, doublet; t, triplet; br, broad; m, multiplet.

The UV-Vis spectra were recorded on and JASCO V-780 UV-Visible/NIR spectrophotometers, using spectroscopic grade THF (Sigma-Aldrich), in normal quartz cuvette having 1 cm path length, for different solutions for each compound in the range 10^{-4} to 10^{-5} M in order to calculate the molar extinction coefficients (Φ) were run on a with a quartz cell having a path length of 1 cm in the range of 190-600 nm. Solid-state electronic spectra were run on a JASCO V-780 UV-Visible/NIR spectrophotometer equipped with a 60 mm integrating sphere model ISN-901i/A001461872. The fluorescence emission and excitation spectra for all samples in solution were recorded in a VARIANT Cary Eclipse Fluorescence spectrometer. No fluorescent contaminants were detected on excitation in the wavelength region of experimental interest. The fluorescence quantum yields were determined by the “single point method” and repeated three times with

similar optical density for reproducibility, against quinine sulfate in 0.5 M aqueous sulfuric acid with Φ_F = 0.54 as a standard.

Materials.

All reactions were performed under atmosphere of nitrogen employing standard Schlenk techniques. Toluene was purchased from Merck and distilled from sodium benzophenone prior to use. Commercial grade diethyl ether, hexane, petroleum ether, *n*-heptane, chloroform and dichloromethane were used without further purification. $B_{10}H_{14}$ was supplied from KatChem Ltd. (Prague) and used as received. Chemicals such as 1,3,5-tris(7-bromo-9,9-dihexyl-9H-fluoren-2-yl)benzene, 1,3,5-tris(7-ethynyl-9,9-dihexyl-9H-fluoren-2-yl)benzene and tris(7-ethynyl-9,9-dihexyl)truxene were prepared by the research group of Dr. Norberto Farfan at UNAM, department of chemistry, Mexico.

2-Acetyl-7-bromo-9,9-di-n-hexylfluorene(II)

RMN ^{1}H (400 MHz, $CDCl_3$): δ 7.95-7.97 (m, 2H), 7.75 (d, J=7.87 Hz, 1H), 7.61 (d, J=7.87 Hz, 1H), 7.46-7.52 (m, 2H) 2.67 (s, 3H), 1.90-2,06 (m, 4H), 0.98-1.11 (m, 12H), 0.76 (t, J=7,2Hz, 6H), 0.50-0.61 (m, 4H).

1,3,5-Tris(7-bromo-9,9-di-n-hexylfluorenyl-2-yl)benzene(28)

RMN ^{1}H (400 MHz, $CDCl_3$): 7.91 (s, 3H), 7.81 (dd,J=7.7 Hz, 6H), 7.70 (s, 3H), 7.65 (d, J=8.6Hz, 3H), 7.50-7.53 (m, 6H), 1.98-2.09 (m, 12H), 1.06-1.25 (m, 36H), 0.80 (t, J=7.2 Hz, 18H), 0.67-0.74 (m, 12H). RMN ^{13}C (100 MHz, $CDCl_3$): 153.32, 151.37, 142.97, 140.6, 139.85, 138.82, 130.2,

126.63, 126.36, 125.4, 121.87, 121.33, 120.28, 55.76, 40.50, 31.53, 29.81, 23,89, 22.73, 14.16

1,3,5-tris(7-ethynyl-9,9-dihexyl-9H-fluoren-2-yl)benzene (29).

RMN ^{1}H (400 MHz, $CDCl_3$) δ 7.91 (s, 3H), 7.79 (dd, J=7.56 Hz, 6H), 7.52 (d, J=8.26, 3H), 7.50 (s, 3H), 7.49-7.53 (m, 6H), 3.16 (s, 3H), 1.96-2.06 (m, 12H), 0.99-1.16 (m, 36H), 0.75 (t, J=7.2 Hz,18H), 0.61-0,72 (m, 12H).

RMN ^{13}C (125 MHz, $CDCl_3$) δ 152.2, 151,1, 142.9, 141.6, 140.7, 140.0, 131.4, 126.7, 126.6, 125.4, 121.9, 120.6, 120.4, 119.8, 84.6, 77.28, 55.5, 40.5, 31.6, 29.8, 23.8, 22.7, 14.1.

Figure S.6.1. ^{1}H NMR of 1,3,5-Tris(7-bromo-9,9-di-n-hexylfluorenyl-2-yl)benzene **28**

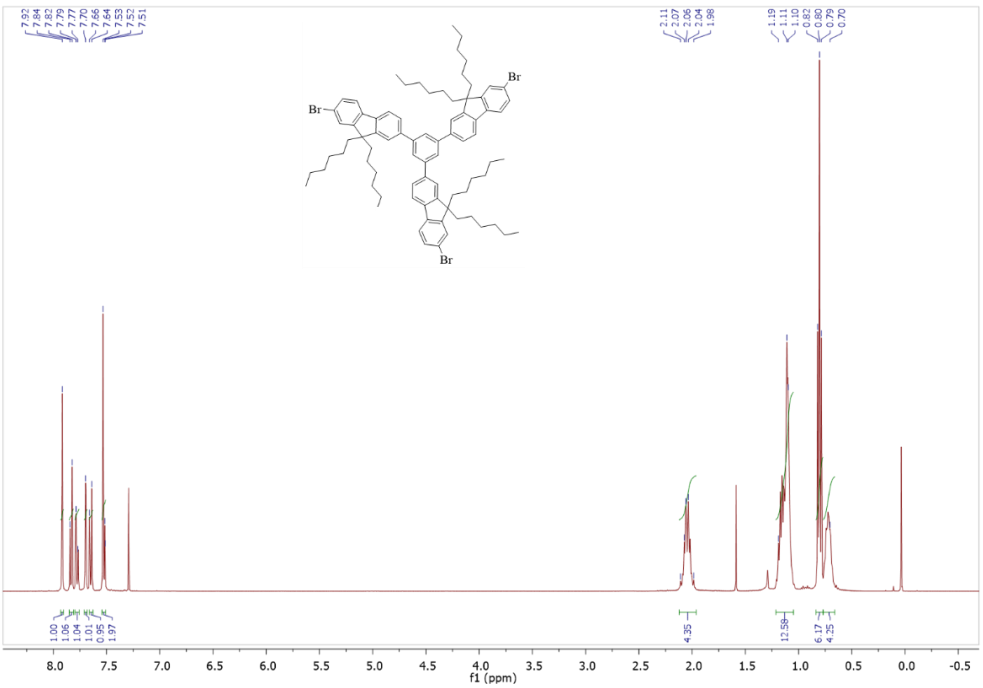

Figure. S.6.2. ^{1}H NMR of 2,7,12-tribromo-10,15-dihydro-5,5,10,10,15,15-hexahexyl-5*H*-tribenzo[*a,f,k*]trindene

2,7,12-Tribromo-10,15-dihydro-5,5,10,10,15,15-hexahexyl-5*H*-tribenzo[*a,f,k*]trindene

^{1}H NMR (400 MHz, $CDCl_3$), δ (ppm): 8.17 (d, J = 8.4 Hz, 3H, H-4), 7.57 (d, ^{3}J = 1.9 Hz, 3H, H-1), 7.51 (dd, ^{3}J = 8.4 Hz, ^{4}J = 1.9 Hz, 3H, H-3), 2.90 – 2.76 (m, 6H, H-6x), 2.08 – 1.93 (m, 6H, H-6y), 1.00 – 0.75 (m, 36H, H-8, H-9, H-10), 0.62 (t, ^{3}J = 7.1 Hz, 18H, H-11), 0.55 – 0.35 (m, 12H, H-7); **^{13}C NMR (100 MHz, $CDCl_3$), δ (ppm):** 156.01 (C-5a), 145.03 (C-4c), 139.00 (C-4a), 137.77 (C-4b), 129.51 (C-3), 126.04 (C-4), 125.66 (C-1), 121.18 (C-2), 56.13 (C-5), 36.96 (C-6), 31.60 (C-9), 29.52 (C-8), 24.03 (C-7), 22.41 (C-10), 14.02 (C-11).

^{1}H NMR (400 MHz, $CDCl_3$), δ (ppm): 8.30 (d, ^{3}J = 8.3 Hz, 3H, H-4), 7.57 (d, ^{3}J = 1.6 Hz, 3H, H-1), 7.54 (dd, ^{3}J = 8.2 Hz, ^{4}J = 1.6 Hz, 3H, H-3), 3.20 (s, 3H), 2.93 – 2.83 (m, 6H, H-6x), 2.10 – 2.02 (m, 6H, H-6y), 1.00 – 0.75 (m, 36H, H-8, H-9, H-10), 0.62 (t, ^{3}J = 7.1 Hz, 18H, H-11), 0.53 – 0.35 (m, 12H, H-7); **^{13}C NMR (100 MHz, $CDCl_3$), δ (ppm):** 153.61 (C-5a), 146.04 (C-4c), 140.72 (C-4a), 137.98 (C-4b), 130.57 (C-3), 125,82 (C-4), 124.57 (C-1), 120.05(C-2), 84.15 (C-alquino), 77.21(C-alquino), 56.13 (C-5), 36.96 (C-6), 31.44 (C-9), 29.49 (C-8), 23.90 (C-7), 22.17 (C-10), 13.91 (C-11).

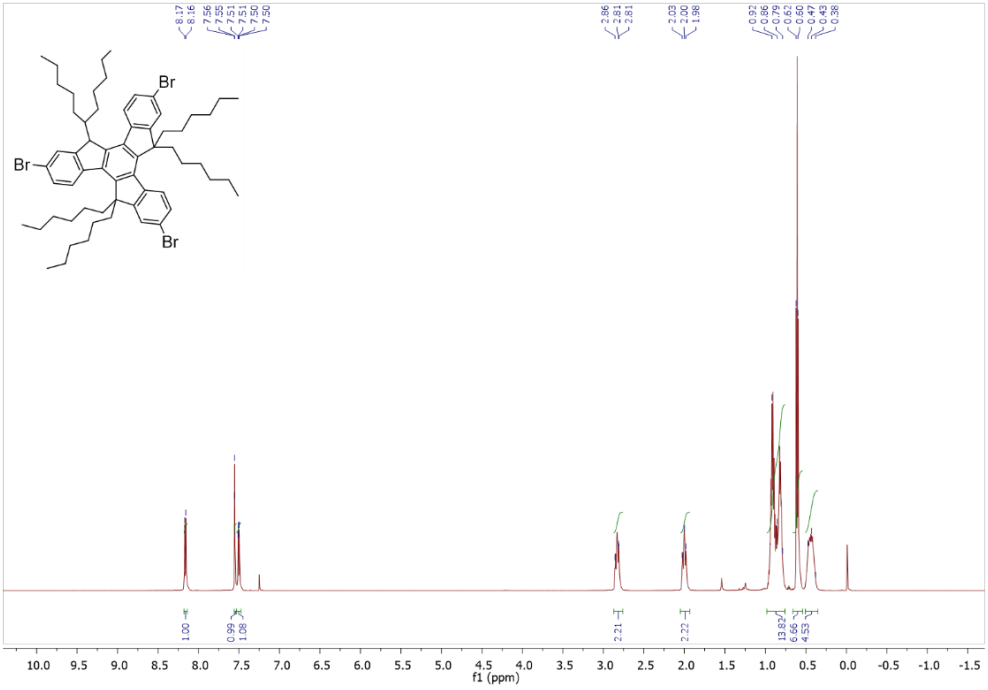

Figure S.6.3. ^{13}C NMR of 1,3,5-tris(7-ethynyl-9,9-dihexyl-9H-fluoren-2-yl) benzene

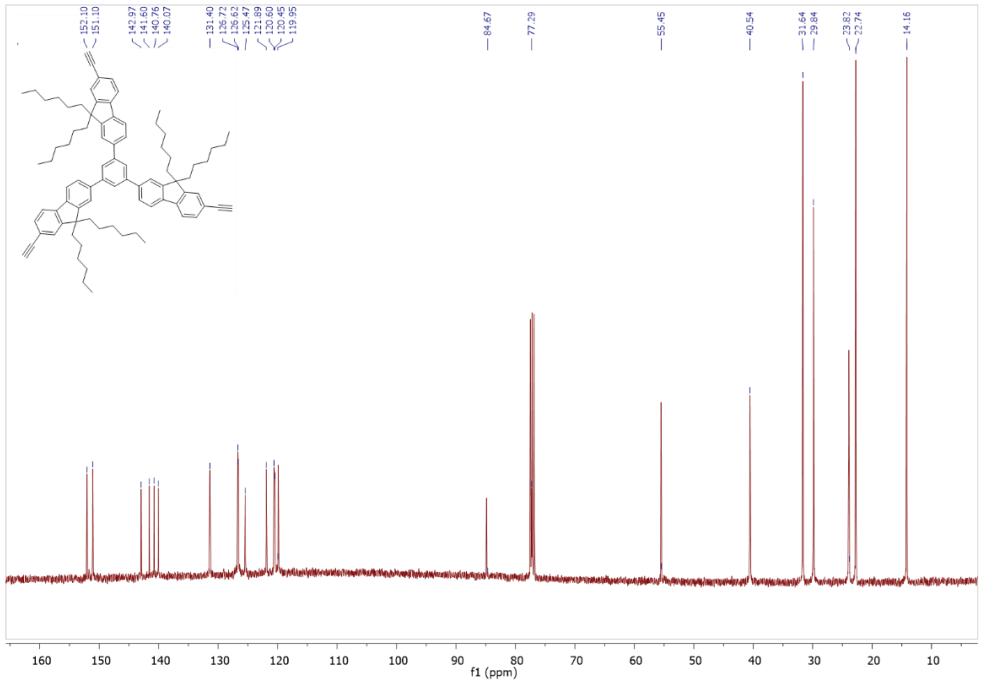

Figure S.6.4. ^{13}C NMR of triethynylhexahexyltruxene

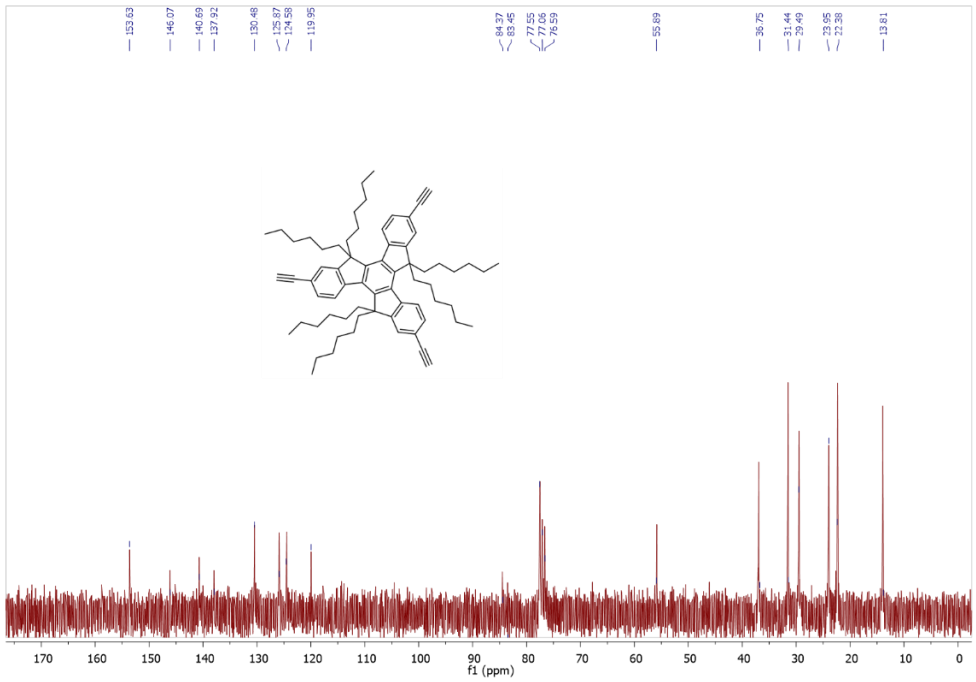

S.6.2. Theoretical studies using DFT Calculations

First our purpose was to calculate the torsion angle or the dihedral angle between the C-C bond of *o*-carborane cluster bearing disubstituted aromatic groups directly attached which was found to be 90°, whereas it was 30° in case of mono-substitution (Figure S.6.1). As observed earlier, for *o*-carborane clusters incorporated in between two fluorophores gives rise to aggregation induced effect (AIE) due to perpendicular alignment between C-C bond in *o*-carborane and π-planes favouring AIE and ICT.[1] However, this is exactly not the case for *o*-carborane units attached at the terminal of the structure, C-C bond is in fact found to be in the same plane as the fluorophore directly attached inhibiting a charge transfer process between the two fragments. This could be a possible explanation of why we did not see AIE in tri-branched fluorophores containing *o*-carborane clusters reported this chapter, whereas AIE was observed earlier in chapter 3.[2]

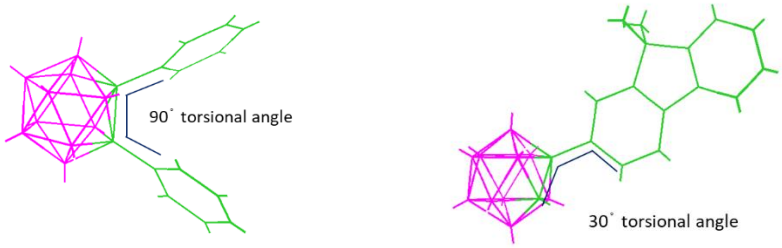

Figure S.6.5. Method used DFT with function B3LYP and base 631G*

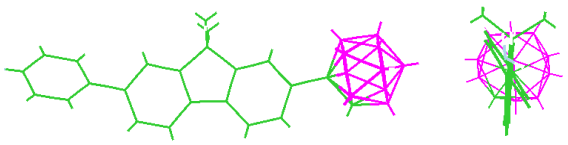

(a) Before optimisation: Dihedral angle is 30 degrees

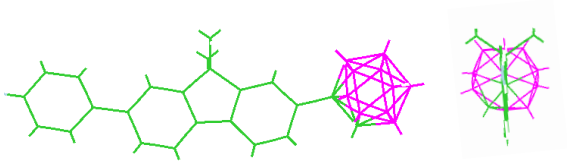

(b). After optimisation: Dihedral angle is 35 degrees

Figure S.6.6. Geometry of one-arm based structures before (a) and after (b) optimisation using CAM-B3LYP/6-31G* in THF

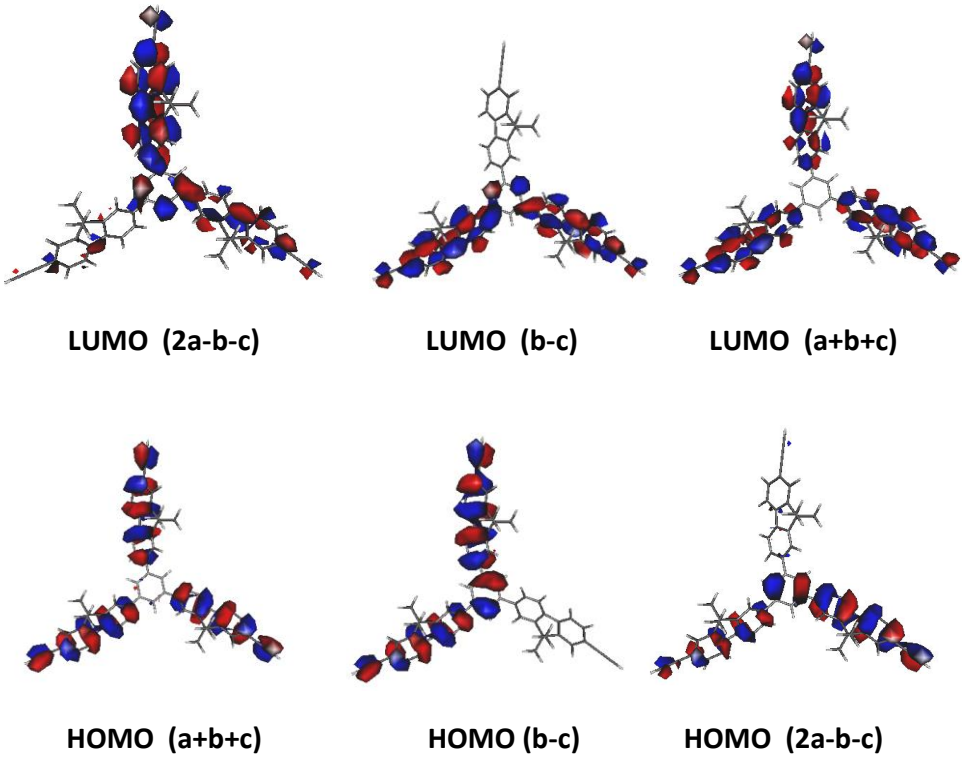

Figure S.6.7. Calculated functional molecular orbitals of the optimized structures of tri-branched systems **28**

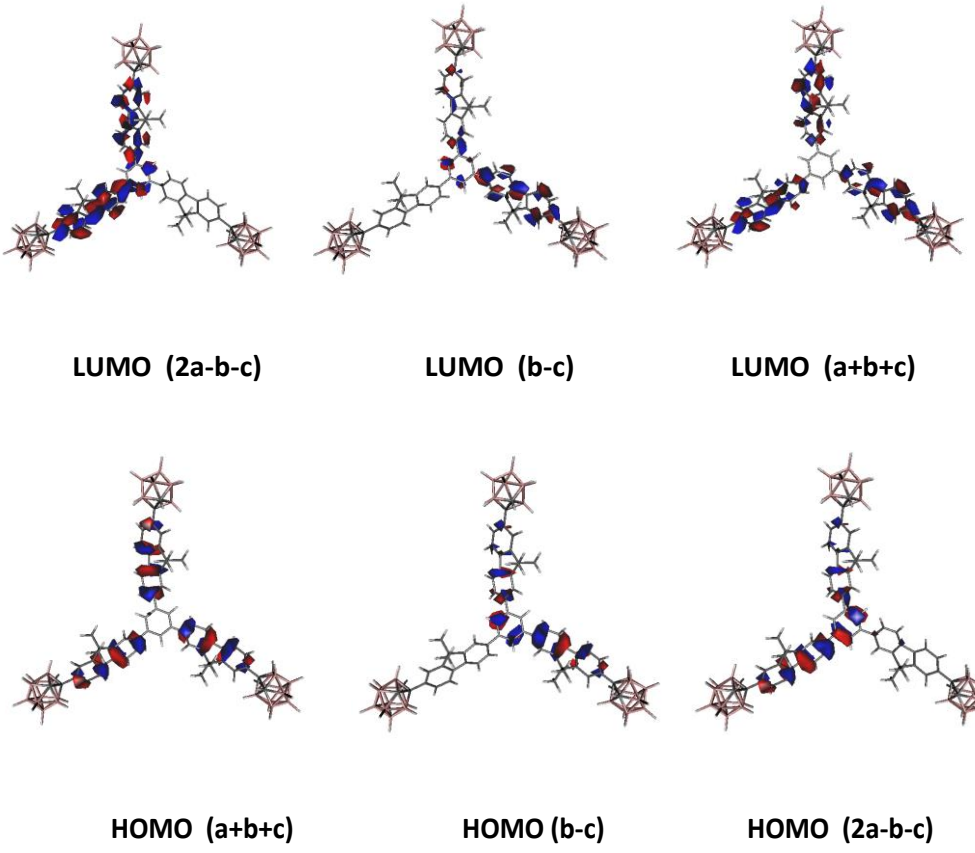

Figure S.6.8. Calculated functional molecular orbitals of the optimized structures of tri-branched systems **29**

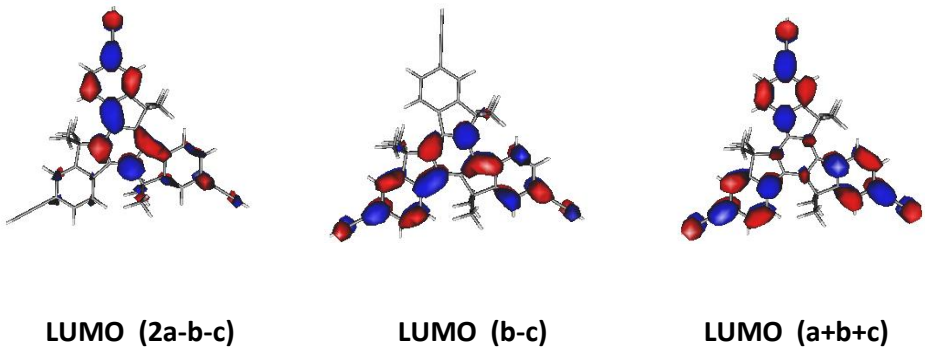

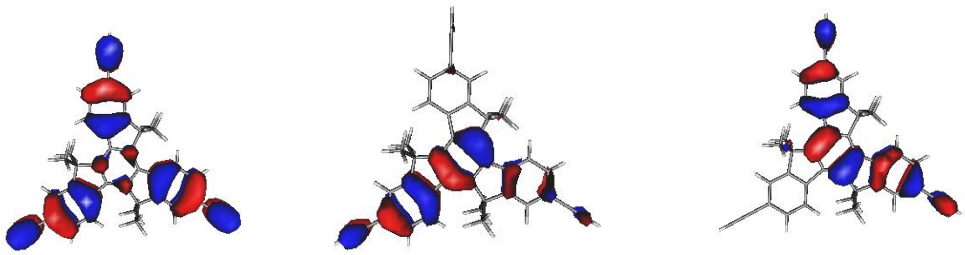

HOMO (a+b+c) HOMO (b-c) HOMO (2a-b-c)

Figure S.6.9. Calculated functional molecular orbitals of the optimized structures of tri-branched systems **31**

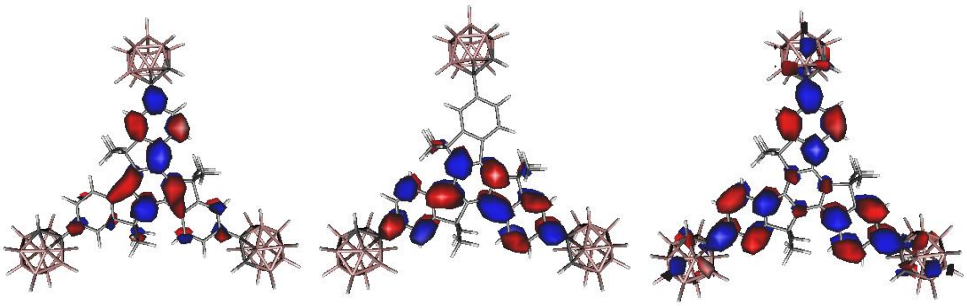

LUMO (2a-b-c) LUMO (b-c) LUMO (a+b+c)

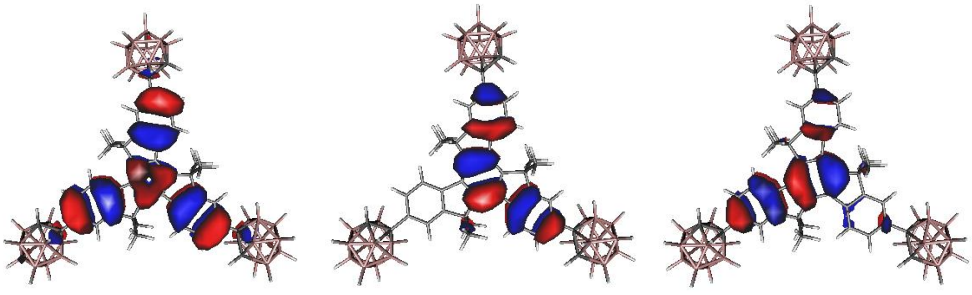

HOMO (a+b+c) HOMO (b-c) HOMO (2a-b-c)

Figure S.6.10. Calculated functional molecular orbitals of the optimized structures of tri-branched systems **31**

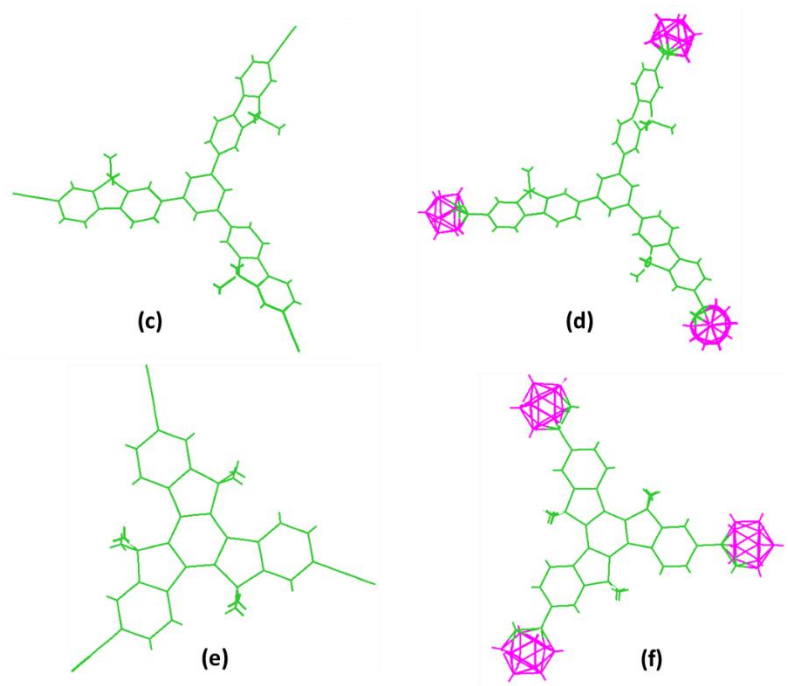

Figure S.6.11. Optimised structures of the tri-branched systems

Excitation energies and oscillator strengths of tri-branched structure of **29**

Excited State 1: Singlet-E 4.2373 eV 292.60 nm f=2.1231 <S**2>=0.000

1->2

190 ->193 0.17788

190 ->194 0.32857

191 ->193 -0.15859

191 ->194 0.27604

192 ->193 -0.27604

192 ->194 -0.15859

192 ->195 0.34891

This state for optimization and/or second-order correction.

Total Energy, E(TD-HF/TD-KS) = -2195.81966713

Copying the excited state density for this state as the 1-particle RhoCI density.

Excited State 2: Singlet-E 4.2373 eV 292.60 nm f=2.1231 <S**2>=0.000

1->3

190 ->193 -0.32856

190 ->194 0.17788

191 ->193 0.27604

191 ->194 0.15859

191 ->195 0.34891

192 ->193 -0.15859

192 ->194 0.27604

Excited State 3: Singlet-A 4.4436 eV 279.02 nm f=0.0385 <S**2>=0.000

190 ->195 -0.32286

191 ->193 0.38184

191 ->194 -0.17296

192 ->193 -0.17296

192 ->194 -0.38183

Excited State 4: Singlet-A 4.6603 eV 266.04 nm f=0.0000 <S**2>=0.000

188 ->193 -0.14410

188 ->194 -0.15148

188 ->197 -0.10412

188 ->200 -0.10624

189 ->193 0.15150

189 ->194 -0.14410

189 ->196 -0.10412

189 ->199 -0.10625

191 ->193 0.14548

191 ->194 0.31184

191 ->197 0.12017

191 ->199 0.11000

192 ->193 0.31184

192 ->194 -0.14548

192 ->196 -0.12018

192 ->200 0.10999

Excited State 5: Singlet-E 4.8837 eV 253.87 nm f=0.0209 <S**2>=0.000

182 ->194 0.14899

182 ->195 0.20436

183 ->193 0.14905

184 ->193 -0.10620

184 ->194 0.17922

190 ->196 0.18240

190 ->197 -0.15848

190 ->199 -0.12646

190 ->200 0.14650

191 ->196 0.17494

191 ->198 0.26290

191 ->199 -0.12755

192 ->197 -0.17497

192 ->198 0.18178

192 ->200 0.12755

Excited State 6: Singlet-E 4.8837 eV 253.87 nm f=0.0209 <S**2>=0.000

182 ->193 -0.14903

183 ->194 0.14900

183 ->195 -0.20436

184 ->193 0.17922

184 ->194 0.10620

190 ->196 0.15848

190 ->197 0.18240

190 ->199 -0.14650

190 ->200 -0.12646

191 ->197 -0.17498

191 ->198 -0.18178

191 ->200 0.12757

192 ->196 -0.17493

192 ->198 0.26291

192 ->199 0.12753

Excited State 7: Singlet-A 4.8849 eV 253.81 nm f=0.0001 <S**2>=0.000

182 ->193 -0.11769

182 ->194 0.17247

183 ->193 -0.17240

183 ->194 -0.11773

184 ->195 0.20136

190 ->198 0.30712

191 ->197 -0.24309

191 ->200 0.19119

192 ->196 0.24315

192 ->199 -0.19123

Excited State 8: Singlet-E 5.0264 eV 246.66 nm f=0.0040 <S**2>=0.000

185 ->194 -0.19916

185 ->195 0.11759

186 ->193 0.19931

186 ->195 -0.24613

187 ->193 -0.16835

187 ->194 -0.24902

190 ->203 0.21728

191 ->202 0.14373

192 ->201 0.22508

192 ->203 -0.14446

Excited State 9: Singlet-E 5.0264 eV 246.66 nm f=0.0040 <S**2>=0.000

185 ->193 0.19876

185 ->195 0.24613

186 ->194 0.19972

186 ->195 0.11759

187 ->193 -0.24903

187 ->194 0.16834

190 ->202 -0.21729

191 ->201 -0.22507

191 ->203 -0.14404

192 ->202 -0.14414

Excited State 10: Singlet-A 5.0268 eV 246.65 nm f=0.0050 <S**2>=0.000

185 ->193 -0.29842

186 ->194 0.29743

187 ->195 0.27345

190 ->201 -0.22157

191 ->202 -0.21915

192 ->203 -0.21843

Excitation energies and oscillator strengths of tri-branched structure of **30**

Excited State 1: Singlet-E 4.3470 eV 285.22 nm f=1.9740 <S**2>=0.000

1 > 2

280 -> 283 -0.10636

280 -> 284 0.35106

281 -> 283 -0.14086

281 -> 284 0.29315

281 -> 285 0.31510

282 -> 283 -0.29315

282 -> 284 -0.14086

282 -> 285 -0.13143

This state for optimization and/or second-order correction.

Total Energy, E(TD-HF/TD-KS) = -2959.45560705

Copying the excited state density for this state as the 1-particle RhoCI density.

Excited State 2: Singlet-E 4.3470 eV 285.22 nm f=1.9740 <S**2>=0.000

1 -> 2

280 -> 283 0.35106

280 -> 284 0.10636

281 -> 283 -0.29315

281 -> 284 -0.14086

281 -> 285 0.13143

282 -> 283 0.14086

282 -> 284 -0.29315

282 -> 285 0.31510

Excited State 3: Singlet-A 4.5596 eV 271.92 nm f=0.0433 <S**2>=0.000

280 -> 285 0.30264

281 -> 284 0.41962

282 -> 283 0.41962

Excited State 4: Singlet-A 4.6825 eV 264.78 nm f=0.0000 <S**2>=0.000

275 -> 284 -0.13625

275 -> 290 -0.10212

276 -> 283 -0.13625

276 -> 289 -0.10212

281 -> 283 0.35664

281 -> 289 0.19979

282 -> 284 -0.35664

282 -> 290 -0.19979

Excited State 5: Singlet-A 4.9351 eV 251.23 nm f=0.0005 <S**2>=0.000

272 -> 283 0.14682

273 -> 284 0.14642

274 -> 285 0.16346

277 -> 285 -0.10439

278 -> 283 0.11004

278 -> 284 0.10946

279 -> 283 -0.11045

279 -> 284 0.11034

280 -> 288 0.28400

281 -> 286 0.24307

281 -> 287 0.17011

282 -> 286 -0.17211

282 -> 287 0.24330

Excited State 6: Singlet-E 4.9352 eV 251.22 nm f=0.0300 <S**2>=0.000

272 -> 285 0.12356

274 -> 283 0.14833

277 -> 283 -0.11928

278 -> 284 -0.10142

279 -> 283 -0.10061

279 -> 285 -0.11443

280 -> 286 -0.24373

280 -> 287 0.15077

281 -> 286 -0.15429

281 -> 287 -0.14714

281 -> 288 -0.12301

282 -> 286 -0.14590

282 -> 287 0.15251

282 -> 288 0.26633

282 -> 291 0.11353

Excited State 7: Singlet-E 4.9352 eV 251.22 nm f=0.0300 <S**2>=0.000

273 -> 285 0.12356

274 -> 284 0.14833

277 -> 284 -0.11928

278 -> 283 -0.10135

278 -> 285 0.11443

279 -> 284 0.10068

280 -> 286 0.15078

280 -> 287 0.24373

281 -> 286 0.14578

281 -> 287 -0.15392

281 -> 288 0.26634

281 -> 291 0.11353

282 -> 286 -0.15288

282 -> 287 -0.14726

282 -> 288 0.12300

Excited State 8: Singlet-E 5.0799 eV 244.07 nm f=0.0049 <S**2>=0.000

275 -> 285 -0.13237

277 -> 283 0.21524

277 -> 284 -0.16521

278 -> 284 0.15214

279 -> 283 0.15239

279 -> 285 0.21336

280 -> 292 0.19505

281 -> 291 0.10506

281 -> 293 0.12077

282 -> 291 -0.17140

282 -> 292 0.12100

Excited State 9: Singlet-E 5.0799 eV 244.07 nm f=0.0049 <S**2>=0.000

276 -> 285 0.13237

277 -> 283 0.16521

277 -> 284 0.21524

278 -> 283 0.15204

278 -> 285 -0.21336

279 -> 284 -0.15249

280 -> 293 -0.19505

281 -> 291 -0.17140

281 -> 292 -0.12103

282 -> 291 -0.10506

282 -> 293 0.12073

Excited State 10: Singlet-A 5.0802 eV 244.05 nm f=0.0070 <S**2>=0.000

272 -> 283 0.10155

273 -> 284 0.10158

274 -> 285 0.14145

275 -> 283 -0.10095

276 -> 284 0.10115

277 -> 285 0.24144

278 -> 283 -0.17593

278 -> 284 -0.17699

279 -> 283 0.17655

279 -> 284 -0.17566

280 -> 288 0.11656

280 -> 291 -0.19506

281 -> 292 -0.11562

281 -> 293 -0.16327

282 -> 292 0.16291

282 -> 293 -0.11583

Excited State 11: Singlet-A 5.3932 eV 229.89 nm f=0.0185 <S**2>=0.000

275 -> 283 -0.20344

275 -> 284 0.14039

276 -> 283 0.14038

276 -> 284 0.20345

280 -> 285 0.31168

281 -> 284 -0.10935

281 -> 290 -0.27570

282 -> 283 -0.10933

282 -> 289 -0.27569

Excited State 12: Singlet-E 5.4192 eV 228.79 nm f=0.0261 <S**2>=0.000

275 -> 284 0.12480

276 -> 283 -0.12481

280 -> 284 0.32273

281 -> 283 0.20680

281 -> 284 -0.24352

281 -> 285 0.25477

281 -> 289 0.11191

281 -> 290 -0.11411

282 -> 283 0.24352

282 -> 284 0.20680

282 -> 289 0.11413

282 -> 290 0.11191

Excited State 13: Singlet-E 5.4192 eV 228.79 nm f=0.0261 <S**2>=0.000

275 -> 283 -0.12481

276 -> 284 -0.12480

280 -> 283 0.32273

281 -> 283 0.24352

281 -> 284 0.20680

281 -> 289 0.11412

281 -> 290 0.11190

282 -> 283 -0.20680

282 -> 284 0.24352

282 -> 285 0.25477

282 -> 289 -0.11192

282 -> 290 0.11412

Excited State 14: Singlet-E 5.6788 eV 218.33 nm f=0.0034 <S**2>=0.000

276 -> 285 -0.10315

280 -> 283 -0.24995

280 -> 284 -0.33371

280 -> 289 -0.12685

280 -> 290 -0.19332

281 -> 285 0.39805

282 -> 285 0.23393

Excited State 15: Singlet-E 5.6788 eV 218.33 nm f=0.0034 <S**2>=0.000

275 -> 285 0.10315

280 -> 283 -0.33371

280 -> 284 0.24995

280 -> 289 -0.19332

280 -> 290 0.12685

281 -> 285 -0.23393

282 -> 285 0.39805

Excitation energies and oscillator strengths of tri-branched structure of **32**

Excited State 1: Singlet-A 4.2169 eV 294.02 nm f=0.0000 <S**2>=0.000

125 ->134 -0.12597

126 ->133 -0.12598

131 ->133 -0.45202

132 ->134 0.45202

This state for optimization and/or second-order correction.

Total Energy, E(TD-HF/TD-KS) = -1503.03029985

Copying the excited state density for this state as the 1-particle RhoCI density.

Excited State 2: Singlet-A 4.4263 eV 280.11 nm f=0.0000 <S**2>=0.000

130 ->135 0.12650

131 ->134 0.46375

132 ->133 0.46377

Excited State 3: Singlet-A 4.4470 eV 278.81 nm f=1.1523 <S**2>=0.000

1->4

130 ->133 -0.19785

131 ->133 0.35259

131 ->134 0.23505

132 ->133 -0.23505

132 ->134 0.35259

132 ->135 -0.25817

Excited State 4: Singlet-A 4.4470 eV 278.81 nm f=1.1523 <S**2>=0.000

1->5

130 ->134 0.19784

131 ->133 -0.23505

131 ->134 0.35260

131 ->135 0.25817

132 ->133 -0.35258

132 ->134 -0.23505

Excited State 5: Singlet-E 4.9435 eV 250.80 nm f=0.0562 <S**2>=0.000

127 ->134 0.14922

128 ->133 0.14923

128 ->135 0.18580

129 ->133 0.27174

130 ->134 0.20044

130 ->136 -0.16636

130 ->137 -0.11154

131 ->135 0.17847

131 ->136 0.13864

131 ->137 -0.14121

131 ->138 -0.13807

132 ->135 0.11119

132 ->136 -0.14122

132 ->137 -0.13864

132 ->138 0.21830

Excited State 6: Singlet-E 4.9435 eV 250.80 nm f=0.0562 <S**2>=0.000

127 ->133 0.14923

127 ->135 -0.18580

128 ->134 -0.14922

129 ->134 0.27174

130 ->133 -0.20044

130 ->136 -0.11154

130 ->137 0.16636

131 ->135 0.11119

131 ->136 0.14122

131 ->137 0.13863

131 ->138 0.21830

132 ->135 -0.17847

132 ->136 0.13864

132 ->137 -0.14122

132 ->138 0.13807

Excited State 7: Singlet-A 4.9916 eV 248.38 nm f=0.0000 <S**2>=0.000

127 ->133 0.18371

127 ->134 0.21835

128 ->133 -0.21837

128 ->134 0.18372

129 ->135 -0.26175

130 ->138 -0.22657

131 ->137 -0.29944

132 ->136 0.29946

Excited State 8: Singlet-E 5.3264 eV 232.77 nm f=0.0950 <S**2>=0.000

128 ->135 -0.13645

129 ->133 -0.15230

130 ->133 0.14156

130 ->134 0.22587

131 ->133 0.20917

131 ->135 0.27656

132 ->134 0.20917

132 ->135 0.34197

Excited State 9: Singlet-E 5.3264 eV 232.77 nm f=0.0950 <S**2>=0.000

127 ->135 0.13644

129 ->134 -0.15229

130 ->133 -0.22587

130 ->134 0.14156

131 ->134 -0.20917

131 ->135 0.34197

132 ->133 0.20917

132 ->135 -0.27656

Excited State 10: Singlet-E 5.6198 eV 220.62 nm f=0.0631 <S**2>=0.000

126 ->135 -0.15377

130 ->134 0.51492

131 ->135 -0.36655

132 ->135 -0.16898

Excitation energies and oscillator strengths of tri-branched structure of **33**

Excited State 1: Singlet-A 4.3067 eV 287.89 nm f=0.0000 <S**2>=0.000

221 -> 223 0.30717

221 -> 224 0.35052

222 -> 223 -0.35052

222 -> 224 0.30717

This state for optimization and/or second-order correction.

Total Energy, E(TD-HF/TD-KS) = -2266.66725884

Copying the excited state density for this state as the 1-particle RhoCI density.

Excited State 2: Singlet-A 4.5481 eV 272.61 nm f=0.0001 <S**2>=0.000

220 -> 225 -0.11093

221 -> 223 0.35495

221 -> 224 -0.31468

222 -> 223 0.31467

222 -> 224 0.35496

Excited State 3: Singlet-A 4.6177 eV 268.50 nm f=1.1286 <S**2>=0.000

1->4

220 -> 224 0.15650

221 -> 223 -0.33441

221 -> 224 0.27747

222 -> 223 0.27747

222 -> 224 0.33441

222 -> 225 -0.22555

Excited State 4: Singlet-A 4.6177 eV 268.50 nm f=1.1286 <S**2>=0.000

1->5

220 -> 223 -0.15650

221 -> 223 0.27748

221 -> 224 0.33440

221 -> 225 0.22555

222 -> 223 0.33441

222 -> 224 -0.27746

Excited State 5: Singlet-E 5.0624 eV 244.91 nm f=0.1025 <S**2>=0.000

217 -> 223 0.16416

218 -> 224 -0.16417

218 -> 225 0.20130

219 -> 223 -0.23954

219 -> 224 -0.12909

220 -> 224 -0.19008

220 -> 226 0.18144

221 -> 225 -0.18876

221 -> 226 -0.14050

221 -> 227 -0.14560

221 -> 228 0.10874

222 -> 226 0.14562

222 -> 227 -0.14051

222 -> 228 0.24768

Excited State 6: Singlet-E 5.0625 eV 244.91 nm f=0.1025 <S**2>=0.000

217 -> 224 0.16414

217 -> 225 0.20130

218 -> 223 0.16420

219 -> 223 -0.12909

219 -> 224 0.23954

220 -> 223 -0.19008

220 -> 227 0.18144

221 -> 226 -0.14562

221 -> 227 0.14047

221 -> 228 0.24768

222 -> 225 0.18876

222 -> 226 -0.14055

222 -> 227 -0.14560

222 -> 228 -0.10874

Excited State 7: Singlet-A 5.0837 eV 243.88 nm f=0.0000 <S**2>=0.000

217 -> 223 -0.16002

217 -> 224 0.22040

218 -> 223 -0.22035

218 -> 224 -0.16000

219 -> 225 0.23513

220 -> 228 0.21777

221 -> 227 0.29873

222 -> 226 0.29868

Excited State 8: Singlet-E 5.5404 eV 223.78 nm f=0.1019 <S**2>=0.000

219 -> 223 0.13341

220 -> 224 -0.19098

221 -> 224 0.17701

221 -> 225 -0.17522

222 -> 223 0.17701

222 -> 225 0.48873

Excited State 9: Singlet-E 5.5404 eV 223.78 nm f=0.1019 <S**2>=0.000

219 -> 224 -0.13341

220 -> 223 -0.19098

221 -> 223 -0.17701

221 -> 225 0.48873

222 -> 224 0.17701

222 -> 225 0.17522

Excited State 10: Singlet-E 5.9305 eV 209.06 nm f=0.2447 <S**2>=0.000

219 -> 224 0.14365

220 -> 223 0.52150

220 -> 224 -0.10375

221 -> 225 0.28064

222 -> 225 0.11420

Excited State 11: Singlet-E 5.9305 eV 209.06 nm f=0.2447 <S**2>=0.000

219 -> 223 -0.14365

220 -> 223 0.10375

220 -> 224 0.52150

221 -> 225 -0.11420

222 -> 225 0.28064

Excited State 12: Singlet-A 6.0007 eV 206.61 nm f=0.0000 <S**2>=0.000

215 -> 224 0.10516

216 -> 223 -0.10516

217 -> 224 -0.22043

217 -> 227 0.11883

218 -> 223 0.22043

218 -> 226 0.11884

219 -> 228 0.11910

220 -> 225 -0.23208

221 -> 226 -0.16808

221 -> 227 0.29951

222 -> 226 0.29950

222 -> 227 0.16807

Excited State 13: Singlet-A 6.0844 eV 203.77 nm f=0.0000 <S**2>=0.000

217 -> 223 0.19740

217 -> 224 -0.17104

218 -> 223 0.17104

218 -> 224 0.19740

219 -> 225 -0.18123

219 -> 228 -0.12727

220 -> 225 0.11380

221 -> 226 0.29612

221 -> 227 0.15619

221 -> 229 -0.11294

222 -> 226 0.15618

222 -> 227 -0.29611

222 -> 230 -0.11294

Excited State 14: Singlet-E 6.1340 eV 202.12 nm f=0.3344 <S**2>=0.000

219 -> 223 0.33703

219 -> 224 0.10067

220 -> 223 -0.13894

220 -> 224 0.17043

221 -> 226 -0.23766

221 -> 227 -0.23742

221 -> 228 0.10322

222 -> 226 0.23742

222 -> 227 -0.23767

Excited State 15: Singlet-E 6.1340 eV 202.12 nm f=0.3344 <S**2>=0.000

219 -> 223 -0.10067

219 -> 224 0.33703

220 -> 223 -0.17043

220 -> 224 -0.13894

221 -> 226 0.23742

221 -> 227 -0.23766

222 -> 226 0.23767

222 -> 227 0.23742

222 -> 228 0.10321

[1] S. Sinha, Z. Kelemen, E. Hümpfner, I. Ratera, J. P. Marval, J. P. Jurado, C. Viñas, F. Teixidor, R. Núñez, *Chem. Commun.*, 2022, **58**, 4016–4019
[2] J. Ochi, K. Tanaka, Y. Chujo, *Angew. Chem. Int. Ed.* 2020, 59, 9841–9855.

List of publications

1) Red light-emitting Carborane-BODIPY dyes: Synthesis and properties of visible-light tuned fluorophores with enhanced boron content. Chiara Bellomo, Davide Zanetti, Francesca Cardano, Sohini Sinha, Mahdi Chaari, Andrea Fin, Andrea Maranzana, Rosario Núñez, Marco Blangetti and Cristina Prandi, *Dyes & Pigments*, 2021, 194, 109644.

2) *o*-Carborane-based fluorophores as efficient luminescent systems both as solids and as water-dispersible nanoparticles. Sohini Sinha, Zsolt Kelemen, Evelyn Hümpfner, Imma Ratera, Jean-Pierre Malval, José Piers Jurado, Clara Viñas, Francesc Teixidor and Rosario Núñez, *Chem.Comm.* 2022, 58, 4016.